SPATIAL INFORMATION TECHNOLOGY BASED MODELING APPROACH FOR AIR POLLUTION ASSESSMENT

BAO ZHEN WANG

A Thesis

In the Department

of

Building, Civil and Environmental Engineering

Presented in Partial Fulfillment of the Requirements

For the Degree of

Doctor of Philosophy (Civil Engineering) at

Concordia University

Montreal, Quebec, Canada

August 2013

CONCORDIA UNIVERSITY
SCHOOL OF GRADUATE STUDIES

This is to certify that the thesis prepared

By: Bao Zhen Wang

Entitled: Spatial Information Technology Based Modeling Approach for Air Pollution Assessment

and submitted in partial fulfillment of the requirements for the degree of

Doctor of Philosophy (Civil Engineering)

complies with the regulations of the University and meets the accepted standards with respect to originality and quality.

Signed by the final examining committee:

Dr. Narayanswamy R Sivakumar — Chair

Dr. Francois Cavayas — External Examiner

Dr. Yong Zeng — External to Program

Dr. Fariborz Haghighat — Examiner

Dr. Amruthur S. Ramamurthy — Examiner

Dr. Zhi Chen — Thesis Supervisor

Approved by

Chair of Department or Graduate Program Director

August 10th, 2013

Dean of Faculty

ABSTRACT

It is an accepted fact that our atmosphere bears an increasing load of pollutants: carbon dioxide, ozone, oxides of nitrogen and sulfur, volatile organic compounds (VOC_s), particulates, and heavy metals. The adverse health and environment effects of air pollution have been a major concern in shaping our environmental quality. The World Health Organization (WHO) estimates that 1.5 billion people living in the urban areas throughout the world are exposed to dangerous levels of air pollution and 2 million premature deaths occur annually. A year shortening of life expectancy by an average is also the result of air pollution. Air pollution risk assessment, especially in urban areas, is currently one of the most important environmental issues for human health.

Air quality model is a useful tool to simulate the complex dispersion of pollutants in the atmosphere and to predict the long-term effects on ground and spatial levels, and it plays an important role in air pollution risk assessment. Since there are inherent complexities and uncertainties associated with land use information, meteorological conditions, emission spatial allocation, as well as physical and chemical reactions in air quality modeling, it still needs to be further explored. The emergences of new spatial information technologies, such as satellite remote sensing technology and Geographic Information Systems (GIS) open a new era for air quality modeling and air pollution risk assessment, making it possible to predict the spatial concentration distributions of air pollutants on larger scales with finer details.

The objectives of the work in this thesis include the development of GIS-based air quality modeling system to predict the spatial concentration distributions of ambient air pollutants ($PM_{2.5}$, NO_2, SO_2, and CO), the development of satellite remote sensing approach to retrieve aerosol optical depth (AOD) and to derive ground-level pollutant concentrations ($PM_{2.5}$ and NO_2), and the development of fuzzy aggregation risk assessment approach to evaluate the health risks of multiple air pollutants.

A GIS-based multi-source and multi-box (GMSMB) air quality modeling approach is developed to predict the spatial concentration distribution of four air pollutants ($PM_{2.5}$, NO_2, SO_2, and CO) for the state of California. A satellite remote sensing approach is investigated to derive the ground-level NO_2 concentrations from the satellite Ozone

Monitoring Instrument (OMI) tropospheric NO_2 column data for the same location and same period. The GMSMB modeling and satellite-derived results are cross-verified through comparing with each other and with the in-situ surface measurements. Furthermore, a fuzzy aggregation-ordered weighted averaging (OWA) risk assessment approach is developed to evaluate the integrated health risks of the four air pollutants.

An improved aerosol optical depth (AOD) retrieval algorithm is proposed for the MODIS satellite instrument at 1-km resolution. In order to estimate surface reflectances over variable cover types, including bright and dark surfaces, a modified minimum reflectance technique (MRT) is used. A new lookup table (LUT) is created using the Second Simulation of the Satellite Signal in the Solar Spectrum (6S) Radiative Transfer Code for the presumed aerosol types. The MODIS-retrieved AODs are used to derive the ground-level $PM_{2.5}$ concentrations using the aerosol vertical profiles obtained from the GEOS-Chem simulation. The developed method has been examined to retrieve the AODs and evaluate the concentration distribution of $PM_{2.5}$ over the city of Montreal, Canada in 2009. The satellite-derived $PM_{2.5}$ concentrations are ranging from 1 to 14 $\mu g/m^3$ in Montreal, which are in good agreement with the in-situ surface measurements at all monitoring stations. This suggests that the method in this study can retrieve AODs at a higher spatial resolution than previously and can operate on an urban scale for $PM_{2.5}$ assessment.

Furthermore, the ground-level $PM_{2.5}$ concentrations and corresponding health risks are investigated using the retrieved AOD from the satellite instruments of MODIS and MISR for the extended East Asia, including China, India, Japan, and South Korea. The results are validated with the monitoring values and literatures. Depending on the regression analysis, the GDP growth rates, population growth rates, and coal consumptions are the main reasons of the higher $PM_{2.5}$ concentrations in Beijing. Some mitigating measurements are then proposed and the future trend is predicted. The developed method can be used to other regions for making cost-effective strategy to control and improve air pollution.

ACKNOWLEDGEMENTS

First and foremost, I would like to express my deep and sincere gratitude and acknowledge to my supervisor, Dr. Zhi Chen, for his guidance, patience, and financial support throughout my Ph.D. study. His academic advices and professional mentorship have helped me establish a solid foundation for my research. Especially, his wisdom, vision and inspiration have pushed me to the limit beyond what I had thought impossible.

I would also like to thank other committee members: Dr. Fariborz Haghighat, Dr. A.S Ramamurthy, and Dr. Yong Zeng, for their valuable advices and helpful suggestions during my doctoral study. I have been fortunate to have Dr. François Cavayas as the External Examiner in my thesis committee. He has extensive knowledge and experiences in satellite remote sensing and he has given me many valuable suggestions. I should pay my special appreciation to him.

I would also like to express my sincere thanks to my friends and colleagues: Dr. Sangsoo. Han, Dr. Lin Zhao, Fang Lu, Yuan Yuan, and all of them who have directly or indirectly helped me to complete this work.

Last but not the least, I wish to extend my deepest gratitude and appreciation to my families for their unconditional support and encouragement. In particular, my husband Hao Zhang, I have been accompanied and supported by him who made this long journey easier. This thesis is simply impossible without his understanding, strength and help. I must say a thank-you to him from the bottom of my heart for everything he has done to me that no word could explain.

TABLE OF CONTENTS

LIST OF TABLES

LIST OF FIGURES

LIST OF SYMBOLS

Section 2.3

C_i	chemical mixing ratio
U	wind vector
∇	vector of partial derivatives
Pi	local source of chemical *i*
Li	local sink

Section 3.1

d	wind direction
i, *j*, *k*	sub-boxes number at wind, crosswind and vertical direction, respectively
$C^d_{i-1,\,j,k}$	inflow pollutant concentration (i.e., "background concentration") into the sub-box *i,j,k* under wind direction *d* ($\mu g/m^3$)
$C^d_{i,j,k}$	average pollutant concentration in sub-box *i,j,k* under wind direction *d* ($\mu g/m^3$)
E	diffusion coefficient at vertical direction (m^2/sec)
E'	diffusion coefficient at crosswind direction (m^2/sec)
h	height of each sub-box (m)
L	length of each sub-box (m)

W	width of each sub-box (m)
$Q_{i,j,k}$	average pollutant emission rate into sub-box i,j,k ($\mu g/m^2 \cdot sec$)
U_k^d	mean wind speed of layer k at wind direction d (m/sec)
$R^d_{ci,j,k}$	chemical removal rate in sub-box i,j,k at wind direction d ($\mu g/sec$)
$R^d_{pi,j,k}$	physical removal rate in sub-box i,j,k at wind direction d ($\mu g/sec$)
$R^d_{dpi,j,k}$	dry deposition rate in sub-box i,j,k under wind direction d ($\mu g/sec$)
v_d	deposition velocity (m/sec)
r_a	aerodynamic resistance (s/m)
r_d	deposition layer resistance (s/m)
v_g	gravitational settling velocity for particles (m/s)
f	fraction of particulate substance smaller than 2.5 μm in diameter
v_{df}	deposition velocity of fine particulates (m/s)
v_{dc}	deposition velocity of coarse particulate substance (m/s)
Λ	scavenging ratio (1/sec)
λ	wet scavenging coefficients (1/sec)

P	precipitation rate (mm/hr)
P_0	reference precipitation rate (mm/hr)
$R^d_{wpi,j,k}$	wet deposition rate in sub-box i,j,k under wind direction d (μg/sec)
k	first order rate constant (1/sec), $k = 0.693 / t_{1/2}$
$t_{1/2}$	half-life of pollutant
$C_{i,j,k}$	concentration of the pollutant in sub-box i,j,k (μg/m^3)
f^d	annual frequency of wind in direction d
$\{x_r, y_r, z_r\}$	coordinates of a receptor (m)
z_r	height of a receptor relative to the stack base (m)
Q	emission rate (μ g/sec)
u	wind speed at stack top (m/s)
z_{ieff}	effective mechanical mixed layer height (m)
σ_y	total lateral dispersion (m)
σ_z	total vertical dispersion (m)
h_e	effective plume height (i.e., stack height plus the plume rise) (m)
f_y	lateral distribution function with meander (m^{-1})
Δh	plume rise height
F_b	stack buoyant flux (m^4/s^3)

F_m	stack momentum flux (m^4/s^2)
g	gravitational acceleration (m/s^2)
w_s	exit velocity (m/s)
r_s	stack radius (m)
T_s	temperature (K)
T_a	ambient air temperature (K)
u_p	wind speed (m/s)
N	Brunt-Vaisala frequency
θ	temperature at the height z_i (K)
z_{im}	mechanical mixed layer height (m)
z_{ieff}	effective mechanical mixed layer height (m)
u_*	surface friction velocity (m/s)
$C_T\{x_r, y_r, z_r\}$	total pollutant concentration at receptor ($\mu g/m^3$)
$C\{x_r, y_r, z_r\}$	concentration contributed from the horizontal plume ($\mu g/m^3$)
$C\{x_r, y_r, z_p\}$	concentration contributed from the terrain-following state ($\mu g/m^3$)
λ	plume state weighting function (dimensionless)
z_p	height of a receptor above the local ground (m)
z_t	terrain height at a receptor referenced to the stack base

	elevation (m)
ϕ_p	fraction of the plume mass below the dividing streamline height H_c (m)
$C_s\{x_r, y_r, z_r\}$	pollutant concentration in the absence of a hill for stable conditions (μg/m^3)
C_m	modeling concentrations
C_o	monitoring concentrations

Section 3.2

$I(\lambda)$	solar spectrum after absorption (earthshine radiance)
$I_0(\lambda)$	extraterrestrial solar spectrum (solar irradiance)
σ_i	relevant cross sections of absorbing species
ci	unknown species column densities
l	index of atmospheric layer
m_l	altitude dependent box air mass factors
x_a	a priori profile shape of NO_2 (molecules/cm^2)
b	model parameters
S	surface level NO_2 mixing ratio (ppb)
Ω	tropospheric NO_2 vertical column density (10^{15} molecules/cm^2)
v	ratio of local OMI NO_2 column to the mean OMI NO_2

	column field over a GEOS-Chem grid (dimensionless)
Ω_G^F	simulated free-tropospheric NO_2 vertical column density over a GEOS-Chem grid (10^{15} molecules/cm^2)

Section 3.3

λ	wavelength
ρ_λ^S	surface reflectance
ρ_λ^*	top-of-atmosphere reflectance
ρ_λ^{Ray}	Rayleigh path reflectance
ρ_λ^a	aerosol reflectance
ρ_λ^h	hemispheric reflectance
θ_0	sun zenith angle
θ_s	satellite zenith angle
$T_\lambda(\theta_0)$	total atmospheric transmittance
T_λ^{Ray}	Rayleigh scattering
T_λ^a	aerosol extinction
τ_λ^{Ray}	Rayleigh scattering optical thickness
p_λ^{Ray}	phase function of Rayleigh scattering
$m(\theta_0)$	airmass factors for the illumination
$m(\theta_s)$	airmass factors observation

Θ	scattering angle
δ_{λ}^{Ray}	Rayleigh polarization factor
ρ_{λ}^{6Sa}	aerosol reflectance modeled from 6S code
x^2	residual of aerosol reflectance
τ_{λ}	aerosol optical depth
$\Delta\rho_{\lambda}^{*}$	error tolerance
η	factor relating satellite-derived surface factor AOD to ground-level $PM_{2.5}$ concentration ($\mu g/m^3$)

Section 3.4

$\mu(x)$	membership function
F	membership grade for integrated risk level
w_i	weighting coefficient of pollutant *i*
r_{ij}	membership grade between pollutant *i* and risk level *j*

Section 5.1

e_i	classifying representative value
s_i	benchmark
m	number of fuzzy set
$e(m)$	classifying representative value of each fuzzy set
$r_m(x)$	membership grade of each pollution factor belongs to each classifying representative value

LIST OF ACRONYMS

6S	Satellite Signal in the Solar Spectrum radiative transfer code
AHP	Analytic Hierarchy Process
AN	Alkyl Nitrates
AOD	Aerosol Optical Depth
AMFtrop	Tropospheric Air Mass Factor
AQI	Air Quality Index
AQMIS	Air Quality and Meteorological Information System
AQS	Air Quality System
BRDF	Bidirectional reflectance distribution function
BTH	Beijing, Tianjin, and Hebei
CAAQS	California Ambient Air Quality Standard
CARB	California Air Resources Board
CCRS	Canada Centre for Remote Sensing
CF	Correction Factor
CIESIN	Columbia's Center for International Earth Information Science Network
CMAQ	Community Multiscale Air Quality
CTM	Chemical transport model s

DOAS	Differential Optical Absorption Spectroscopy technique
DOMINO	Dutch OMI NO_2 algorithm
EOF	Empirical Orthogonal Function
EOS	Earth Observing System
EPI	Environmental Performance Index
ERSI	Environmental Systems Research Institute, Inc.
ESA	European Space Agency
FGD	Fuel-Gas Desulfurization
GDP	Gross Domestic Product
GEOS	Goddard Earth Observing System
GHGs	Greenhouse Gases
GIS	Geographic Information System
GLM	General Linear regression Model
GMAO	NASA Global Modeling and Assimilation Office
GMSMB	GIS-based Multi-Source and Multi-Box model
GOME	Global Ozone Monitoring Experiment
HDF	Hierarchical Data Format
IMPROVE	Interagency Monitoring of Protected Visual Environments
KNMI	Royal Netherlands Meteorological Institute

LAADS	Level 1 and Atmosphere Archive and Distribution System at NASA Goddard Space Flight Center
LULC	Land Use/Land Cover
LUT	LookUp Table
MISR	Multi-angle Imaging Spectroradiometer
MODIS	Moderate Resolution Imaging Spectroradiometer
MRT	Minimum Reflectance Technique
NAAQO	National Ambient Air Quality Objectives in Canada
NAAQS	National Ambient Air Quality Standards in the U. S.
NAPS	National Air Pollution Surveillance Network in Canada
NASA	National Aeronautics and Space Administration
NDVI	Normalized Difference Vegetation Index
NED	National Elevation Dataset
NEI	National Emission Inventory
NISE	Near Real-Time Ice and Snow Extent
NMB	Normalized Mean Bias
NME	Normalized Mean Error
NOAA	National Oceanic and Atmospheric Administration
NRCan	Natural Resources Canada
NSIDC	National Snow and Ice Data Center

NTS	National Topographic System
OMI	Ozone Monitoring Instrument
OWA	Ordered Weighted Averaging
PAH	Polycyclic Aromatic Hydrocarbon
PAN	PeroxyAcyl Nitrates
$PM_{2.5}$	Particulate matter with aerodynamic diameter less than 2.5 μm
PNAM	Parallel Naples Airshed Model
RAM	Retrieval-Assimilation-Modeling
REEF	Resource Efficient and Environment-Friendly
RIAT	Regional Integrated Assessment Tool
RMSE	Root Mean Square Error
ROG	Reactive Organic Gas
RS	Remote Sensing
RSPM	Respirable Suspended Particulate Matter
RSQA	Réseau de surveillance de la qualité de l'air de la ville de Montréal
SCD	Slant Column Density
SCDtrop	Tropospheric Slant Column Density
SCIAMACHY	SCanning Imaging Absorption spectroMeter for

	Atmospheric CHartographY
SNA	Sulfate-Nitrate-Ammonium
SPSS	Statistical Package for the Social Science
TEMIS	Tropospheric Emission Monitoring Internet Service
TOA	Top-Of-Atmosphere
UAM	Urban Airshed Model
USGS	the United States Geological Survey
UTM	Universal Transverse Mercator coordinate system
VBA	Visual Basic Application
VCD	Vertical Column Density
VOC	Volatile Organic Compound
WHO	World Health Organization

Chapter 1 Introduction

1.1 Background

Breathing is not optional. It is essential to a life, and air has to be used (Harrop, 2002). However, serious air pollution has happened since the first industrial revolution (Vallero, 2008). Especially, an accelerating urban growth as a global phenomenon since 1960s has elevated the air pollution to become a major environmental concern all over the world due to their potential adverse effects on human health and environment (Karnosky, 2003).

Air pollution can be defined as the presence of one or more pollutants, or combinations thereof in the external atmosphere, in such quantities and of such duration as may be or may cause injury to human health, plant, animal life, properties, or which unreasonably interfere with the comfortable enjoyment of life (Canter, 1996; USEPA, 2007).

The World Health Organization (WHO) estimates that 1.5 billion people living in urban areas throughout the world are exposed to the dangerous levels of air pollution, 2 million premature deaths occur annually, and a year of life expectancy by average is shortened as the results of air pollution (Krzyzanowski et al., 2005; Ayres et al., 2006). Air pollution has been ranked within the top 10 causes of worldwide death and disability (WHO, 2009).

In fact, for most developed and developing countries, motor traffic emissions now pose a principal threat to air quality, particularly in urban areas (Austin et al., 2002). Petrol and diesel engines emit a wide variety of pollutants, principally carbon monoxide (CO), nitrogen oxides (NO_x), volatile organic compounds (VOC_s) and particulates, which have an increasing impact on air quality (Harrop, 2002). Air pollution hovers at unhealthy levels in almost every major city, threatening people's ability to breathe and placing lives at risk (Vallero, 2008). In the U.S., air pollution remains a real and urgent threat to public health, despite real progress since 1970. 70,000 premature deaths each year are tied to air pollution (Peled, 2011). In the UK, air pollution is estimated to reduce

the life expectancy of every person by an average of 7-8 months (Defra, 2007). In Canada, scientific evidence based on data from eight Canadian cities shows that 5,900 deaths can be linked to air pollution every year (Environment Canada, 2012). 14,000 citizens of Sweden die each year due to the exposure to environmental pollutants (WHO, 2008). A report of WHO estimates that diseases triggered by indoor and outdoor air pollution kill 656,000 Chinese citizens each year (Platt, 2007). In addition, stratospheric ozone depletion due to air pollution has long been recognized as a threat to human health as well as to the Earth's ecosystems (WMO, 2010). Even with the growing "green movement," air pollution in some parts of the world actually is worsening in the past several years. Therefore, it is emergent and paramount to protect and manage air quality for human health and environment. New efforts are essential to assess the current and future air quality for effective air pollution control and management planning.

Air quality modeling plays an important role in air pollution risk assessment and management as a useful tool to simulate the complex dispersion of air pollutants in the atmosphere and predict the long-term effects on ground and spatial levels. Many air quality models, such as Gaussian models, airshed models, box models and photochemical models have been developed in the past (Holmes and Morawska, 2006). For example, the Gaussian-type models have been developed to predict the air quality for decades (Owen et al., 2000; Kuhlwein et al., 2002; Tsuang et al., 2003). Two widely applied models, AERMOD and CALPUFF, use Gaussian models for steady-state conditions (Scire et al., 2000; Cimorelli et al., 2004). The Gaussian models are often limited to point sources on a local scale, usually less than 50 km with limited consideration of chemical and physical removal mechanisms in the atmosphere (British Columbia Ministry of Environment, 2008). The airshed models are developed based on extended analyses of the interrelationships among a number of factors that affect ambient air quality. However, their applicability could be affected by data availability and quality as well as the high computational requirements for the field calibration (Lashmar and Cope, 1995; Vivanco et al., 2009). The box model has been considered as a practical tool to handle the regional physical characteristics of air pollutants in the ambient atmospheric environment with relatively low requirements for meteorological data and computational efforts (Stein et al., 2007). However, box model itself is designed to examine the pollutant concentrations on regional rather than on local scale, which

ignores the contributions from individual sources (Stein et al., 2007). Recent studies on box models extend the smallest grid size applied in such models to the order of 1 km or greater (Weijers et al., 2004; Isakov et al., 2007).

One potential improvement for the existing air quality models is to put forward a hybrid approach, namely, a regional scale model coupled with a local scale model, which allows taking into account the emissions from both point and area source, as well as complex meteorological conditions. Only few previous studies have reported this combination (Gillani and Godowitch, 2005; Stein et al., 2007).

Moreover, there are some significant effects resulting from the various geographical features, such as complicated surfaces (open water, land, forests, deserts, snow/ice, urban zones and coastal areas) and terrain features (mountains, valleys, hills, bowls and plains), when trying to use air quality models to simulate the air pollutant dispersion. These geophysical features cause complex flows and dispersion patterns and present many challenges for air quality modeling (British Columbia Ministry of Environment, 2008). Therefore, accurate land use information is important in meteorology for land surface exchanges, in emission modeling for emission spatial allocation, and in air quality modeling for chemical surface fluxes (Steyn et al., 2009). Since air quality modeling involves obvious spatial and geographic features, the Geographic Information System (GIS) is the effective tool for spatial analyst and environmental modeling (Goodchild, 2003; Ivanov and Zatyagalova, 2008). GIS provides an efficient way to store spatial data for use in air quality modeling and to spatially express the modeling results. The methods for integrating environmental models with GIS have been discussed by many researchers (Karimi and Houston, 1996; Matejicek et al., 2006). In general, GIS can be used to support environmental models through “low”, “medium” and “high” level integrations, which are generally referred to as loosely-coupled, closely-coupled and fully-coupled modes, respectively (Goodchild, 2003). Though loosely- and closely-coupled mode may have issues on data exchange, compatibility and efficiency while utilizing GIS, the integration has extended traditional environmental simulation to GIS-based modeling with geo-referenced information (Matejicek et al., 2006; Elbir et al., 2010).

The fully-coupled mode is known as an embedded-coupling, where the environmental models are developed within a GIS framework, so that all GIS functions and spatial database are accessed directly (Lakhan, 2003). Additionally it can improve the computational efficiency and accuracy by reducing data redundancy and data exchange errors in modeling process (Lakhan, 2003). However, most of the recent modeling efforts involving GIS are based on the loosely or closely coupled modes (Canepa et al., 2007; Elbir et al., 2010). Few studies have been reported on the fully-coupled mode with GIS in air quality models (Gulliver and Briggs, 2011).

In addition, complete spatial coverage of ground-level pollutant measurements are needed for air quality assessment (Brook et al., 2007). However, the stations in the current pollutants monitoring network are sparse and unevenly spaced, which leads to an impaired air quality assessment by insufficient observations in clean versus polluted areas (Lamsal et al., 2008). Recent advances in satellite remote sensing (RS) technology coupled with experimental verification bring remote pollution measurements very close to a practical state. It can provide two important sources of information compared with surface and aircraft monitoring data: more complete spatial coverage and a vertically integrated measure of atmospheric components (Engel-Cox, et al., 2004; Edwards, 2006). An increasing number of studies have reported the applications of RS for air quality prediction in the past two decades (Schaub et al., 2006; Uno et al., 2007; Sheel et al., 2010). The surface concentrations of pollutant obtained from RS have been an important complement to the existing ground-based monitoring networks by extending spatial coverage and by being specific to pollutants (Lamsal et al., 2008). However, there are inherent problems in derivation of ground-level pollutant concentrations using satellite remote sensing measurements. For example, cloud and surface albedo interferences, a priori profile shape, coarse resolution, and lower accuracy, make the applications of RS for air quality prediction only on global or regional scales (e.g. Liu et al., 2004; 2005; van Donkelaar et al., 2006; Lamsal et al., 2008; Hains et al., 2010; Lee et al., 2011; Halla et al., 2011). It is desirable to further explore the applications of RS at local scale with higher spatial resolution and accuracy.

Consequently, a fully integrated GIS-based multi-source and multi-box (GMSMB) air quality modeling approach is proposed in this study, where a spatial extended multi-

box model coupled with a multi-source and multi-grid Gaussian model are built within the ArcGIS framework. Through the integration with GIS, it allows the spatial analyst on both regional and local scales with geo-referenced database. The physical and chemical processes are also taken into account with land use/land cover characterizations. In addition, the satellite remote sensing measurements from OMI, MODIS, and MISR are employed to derive the ground-level concentrations of air pollutants (NO_2 and $PM_{2.5}$) at local scale with higher spatial resolution and accuracy. The GMSMB modeling results, the satellite-derived ground-level pollutant concentrations, and the in-situ surface measurements are cross-verified by intercomparison. Based on the validated results, a fuzzy aggregation-ordered weighted averaging (OWA) analysis approach is developed to evaluate the integrated air pollution risk associated with multiple air pollution factors and evaluation criteria in a GIS-based air quality management system. The integrated air pollution risk assessment can be used to support decision making on air quality control and management planning.

1.2 Objectives

The objectives of this thesis include the development of GIS-based air quality modeling system to predict the spatial concentration distributions of ambient air pollutants; the application of satellite remote sensing approach to derive the ground-level NO_2 concentrations; the development of satellite remote sensing approach to retrieve aerosol optical depth (AOD) and to derive ground-level $PM_{2.5}$ concentrations; and the development of fuzzy aggregation risk assessment approach to evaluate the health risks arising from multiple air pollutants. More specifically, this thesis includes the following tasks:

(1) To develop a fully integrated GIS-based multi-source and multi-box (GMSMB) air quality modeling approach to predict the spatial concentration distribution of ambient air pollutants. Through the integration with GIS, it allows the spatial analyst on both regional and local scales with geo-referenced database. The physical and chemical processes are also taken into account with land use/land cover characterizations. The developed modeling approach is applied to predict the spatial concentration distributions of air pollutants in the state of California.

(2) To investigate a fuzzy aggregation-ordered weighted averaging (OWA) risk assessment approach to evaluate the integrated health risks arising from multiple air pollutants with aid of GIS. This approach is used to assess the integrated health risks based on the GMSMB modeling results in the state of California.

(3) To derive the ground-level NO_2 concentrations from the satellite Ozone Monitoring Instrument (OMI) tropospheric NO_2 vertical column densities (VCDs) using the global three-dimensional chemical transport model GEOS-Chem. A case study of North America, which focuses on the state of California is conducted.

(4) To develop an improved aerosol optical depth (AOD) retrieval algorithm for the Moderate Resolution Imaging Spectroradiometer (MODIS) satellite instrument at 1-km resolution for urban area. A new lookup table (LUT) is created using the Second Simulation of the Satellite Signal in the Solar Spectrum (6S) radiative transfer code and the MODIS Sun-Sat geometry for the AOD retrieval. The retrieved AODs are used to derive the ground-level $PM_{2.5}$ concentrations using the local scaling factors acquired from the GEOS-Chem simulation. The developed approach is employed to evaluate the ground-level $PM_{2.5}$ concentrations for the island of Montreal, Canada.

(5) To estimate the ground-level $PM_{2.5}$ concentrations and corresponding health risks using the combined AOD from the satellite instruments of MODIS and MISR (Multi-angle Imaging Spectroradiometer) for the extended East Asia, including China, India, Japan, and South Korea.

1.3 Thesis Organization

This thesis is organized in nine chapters:

Chapter 1 introduces the research background, states the research problems, specifies the research objectives and significance, and introduces the research methodologies.

Chapter 2 provides an extensive review of the literatures on air quality modeling, GIS and RS application, and fuzzy aggregation risk assessment approach.

Chapter 3 describes the theories and methodologies about developing the fully integrated GMSMB modeling approach, deriving the ground-level NO_2 concentrations from OMI tropospheric NO_2 column retrievals, developing the improved AOD retrieval algorithm for MODIS satellite instrument, estimating the ground-level $PM_{2.5}$ concentrations from satellite AOD retrievals, and developing the fuzzy aggregation - OWA risk assessment approach.

Chapter 4 presents a case study of applying the GMSMB modeling approach to predict the spatial concentration distributions of four criteria pollutants ($PM_{2.5}$, NO_2, SO_2, and CO) in the state of California in 2008.

Chapter 5 depicts a case study of evaluating the integrated air pollution risk using the fuzzy aggregation- OWA risk assessment approach based on the modeling results in Chapter 4.

Chapter 6 presents a case study of deriving the ground-level NO_2 concentrations from OMI tropospheric NO_2 VCDs for the state of California in 2008. The OMI-derived, GMSMB modeling, and in-situ surface measurement results of the ground-level NO_2 concentrations are cross-verified through regression analysis.

Chapter 7 depicts a case study of retrieving AOD at 1-km resolution from MODIS aerosol measurements for the island of Montreal, Canada in 2009.

Chapter 8 provides a case study of deriving ground-level $PM_{2.5}$ concentrations and assessing the health risk from the combined MODIS and MISR AOD retrievals for the extended East Asia in 2001-2011.

Chapter 9 presents the conclusions and contributions as well as the recommendations for further research.

Chapter 2 Literature Review

This chapter presents an overview of the air quality modeling, the application of GIS and satellite remote sensing (RS) in air quality modeling, and the fuzzy aggregation risk assessment approach. These modeling, spatial information techniques and risk assessment method are used in this research to estimate the air pollutant concentrations at ground-level and the corresponding health risk.

2.1 Air Quality Modeling

Many air quality models, such as Gaussian model, airshed model, box model and photochemical model, have been reported to be used for the prediction of air quality in the past decades (Lashmar and Cope, 1995; Macdonald et al., 1996; Winkler and Chock, 1996; Middleton, 1998; Barone et al., 2000; Muller et al., 2000; Jorquera, 2002a; 2002b; Arystanbekova, 2004; Holmes and Morawska, 2006; Defra, 2007; Vivanco et al., 2009).

For Gaussian-type models, Owen et al. (2000) calculated the concentrations of NO_x in London by using an urban scale Gaussian dispersion model; Kuhlwein et al. (2002) developed a Gaussian multi-source model to calculate pollutant concentrations in the Augsburg area of southern Germany; Tsuang et al. (2003) applied a Gaussian trajectory transfer-coefficient model for the estimation of the source/receptor relationship; Arystanbekova (2004) proposed Gaussian model for diagnosis and prognosis of atmospheric pollution level at damage emissions. Even two widely applied models, AERMOD and CALPUFF, are also based on Gaussian models for steady-state conditions (Scire et al., 2000; Cimorelli et al., 2004). Generally, the Gaussian models are often limited to point sources on a local scale, usually less than 50 km with limited consideration of chemical interactions and physical removal mechanisms in the atmosphere (British Columbia Ministry of Environment, 2008).

For airshed models, Barone et al. (2000) developed the Parallel Naples Airshed Model (PNAM) for the numerical simulation of air pollution episodes in urban and regional scale domains; Baertsch-Ritter et al. (2003) applied the 3-D photochemical Urban Airshed Model (UAM) with variable grid to investigate the temporal and spatial

dynamics of the photo-oxidant production in the highly polluted Milan area of Italy; Oanh and Zhang (2004) applied the integrated variable-grid urban airshed model to investigate photochemical pollution in Thailand. The airshed models were developed based on detailed analyses of complicated interrelationships among a number of factors that affect ambient air quality. However, their applicability is often affected by limitations in data availability/quality and the costly processes of meteorological survey, as well as the high computational requirements for field calibration (Lashmar and Cope, 1995; Vivanco et al., 2009).

For box models, Jorquera (2002a, 2002b) applied a box model to estimate the contributions of different economic activities to the air pollutant in Santiago of Chile; Aumont et al. (2003) applied a two-layer box model to examine the contribution of nitrous acid (HONO) photolysis to the primary production of OH radicals and the impact of HONO sources to the O_3 and NO_x budgets; Lin et al. (2004) proposed a Lagrangian box model to locate the influential pollution sources and estimate their contributions to pollutant concentrations observed at a receptor site in southern Taiwan by taking into account the effects of source emissions, atmospheric dilution, and chemical transformation and deposition; Meszaros et al. (2004) examined the European carbon monoxide (CO) budget with the help of a box-model which allows the assessment of atmospheric CO concentration change caused by the CO emission and chemical production in Europe; Shon et al. (2005) employed a photochemical box model to estimate reactive gaseous mercury concentrations in the urban atmospheric boundary layer of Seoul in Korea. The box model has been considered as a practical tool to handle the regional physical characteristics of air pollutants in the ambient atmospheric environment with relatively low requirements for meteorological data and computational efforts (Middleton, 1998; Stein et al., 2007). However, box model itself is designed to examine the pollutant concentrations on regional rather than on local scale, which ignores the contributions from individual sources (Stein et al., 2007). Recent studies on box models extend the smallest grid size applied in such models on the order of 1 km or greater (Weijers et al., 2004; Isakov et al., 2007). For many pollutants, there were evidences of significant spatial variability at scales smaller than 1 km (Weijers et al., 2004). Even modeling assumptions regarding subgrid processes could affect the model outcomes (Miao et al., 2006). Such models have difficulties in effectively

simulating the effects of point source emissions, especially when the emission stacks are high.

To conclude, despite their usefulness, these existing air quality models are limited in their abilities to accurately predict the concentrations of air pollutants due to the simplistic assumptions, the high computational requirements and the faineancy of terrain and surface factors, etc. (Han, 2007; Menesguen et al., 2007; British Columbia Ministry of Environment, 2008; Ying, 2008; Liu, 2009). In general, the Gaussian models are often limited to point sources and their applications neglect the chemical interactions and physical removal mechanisms in the atmosphere. The airshed models are often affected by the limitations in data availability/quality and the costly processes, as well as the high computational requirements. The box models are considered to be easier to implement with the relatively low requirements for meteorological data and computational efforts. However, such models are designed to resolve pollutant concentrations on regional scale rather than on local scale.

It is evident that the incorporation of Gaussian model within box model framework would improve the simulation of the integrated impact from point- and area- sources, and better represent the details of spatial variations in source distributions and meteorological conditions. Only few previous studies have reported this combination. Gillani and Godowitch (2005) examined a plume-in-grid (PinG) method which included a Plume Dynamics Model (PDM) and a Lagrangian reactive plume code in a Community Multiscale Air Quality (CMAQ) modeling system. Stein et al. (2007) used the HYSPLIT, AERMOD, and CMAQ models in combination to calculate the high-resolution benzene concentrations in the Houston area.

2.2 Application of GIS in Air Quality Modeling

Geography is seen as a key component in various decision-making, because there is almost always a spatial element to the decisions to be made and the data used to make them, as illustrated in Figure 2-1. A Geographic Information System (GIS) is a computer system capable of capturing, storing, analyzing, and displaying geographically referenced information; that is, data identified according to location (http://www.esri.com/). GIS has been proven successful in handling, integration, and

analysis of spatial data. It has been applied as a useful tool in various disciplines, organizations, and activities, since more than 80 % of all data has a spatial component, GIS allows an immediate determination of the relationships between maps and variables, and can create new maps of those relationships (Goodchild, 2003).

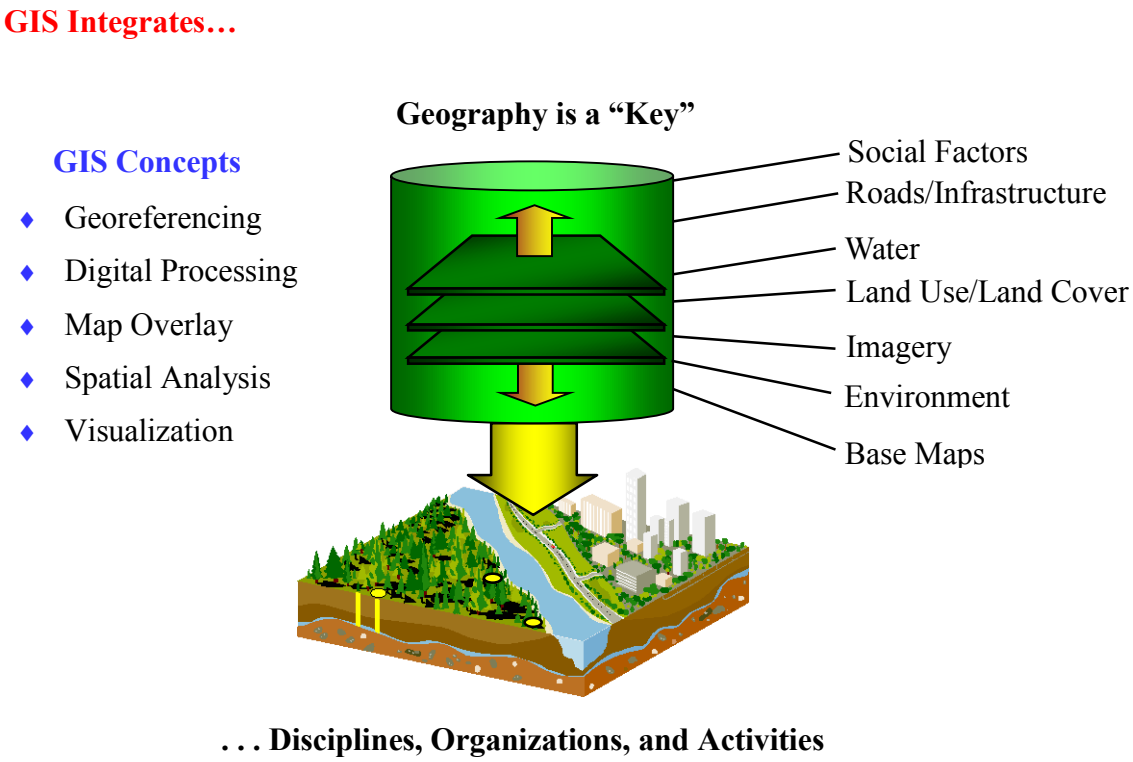

Figure 2-1 Illustration of GIS integration in various decision-making (Buckley, 2006).

When trying to use air quality models to simulate the air pollutant dispersion, there are some significant effects resulting from the varied geographical features, such as complicated surfaces (open water, land, forests, deserts, snow/ice, urban zones and coastal areas) and terrain features (mountains, valleys, hills, bowls and plains). These geophysical features cause complex flows and dispersion patterns and present many challenges for air quality modeling (British Columbia Ministry of Environment, 2008). GIS is the most effective tool for spatial analyst and air quality modeling (Goodchild, 2003; Ivanov and Zatyagalova, 2008). GIS provides a useful workspace for representation of the topological relationships and data integration due to the ability to synchronously process multiple models and communicate among them. Therefore, GIS has become essential for providing boundary conditions and visualization tools,

processing the terrain and surface data, managing multi-source data, spatial analyst and spatial overlay, and spatially expressing the results for air quality modeling (Goodchild et al., 1996).

However, the link between simulation modeling and GIS is quite new, offers tremendous possibilities for improved environmental modeling (Brimicombe, 2010). Applied work in GIS has been a persistent component of research activity in environmental science since early 1990's. The methodologies for integrating environmental models with GIS have been discussed by many researchers (Goodchild et al., 1993; 1996; Batty and Xie, 1994; Karimi and Houston, 1996; Longley and Batty, 1996; Maguire and Batty, 2005; Matejicek et al., 2006; Brimicombe, 2010). In general, GIS can be used to support environmental models through "low", "medium" and "high" level integrations, which are generally referred to as loosely-coupled, closely-coupled and fully-coupled modes, respectively (Goodchild, 2003).

For the loosely-coupled mode, GIS and air quality modeling are two separate systems and have their own user interfaces. The data files are simply transferred from air quality modeling to GIS rather than using data structures in shared memory, while GIS provides input data for air quality modeling, and helps to display the output results after computing (Brandmeyer and Karimi, 2000). As the shortcomings of this mode, the powerful functions of GIS in spatial and attribute data integrated management, spatial analyst and geostatistical analyst are not effectively used; tending to produce data redundancy and data exchange errors (Lakhan, 2003).

A closely-coupled mode involves a closer integration of GIS and air quality modeling. In this mode, the air quality modeling is usually developed in the Dynamic Link Libraries (DLLs) using FORTRAN, C/C++ or other advanced programming languages and then linked to the GIS macro-language with its own data structures and exchange mechanisms (Fotheringham and Wegener, 2000). This mode can reduce the data redundancy and exchange errors by directly accessing the spatial database (Clarke, 2002). But it implies significant requirements for programming and data management and also has portability limitations and difficulties in linking GIS macro-language and DLLs due to the mismatch of data formats or data structures (Skidmore and Prins, 2002; Goodchild, 2003).

The fully-coupled mode is known as an embedded-coupling, where the environmental models are developed within a GIS framework, so that all GIS functions and spatial database are accessed directly. This can improve the computational efficiency and accuracy by reducing data redundancy and data exchange errors in modeling process, and the longevity, stability and compatibility of the modeling system (Lakhan, 2003). It can also avoid reprogramming GIS functionality (Goodchild, 1996). Moreover, the end-users can make on-the-fly changes and further development of the powerful GIS functions.

Numerous applications of environmental model coupling with GIS have been developed over the past decades. However, most of the recent modeling efforts involving GIS are based on the loosely coupled modes (Canepa et al., 2007; Vienneau et al., 2009; Beelen et al., 2010; Elbir et al., 2010; Vlachokostas et al., 2010). Compared with the loosely-coupled mode, the closely-coupled mode is considered to be a more effective integration method due to accessing the spatial database directly and providing users with GIS spatial analyst functions (Huang and Jiang, 2002). Few studies have used the closely-coupled mode (e.g., Dai and Rocke, 2000; Hatefi Afshar and Delavar, 2007). Despite there are some issues on data exchange, compatibility and efficiency in the loosely- and closely-coupled mode, the integration has extended the traditional environmental simulation to the GIS-based modeling with geo-referenced information (Matejicek et al., 2006; Elbir et al., 2010).

Up to date, few studies have been reported on the fully-coupled mode with GIS in air quality modeling (Gulliver and Briggs, 2011). This is probably due to the fact that many well-developed models have been implemented without GIS (Wark and Warner, 1997), and there are some technological difficulties in seamlessly integrating air quality models with GIS in the earlier GIS technology (Brimicombe, 2010). For example, GIS provides little support for dynamic modeling, i.e. integration across spatial scales and time series, so it is difficult to describe the continuous phenomena and express simultaneous changes in the reality. And also, it is hard to link external models to GIS (Fotheringham and Wegener, 2000; Goodchild, 2003). However, with the rapid development of GIS technologies, the technical provision has greatly matured in recent years, which has made GIS more widespread, sophisticated, and easier to use. Some

commercial GIS software, such as ArcGIS 9.3, are now ready to meet most of the demands of air quality modeling except some particular ones which need to be developed independently as external application programs (Brandmeyer, 2000, Skidmore and Prins, 2002). Therefore, it is possible to realize the fully-coupled mode in integrating air quality modeling with GIS now.

2.3 Application of Satellite Remote Sensing in Air pollution Assessment

Current monitoring of ground-level pollutant concentrations is typically conducted through surface measurements with in-situ data. Unfortunately, the stations in current monitoring network are sparse and unevenly spaced which leads to air quality assessment impaired by insufficient observations (Lamsal et al., 2008). Recent advances in satellite remote sensing technology make remote air pollution measurements available. Remote sensing refers to the use of electromagnetic radiation to acquire information about an object or phenomenon without making physical contact with the object (Martin, 2008). Satellite observations of chemical species in the atmosphere have become available as an integral and in many cases complementary development to existing ground-based and airborne measurements (Chance et al., 2000; Leue et al., 2001; Richter and Burrows, 2002; Richter et al., 2004, 2005; Martin et al., 2002, 2003, 2006; Boersma et al., 2004, 2007; Blond et al., 2007; Lee et al., 2009, Leitao et al., 2010). This thesis focuses on satellite remote sensing of the composition in the atmosphere.

Since late 1980s, NASA (National Aeronautics and Space Administration) has been developing the Earth Observing System (EOS), which is an integrated, multi-satellite, long-term program designed for monitoring Earth's land, ocean, and atmosphere as an integrated system (Asrar and Dozier, 1994; King, 1999). Since the Terra and Aqua satellites launched in December 1999 and May 2002, we have entered a new era of satellite remote sensing on earth science.

Satellite sensors record the reflected energy from the earth and the atmosphere in various wavelengths of the electromagnetic spectrum, as illustrated in Figure 2-2. Spectral reflectance, namely, the ratio of reflected energy to incident energy as a function

of wavelength can be obtained from the reflected-light spectroscopy. Reflectance varies with wavelength for most compositions because energy at certain wavelengths is scattered or absorbed to different degrees. The overall shape of a spectral curve and the position and strength of absorption bands in many cases can be used to identify and discriminate different compositions, such as several trace gases (O_3, CO, NO_2, HNO_3, and HCHO) and together with aerosols and clouds.

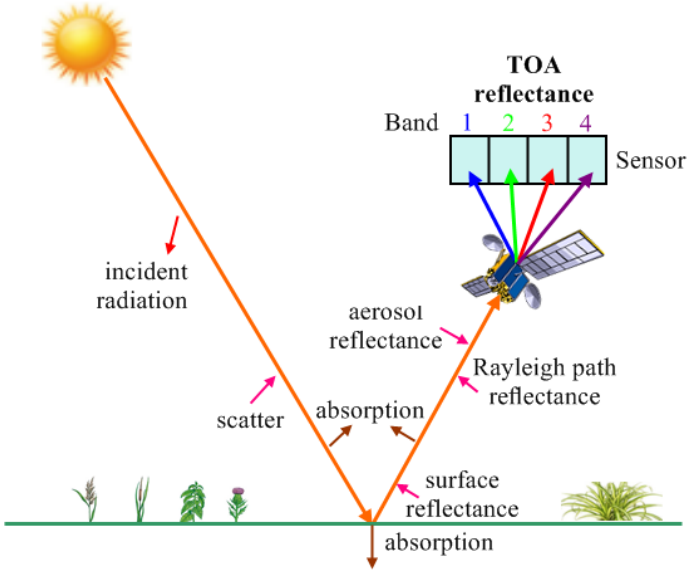

Figure 2-2 Illustration of satellite remote sensing for spectral reflectance.

The satellite measurements can be converted to the ground-level concentrations by a chemical transport model (CTM). CTMs solve coupled continuity equations for chemicals on global 3D Eulerian grid (Jacob, 1999):

$$\frac{\partial C_i}{\partial t} = -\mathbf{U} \bullet \nabla C_i + P_i(\mathbf{C}) - L_i(\mathbf{C})$$

where C_i is the chemical mixing ratios; $\mathbf{U}$ is the wind vector; ∇ is the vector of partial derivatives; P_i is the local source of chemical i; and L_i is the local sink. Compared to surface and aircraft monitoring data, satellite remote sensing data provide two important information sources: more complete spatial coverage and a vertically integrated measure of atmospheric components (Engel-Cox et al., 2004; Edwards, 2006), as illustrated in Figure 2-3.

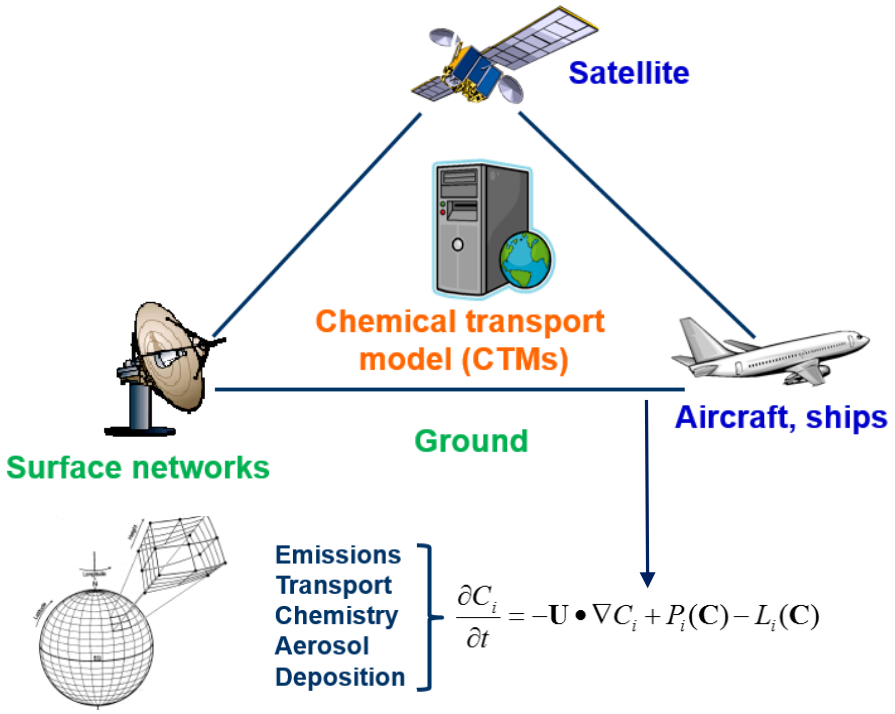

Figure 2-3 Illustration of satellite remote sensing, surface and aircraft measurements. The satellite measurements can be converted to the ground-level concentrations by a chemical transport model (CTM) (Jacob, 1999).

There are several applications of satellite remote sensing for air quality assessment at present. Most researches are focused on the retrieval of tropospheric NO_2 columns and derivation of ground-level NO_2 concentrations, and the retrieval of aerosol optical depth (AOD) and derivation of ground-level $PM_{2.5}$ concentrations. There are also some other applications, such as the derivation of ground-level O_3 concentrations (Horowitz et al., 2003), evaluation of NO_x (Martin et al., 2003), CO and SO_2 emissions (Rix et al., 2008), and long distance transport, which are not discussed in this thesis.

2.3.1 Retrieval of tropospheric NO_2 columns and derivation of ground-level NO_2 concentrations from satellite remote sensing data

Nitrogen dioxide (NO_2) as one of the most important air pollutants directly affects human health and plays a major role in the formation of ground-level ozone (Seinfeld and Pandis, 2006). Significant correlation has been found between NO_2 level and nonaccidental mortality in daily time series studies (Burnett et al., 2004; Samoli et al.,

2006). NO_2 is also one of the key greenhouse gases (GHGs) which is responsible for the global warming (Solomon et al., 1999). Therefore, it is important to evaluate NO_2 concentration in the atmosphere, especially the ground-level concentration. However, monitoring and prediction of NO_2 in the atmosphere has been a challenging mission.

Satellite observation of tropospheric NO_2 columns began in 1995 with the Global Ozone Monitoring Experiment (GOME-1) (Burrows et al., 1999) flying on ERS-2 (data available from 1996-2003), and is continued with the SCanning Imaging Absorption spectroMeter for Atmospheric CHartographY (SCIAMACHY) (Burrows et al., 1995; Bovensmann et al., 1999) on the ENVISAT platform (data available from 2002-today), Ozone Monitoring Instrument (OMI) (Levelt et al., 2006) on EOS-AURA (data available from 2004-today), and GOME-2 (Callies et al., 2000) launched on MetOp-A (data available from 2007-today). One common technique used in these instruments is the use of backscattered solar radiation from which information can be retrieved on the amounts of trace gases and aerosols in the atmosphere (Leitao et al., 2010). These instruments also provide information on aerosol optical depth (AOD) and aerosol size distribution albeit at low spatial resolution.

An increasing number of studies have been reported using satellite remote sensing to retrieve tropospheric NO_2 columns in recent years. Velders et al. (2001) have compared the data products of GOME with the model calculations from two global three dimensional chemistry transport models which show similar spatial and seasonal patterns. Lauer et al. (2002) calculated the tropospheric NO_2 columns by the chemistry-climate model and compared the results with tropospheric NO_2 columns retrieved from GOME. Martin et al. (2003) used the tropospheric NO_2 columns from GOME to derive an optimized estimate of the global distribution of surface NO_x emissions. Richter et al. (2005) retrieved the tropospheric column amounts of NO_2 from two satellite instruments GOME and SCIAMACHY. Kim et al. (2006) assessed the change of regional NO_x emissions in the eastern U.S. by comparing NO_2 columns derived from the SCIAMACHY with three-dimensional regional scale chemical transport model results. Schaub et al. (2006) compared tropospheric NO_2 vertical column densities (VCDs) retrieved from GOME to coincident ground-based tropospheric NO_2 columns. van Noije et al. (2006) have performed a multi-model inter-comparison for NO_2 retrievals from

GOME and also compared with results from 17 atmospheric chemistry models on a global scale. Uno et al. (2007) presented systematic analyses of inter-annual and seasonal variability of tropospheric NO_2 vertical column densities based on GOME satellite observations and the regional scale CTM CMAQ (Community Multi-scale Air Quality) over Asia. Blond et al. (2007) reported a new tropospheric retrieval data set based on the SCIAMACHY and the results were used to evaluate the NO_2 fields produced by a new version of the high-resolution regional-scale CHIMERE CTM over Western Europe. Ghude et al. (2009) have detected the increasing trends of NO_2 column over polluted regions of India using data from GOME and SCIAMACHY. Sheel et al. (2010) took recourse to satellite data and compare tropospheric NO_2 column abundances simulated by a chemical transport model, MOZART, with data from GOME.

However, most of previous studies were focused on the retrieval of tropospheric NO_2 columns from GOME and SCIAMACHY. In comparison, few studies have reported the retrieval from OMI. Boersma et al. (2007) presented a new algorithm for the near-real time retrieval the tropospheric NO_2 columns from OMI based on the combined retrieval-assimilation-modeling (RAM) approach. Bucsela et al. (2008) performed error-weighted linear regressions to compare OMI tropospheric NO_2 columns from the near-real-time product and standard product with the integrated in-situ columns. Kramer et al. (2008) performed a comparison between tropospheric NO_2 columns retrieved from OMI and those from the Concurrent Multiaxis Differential Optical Absorption Spectroscopy. Hains et al. (2010) made a sensitivity analysis of the tropospheric NO_2 retrieval from OMI using the measurements from the Dutch Aerosol and Nitrogen Dioxide Experiments for Validation of OMI. Wang et al. (2011) presented the assimilation of satellite NO_2 observations into a chemistry-transport model using NO_2 columns from OMI in order to better forecast NO_2 in Europe. All of above focused on the tropospheric NO_2 column retrievals from satellite remote sensing measurements. Only Lamsal et al. (2008) described an approach to infer ground-level NO_2 concentrations by applying local scaling factors from a global three-dimensional model GEOS-Chem to tropospheric NO_2 columns retrieved from OMI.

Due to the diversity of models and retrieval products, it is difficult to draw firm conclusions on whether and where models and retrievals agree or rather disagree beyond

their respective uncertainties (van Noije et al., 2006). However, most studies mentioned above have demonstrated the enormous potential of satellite NO_2 data sets for model evaluation and emission estimates. To be sure, OMI has a better spatial resolution (13 km × 24 km at nadir, larger at non-nadir viewing) than the earlier instruments of GOME and SCIAMACHY (320 km × 40 km and 60 km × 30 km, respectively), and a better temporal resolution (a daily global coverage) compared to GOME and SCIAMACHY (three and six days to achieve a global coverage, respectively) (Boersma et al., 2007). The OMI NO_2 data has been validated against surface, in-situ, aircraft and other satellite observations (Boersma et al., 2008a, 2008b; Brinksma et al., 2008; Kramer et al., 2008; Lamasal et al., 2008) and shows good consistency with those observations. Therefore, the OMI NO_2 data is used to validate the developed GMSMB modeling approach.

2.3.2 Retrieval of aerosol optical depth and derivation of ground-level $PM_{2.5}$ concentrations from MODIS and MISR

Particulate matter (PM) in ambient air is considered one of the most hazardous pollutants to human health. Especially, $PM_{2.5}$ (particulate matter with aerodynamic diameter less than 2.5 μm) affects the health of most population, leading to a wide range of acute and chronic health problems and reductions in life expectancy (WHO, 2006a). Epidemiologic studies have illustrated a consistent positive association between ambient $PM_{2.5}$ pollution levels and adverse health effects, such as increased mortality and morbidity, particularly among those with chronic respiratory and cardiovascular diseases (Pope and Dockery, 2006). When $PM_{2.5}$ concentration reaches 35 $\mu g/m^3$, the risk of mortality increases 15 % compared to 10 $\mu g/m^3$ (WHO, 2006b). Therefore, it is desirable to evaluate ground-level $PM_{2.5}$ concentrations, identify the speciation and sources, and to assess the health risks for making cost-effective strategy to control and improve $PM_{2.5}$ air pollution.

However, most routine air quality monitoring systems generate data based on the measurements of PM_{10} (particulate matter with aerodynamic diameter less than 10 μm) as opposed to other particulate matter sizes at present (WHO, 2006b). Only a few areas, such as the United States, Canada and some cities in China, have the official $PM_{2.5}$ monitoring values. As a supplement, satellite remote sensing of atmospheric aerosol has

provided a rich data source about particulate matter concentrations and is increasingly being used for air quality assessment studies (van Donkelaar et al., 2011).

The launch of MODIS sensors aboard two of the NASA Earth Observing System (EOS) satellites (Terra in 1999 and Aqua in 2002) began a new era of aerosol remote sensing over land (Kaufman et al., 1997; King et al., 1999). The wide spectral range of MODIS channels, together with near-daily global coverage and enhanced spatial resolution, provides sufficient information for retrieving total column aerosol, water vapor, and ozone simultaneously (Remer et al., 2006). Other instruments such as MISR (Diner et al., 1998) also on Terra measuring with multi-angle viewing directions (data available from 1999-today), or MERIS (Bezy et al., 2000) on the ENVISAT platform (data available from 2002-today), are better suited for aerosol retrievals since they provide high spatial resolution and, in some cases, multiple viewing directions. More recently, the active Lidar system CALIOP (Winker et al., 2003) flying on the CALIPSO satellite (data available from 2006-2009), has become available which for the first time can resolve aerosol vertical distributions with high resolution.

The aerosol optical depth (AOD), a measure of the total extinction by aerosol of light passing through the atmospheric column, can be retrieved from satellite remote sensing of atmospheric aerosol. Retrieving AODs from the residual atmospheric reflectances requires independent estimation of the wavelength-dependent single scattering albedo (ω), and the scattering phase function (P). These aerosol optical properties depend on the aerosol chemical composition, size distribution, phase, and mixing state (Remer et al., 2006; Levy et al., 2007a).

The satellites-retrieved AOD from the MODIS and MISR satellite instruments are most commonly used to evaluate ground-level $PM_{2.5}$ concentrations. The applicability of AOD to surface air quality depends on several factors, such as the vertical structure, composition, size distribution, and water content of atmospheric aerosol (van Donkelaar et al., 2010). Many studies have investigated the relationship between total columnar AOD and surface $PM_{2.5}$ distributions. Liu et al. (2004) first estimated the surface-level $PM_{2.5}$ from the MISR observations by using CTM output to represent the local AOD-$PM_{2.5}$ conversion factors. The empirical relationships between satellite remote sensing AOD and surface $PM_{2.5}$ have been developed using both MODIS (Wang and

Christopher, 2003) and MISR (Liu et al., 2005). Statistical models have also been used to relate AOD to $PM_{2.5}$ (Liu et al., 2007a; 2007b; Liu, 2009). van Donkelaar et al. (2006; 2010) extended the approach used by Liu et al. (2004) to estimate $PM_{2.5}$ from both MODIS and MISR observations and investigated the factors affecting the agreement between AOD and surface-level $PM_{2.5}$ on a global scale. Local observations of $PM_{2.5}$, vertical structure and relative humidity have all been used to improve the accuracy of remote sensing $PM_{2.5}$ (Engel-Cox et al., 2006; Schaap et al., 2009; Di Nicolantonio et al., 2009). More recently, chemical transport models (CTMs), which calculate the four-dimensional distribution of atmospheric aerosol mass, have been proven that can accurately relate AOD to ground-level $PM_{2.5}$ without nearby ground-based observations (Drury et al., 2008; van Donkelaar et al., 2010; Wang et al., 2010).

Despite much progress made recently in AOD retrievals from satellite observations and $PM_{2.5}$ estimation from satellite-retrieved AOD, several challenges exist. First of all, the operational MODIS AOD algorithm assigns fixed aerosol optical properties for individual continental regions and seasons in collection 4 (Kaufman et al., 1997; Remer et al., 2005) and collection 5 (Remer et al., 2006; Levy et al., 2007a). This set of aerosol optical properties is inconsistent with the corresponding set employed in the chemical transport models (CTMs) which varies with aerosol chemical composition in each model grid and time step in the model simulation. This inconsistency not only adds difficulty and confusion to resolving discrepancies between modeled and satellite-retrieved AOD, but also makes CTM simulations constrained by satellite-based aerosol products unable to reproduce reflectance data that satellites actually measure. To overcome these issues, recent studies have started using satellite reflectance data to constrain the CTM simulations. The principle here is that the aerosol mass fields in a CTM are iteratively updated (retrieved) until the reflectance computed from the CTM agrees with the satellite-measured reflectance, while the single scattering properties of each aerosol species are kept as constants (Drury et al., 2008; Weaver et al., 2007).

Secondly, the aerosol retrieval over bright surfaces such as urban areas is a challenge for MODIS because the land surface and the atmospheric aerosol content both have high reflectance which is difficult to infer AOD. Hsu et al. (2006; 2004) developed the deep blue algorithm for aerosol retrieval over desert and urban areas for MODIS

images. Herman and Celarier (1997) and Koelemeijer et al. (2003) developed the minimum reflectance techniques (MRT) for TOMS and GOME, respectively, over variable cover types, including bright and dark surfaces. Both of them are at a coarse resolution (> 1◦). Furthermore, it is generally admitted that the approach used to estimate surface reflectances in the visible bands at the planetary scale, against which atmospheric AOD is retrieved, can lead significant errors in AOD retrieval over urban areas (Oo et al., 2010). Even if the exactness of the retrieved AOD is improved using approaches more adapted to urban areas, estimation of the $PM_{2.5}$ concentrations from total columnar AOD may be erroneous due to the particularities of the aerosol vertical distribution at the moment of satellite passage. In fact, a high level of total AOD does not necessary means high concentrations of $PM_{2.5}$ at the surface level and vice-versa. For instance, even if the aerosol loading in the troposphere is high (resulting in high total AOD), the concentrations of $PM_{2.5}$ at surface level could be low due to a high planetary boundary layer.

In addition, the standard aerosol products are offered at coarse spatial resolutions (10 km × 10 km for MODIS, 17.6 km × 17.6 km for MISR), which are not appropriate for mapping $PM_{2.5}$ concentrations at intraurban scales as usually needed in health studies (Jerret et al., 2005).

2.4 Application of Fuzzy Set Theory for Air Pollution Risk Assessment

In most developed and developing countries, emissions from transportation and energy sectors pose a serious impact on air quality, particularly in urban areas. For example, petrol and diesel engines emit a wide variety of pollutants, principally carbon monoxide (CO), oxides of nitrogen (NO_x), volatile organic compounds (VOCs) and particulates, creating the need for air pollution risk assessment (Harrop, 2002).

In recent years, air pollution risk assessment is evolving away from a focus on individual pollutant toward a multi-factor integrated risk assessment involving multiple pollutants that may cause different physical, chemical and toxic characteristics on humans, plants, animals, ecological systems and environment (USEPA, 1997). The assessment of effect of each pollutant on environment may be inaccurate or uncertain to

various degrees and should be considered when various factors and information are taken into account. That means there are some inherent complexities and uncertainties in the integrated risk assessment of air pollution. Therefore, it is extremely important to study an efficient approach to evaluate the multi-factor integrated risk of air pollution for decision making in air quality management and planning.

During the past decades, several stochastic methodologies were developed for assessing the risks of air pollution and health impacts. Kontos et al. (1999) employed a stochastic dynamic analysis approach for dealing with short term effects of air pollution on childhood respiratory illness. Bhattacharya et al. (2000) presented a probabilistic method for determining the cumulative effect of various elements in the air. Economopoulou and Economopoulos (2002) estimated the health risk of air pollution by deriving the air pollutant concentrations and percent increases in mortality. Oettl et al. (2003) used a Markov Chain–Monte Carlo model to assess air pollution caused by road traffic. Ishii et al. (2007) estimated the phytotoxic risk of ambient air pollution on agricultural crops using yield loss functions matching the monitored concentrations. Cangialosi et al. (2008) estimated the ground-level air pollutant concentrations using an atmospheric dispersion model and calculated the health risk values based on the probability of contracting cancer through exposure to site related chemicals. Carnevale et al. (2012) proposed a regional integrated assessment tool (RIAT) based on multi-objective optimization methods to define effective air quality policies. These previous studies were mostly based on stochastic approaches. However, when the uncertain factors, such as pollutants' physical, chemical and toxic characteristics, media conditions, receptor sensitivities, and dose–response effects, cannot be expressed as probability distributions, such stochastic methods of risk assessment are inapplicable.

Since the publication of a seminal paper by Lotfi A. Zadeh in 1965, fuzzy logic has been established as an ideal method for dealing with various kinds of uncertainty and vagueness (Zadeh, 1999). Many studies have reported the risk assessment associated with environmental problems based on fuzzy set theory. For example, Smith (1995) developed a fuzzy aggregation approach for environmental quality evaluation. Chen et al. (1998) developed an integrated fuzzy risk assessment approaches for evaluating environmental risks derived from petroleum-contaminated sites. Chen et al. (2003) also

proposed a hybrid fuzzy-stochastic risk assessment approach for examining uncertainties associated with both source/media conditions and evaluation criteria in a groundwater quality management system. Sasikala and Petrou (2001) assessed the risk of desertification after a forest fire using fuzzy logic aggregation operators. Iliadis (2005) developed a decision support system applying an integrated fuzzy model for long-term forest fire risk estimation. Sadiq and Husain (2005) developed a fuzzy-based methodology for an aggregative environmental risk assessment of drilling waste. Sadiq and Tesfamariam (2009) applied the intuitionistic fuzzy set to analytic hierarchy process (AHP) to handle both vagueness and ambiguity related uncertainties in environmental decision-making process.

Despite many published studies, only few studies have reported the application of fuzzy set theory to the risk assessment of air pollution. Fisher (2003) explained how concepts from fuzzy set theory might be applied to decision-making in air pollution, and to formulate the underlying uncertainty. Li et al. (2008) proposed an integrated fuzzy-stochastic modeling approach for quantifying uncertainties associated with both source/medium conditions and evaluation criteria and assessing air pollution risks. Reshetin (2008) described the application of a formalism of fuzzy sets to model and to assess the risk of carcinogenesis and additional mortality associated with air-pollution. Kaya and Kahraman (2009) evaluated the air pollution's level by using fuzzy specification limits and fuzzy standard deviation to obtain the process capability indices. Liu and Yu (2009) examined a case-based fuzzy reasoning method to quantify environmental risks. However, none of these studies was incorporated with multi-factor air pollution integrated risk assessment based on fuzzy aggregation approach and spatial air quality modeling. Therefore, it is desirable to extend fuzzy aggregation approach to multi-factor air pollution for effective evaluation and decision-making.

2.5 Summary

In summary, every existing air quality model has limitations and only few models have been fully integrated with GIS and RS. It has been lack of studies which are desirable on: 1) spatial analyst for both regional and local scales (Stein et al., 2007); 2) improvement of the existing models to consider both point and area source (Isakov et

al., 2007) and complex meteorological and terrain conditions (Gillani and Godowitch, 2005; Stein et al., 2007); 3) full integration with GIS and RS (Brandmeyer, 2000; Lakhan, 2003); 4) challenges existing in aerosol retrieval from satellite data; 5) derivation of ground-level pollutant concentrations from satellite remote measurements; and 6) application of fuzzy aggregation approach to multi-factor air pollution risk assessment with spatial air quality modeling.

Chapter 3 Methodology

3.1 Development of GIS-Based Multi-Source and Multi-Box Modeling Approach

The GIS-based multi-source and multi-box (GMSMB) air quality modeling approach is a hybrid approach, where a regional scale model (i.e. a spatially extended multi-box model) and a local scale model (i.e. a multi-source and multi-grid Gaussian model) are combined as an efficient way to simulate and predict the airborne pollutant concentrations. In this approach, the spatial multi-box model provides the pollutant concentrations due to area source emissions, while the multi-source and multi-grid Gaussian model predicts the pollutant concentrations due to point source emissions. The results of both model simulations are combined to generate the total ambient air pollutant concentrations.

3.1.1 Spatial multi-box model

The spatial multi-box model is spatially extended and improved upon the conventional box models by allowing investigations of more details in spatial variations of emission sources and wind directions, as well as their impacts on the ambient air quality.

In this model, the study domain is spatially divided into a number of sub-boxes based on the area with a certain height in three dimensions, as shown in Figure 3-1. The following assumptions are made to accommodate data availability and computational requirements (Wark et al., 1997):

- The impact of pollutant diffusion in the wind direction is negligible since the wind force dominates the movement of pollutants.
- The impacts of pollutant diffusion are significant in both the vertical and transverse directions, leading to interactions among sub-boxes.
- No pollutant leaves or enters the whole box system through top and the sides parallel to the wind direction.

- The pollutants will be evenly and completely mixed in each sub-box up to the mixing height and there is no mixing above this height.

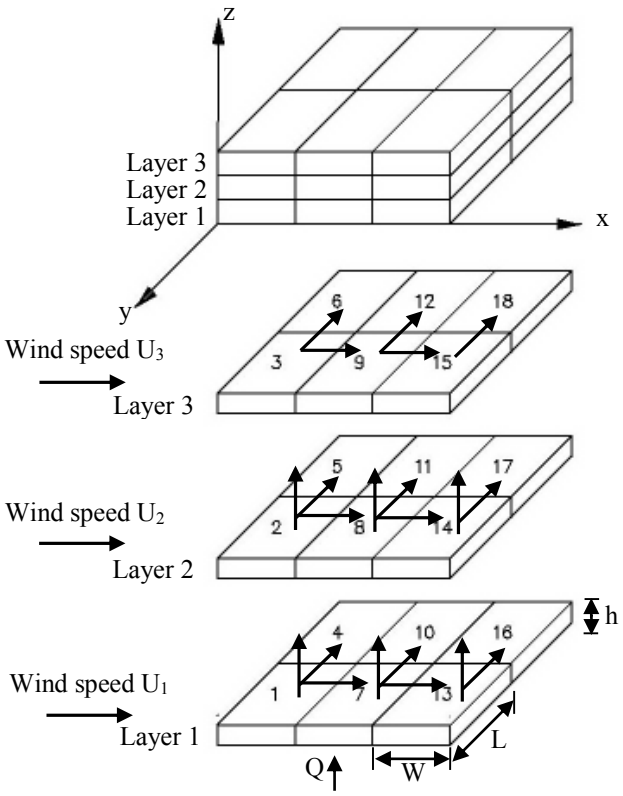

Figure 3-1 Spatial extended multi-box model.

By examining the interrelationships among the sub-boxes for each wind direction, the mass balance equation of airborne pollutant in each sub-box is established. For example, under the west wind as shown in Figure 3-1, the advection along the wind direction and the dispersion at the vertical and crosswind directions are considered for the pollutant. The physical and chemical removals are both taken into account and improved by land use/land cover characterizations. The mass balance equation is expressed as follows:

$$Lh_{i,j,k}U_k^d C_{i-1,j,k}^d - Lh_{i,j,k}U_k^d C_{i,j,k}^d + WLQ_{i,j,k} + ELW(C_{i,j,k-1} - C_{i,j,k})^d / h_{i,j,k} - ELW(C_{i,j,k} - C_{i,j,k+1})^d / h_{i,j,k} + E'Wh_{i,j,k}(C_{i,j-1,k} - C_{i,j,k})^d / L - E'Wh_{i,j,k}(C_{i,j,k} - C_{i,j+1,k})^d / L - R_{pi,j,k}^d - R_{ci,j,k}^d = 0 \quad (3\text{-}1)$$

where d denotes the wind direction; i, j and k are the sub-boxes number at wind, crosswind and vertical direction, respectively; $C^d_{i\text{-}1,\ j,k}$ is the inflow pollutant concentration (i.e., "background concentration") into the sub-box i,j,k under wind

direction d (μg/m^3); $C^d_{i,j,k}$ is the average pollutant concentration in sub-box i,j,k under wind direction d (μg/m^3); E is the diffusion coefficient at vertical direction (m^2/sec); E' is the diffusion coefficient at crosswind direction (m^2/sec); $h_{i,j,k}$ is the height of sub-box i,j,k (m); L is the length of each sub-box (m); W is the width of each sub-box (m); $Q_{i,j,k}$ is the average pollutant emission rate into sub-box i,j,k (μg/m^2·sec); U_k^d is the mean wind speed of layer k at wind direction d (m/sec); $R^d_{pi,j,k}$ is the physical removal rate in sub-box i,j,k at wind direction d (μg/sec); and $R^d_{ci,j,k}$ is the chemical removal rate in sub-box i,j,k at wind direction d (μg/sec).

The physical removals of pollutants considered in this study include dry and wet depositions. The dry deposition rate of pollutant is given (Seinfeld and Pandis, 2006):

$$R^d_{dpi,j,k} = LWC^d_{i,j,k} v_d - LWC^d_{i,j,k+1} v_d \tag{3-2}$$

where $R^d_{dpi,j,k}$ is the dry deposition rate in sub-box i,j,k under wind direction d (μg/sec); v_d is the deposition velocity (m/sec).

For gases, v_d is expressed as the inverse of a sum of aerodynamic resistance, deposition layer resistance, and vegetation layer resistance (Wesely and Hicks, 1977). The aerodynamic resistance is varied with meteorological conditions and receptor height, which is set a lower limit of 1000 s/m if the surface is wetted by dew (Wesely et al., 2001). The vegetation layer resistance is associated with aerodynamic resistance in the vegetative canopy and leaf area index which depend on the land use/land cover types (Scire et al., 2000). The land use land cover types, and the leaf area index as a function of land use/land cover types, are collected from the geodatabase created in GIS based on the U.S. Geological Survey Land Use Classification System Level I (9-Category System) (Scire et al., 2000). The default values for typical dry deposition velocities for urban or built-up land are: 0.03 cm/sec for CO; 0.1 cm/sec for NO_2 (Hauglustaine et al., 1994); and 0.5 cm/sec for SO_2 (Voldner et al., 1986).

For particulates, the deposition velocity v_d is described (Pleim et al., 1984):

$$v_d = \frac{1}{r_a + r_d + r_a r_d v_g} + v_g \tag{3-3}$$

where r_a is the aerodynamic resistance (s/m); r_d is the deposition layer resistance (s/m); and v_g is the gravitational settling velocity for particles (m/s). However, this method is used when a significant fraction (greater than about 10 percent) of the total particulate mass has a diameter of 10 μm or larger. For $PM_{2.5}$, the settling velocity is very small so that particles are not efficiently transported across the deposition layer by either the Brownian diffusion or the inertial impaction mechanism. As a result, these particles have the minimal deposition velocities. In this study, the deposition velocity for $PM_{2.5}$ is given as the weighted average of the deposition velocity as follows:

$$v_d = f v_{df} + (1 - f) v_{dc} \tag{3-4}$$

where f is the fraction of particulate substance smaller than 2.5 μm in diameter; v_{df} is the deposition velocity of fine particulates, calculated from Equation 3 with v_g set to zero (m/s); v_{dc} is the deposition velocity of coarse particulate substance (m/s), calculated from Equation 3 with v_g set to 0.002 m/s. According to the study of Sehmel et al. (1978), the deposition velocity of 1cm/sec is used for $PM_{2.5}$ in urban areas.

The wet deposition rate of pollutant is proportional to the scavenging ratio (Scire et al., 2000):

$$\Lambda = \lambda \cdot \left(P / P_0 \right) \tag{3-5}$$

where Λ is the scavenging ratio (1/sec); λ is the wet scavenging coefficients (1/sec), which depends on the characteristics of the pollutant as well as the nature of precipitation. It is served as an empirical constant of 10^{-4}/sec for $PM_{2.5}$ (Chate et al., 2011), 3×10^{-5}/sec for SO_2, and 0.00/sec for NO_2 and CO (Scire et al., 2000); P is the precipitation rate (mm/hr); and P_0 is the reference precipitation rate (mm/hr), which is usually taken as 1 mm/hr. So the wet deposition rate is calculated by:

$$R^d_{wpi,j,k} = LWh_{i,j,k} C^d_{i,j,k} \Lambda - LWh_{i,j,k} C^d_{i,j,k+1} \Lambda \tag{3-6}$$

where $R^d_{wpi,j,k}$ is the wet deposition rate in sub-box i,j,k under wind direction d (μg/sec).

The chemical removal described by a first-order reaction is commonly adopted in regional scale modeling (Seinfeld and Pandis, 2006). The chemical removal rate of air pollutants is estimated by:

$$R^{d}_{ci,j,k} = Lh_{i,j,k} U^{d}_{k} C^{d}_{i,j,k} \left[1 - \exp\left(-kW / U^{d}_{k} \right) \right] \quad (3\text{-}7)$$

where the ratio of W/U_k^d represents the residence time of the compound in each sub-box in layer k at wind direction d (sec); k is the first order rate constant (1/sec), $k = 0.693 / t_{1/2}$. $t_{1/2}$ is the half-life of pollutants. In this study, the default value of k is set as 4.81×10^{-5} /s for SO_2 (USEPA, 2005); 6.42×10^{-5} /s for NO_2 (Kelm and Yoshida, 1996); 4.7×10^{-7} /s for CO (Viggiano et al., 2005). For $PM_{2.5}$, the U.S. EPA's Revision to the Guideline on Air Quality Models indicated that the 'infinite half-life' should be used for estimates of particle concentrations (USEPA, 2005), which means the first order rate constant of $PM_{2.5}$ is 0. However, $PM_{2.5}$ has a major multiplier from nitrate NO_3^- and sulphate SO_4^{2-} which exist as NH_4NO_3 and $[NH_4]2SO_4$. This multiplier is calculated with the predicted sulphate and nitrate concentrations multiplied by factors of 1.375 for sulphate and 1.290 for nitrate (Malm, 2000).

Based on the mass balance equation for each sub-box under each wind direction, the pollutant concentration in sub-box i,j,k for all wind directions is calculated as follows:

$$C_{i,j,k} = \sum f^{d} C^{d}_{i,j,k} \quad (3\text{-}8)$$

where $C_{i,j,k}$ is the concentration of the pollutant in sub-box i,j,k (μg/m^3); f^d is the annual frequency of wind in direction d, which is the percentage of the time the wind is coming from a particular direction (%) (NRCS, 2009).

3.1.2 Multi-source and multi-grid Gaussian model

For point sources, the pollutant dispersion is assumed to be Gaussian in both the vertical and horizontal directions. The Gaussian formula introduces the current state-of-the-art air dispersion modeling concepts, which is applicable to rural and urban areas, flat and complex terrain, surface and multiple sources.

In each sub-box, for stable and neutral conditions, the point source dispersion is considered to be Gaussian in both the vertical and horizontal directions with the concentration equation adapted from Hanna and Paine (1989):

$$C\{x_r, y_r, z_r\} = \frac{Q}{\sqrt{2\pi}u\sigma_z} \cdot f_y \cdot \sum_{m=-\infty}^{\infty} \left[\exp\left(-\frac{\left(z_r - h_e - 2mz_{ieff}\right)^2}{2\sigma_z^2} \right) + \exp\left(-\frac{\left(z_r + h_e + 2mz_{ieff}\right)^2}{2\sigma_z^2} \right) \right] \tag{3-9}$$

where $\{x_r, y_r, z_r\}$ is the coordinate representation of a receptor (m), and z_r is the height of a receptor defined relative to the stack base elevation (m); Q is the emission rate (μg/sec); u is the wind speed at stack top (m/s); z_{ieff} is the effective mechanical mixed layer height (m); σ_z is the total vertical dispersion (m); h_e is the effective plume height (i.e., stack height plus the plume rise) (m); and f_y is the lateral distribution function with meander (m^{-1}). f_y is defined as:

$$f_y = \frac{1}{\sqrt{2\pi}\sigma_y} \cdot \exp\left(-\frac{y^2}{2\sigma_y^2} \right) \tag{3-10}$$

where σ_y is the total lateral dispersion (m). In rural area, σ_y and σ_z are calculated from the modified Pasquill-Gifford (P-G) stability categories and dispersion parameters, while in urban area, σ_y and σ_z are calculated based on Briggs' formula (USEPA, 1992).

The effective plume height h_e equals to the stack physical height plus the plume rise height Δh which is estimated as follows (Weil et al., 1988):

$$\Delta h = 2.66 \left(\frac{F_b}{N^2 u_p} \right)^{1/3} \cdot \left[\frac{N' F_m}{F_b} \sin\left(\frac{N' x}{u_p} \right) + 1 - \cos\left(\frac{N' x}{u_p} \right) \right]^{1/3} \tag{3-11}$$

where $F_b = g w_s r_s^2 \left(\Delta T / T_s \right)$ is the stack buoyant flux (m^4/s^3); $F_m = w_s^2 r_s^2 \left(T / T_s \right)$ is the stack momentum flux (m^4/s^2) (Briggs, 1984); g is the gravitational acceleration (m/s^2); w_s, r_s and T_s are the stack exit velocity (m/s), radius (m) and temperature (K), respectively; $\Delta T = T_s - T_a$ where T_a is the ambient air temperature (K); u_p is the wind

speed used for calculating plume rise (m/s); and N is the Brunt-Vaisala frequency, which is based on the potential temperature gradient in the elevated stable layer (Cimorelli et al., 2004):

$$N = \left[\frac{g}{\theta\{z_i\}} \cdot \frac{\partial \theta}{\partial z}\Big|_{z>z_i} \right]^{1/2} \tag{3-12}$$

where θ is the temperature at the height z_i, $\frac{\partial \theta}{\partial z}\Big|_{z>z_i}$ is the temperature gradient at height higher than z_i; $N' = 0.7N$.

The effective mechanical mixed layer height z_{ieff} is defined as the larger of mechanical mixed layer height z_{im} and upper edge (e.g., plume height plus $2.15\sigma_z$) (Hanna and Paine, 1989):

$$z_{ieff} = MAX\left[\left(h_e + 2.15\sigma_z \{h_e\}; z_{im} \right) \right] \tag{3-13}$$

The mechanical mixed layer height z_{im} is estimated as (Venkatram, 1980):

$$z_{im} = 2300 u_*^{3/2} \tag{3-14}$$

where the constant 2300 has units of ($s^{3/2}$ $m^{-1/2}$); u_* is the surface friction velocity (m/s).

The physical and chemical removals are calculated using the methods described in the spatial multi-box model and removed from the results of eq. (3-9) by a post-processing. Considering the terrain effect, the total pollutant concentration is calculated using a weighted average of concentration associated with two parts: a horizontal plume $C\{x_r, y_r, z_p\}$ (terrain impacting) and a terrain-following plume, as shown in the following equation (Cimorelli et al., 2004):

$$C_T\{x_r, y_r, z_r\} = \lambda \cdot C\{x_r, y_r, z_r\} + (1-\lambda) \cdot C\{x_r, y_r, z_p\} \tag{3-15}$$

where $C_T\{x_r, y_r, z_r\}$ is the total concentration at receptor (μg/m^3); $C\{x_r, y_r, z_r\}$ is the concentration contributed from the horizontal plume state (μg/m^3); $C\{x_r, y_r, z_p\}$ is the concentration contributed from the terrain-following state (μg/m^3); λ is the plume state

weighting function (dimensionless); $z_p = z_r - z_t$ is the height of a receptor above the local ground (m); and z_t is the terrain height at a receptor referenced to the stack base elevation (m).

The terrain heights of sources and receptors are obtained from the Digital Elevation Model (DEM) in GIS geodatabase. The plume state weighting factor λ is given as (Venkatram et al., 2001):

$$\lambda = 0.5(1 + \phi_p) \tag{3-16}$$

where ϕ_p is the fraction of the plume mass below the dividing streamline height H_c (m) which is defined as the minimum of the highest actual terrain and the terrain-following height at that receptor. ϕ_p is computed by the following equation:

$$\phi_p = \frac{\int_0^{H_c} C_s\{x_r, y_r, z_r\}dz}{\int_0^{\infty} C_s\{x_r, y_r, z_r\}dz} \tag{3-17}$$

where $C_s\{x_r, y_r, z_r\}$ is the pollutant concentration in the absence of a hill for stable conditions (μg/m^3). When the plume is entirely below the dividing streamline height H_c, ϕ_p = 1 and λ = 1. Therefore, the pollutant concentration at an elevated receptor is determined only by the horizontal plume. When the plume is entirely above H_c or when the atmosphere is either neutral or convective, ϕ_p = 0 and λ = 0.5, the pollutant concentration at an elevated receptor is simply the average of the contributions from the two plumes.

Using this model, the downwind ground-level pollutant concentration at a certain location is calculated. The prediction result of pollutant concentration at a certain ground-level location due to each single point source emission is then superimposed to obtain the pollutant concentration at that location due to multiple point source emissions.

3.1.3 GIS-based modeling method

In this GIS-based modeling approach, there are three main components: geodatabase, air quality model, and result processing with visual representation (Figure

3-2). The GIS-based multi-source and multi-box (GMSMB) model consists of an array of horizontal sub-boxes at multiple vertical layers, which is developed within the ArcGIS framework using Visual Basic Application (VBA) and ArcObjects Components. There are a number of models and setup parameters to be established for air quality modeling.

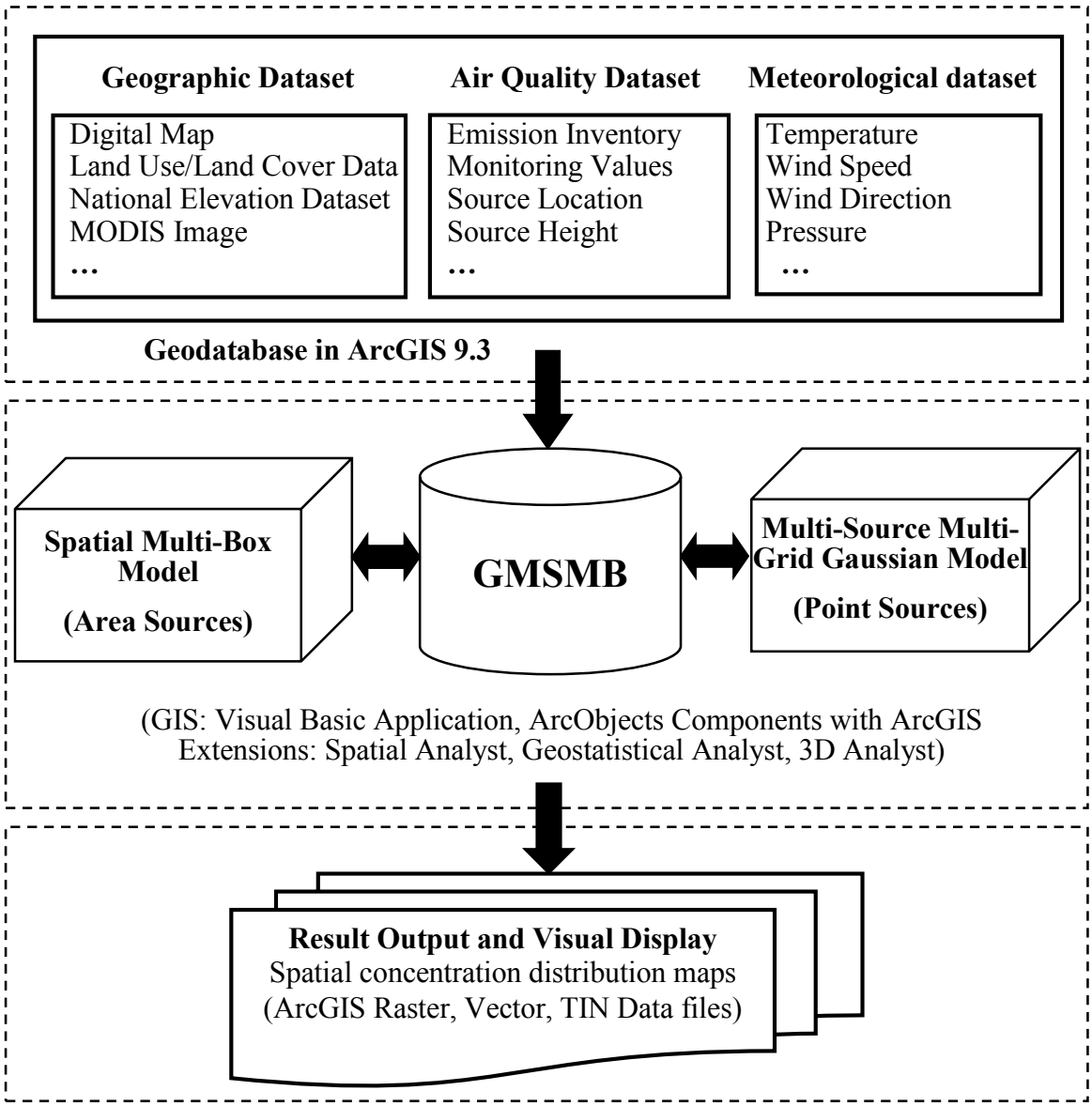

Figure 3-2 Framework of the GMSMB modeling system.

Creation of a geodatabase, which consists of various types of geographic datasets, is the basis of design and development of a spatial modeling system (ERSI, 2009). In this study, the geodatabase consists of three types of datasets: spatial dataset, air quality dataset and meteorological dataset. The spatial dataset includes digital map, land

use/land cover data and National Elevation Dataset (NED). The surface roughness length, surface albedo, and vegetation leaf area index are derived from terrain and land use/land cover data and processed into gridded surface within the modeling domain.

The air quality dataset includes the emission inventory data which is divided into area source and point source data depending on the emission source characteristics. Mobile sources are modeled as a series of area sources along the travel routes. Model parameters for area sources include emission rate, release height, lengths of sides of rectangular, areas or vertices for polygons. Model parameters for point sources include emission rate, stack height, stack diameter, stack exhaust temperature, and stack exhaust exit velocity.

The meteorological dataset consists of surface and upper air data. The surface data includes ambient temperature, wind speed and direction, cloud cover, surface pressure, relative humidity, precipitation, and monitoring height. The upper air data includes wind speed, wind direction, temperature, pressure, and elevation. All of these datasets are spatially allocated and stored into corresponding sub-box by GIS mapping and geodatabase creating and geocoding. Here, the computational efficiency and spatial representation are enhanced in a way that all datasets are managed through an embedded geodatabase with spatial coordinate locations.

For the integrated modeling based on GIS, recent GIS technique provides an object-oriented developing environment for air quality modeling. The GMSMB model, which consists of the spatial multi-box model coupled with the multi-source and multi-grid dispersion model, is developed in the ArcGIS 9.3. The spatial multi-box model is used for the simulation of emissions from area and mobile sources, while the multi-source and multi-grid Gaussian model is used in each sub-box for the emissions from point sources. GIS is employed to handle the spatial location, terrain features, and land use/land cover characterizations for elevated airflow using digital map and National Elevation Dataset (NED), which allows the modeling approach to consider complex terrain. The ArcGIS extension functions, including Spatial Analyst, Geostatistical Analyst and 3D Analyst are employed for pre- and post- processing of the developed air quality model within the GIS environment. For example, the source location layer is created using the geocoding method; the terrain features and surface slope are calculated

using the 3D analyst function for modeling terrain process. For the sub-box without weather station, GIS spatial interpolation methods are examined to determine the meteorological parameters.

In the multi-source and multi-grid Gaussian model, each emission source is calculated in an individual coordinate system, which is also different from the coordinate system used in the spatial multi-box model. They must be transformed into a uniform coordinate system by coordinate transformation. In this study, we employ the Universal Traverse Mercator (UTM) as a uniform coordinate system.

For the third component of the developed GMSMB, the simulating results from two models are spatially overlayed at the center of each sub-box to produce the integrated modeling results, which are visually represented on the modeling domain map within GIS. The results correspond to the locations of discrete receptors including residences, natural areas, monitoring stations, and industrial sites can also be acquired from the modeling system by spatial overlay or spatial interpolation. This development enables the application of the GIS-based modeling approach to regional scale area with extended simulation of dynamic air quality and complex meteorological and terrain conditions.

3.1.4 Evaluation of model performance

The performance of modeling approach is evaluated by comparing the modeling results with the monitoring values. The Normalized Mean Bias (NMB) is considered as a measure of the model performance, while the Normalized Mean Error (NME) and Root Mean Square Error (RMSE) are used to examine the model errors. RMSE provides an absolute while NMB and NME provide normalized (%) measures for validation of the modeling approach (Appel et al., 2007):

$$NMB = \frac{\sum_{1}^{N}(C_m - C_0)}{\sum_{1}^{N} C_0} \bullet 100\% \qquad (3\text{-}18)$$

$$NME = \frac{\sum_{1}^{N}\left|\left(C_m - C_0\right)\right|}{\sum_{1}^{N} C_0} \bullet 100\% \tag{3-19}$$

$$RMSE = \sqrt{\frac{1}{N}\sum_{1}^{N}\left(C_m - C_0\right)^2} \tag{3-20}$$

where C_m and C_o are the modeling and monitoring concentrations (the unit for $PM_{2.5}$ is $\mu g/m^3$, and for the rest are ppm), respectively.

3.2 Derivation of Ground-level NO_2 from OMI Analysis

To further validate the developed GMSMB modeling approach, the satellite remote sensing data analysis method is employed. Nitrogen oxides (NO_x = NO + NO_2) are released into the atmosphere by anthropogenic and natural sources. These species largely control the production of ozone in the global troposphere (Jacob, 2000), and also affect OH concentrations, thereby modifying the residence time of greenhouse gases and other pollutants (e.g. Shindell et al., 2009). The chemical decay product of NO_2 is a key air pollutant with important implications for air quality and plays a major role in formation of ground-level ozone (Crutzen, 1970; Brewer et al., 1973; Noxon, 1975; Murphy et al., 1993). It is chosen as a case to be derived from the satellite OMI (Ozone Monitoring Instrument) data analysis and to be compared with the in-situ surface measures and the GMSMB modeling results.

3.2.1 OMI overview

OMI is the first of a new generation of space borne spectrometers. It was launched on the NASA's EOS-Aura satellite by the Netherlands and Finland in 2004. The Aura satellite passes over the equator in a sun-synchronous ascending polar orbit at 13:45 local time and over North America around 13:00 local time. OMI measures the upwelling radiance in the ultraviolet and visible wavelength range between 270 nm and 500 nm, and continuously provides a 2600 km wide spatial swath on the Earth's surface (Levelt et al., 2006). The nadir spatial resolution of 13 km × 24 km allows finer

observation details and higher detection sensitivity for NO_2 compared to other available satellite instruments (Boersma et al., 2007; Hains et al., 2010).

3.2.2 Tropospheric NO_2 vertical column densities retrieval from OMI

The tropospheric NO_2 vertical column densities (VCDs) are retrieved from satellite OMI observations using the Differential Optical Absorption Spectroscopy (DOAS) and the Dutch OMI NO_2 (DOMINO) Algorithm (Boersma et al., 2004). The DOMINO algorithm employs a retrieval-assimilation-modeling (RAM) approach developed by the Royal Netherlands Meteorological Institute (KNMI) and the National Aeronautics and Space Administration (NASA) (Boersma et al., 2007). It consists of three steps:

1) Total OMI NO_2 slant column density (SCD) is determined from a spectral fit to the Earth reflectance spectrum with the Differential Optical Absorption Spectroscopy (DOAS) technique (Boersma et al., 2002; Bucsela et al., 2006; Boersma et al., 2007);
2) The stratospheric contribution to the total slant column is estimated by assimilating OMI slant column density SCD in a chemical transport model (CTM) TM4 and separating the stratospheric contribution from the total slant column density (Dentener et al., 2003; Eskes, 2003; Boersma et al., 2007);
3) The residual tropospheric slant column density (SCDtrop) is converted into a tropospheric vertical column density (VCD) by a tropospheric air mass factor (AMFtrop) (Boersma et al., 2007; Blond et al., 2007).

The tropospheric NO_2 VCDs retrieved from OMI are used to derive the ground-level NO_2 concentrations by applying the global three-dimensional chemical transport model GEOS-Chem. The procedure can be summarized in Figure 3-3.

3.2.2.1 Retrieval of total NO_2 slant column density (SCD)

The total NO_2 slant column density (SCD) retrieved from OMI is based on the Differential Optical Absorption Spectroscopy (DOAS) technique. The DOAS technique is a widely used method to determine concentrations of atmospheric species (Platt, 1994). The DOAS analyses of broadband spectra in the UV and visible region (200-800 nm)

allows the determination of concentrations of atmospheric species, which leave their absorption fingerprints in the spectra.

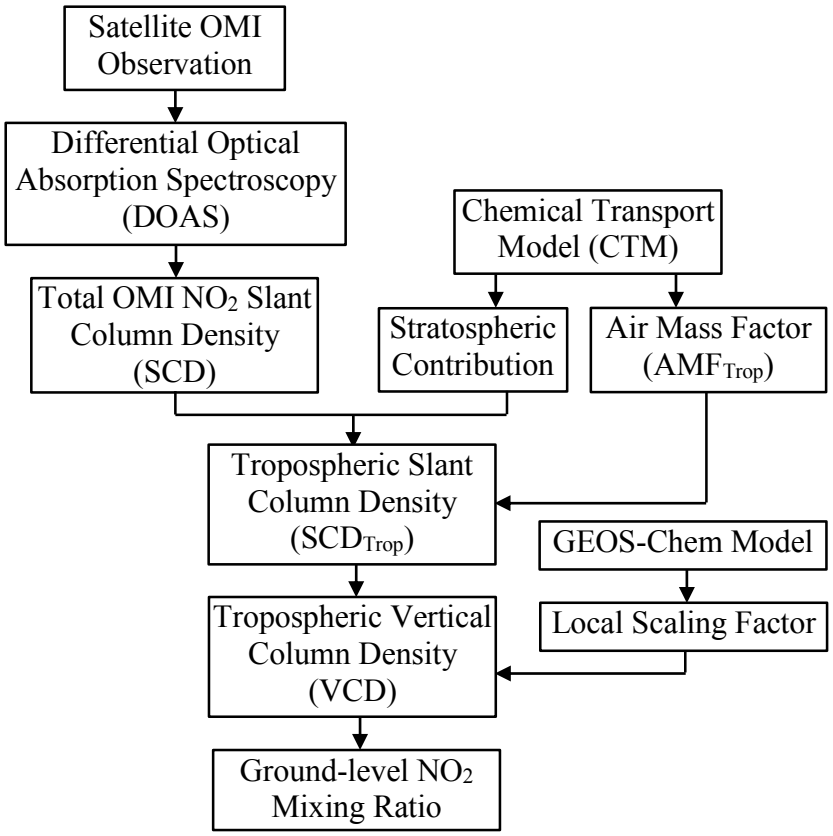

Figure 3-4 Flow chart of derivation of ground-level NO_2 from OMI.

The DOAS technique is based on a straightforward implementation of the Beer-Lambert's law, which describes the extinction of solar radiation in an absorbing atmosphere (van der A et al., 2010):

$$I(\lambda) = I_0(\lambda) \cdot \exp\left(-\sum_i \sigma_i c_i\right) \tag{3-21}$$

where $I(\lambda)$ is the solar spectrum after absorption (earthshine radiance); $I_0(\lambda)$ is the extraterrestrial solar spectrum (solar irradiance); σ_i are the relevant cross sections of the absorbing species, with wavelength and temperature dependent structures; and c_i are the unknown species column densities.

The logarithm of the ratio of the irradiance spectrum $I_0(\lambda)$ and the earthshine spectrum $I(\lambda)$ is denoted by optical density (or optical thickness) (van der A et al., 2010):

$$\log\left(I_0(\lambda) - I(\lambda)\right) = \sum_i \sigma_i c_i \tag{3-22}$$

The total optical density is obtained using a least-square procedure where the slant column density (SCD) of various species are the fitted parameters. For practical applications of DOAS, it is important that the trace gas under investigation has a small absorption optical thickness in the predefined spectral window. NO_2 has a typical slant optical thickness of 0.005 (van der A et al., 2010). The total SCD of NO_2 can be obtained from this step.

3.2.2.2 Separation of stratospheric contribution from total SCD

The stratospheric part of the total SCD is determined by data assimilation of observed OMI slant column density in the chemistry-transport model TM4 proposed and described by Eskes (2003). TM4 is driven by high-quality meteorological fields, based on the latest emission inventories, atmospheric transport, photochemistry, lightning modeling and wet/dry removal processes. The values of the CTM stratosphere are made consistent with the observed slant columns over unpolluted areas. The advantage of this method is that dynamical features in the stratospheric NO_2 – leading to a longitudinally inhomogeneous distribution of NO_2 are taken into account. Subsequently, the estimated stratospheric slant column density is separated from the total SCD to yield the tropospheric slant column density (SCDtrop).

3.2.2.3 Convert of SCDtrop to vertical column density (VCD)

The SCDtrop is converted into the vertical column density (VCD) by applying the tropospheric air mass factor (AMFtrop) (Boersma et al., 2007; Blond et al., 2007):

$$VCD = \frac{SCD_{trop}}{AMF_{trop}} \tag{3-23}$$

The AMFtrop depends on the a priori assumed NO_2 and temperature profile shape, the cloud fraction, the cloud top height, the surface spectral reflectance (surface albedo) and the aerosol optical thickness profile, and also depends on other parameters, such as solar zenith and viewing zenith angle.

The AMFtrop is obtained by multiplying the elements of the troposphere-only a priori NO_2 profile x_a derived from TM4 with the elements of altitude dependent AMFtrop as follows (Palmer, 2001; Boersma et al., 2004):

$$AMFtrop = \frac{\sum_l m_l(b) \cdot x_{a,l}}{\sum_l x_{a,l}} \tag{3-24}$$

where l is an index denoting the atmospheric layer, m_l are the altitude dependent box air mass factors, x_a is the a priori profile shape of NO_2 (molecules/cm^2), and b is the model parameters.

It is obvious that there are some uncertainties in the estimate of the AMFtrop. Actually, most studies pointed to AMFs as the source of most significant retrieval errors. The most important uncertainties associated with the computations of tropospheric AMF are cloud fraction, aerosol characterization, surface albedo, and profile shape (Martin et al., 2002; Boersma et al., 2004; Huijnen et al., 2010). The contributions to the error in tropospheric NO_2 column densities are described in Boersma et al. (2004). The uncertainty due to cloud fraction (and aerosols) is estimated to be up to 30 % for polluted regions, and the uncertainties due the surface albedo is up to 25 %. Moreover, the height dependent sensitivity of the space-borne instrument to the tracer density results in a tracer profile dependence that may introduce large systematic errors in the retrieved columns.

The presence of clouds can increase the instrument's sensitivity to monitor gases above the clouds because of light scattering and/or decrease its sensitivity to trace gases below the clouds due to shielding (Stammes et al., 2008). Therefore, the tropospheric NO_2 columns (i.e. NO_2 vertical column density (VCD)) have been retrieved and averaged monthly in-situations with a cloud radiance fraction < 50 %, corresponding to cloud fractions approximately < 20 % (Boersma et al., 2011). The DOMINO data products (version 2.0, available from 2004 - today) are publicly available from the European Space Agency (ESA) Tropospheric Emission Monitoring Internet Service (TEMIS) project website (http://www.temis.nl).

3.2.3 GEOS-Chem model

The OMI tropospheric NO_2 VCDs are applied to derive the ground-level NO_2 concentrations, which require local tropospheric NO_2 profile information. For this purpose, the global three-dimensional chemical transport model GEOS-Chem (version 9-01-02) is used to simulate the atmospheric composition. The GEOS-Chem model is driven by assimilated meteorological observation data available from the Goddard Earth Observing System (GEOS) of the NASA Global Modeling and Assimilation Office (GMAO) (Yantosca et al., 2011). The model includes a detailed simulation of the tropospheric ozone-NO_x-hydrocarbon chemistry, as well as aerosols and their precursors (Bey et al., 2001; Park et al., 2004). The full chemical mechanism for the troposphere involves 111 species and over 300 reactions. It is applied by research groups around the world to a wide range of atmospheric composition problems (Park et al., 2003, 2006; Liu et al., 2006; van Donkelaar et al., 2006, 2010).

3.2.4 Estimation of ground-level NO_2 concentrations from OMI

The GEOS-Chem model solves for the temporal and spatial evolution of gaseous compounds and aerosol (sulfate, nitrate, ammonium, carbonaceous, mineral dust, and sea salt). The simulation involves meteorological data sets, emission inventories, and equations that represent the physics and chemistry of atmospheric constituents, as well as information on the simulated NO_2 vertical profile. The local NO_2 profile is obtained from the GEOS-Chem simulation. The ground-level NO_2 mixing ratio (refers to the mole fraction of NO_2 to the total amount of air species in a unit of ppb) S is derived from the GEOS-Chem simulation and the OMI-retrieved NO_2 vertical column densities (VCDs) (Lamasal et al., 2008):

$$S = \frac{\nu S_G}{\nu \Omega_G - (\nu - 1)\Omega_G^F} \times \Omega \tag{3-25}$$

where S represents the surface level NO_2 mixing ratio (ppb); Ω represents the tropospheric NO_2 vertical column density (10^{15} molecules/cm^2); the subscript G denotes GEOS-Chem and the subscript O denotes OMI; the symbol ν represents the ratio of the local OMI NO_2 column to the mean OMI NO_2 column field over a GEOS-Chem grid

(dimensionless); and Ω_G^F is the simulated free-tropospheric NO_2 vertical column density over a GEOS-Chem grid (10^{15} molecules/cm^2), reflecting the longer NO_x lifetime in the free troposphere.

The satellite-derived NO_2 mixing ratio at the lowest vertical layer (100 m) represents the NO_2 concentrations at ground-level (Lamasal et al., 2008). More details about the GEOS–Chem algorithms see Appendix C.

3.3 Derivation of Ground-level $PM_{2.5}$ from MODIS

3.3.1 MODIS AOD retrieval at 1-km resolution

MODIS was launched aboard two polar orbiting satellites Terra and Aqua of the Earth Observing System's (EOS) of National Aeronautics and Space Administration (NASA), in 1999 and 2002, respectively. Terra has a 10:30 am local equatorial overpass time, and Aqua has a 1:30 pm local equatorial overpass time. Both instruments have a swath width of 2300 km and measure a given location on the Earth at least once daily. MODIS measures the upwelling radiance from the Earth-atmosphere system at 36 wavelength bands which range from 0.412 to 14.2 μm representing three spatial resolutions: 250 m (2 channels), 500 m (5 channels), and 1 km (29 channels). The aerosol retrieval makes use of seven of these wavelength bands (0.47–2.13 μm), and a number of other bands to identify cloud and other screening procedures (Ackerman et al., 1998; Gao et al., 2002; Martins et al., 2002; Li et al., 2005).

An individual MODIS image scene, called a granule, consists of a 5-min swath of data. MODIS data products are broadly categorized into five levels from level-0 to level-4 (Vermote et al., 2011). Level 0 data is the initial dataset automatically converted from instrumental raw feeds. Level 1 data has been added geodetic position information, such as latitude, longitude, height, satellite zenith/azimuth and solar zenith/azimuth angles to each MODIS granule (called level 1A data), and calibrated radiance for all bands and surface reflectance values for selected bands (called level 1B data). Level 2 data has been atmospherically corrected to yield the surface reflectance product at the same resolution and location as level-1 data. Level 3 data has been gridded into a map projection, and usually has also been temporally composited or averaged (e.g., daily,

eight-day, and monthly). Level 4 data is generated through a variety of algorithms, models, and statistical methods with additional ancillary data.

MODIS data products are also organized by collections (collection 3 - collection 6). Each collection indicates a complete set of MODIS files corresponding to a specific data updating or re-processing stage. The MODIS operational algorithm derives aerosol properties at 10 km × 10 km resolution (at nadir) based upon the 500 m pixels of 0.47 to 2.13 μm and 250 m pixels of 0.66 μm bands. All channels are organized into nominal 10 km boxes corresponding to 20 by 20, or 400 pixels for each box (the 250 m resolution 0.66 μm channel to be degraded to 500 m in order to match the resolution of the other two channels). The details about MODIS aerosol optical depth (AOD) retrieval algorithm over land can be found in Kaufman et al. (1997) and the updates of the algorithm in Chu et al. (2003) and Remer et al. (2005).

The MODIS standard aerosol products (collection 5, level 2) are provided at 10 km × 10 km resolution (Levy et al., 2007), which are sufficient to study air quality at global and regional scale (van Donkelaar et al., 2010; Remer et al., 2005; Levy et al., 2007b). However, it is insufficient to depict aerosol variation on local or urban scales due to inherent aerosol variability and complex surface terrain (Li et al., 2005a). Thus, it is desired to retrieve the AODs at a higher resolution for local or urban applications.

The MODIS level 1B granule data consist of calibrated radiances or reflectances, which are corrected for water vapor, ozone, and carbon dioxide before the algorithm proceeds and provided at 250 m, 500 m and 1km resolutions, respectively, which can be used to retrieve the AOD at a higher resolution. In this thesis, an exploration to retrieve AOD at 1 km × 1 km resolution for urban scale application is performed. The Terra/MODIS level 1B 1 km calibrated reflectance (MOD021km), geolocation data (MOD03, including sun-sat Geometry and digital elevation model (DEM)), MODIS level 2 surface reflectance (MOD09), MODIS cloud mask (MOD35), atmospheric profile (MOD07), and ancillary data (such as water vapor profiles), comprise the set of inputs to the MODIS aerosol retrieval. All of these data are in HDF (Hierarchical Data Format) and downloaded from the NASA Goddard Space Flight Center Level 1 and Atmosphere Archive and Distribution System (LAADS) (NASA, 2012a).

The AOD retrieval algorithm involves the following processes, as shown in Figure 3-4.

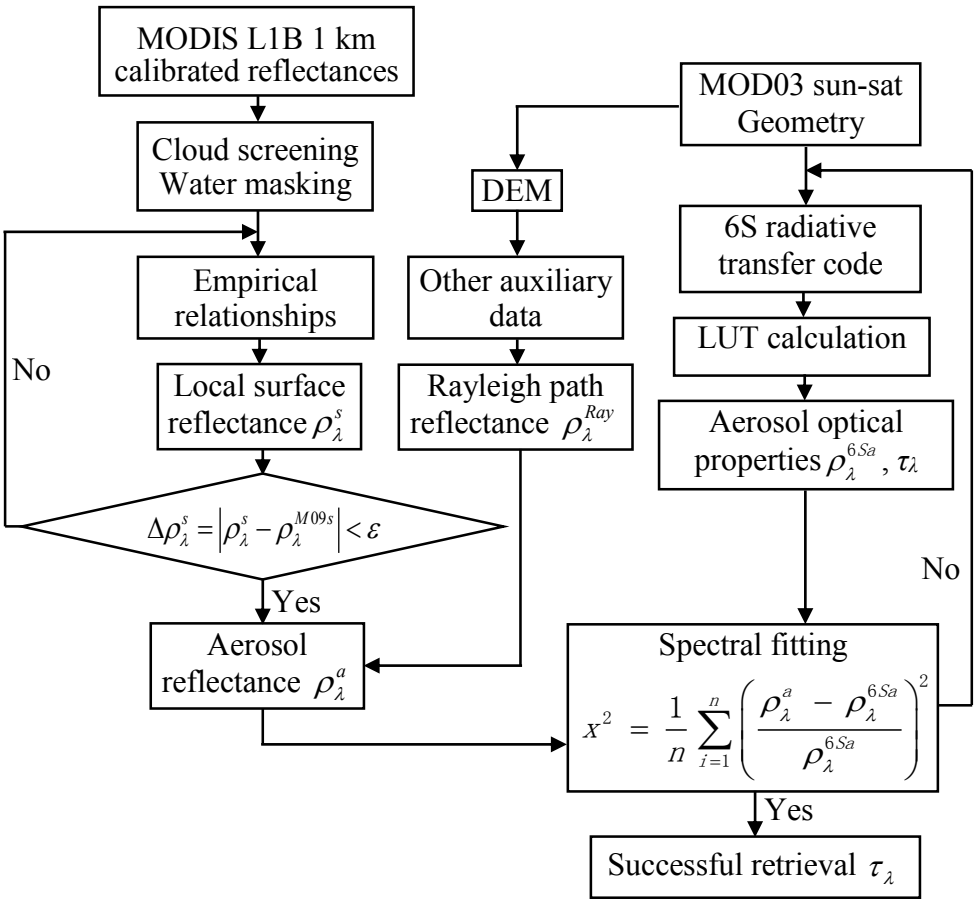

Figure 3-5 Flow chart of aerosol retrieval in this study.

1) Selection of pixels

MODIS AOD retrieval employs primarily three spectral channels centered at 0.47, 0.66, and 2.13 μm wavelengths. The cloud-free pixels (both "probably clear" – 95 % cloud free and "confident clear" – 99 % cloud free) are first selected using the MODIS cloud mask (MOD35) (Platnick et al. 2003; Martins et al., 2002; Gao et al., 2002). Then followed by the screening of water-body pixels using the normalized difference vegetation index (NDVI > 0.1) from the Canada Centre for Remote Sensing (CCRS, 2010), and snow/ice pixels using Near Real-Time Ice and Snow Extent (NISE) data from the National Snow and Ice Data Center (NSIDC, 2010). For the remaining clear (cloud-free, water-free, and snow-free) pixels, dark pixels are selected based only on their reflectance at 2.13 μm, i.e. $0.01 \leq \rho_{2.13} \leq 0.25$. To minimize the residual cloud and odd surface contamination, the pixels remaining after masking and dark target selection are

sorted in terms of their visible reflectance $\rho_{0.66}$. The darkest 20 % and brightest 50 % of $\rho_{0.66}$ are discarded (Remer et al., 2005). This procedure is possible to derive aerosol properties when the 2.13 μm reflectance is brighter than 0.25, but it is expected to be less accurate (Remer et al., 2005). It cannot be used on bright surfaces such as deserts and urban areas (Levy et al., 2004, 2007). In order to estimate aerosols over variable cover types, including bright and dark surfaces, the minimum reflectance technique (MRT) was developed for TOMS (Herman and Celarier, 1997) and GOME (Koelemeijer et al., 2003) data at coarse resolution (> 1◦). In this study, a modified MRT method developed by Wong et al. (2010) is used for aerosol retrieval over urban areas at 1 km × 1 km resolution. The remaining pixels are used in the aerosol retrieval.

2) Determination of Rayleigh path reflectance

The upward spectral ‘‘reflectance’’ (normalized solar radiance) observed by a satellite at the top of the atmosphere (TOA) is a function of successive orders of radiation interactions within the coupled surface-atmosphere system (Levy et al., 2007). The top-of-atmosphere (TOA) reflectance ρ_λ^* observed by MODIS can be expressed as the sum of the contributions due to the atmospheric reflectance, which includes the Rayleigh path reflectance ρ_λ^{Ray} and the aerosol reflectance ρ_λ^a, and the surface reflectance ρ_λ^s. Assuming a Lambertian surface extended to infinity, the environment function is neglected so that to a good approximation, the TOA reflectance ρ_λ^* is described by Kaufman et al. (1997):

$$\rho_\lambda^* = \rho_\lambda^a + \rho_\lambda^{Ray} + \frac{T_\lambda(\theta_0)\cdot T_\lambda(\theta_s)\cdot \rho_\lambda^s}{1-S_\lambda \cdot \rho_\lambda^s} \tag{3-26}$$

where λ is the wavelength; S_λ is the spherical albedo of the atmosphere; θ_0 and θ_s are the sun and satellite zenith angles; and $T_\lambda(\theta_0)$ and $T_\lambda(\theta_s)$ are the total atmospheric transmittances, containing both direct and diffuse transmissions for sun illumination and satellite viewing geometry. The total transmittances include Rayleigh scattering and aerosol extinction, which can be given as $T_\lambda = T_\lambda^{Ray} \cdot T_\lambda^a$. Details of the determination of total transmission and hemispheric reflectance can be found in von Hoyningen-Huene et al. (2007). In practice, T_λ is approximated based upon the Rayleigh optical thickness (Drury et al., 2008).

The Rayleigh path reflectance is calculated based on the spectral dependence of the Rayleigh optical depth and phase function using the following equation (Wong et al., 2010):

$$\rho_{\lambda}^{Ray} = \pi \cdot \tau_{\lambda}^{Ray} \cdot p_{\lambda}^{Ray} \cdot m(\theta_0) \cdot m(\theta_s) \tag{3-27}$$

where τ_{λ}^{Ray} is the Rayleigh scattering optical thickness; p_{λ}^{Ray} is the phase function of Rayleigh scattering; $m(\theta_0)$ and $m(\theta_s)$ are the air mass factors (AMFs) for the solar elevation and satellite elevation, respectively.

The Rayleigh scattering optical thickness is calculated using the analytic formula developed by Bucholtz (1995):

$$\tau_{\lambda}^{Ray} = A \cdot \lambda^{-(B+C\lambda+D/\lambda)} \cdot \frac{p(z)}{p_0} \tag{3-28}$$

where λ is the wavelength; A, B, C, and D, are the constants of the total Rayleigh scattering cross section and the total Rayleigh volume scattering coefficient at standard atmosphere. $A = 3.01577 \times 10^{-28}$, $B = 3.55212$, C = 1.35579, and D = 0.11563 for the wavelength range 0.2–0.5 μm; and $A = 4.01061 \times 10^{-28}$, $B = 3.99668$, $C = 1.10298 \times 10^{-3}$, and $D = 2.71393 \times 10^{-2}$ for wavelengths greater than 0.5 μm. z is the surface elevation in kilometers, which is obtained from the digital elevation model (DEM) in MOD03 geolocation data. p_0 is the standard pressure and $p_{(z)}$ is the pressure at the surface elevation z, which is determined by the parameterized barometric equation (von Hoyningen-Huene et al., 2003):

$$p(z) = p_0 \cdot \exp\left[\frac{-29.87 \cdot g \cdot 0.75 \cdot z}{8.315 \cdot (T_{surf} - g \cdot 0.75 \cdot z)}\right] \tag{3-28-1}$$

where g is the gravity acceleration (9.807m/s^2) and T_{surf} is the surface temperature (K).

The phase function of Rayleigh scattering p_{λ}^{Ray} is given as (Bucholtz, 1995):

$$p_{\lambda}^{Ray} = \frac{4}{3}\left(1+\cos\Theta^2\right)\left(\frac{1-\delta_{\lambda}^{Ray}}{1+2\delta_{\lambda}^{Ray}}\right) \quad (3\text{-}29)$$

where Θ is the scattering angle and δ_{λ}^{Ray} is the Rayleigh polarization factor (i.e., 0.0279).

3) Determination of surface reflectance

When performing atmospheric retrievals from MODIS satellite, the major challenge is separating the total observed reflectance into atmospheric and surface contributions (Levy et al., 2007). The surface reflectances are determined in three wavelengths, $\rho_{0.47}^{S}$, $\rho_{0.66}^{S}$, and $\rho_{2.13}^{S}$. Assuming the atmosphere is approximately transparent at 2.13 μm since fine-mode particles (urban/industrial and biomass-burning aerosols) allows direct observation of surface (Kaufman et al., 2002), the top-of-atmosphere (TOA) reflectance at that wavelength can be equal to the surface reflectance, i.e., $\rho_{2.13}^{*}=\rho_{2.13}^{S}$. The surface reflectances at 0.47 and 0.66 μm ($\rho_{0.47}^{S}$, $\rho_{0.66}^{S}$) are first derived from the mean measured TOA reflectance at 2.13 μm ($\rho_{2.13}^{*}$) using the empirical relationships (Kaufman et al., 1997):

$$\rho_{0.47}^{s} = 0.25\rho_{2.13}^{*} \quad \text{and} \quad \rho_{0.66}^{s} = 0.50\rho_{2.13}^{*} \quad (3\text{-}30)$$

The MODIS surface reflectance products (MOD09) at 1 km are applied to validate the surface reflectances derived from the empirical relationships. The surface reflectances at 0.47 and 0.66 μm ($\rho_{0.47}^{S}$, $\rho_{0.66}^{S}$) are iteratively scaled (updated) until the difference with the surface reflectances in MOD09 within error tolerances ε = ± 0.005 at 0.47 μm and 0.001 at 0.66 μm (Drury et al., 2008).

In order to estimate the surface reflectances over variable cover types, including bright and dark surfaces, minimize the effects of bright surfaces, a modified minimum reflectance technique (MRT) (Wong et al., 2010) is used. Considering seasonal variations, the second minimum surface reflectance values are retrieved based on at least 30 cloud-free images for each season and are averaged to the annual mean surface reflectance in the image, so that avoid un-normal low reflectance caused by noise or shadow (Wong et al., 2010).

In addition, only nadir images with satellite viewing angle < 35◦ are considered in order to minimize the angular effects caused by the bidirectional reflectance distribution function (BRDF) effect in heterogeneous areas. The viewing angles are restricted in determining surface reflectance, but they are all considered during AOD calculation.

4) Determination of aerosol reflectance

The aerosol reflectances ρ_λ^a at 0.47 and 0.66 μm are decomposed from TOA reflectance, Rayleigh path reflectances and surface reflectances:

$$\rho_\lambda^a = \rho_\lambda^* - \rho_\lambda^{Ray} - \frac{T_\lambda(\theta_0)\cdot T_\lambda(\theta_s)\cdot \rho_\lambda^s}{1-S_\lambda \cdot \rho_\lambda^s} \tag{3-31}$$

5) Retrieval of aerosol optical depth

A new lookup table (LUT) describing relationship between the measured reflectances and the aerosol optical depth (τ_λ) is created using the Second Simulation of the Satellite Signal in the Solar Spectrum (6S) Radiative Transfer Code which is also based on the Lambertian uniform target assumption (Vermote et al., 1997) and the sun-satellite geometry in MOD03 at 1km (NASA, 2012a). This requires taking into account all factors which influence the radiative transfer in the atmosphere: i.e. solar elevation, illumination and observation geometry, Rayleigh scattering, surface reflectance for the different vegetation cover, the surface elevation with its surface pressure conditions, and the aerosol parameters: aerosol phase function, aerosol optical thickness, etc. The sun-satellite geometry in MOD03 at 1 km (NASA, 2012) and seasonal variations of the atmosphere, i.e. mid-latitude summer and mid-latitude winter standard atmospheres are used.

The aerosol optical properties ($\rho_\lambda^{6Sa}, \tau_\lambda$) are derived in the LUT for the presumed aerosol types using the urban model based upon the geolocation and season. The aerosol reflectances ρ_λ^a decomposed from MODIS are compared with the LUT aerosol reflectances ρ_λ^{6Sa} to find the 'best' (least-squares) fit. This best fit is the solution to the retrieval. An optimal spectral shape-fitting technique is executed to select the aerosol model with the smallest systematic errors (Kaufman and Tanré, 1998; Lee et al., 2007):

$$x^2 = \frac{1}{n}\sum_{j=1}^{n}\left(\frac{\rho_{\lambda_j}^{a} - \rho_{\lambda_j}^{6Sa}}{\rho_{\lambda_j}^{6Sa}}\right)^2 \quad (3\text{-}32)$$

The error term of x^2 is described as the residual of the aerosol reflectances derived from MODIS and the aerosol reflectances modeled by the 6S code, j is the number of wavelength. The aerosol optical properties modeled by the 6S code are iteratively updated until the error term of x^2 is minimum (Drury et al., 2008).

The minimum residual of x^2 is selected for each pixel. Then the appropriate aerosol model is allocated:

$$\tau_\lambda = f\left(\rho_\lambda^a\right) \quad (3\text{-}33)$$

The AOD is determined by the LUT which gives the relationship between aerosol reflectance and AOD. The AOD values at 0.47 and 0.66 μm ($\tau_{0.47}$, $\tau_{0.66}$) are derived for each pixel. Since the MODIS collection 5 AOD end products are only at 0.55 μm, the AODs at 0.55 μm, $\tau_{0.55}$, are generated by linear interpolation using $\tau_{0.47}$, $\tau_{0.66}$, so as to compare with the MODIS collection 5 AOD end products.

3.3.2 Estimation of ground-level $PM_{2.5}$ from retrieved AODs

The MODIS aerosol measurements is advantageous due to the near-daily global coverage, while MISR instrument views each scene on the earth from nine different angles, even though at smaller spatial and spectral ranges. MISR is also on board Terra launched in 1999, observes the Earth in reflected sunlight at nine different view zenith angles and four spectral bands (0.446, 0.558, 0.672, and 0.866 μm) (Diner et al., 2005). The zonal overlap swath width is 380 km, which provides the global multi-angle coverage of entire Earth in 9 days at the equator, and 2 days near the poles. The view angle variation of contrast within each 17.6 km cloud-free region is mathematically captured by means of a principal component analysis, which produces empirical orthogonal functions (EOFs) used to describe the surface reflectance contribution to the radiance at the top-of-atmosphere with a resolution of 17.6 km × 17.6 km (Martonchik et al., 2009). The additional angular information allows the MISR AOD retrievals to reduce the algorithmic assumptions and retrieval bias, as well as obtain the information

about microphysical properties and plume heights in the aerosol source regions (Kahn et al., 2007a).

The MODIS and MISR AOD retrievals are expected to differ due to the factors such as processing methods, calibration and retrieval algorithms (Kahn et al., 2007b). In the most idealized field conditions, MISR AOD is slightly higher than MODIS over water, and MODIS AOD is consistently higher than MISR over land (Abdou et al., 2005). Both MISR and MODIS AOD values are highly significant for prediction of $PM_{2.5}$ concentrations (Liu et al., 2007b; van Donkelaar et al., 2010). Therefore, the AODs retrieved from MODIS and MISR are combined to derive the $PM_{2.5}$ concentrations.

A GIS-based approach is developed to combine MODIS and MISR AODs into a single AOD value in each grid cell (10 km × 10 km). The combined AOD values are used to derive ground-level $PM_{2.5}$ concentrations by the local scaling factors and the factor of dry aerosol mass to satellite retrieved AOD, both of them obtained from the GEOS-Chem atmospheric simulation. Figure 3-5 shows the flow chart of data process.

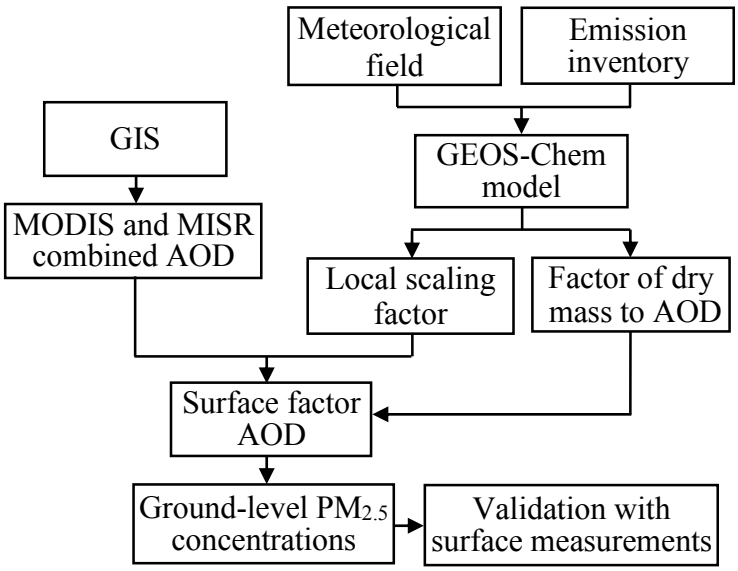

Figure 3-6 Flow chart of derivation of ground-level $PM_{2.5}$ concentrations.

The aerosol vertical profiles, which are used to calculate the local scaling factors of AOD in the lower atmosphere, are simulated by the global 3D chemical transport model GEOS-Chem (version 9-01-02) at 0.5º × 0.667º horizontal resolution and 47 vertical levels for the study area. The assimilated meteorology of GEOS-5 is used in the

simulation to compute the surface factor AOD (Liu et al., 2004). The aerosol mass concentrations are simulated for five aerosol types: (1) dust in five size classes, (2) sulfate-nitrate-ammonium (SNA), (3) black carbon (BC), (4) organic carbon (OC), and (5) fine and coarse mode sea salt (Drury et al., 2010). Detailed descriptions of the GEOS-Chem aerosol emission inventories and simulation evaluations in North America are provided by Fairlie et al. (2007) for dust, Park et al. (2004) and Martin et al. (2004) for SNA, Bond et al. (2007) for EC and OC, Alexander et al. (2005) for sea salt, Park et al. (2003, 2004, 2006) for the other aerosol types. In this study, the anthropogenic emissions are overwritten in areas with the local inventory following the approach of van Donkelaar et al. (2008). All model outputs are saved at 3-hour intervals and interpolated to the satellite overpass time (10:30am and 1:30pm local time). The mass concentrations of five aerosol types are summed to generate the simulated aerosol mass concentrations for each vertical model layer.

The aerosol optical properties are calculated with a standard Mie scattering code (Mischenko et al., 1999) for each aerosol type by assuming that the aerosols have lognormal size distributions (Drury et al., 2010). All aerosol types are assumed externally mixed and summed to generate the AOD, the ensemble single scattering albedo, and the ensemble scattering phase function (Drury et al., 2008). The GEOS-Chem simulated aerosol optical properties are spatially interpolated to the resolution of the retrieved AODs from satellite observation.

The methods developed by Liu et al. (2007a) is used to determine the surface factor AOD:

$$\text{MODIS and MISR surface factor AOD} = \frac{\text{GEOS-Chem surface factor AOD}}{\text{GEOS-Chem columnar AOD}} \times \text{MODIS and MISR columnar AOD} \quad (3\text{-}34\text{-}1)$$

The mass concentrations of five aerosol types (including SO_4^{2-}, NO_3^-, NH_4^+, EC, OC, sea salt, and mineral dust) simulated by GEOS-Chem are summed to generate the simulated dry aerosol mass concentrations for each vertical model layer and interpolated to the satellite overpass time (10:30 and 13:30 local time). The relationship between the

surface factor AOD and the dry aerosol mass is calculated, which is used to estimate the ground-level $PM_{2.5}$ concentrations by van Donkelaar et al. (2010):

$$PM_{2.5} = \eta \times \text{surface factor AOD} \tag{3-34-2}$$

where η is the factor that relates satellite-derived surface factor AOD to ground-level $PM_{2.5}$ concentrations ($\mu g/m^3$). It is determined from the ratio of simulated dry aerosol mass to simulated surface factor AOD at satellite overpass, which is a function of aerosol size, aerosol type, relative humidity, and the vertical structure of aerosol extinction (van Donkelaar et al., 2006). The values of η from 0.5º × 0.667º grid cells (the resolution of the GEOS-Chem simulation) are interpolated to the resolution which is consistent with the retrieved AODs from satellite observation to derive the ground-level $PM_{2.5}$ concentrations.

3.4 GIS-Based Fuzzy Aggregation Risk Assessment

3.4.1 Fuzzy set theory

Fuzzy set theory, an extension of classical set theory was first proposed by Lotfi Zadeh (1965). The theory provided a mathematical framework for handling categories that permitting partial membership (or membership in degree) to model complex systems that were difficult to model through conventional set theories. A fuzzy set is characterized by a membership function which represents numerically the degree to which an element belongs to the set (Zimmermann, 1992). According to Zadeh's definition (Zadeh, 1965), if X is a collection of objects denoted generically by x, a fuzzy set A in X is then defined in terms of a set of ordered pairs of elements x and its membership function:

$$A = \left\{ \left(x, \mu_A(x) \right) | x \in X \right\} \tag{3-35}$$

where $\mu(x)$ is the membership function of x in A. The mapping of the function is denoted by m_x: $X \rightarrow [0, 1]$, allowing for values from the entire unit interval. The closer the value of $\mu(x)$ to unity, the more x belongs to A.

A more convenient notation was proposed by Zadeh (1972). When X is a finite set $\{x_1, x_2, \ldots, x_n\}$, a fuzzy set on X is expressed as

$$A = \mu_A(x_1)/x_1 + \mu_A(x_2)/x_2 + \cdots \mu_A(x_n)/x_n = \sum_{i=1}^{n} \mu_A(x_i)/x_i \qquad (3\text{-}36)$$

For fuzzy sets A and B, the classical operations, intersection, union and complement, are based on the minimum and maximum, i.e.

$$\mu_{A\cap B}(x) = \min\{\mu_A(x), \mu_B(x)\} \qquad \forall(x) \in X \qquad (3\text{-}37)$$

$$\mu_{A\cup B}(x) = \max\{\mu_A(x), \mu_B(x)\} \qquad \forall(x) \in X \qquad (3\text{-}38)$$

$$\mu_{\bar{A}}(x) = 1 - \mu_A(x) \qquad \forall(x) \in X \qquad (3\text{-}39)$$

Functions that qualify as fuzzy intersections and fuzzy unions are usually referred in the literatures as t-norms and t-conorms, respectively (Klir and Yuan, 1995). Nowadays a large class of conjunctive and disjunctive functions, triangular norms and conorms, are used to model fuzzy set intersection and union (Michael and Verkuilen, 2006).

There are three other operations on fuzzy sets that are important, namely, concentration, dilation, and aggregation. Concentration and dilation modify one set, similar to the complement, whereas aggregation is another connective between sets, similar to union and intersection (Beliakov et al., 2007).

Fuzzy aggregation operator combines several fuzzy sets in a desirable way to produce a single fuzzy set. The aggregation operation on n fuzzy sets where $n \geq 2$ is formally defined by a function F: $[0, 1]^n \rightarrow [0, 1]$, with the properties (Cornelis et al., 2010):

i) $f\underbrace{(0,0,\cdots 0)}_{n-times} = 0$ and $f\underbrace{(1,1,\cdots 1)}_{n-times} = 1$

ii) $A \leq B$ implies $f(a) \leq f(b)$ for all $A, B \in [0,1]^n$

There are many different aggregation operators. But there are at least four classes of aggregation operations may consider as being currently investigated (Beliakov et al., 2007):

- Averaging aggregation: an aggregation function *f* has averaging behavior (or is averaging) if for every *x* it is bounded by $\min(x) \leq f(x) \leq \max(x)$.
- Conjunctive aggregation: an aggregation function *f* has conjunctive behavior (or is conjunctive) if for every *x* it is bounded by $f(x) \leq \min(x) = \min(x_1, x_2, \ldots, x_n)$.
- Disjunctive aggregation: an aggregation function *f* has disjunctive behavior (or is disjunctive) if for every *x* it is bounded by $f(x) \geq \max(x) = \max(x_1, x_2, \ldots, x_n)$.
- Mixed aggregation: an aggregation function *f* is mixed if it does not belong to any of the above classes, i.e., it exhibits different types of behavior on different parts of the domain.

3.4.2 Fuzzy relation analysis approach

Fuzzy relations generalize the concept of relations by admitting the notion of partial association between elements of universes. Given two universes *X* and *Y*, a fuzzy relation *R* is any fuzzy subset of the Cartesian product of *X* and *Y* (Zadeh, 1971). Equivalently, a fuzzy relation on $X \times Y$ is a mapping: $R: X \times Y \rightarrow [0, 1]$.

The membership function of *R* for some pair (x, y), $R(x, y) = 1$, denotes that the two elements *x* and *y* are fully related. Conversely, $R(x, y) = 0$, means that these elements are unrelated. Whereas the values in-between, $0 < R(x, y) < 1$, underline a partial association. The basic operations on fuzzy relations, say union, intersection, and complement, conceptually follow the corresponding operations on fuzzy sets once fuzzy relations are fuzzy sets formed on multidimensional spaces (Zadeh, 1975).

A mechanism to construct fuzzy relations is through the use of the concept of Cartesian product extended to fuzzy sets. The concept closely follows the one adopted for sets once they involve the pairs of points of the underlying universes, added with a membership degree (Pedrycz and Gomide, 2007).

If $U: Z \times X \rightarrow [0, 1]$ and $V: Z \times Y \rightarrow [0, 1]$ are fuzzy relations on finite universes, $X = \{x_1, x_2, \ldots, x_n\}$, $Z = \{z_1, z_2, \ldots, z_n\}$, and $Y = \{y_1, y_2, \ldots, y_n\}$, represented by $(p \times n)$ and

($p \times m$) fuzzy relational matrices $[u_{ki}]$ and $[v_{kj}]$, respectively, and $R = [r_{ij}]$ is the ($m \times n$) fuzzy relational matrix associated with a fuzzy relation R: $X \times Y \rightarrow [0,1]$, then the fuzzy relation becomes

$$V = U \bullet R \tag{3-40}$$

Denote by U^k the kth row of U and by V^k the kth row of V, $k = 1, 2, \ldots, p$. Let R^j be the jth column of R, $j = 1, 2, \ldots, m$. Eq. (3-40) can be rewritten as follows:

$$\begin{pmatrix} V^1 \\ V^2 \\ \vdots \\ V^p \end{pmatrix} = \begin{pmatrix} U^1 \\ U^2 \\ \vdots \\ U^p \end{pmatrix} \cdot \left(R^1 R^2 \cdots R^m\right) = \begin{pmatrix} U^1 \cdot R^1 & \cdots & U^1 \cdot R^m \\ \vdots & \ddots & \vdots \\ U^p \cdot R^1 & \cdots & U^p \cdot R^m \end{pmatrix} \tag{3-41}$$

where • can be a t-norm or t-conorm, referred as max-min or max-* composition (Zadeh, 1971).

3.4.3 Fuzzy aggregation - OWA approach

When fuzzy set theory is used to produce an aggregate fuzzy set by operating on the membership grades of fuzzy sets, there are two potential pitfalls, exaggeration and eclipsing that are very important in aggregation process (Ott, 1978). Exaggeration is a case where individual pollution factor possess lower values (i.e., in an acceptable range), yet the aggregate comes out unacceptably high. Eclipsing is the converse phenomenon, where one or more of the pollution factors are of relatively high value (i.e., in an unacceptable range), yet the aggregate comes out as unacceptably low. These phenomena are typically affected by the method of aggregation, thus the challenge is to determine the best aggregation method that can simultaneously reduce both exaggeration and eclipsing (Veiga, 1995).

For tackling this problem, an ordered weighted averaging (OWA) operator (Yager, 1988), which is based on averaging aggregation, is employed. Yager (1988) defined the OWA operator: a mapping F: $R^n \rightarrow R$ (where $R \rightarrow [0, 1]$) as an ordered weighted averaging operator of dimension n if it is associated with a weighting vector $(w_1, w_2, \ldots, w_n)^T$, so that

$$\omega_i \in [0,1] \ , \ \sum_{i=1}^{n} \omega_i = 1 \tag{3-42}$$

and

$$F(a_1, a_2, ...a_n) = \sum_{j=1}^{n} b_j \cdot \omega_j \tag{3-43}$$

where b_j is the jth largest element of (a_1, a_2, ...,a_n). OWA operators are symmetric aggregation functions that allocate weights according to the input values. Thus OWA can emphasize largest, smallest or mid-range inputs. By using OWA operators, the exaggeration and eclipsing in aggregation function can be reduced.

Generally, triangular (TFN) or trapezoidal (ZFN) fuzzy numbers are used to represent fuzzy variables. In this study, the term risk designated by TFN, is defined by two distinct factors, grade and importance, which are synonymous to the membership grade (i.e. fuzzy relation) of a fuzzy set and weight coefficient. The membership grade is the degree of a pollution factor that belongs to each fuzzy air quality criteria. Whereas the weight coefficient denotes the relative importance of a pollution factor on air quality, which is used for identifying different scales of health impact between various pollution factors. The higher the weight is, the larger the impact.

Incorporating the OWA operators into the max-min or max-* composition (Zadeh, 1971), we have two fuzzy aggregation-OWA models for air quality integrated risk assessment.

Max-min composition model:

$$F = (f_j) = \sum_{i=1}^{m} (w_i \bigcap r_{ij}) = \max\{\min(w_1, r_{1j}), \min(w_2, r_{2j}), \cdots, \min(w_m, r_{mj})\}$$

$$j=1, 2, \ldots, n \tag{3-44}$$

Max-* composition model:

$$F = (f_j) = \bigcup_{i=1}^{m} (w_i \cdot r_{ij}) = \max\{(w_1 \cdot r_{1j}), (w_2 \cdot r_{2j}), \cdots, (w_m \cdot r_{mj})\}$$

$$j=1, 2, \ldots, n \tag{3-45}$$

where $F = (f_j)$ represents the membership grade (possibility) for integrated risk level j to occur; w_i is the degree of importance for pollutant i, and r_{ij} is the grade of membership for fuzzy relation between pollutant i and risk level j.

The above fuzzy aggregation-OWA approach is a generalized aggregation transformation that provides flexible aggregation ranging between the minimum and the maximum operators. It can quantify the different impact scales of various pollution factors on air quality and stress the maximum effect. For an air quality system containing several pollutants with high concentrations, the integrated risk level can be obtained through the above models.

3.4.4 Integrated risk assessment

The fuzzy aggregation-OWA approach is implemented in ArcGIS and are combined with the GMSMB modeling system. The integrated risk caused by multiple air pollutants is assessed based on the gridded spatial concentration distributions predicted by the GMSMB modeling system. It involves five stages for the integrated risk assessment: (1) quantification of evaluation criterion using six fuzzy sets based on the U.S. Air Quality Index (AQI) (US EPA, 2009a); (2) construction of fuzzy membership functions; (3) calculation of relative importance (i.e. weighting coefficient w_i for each pollution factor); (4) construction of fuzzy aggregation-OWA modeling; and (5) assessment of integrated risk based on the fuzzy aggregation-OWA modeling. An overview of system framework and five stages of integrated risk assessment (shaded boxes) are shown in Figure 3-6.

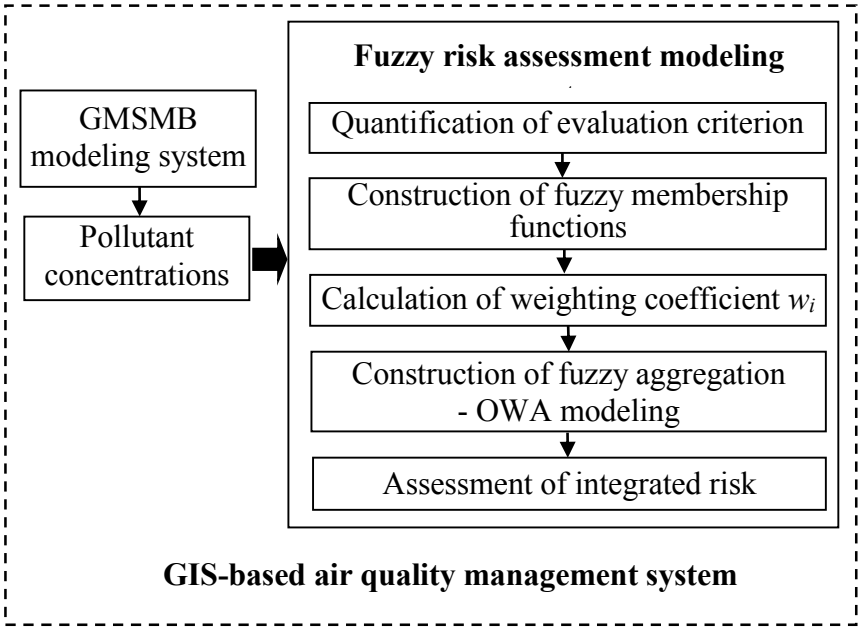

Figure 3-7 Framework of fuzzy aggregation-OWA approach.

The fuzzy aggregation-OWA approach is a generalized aggregation operator that provides flexible aggregation ranging from the minimum to the maximum operators for the integrated risk assessment, which can quantify the different effect scales of various pollution factors on air quality and stress the maximum effect. For an air quality system containing several pollutants with high concentrations, the integrated risk assessment can be obtained through the above modeling system.

3.5 Summary

This chapter described the methodologies of the development of GMSMB modeling system, the application of satellite remote sensing approach to derive the ground-level NO_2 concentrations, the development of satellite remote sensing approach to retrieve aerosol optical depth (AOD) and to derive ground-level $PM_{2.5}$ concentrations, and the development of fuzzy aggregation risk assessment approach to evaluate the health risks arising from multiple air pollutants. Specifically, the methodologies used in this thesis are summarized as follows:

(1) Developing the GMSMB air quality modeling system, which consists of a spatially extended multi-box model combined with a multi-source and multi-grid

Gaussian model, is developed within the GIS framework to examine the contributions from both point- and area-source emissions. By using GIS, a sizeable amount of data including air quality, meteorological data, and spatial location information required for air quality modeling are brought into an integrated modeling environment. The spatial multi-box model is used for simulating the emissions from area and mobile sources, while the multi-source and multi-grid Gaussian model is used in each sub-box for simulating the emissions from point sources. GIS is employed to handle the spatial location, terrain features, and land use/land cover characterizations for elevated airflow using digital map and the National Elevation Dataset (NED), which allows the modeling approach to consider complex terrain. Through the integration with GIS, it allows the spatial analyst on both regional and local scales with geo-referenced database. The physical and chemical processes are also taken into account with land use/land cover characterizations. Three measurements for evaluating the performance of modeling approach are also listed.

(2) Constructing the fuzzy aggregation-OWA risk assessment approach to evaluate the integrated health risks arising from multiple air pollutants based on the gridded spatial concentration distributions predicted by the GMSMB modeling system. It involves five stages for the integrated risk assessment.

(3) Deriving the ground-level NO_2 concentrations from the satellite OMI tropospheric NO_2 vertical column densities (VCDs) using the local NO_2 profile obtained from the global three-dimensional chemical transport model GEOS-Chem.

(4) Developing the improved aerosol optical depth (AOD) retrieval algorithm for the MODIS satellite instrument at 1-km resolution for the application of urban scale. A new lookup table (LUT) is created with the 6S radiative transfer code which is used for the AOD retrieval by spectral shape-fitting technique. The retrieved AODs are used to derive the ground-level $PM_{2.5}$ concentrations using the local scaling factors obtained from the GEOS-Chem simulation.

Chapter 4 GMSMB Modeling Approach for Air Pollution Risk Assessment

---A North American Case Study

In order to test and evaluate the developed GMSMB modeling approach (see Chapter 3), the state of California is chosen as the study area since there are a wide variety of climates, geographic features, meteorological factors and emission sources in this area, which make it difficult to evaluate the air quality. In this case study, the spatial concentration distributions of four criteria pollutants ($PM_{2.5}$, SO_2, NO_2 and CO) in 2008 are simulated using the developed modeling approach. The modeling results are validated with the in-situ surface measurements.

4.1 Overview of the Study Area

The state of California is located on the West Coast of the United States, bounded by the Pacific Ocean and the States of Oregon, Nevada, Arizona, and the Baja (Mexico) (see Figure 4). The geographic coordinates is from 32°32'N to 42°N, and 114°8'W to 124°26'W. With an area of 160,000 square miles (414,000 km^2), it is the third-largest and the most populous state in the United States (U.S. Census Bureau, 2011). In the middle of the state lies the California Central Valley, bounded by the coastal mountain ranges in the west, the Sierra Nevada to the east, the Cascade Range in the north and the Tehachapi Mountains in the south (Friedemann, 2007).

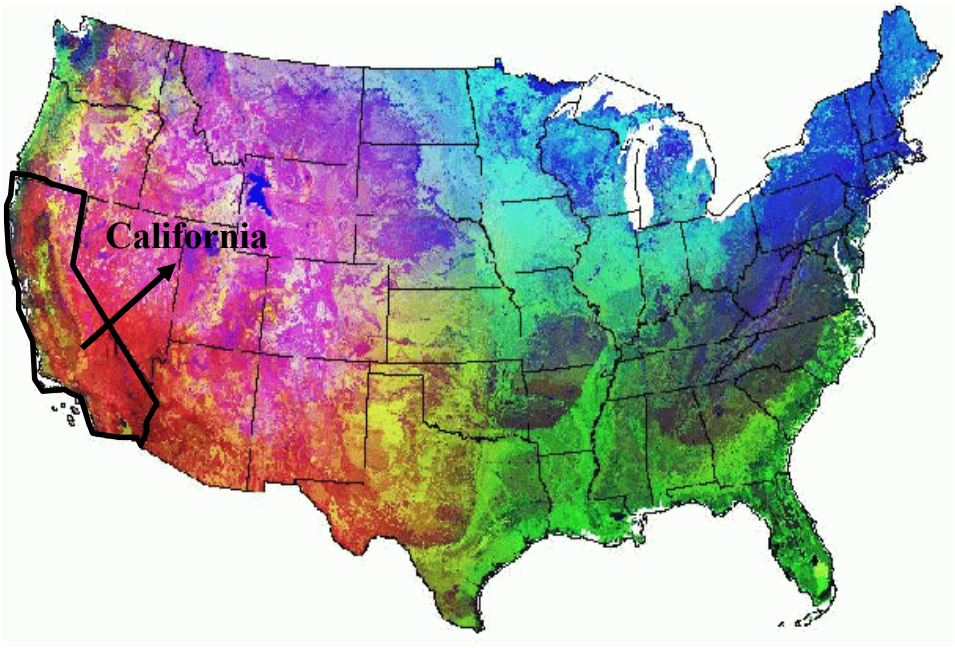

Figure 4-1 Study area

There are a wide variety of climates, geographic features, meteorological factors and emission sources in the state of California which make it difficult to assess the air quality in this area. For the purpose of managing air resources on a regional scale, the state of California is divided into 15 air basins by the California Air Resources Board (CARB) based on the similar meteorological and geographic conditions, as well as the state political boundaries (CARB, 2009a), as shown in Figure 4-2.

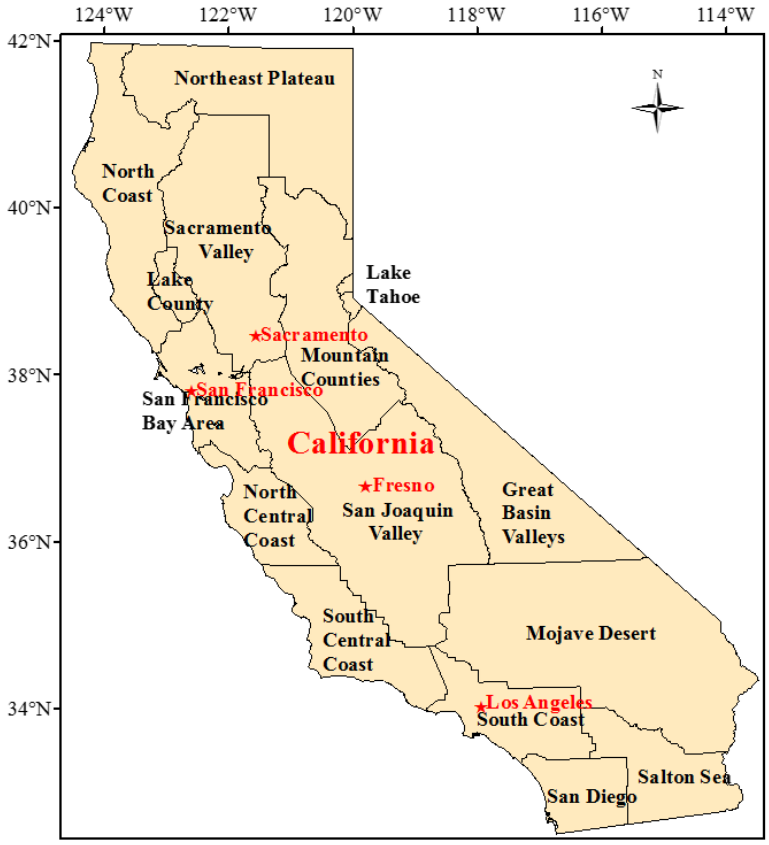

Figure 4-2 Air basins map of the state of California (CARB, 2009a).

To estimate the emission sources of air pollutants and quantities of the pollution levels, the CARB, in cooperation with the local air districts and industries, maintains an emission inventory for the state of California (Cox et al., 2009). The CARB also operates a statewide monitoring network with more than 250 monitoring sites for measuring the airborne pollutant concentrations (Cox et al., 2009).

4.2 Data Preparation

4.2.1 Spatial information data

The digital maps at 7.5-minute quadrangle, Land Use/Land Cover (LULC) data at 1:250,000-scale, and the new generation DEM - National Elevation Dataset (NED) with a resolution of 1/3 arc-second (roughly 10 meters) are obtained from the U.S. Geological Survey (USGS) (USGS, 2010). Based on the spatial information data, the study area is horizontally divided into 10 km × 10 km grid cells. In vertical, a height of 750 m above

ground level is divided into equal layers of 250 m each. The raw terrain data and terrain elevations from the digital maps and NED are processed into each grid cell with major land features required in modeling process. The land use data is analyzed to produce land use category layers based on the USGS Land Use Classification System Level I (9-Category system) (Scire et al., 2000). The surface properties, including albedo, roughness length, and leaf area index as functions of land use/land cover type are processed for each grid cell.

4.2.2 Emission inventory data

The statewide emission inventory data during the year 2008 (annual average) is collected from the Air Emission Inventory Database of the CARB (CARB, 2009b), which focused on four pollutants ($PM_{2.5}$, NO_2, SO_2, and CO) emitted from 13,327 sources. The California emission inventory contains information on three air pollution sources: 1) stationary sources - approximately 13,000 individual facilities, namely point sources; 2) area-wide sources - approximately 80 source categories; and 3) mobile sources - all on-road vehicles (e.g., automobiles and trucks), off-road vehicles (e.g. trains, ships and aircraft) and farm equipment. The summary of California Statewide Emission Inventory for the year 2008 is presented in Table 4-1 (Cox et al., 2009).

Table 4-1 A summary of California statewide emission inventory for the year 2008.

Major Emission Category	**Emission (Tons/Day, Annual Average)**			
	CO	**NO_2**	**SO_2**	**$PM_{2.5}$**
Stationary Sources	317	368	109	95
Fuel Combustion	245	262	39	31
Waste Disposal	4	3	1	1
Cleaning and Surface Coatings	0	0	0	1
Petroleum Production	12	8	40	3
Other Industrial Processes	56	94	30	58
Area-Wide Sources	1968	95	6	448
Solvent Evaporation	0	0	0	0
Miscellaneous Processes	1968	95	6	448

Mobile Sources	9042	2747	166	133
Light Duty Passenger Vehicles	2207	189	2	9
Light and Medium Duty Trucks	2568	300	2	13
Heavy Duty Trucks	796	1020	1	34
Other On-Road	529	75	0	2
Ocean Going Vessels & Commercial Harbor Craft	40	315	154	22
Pleasure Crafts	740	40	0	7
Recreational Vehicles	192	2	1	1
Off-road Equipment	1546	503	0	27
Other Off-Road	113	104	0	6
Total Statewide - All Sources	11327	3209	281	677

Notes: The data is from California Almanac of Emissions & Air Quality - 2009 Edition (Cox et al., 2009).

4.2.3 Background concentrations

In the spatial multi-box model, the background concentration must be added to the modeling concentrations. In the absence of "pristine" monitoring sites for the four pollutants in the state of California, literature survey together with statistical analysis of available monitoring data provides an estimation of the magnitude and spatial variability of background concentrations across the region. As an example, for $PM_{2.5}$, 2.0 $\mu g/m^3$ is used in the coastal areas, and 6.5 $\mu g/m^3$ in the urban, inland valleys and desert areas (Leonard, 2010); for CO, 2 ppm is used in the rural locations, and 3 ppm in the urban, inland valleys and desert areas (Shrouds, 2010); for NO_2, 0.005 ppm is used in the rural locations, and 0.015 ppm in the urban, inland valleys and desert areas (Leonard, 2010); for SO_2, 0 ppm is used in the rural locations, and 0.001 ppm in the urban, inland valleys and desert areas (Leonard, 2010).

4.2.4 Meteorological data

The surface meteorological data, including the ambient temperature, wind speed and direction with frequency distributions, humidity, precipitation and cloud cover measured from over 800 surface meteorological sites, are extracted from the CARB's real-time Air Quality and Meteorological Information System (AQMIS 2) (CARB, 2009c). The upper air meteorological data of monthly average at heights from 3 meter and up from the ground are obtained from the NOAA (National Oceanic and Atmospheric Administration) Upper-Air Data products (NOAA, 2010). The wind data are processed through interpolations between measurements for the intermediate height levels. Imported data include location, name ID, time zone and anemometer height, which are managed through GIS to determine the meteorological parameters for each sub-box.

4.3 Results and Discussion

The spatial concentration distributions of the four pollutants at different layers are simulated using the developed modeling approach with the California emission inventory data for 2008 (annual average). The modeling results of first layer for the integrated assessment of air pollution levels based on the California air basins are shown in Figure 4-3.

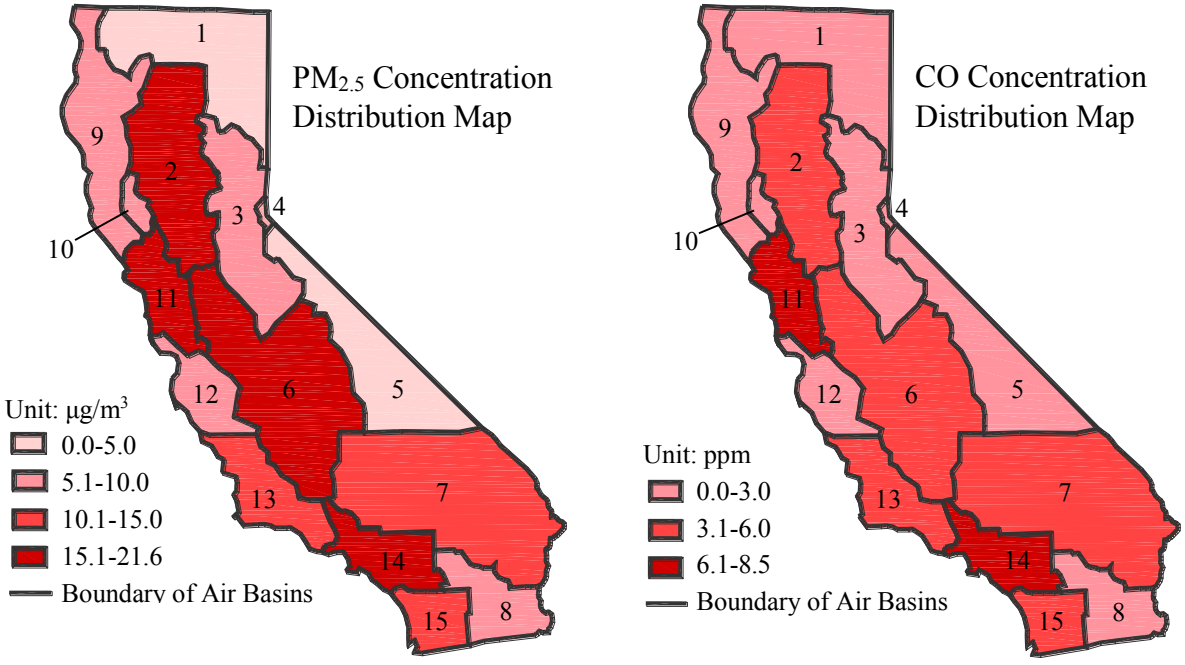

(a) (b)

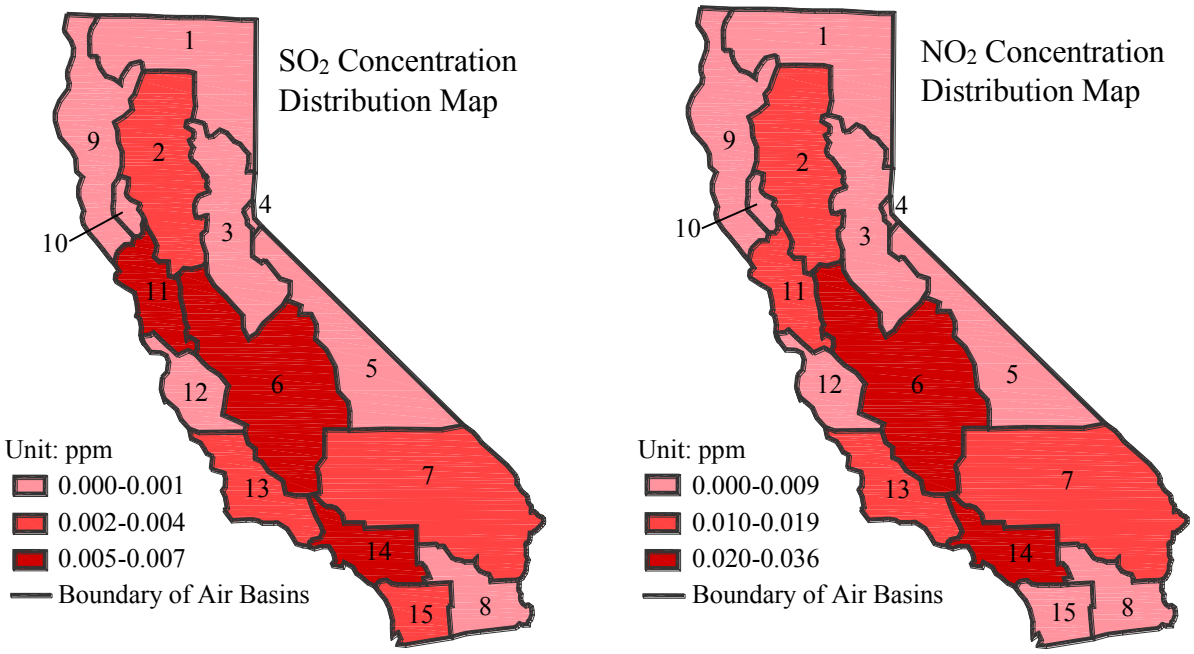

(c) (d)

Figure 4-3 Concentration distribution maps of four criteria pollutants for the state of California (2008 annual average): (a) $PM_{2.5}$; (b) CO; (c) SO_2; and (d) NO_2. 1 - 15 are the numbers of California air basins.

Figure 4-3 (a) shows that the state of California is divided into four pollution impact level areas according to the predicted concentration distributions of $PM_{2.5}$ in 2008. The highest level (at a range of 15.1-21.6 μg/m^3, shown in dark red) is predicted in four regions: a) the South Coast; b) the San Joaquin Valley; c) the San Francisco Bay Area; and d) the Sacramento Valley. The maximum modeling concentration for these areas is 21.6 μg/m^3, which is 1.8 times higher than the California Ambient Air Quality Standards (CAAQS) (12 μg/m^3) (CARB, 2009d, same as below), and the National Ambient Air Quality Standards (NAAQS) (12 μg/m^3) (USEPA, 2012, same as below). The second highest $PM_{2.5}$ pollution level (at a range of 10.1-15.0 μg/m^3, shown in salmon color) is found in: a) the South Central Coast; b) Mojave Desert Kern; and c) San Diego. The maximum concentration for these areas is 15.0 μg/m^3, which exceeds the NAAQS and the CAAQS by 1.25. The third highest $PM_{2.5}$ pollution level (at a range of 5.1-10.0 μg/m^3, shown in dark pink) is obtained in: a) the North Central Coast; b) Mountain Counties; and c) the North Coast; d) Salton Sea. The maximum concentration for these areas is

10.0 μg/m^3, which meets the NAAQS and the CAAQS. For the rest regions, the lowest $PM_{2.5}$ pollution levels (0.0-5.0 μg/m^3, shown in light pink) are predicted.

Figure 4-3 (b) presents the map of the modeling CO concentration distribution for the year 2008, which is marked with colors red to pink according to three impact levels. The maximum modeling result is 8.5 ppm occurring in the South Coast and San Francisco Bay Area, which meets the NAAQS and the CAAQS (8 hour value at 9 ppm).

Similarly, Figure 4-3 (c) and (d) present the maps of the predicted SO_2 and NO_2 concentration distribution for the year 2008, marked in red to pink based on the pollution levels (level is defined by a specific concentration range being represented with a color on GIS map). The maximum SO_2 concentration is 0.0066 ppm in the South Coast, San Francisco Bay Area and San Joaquin Valley, which is lower than the NAAQS (0.030 ppm for certain areas). The highest NO_2 concentrations also occur in the South Coast and San Joaquin Valley, with a maximum of 0.036 ppm, which is just over the CAAQS (0.030 ppm) and is lower than the NAAQS (0.053 ppm).

Correspondingly, the modeling results confirm with the following observations:

i). The modeling results have shown the detailed spatial concentration gradients within the local areas, which are not predicted by the traditional box model without consideration of point dispersion sources. It indicates that the emissions from local sources at different locations are significant for the geographic distribution of air pollution levels in the region.

ii). The highest concentrations of four contaminants all occur in the central and southern urbanized areas, due to the significant point emission sources, relatively higher ambient temperatures, and the effects of nearby mountains on the dispersion of air pollutants (Cox et al., 2009). For example, in the Los Angeles area, the Basin is surrounded by mountains on the north and east. Hence, pollutants tend to accumulate and remain within the area, and it is confirmed with the modeling results.

iii). There are relatively higher pollutant concentrations in the inland valleys and desert regions as they are the receptors of pollutants transported from upwind areas (Cox et al., 2009). The State of California lies within the zone of prevailing

westerlies. Wind carries locally produced air pollutants away from the Bay area, but may lead to higher concentrations in the regions on south and east of the source area.

iv). The North Coast, Northeast Plateau and Great Basin Valleys have better air quality because there are less air emission sources, a moderate climate and relatively cool temperature, as well as frequent changes of onshore/offshore airflow in these areas (Cox et al., 2009).

4.4 Model Validation and Discussion

4.4.1 Model validation

The developed GMSMB approach is evaluated by comparing the modeling results with the observed values under the same model configuration using 2008 data for the state of California. The traditional box model is also carried out to produce the prediction results with elevated area emission sources (point sources are converted to the area emission sources). The results from the traditional box model are included in the model verification analysis. 102, 36 and 96 monitoring results (annual average for the year 2008) with monitoring station IDs and addresses are obtained from the U.S EPA Air Quality System (AQS) Database for NO_2, SO_2, and $PM_{2.5}$, respectively (USEPA, 2010a). Since the annual average value for CO is not available, CO is not included in the model error analysis. The UTM coordinates of monitoring sites are obtained using geocoding function in ArcGIS. The modeling results of GMSMB and the traditional box model are then extracted corresponding to the UTM coordinates of the monitoring sites within the GIS environment. Two sets of modeling results and one set of monitoring values are matched with the same monitoring site locations and are compared in Table 4-2.

Table 4-2 Comparisons of modeling results and monitoring values of $PM_{2.5}$, SO_2, NO_2 for the year 2008.

Polluted Zone	UTM Coordinates x(m)	UTM Coordinates y(m)	Pollutant	GMSMB Results	Box Results	Monitoring Values	Dev. 1 (%)	Dev. 2 (%)
San Francisco Bay	1632730	4255669	$PM_{2.5}$ ($\mu g/m^3$)	12.20	14.87	10.45	16.7	42.3
			NO_2 (ppm)	0.0290	0.0330	0.0240	18.2	50.0
			SO_2 (ppm)	0.0023	0.0028	0.0020	15.0	40.0
	1663807	4214261	$PM_{2.5}$ ($\mu g/m^3$)	12.61	13.93	10.70	17.8	30.2
			NO_2 (ppm)	0.0140	0.0240	0.0170	-17.6	41.2
			SO_2 (ppm)	0.0024	0.0028	0.0020	20.0	40.0
South Coast	2055809	3898492	$PM_{2.5}$ ($\mu g/m^3$)	14.50	22.62	16.86	-14.0	34.2
			NO_2 (ppm)	0.0250	0.0460	0.0300	-16.7	53.3
			SO_2 (ppm)	0.0013	0.0015	0.0010	30.0	50.0
	2133920	3903568	$PM_{2.5}$ ($\mu g/m^3$)	16.50	28.26	19.84	-16.8	42.4
			NO_2 (ppm)	0.0160	0.0280	0.0200	-20.0	40.0
			SO_2 (ppm)	0.0017	0.0030	0.0020	-15.0	50.0
San Joaquin Valley	1954359	4030903	$PM_{2.5}$ ($\mu g/m^3$)	19.60	28.33	22.43	-12.6	26.3
			NO_2 (ppm)	0.0190	0.0220	0.0150	26.7	46.7
			SO_2 (ppm)	0.0060	0.0100	0.0070	-14.3	42.8
San Diego	2046477	3676258	$PM_{2.5}$ ($\mu g/m^3$)	11.10	16.78	12.74	-12.9	31.7
			NO_2 (ppm)	0.0130	0.0250	0.0180	-27.8	38.9
			SO_2 (ppm)	0.0027	0.0042	0.0030	-10.0	40.0

Note: [1] Only the areas with elevated concentrations are selected at UTM coordinate locations all based on annual mean values); [2] Deviation 1 is between GMSMB modeling results and monitoring values; and [3] Deviation 2 is between multi-box modeling results and monitoring values.

Table 4-2 indicates that the modeling results from GMSMB are more consistent with the monitoring values compared with that from the traditional box model. The traditional box model generally overestimates the air pollutant concentrations, and its results are higher than the GMSMB results. Clearly it is because that the spatial dispersion of location-based point sources is not considered in the traditional box model. Consequently, the GMSMB modeling approach has better performance than traditional box model as shown in Table 4-2.

Figure 4-4 presents the comparisons of the GMSMB modeling results with monitoring values for $PM_{2.5}$, NO_2 and SO_2. The correlations between modeling results and monitoring values are analyzed with R^2 values, which are 0.89, 0.90 and 0.94, for $PM_{2.5}$, NO_2, and SO_2 respectively (Figure 4-5). It is seen that the modeling results show satisfactory agreement with the monitoring values with slopes of 0.84, intercept of 2.25 for $PM_{2.5}$, slopes of 0.82, intercept of 0.003 for NO_2, and slopes of 0.90, intercept of 0.0002 for SO_2.

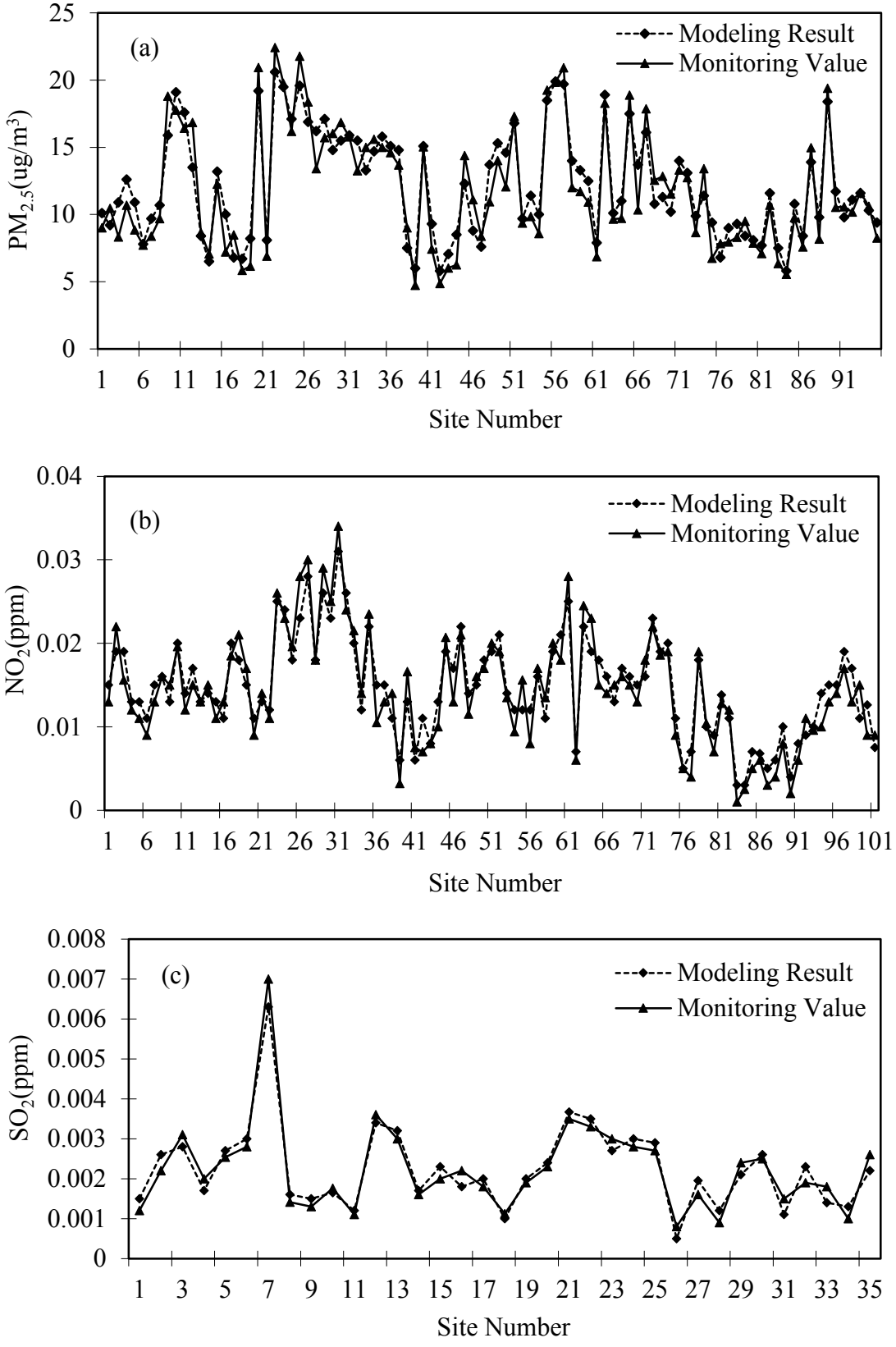

Figure 4-4 Modeling results (dotted lines) and monitoring values (solid lines) (2008 annual average) at the AQS monitoring sites. (a) $PM_{2.5}$; (b) NO_2; (c) SO_2.

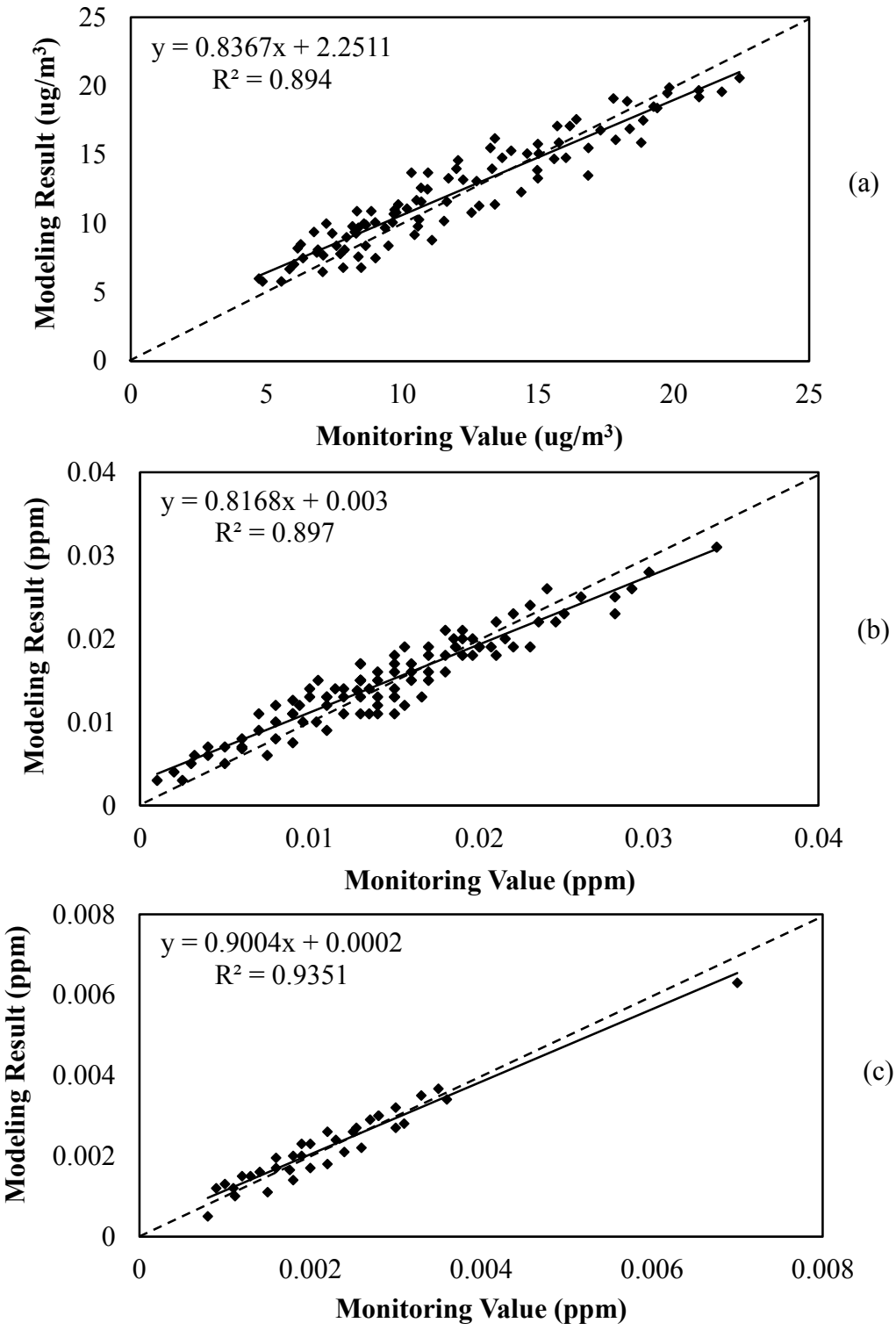

Figure 4-5 Correlations between modeling results and the monitoring data for: (a) $PM_{2.5}$, correlation coefficient r = 0.98; (b) NO_2, r = 0.93; (c) SO_2, r = 0.97. The solid line is trendline and the dashed line is 1:1 line.

Detailed error analysis is performed using the error equations of NMB, NME, and RMSE, and the summary is provided in Table 4-3. It can be seen that there are biases in the modeling results compared to the monitoring values with normalized mean bias (NMB) of 2.6 %, 2.5 % and 3.9 %, normalized mean error (NME) of 10.9 %, 13.4 % and 11.5 %, for $PM_{2.5}$, NO_2 and SO_2, respectively. It is suggested a range of ± 5-15% as an acceptable guideline of model performance for the normalized bias; and a range of 30-35% as an acceptable level of model performance for the mean normalized error (USEPA, 1991). Table 4-3 shows that GMSMB model performance meets the USEPA guideline for the field case study of the state of California.

Table 4-3 Verification and statistical error analysis for the GMSMB modeling case study.

Pollutant	RMSE	NMB (%)	NME (%)	USEPA
$PM_{2.5}$	1.50 μg/m^3	2.6	10.9	Bias: ± 5-15% Error: 30-35%
NO_2	0.0020 ppm	2.5	13.4	
SO_2	0.0003 ppm	3.9	11.5	

4.4.2 Discussion

Despite the reasonable results obtained based on the new model development and satisfactory model validation at a large field scale, the following discussions are extended:

(a) The comparisons also show that the modeling results slightly underestimate NO_2 and SO_2 with slopes of 0.99 and 0.98 (intercepts set as zero) for NO_2 and SO_2, respectively. This might be due to the comparisons are between the grided modeling results and the point monitoring values at the monitoring station locations. In addition, the inherent uncertainties in the monitoring values which are associated with the interferences of local emission sources, data availability, meteorological conditions in the maritime region, assumption of first order reaction for the study pollutants, and the occurrence of radical compound species taking place during photolytic conversion are also possible contributors for the underprediction (Gerboles et al., 2003; Lamsal et al., 2008).

(b) For $PM_{2.5}$, the modeling results show excellent agreement with monitoring values with a slope of 1.0 (intercept sets as zero). However, it tends to slightly underestimate in the areas with higher concentrations, such as the urban and suburban areas, while slightly overestimate in the areas with lower concentrations, like rural areas (see Figure 4-5a). Except the uncertainties as mentioned above, the complexities inherent in secondary particulate formation, pollutant transport, and time variability may also be reasons for the bias of modeling results. In addition, the distribution trends of PM2.5 are larger in urban and suburban areas and smaller in the rural areas (Perry et al., 2005).

(c) It is argued that the above mentioned uncertainties would also affect the performance of fully numerical air dispersion model and atmospheric photochemical reaction model, which may produce accurate simulation results for localized field cases (Isakov and Venkatram, 2006; Vivanco et al., 2009). The GMSMB provides a practical air quality modeling tool with a seamless integration of an extended spatial multi-box and multi-source Gaussian model with spatial GIS analysis. It is intended to assess the air pollution levels together with a greater spatial representation of geo-referenced information, through a collective consideration of various emission sources. It is noted that developing fully-coupled GIS-based air quality modeling approach is technically straightforward based on analytical or semi-numerical analysis as presented in this study.

4.5 Summary

The developed GMSMB modeling approach has been examined to predict the spatial concentration distribution of four air pollutants (CO, NO_2, SO_2 and $PM_{2.5}$) for the state of California. The modeling results were compared with the monitoring values. Good agreement was acquired which demonstrated that the developed modeling approach could deliver an effective air pollution assessment on both regional and local scales to support decision making on air pollution control and management planning.

Chapter 5 Fuzzy Aggregation Approach for Integrated Air Pollution Risk Assessment

Based on the spatial concentration distributions of the four criteria pollutants (i.e. $PM_{2.5}$, NO_2, SO_2, and CO) in the state of California predicted by the GMSMB modeling in chapter 4, the integrated risk caused by these four pollutants is estimated with the fuzzy aggregation-OWA approach, which involves five steps as presented in this chapter. The results are verified with the U.S. EPA Air Quality Index (AQI) Report.

5.1 Fuzzy Aggregation Integrated Air Pollution Risk Assessment

5.1.1 Quantification of fuzzy evaluation criterion

The first step is to quantify the fuzzy evaluation criterion. This is performed by determining the classifying representative values (e_i) and the benchmarks (s_i). According to the AQI made by the U.S. EPA, air quality is divided into six levels with a yardstick that runs from 0 to 500 (USEPA, 2009a). The higher the AQI value is, the higher the risk level of air pollution and the greater the health concern. An AQI value of 50 represents good air quality with little potential to affect public health, and an AQI value of 100 generally corresponds to the national air quality standard for the pollutant, which is the level the U.S. EPA has set to protect public health. While an AQI value over 300 represents hazardous air quality (US EPA, 2009a). Using the AQI calculator developed by the U.S. EPA (USEPA, 2009b), the AQI values can be converted to the concentrations, as shown in Table 5-1.

Table 5-1 AQI values and corresponding concentration intervals of pollution factors (USEPA, 2009a).

Pollution Factors	AQI and Corresponding Concentrations Intervals					
	0-50	50-100	101-150	151-200	201-300	301-500
$PM_{2.5}$ (μg/m^3)	(0.0,15.4)	(15.5,35.4)	(35.5,65.4)	(65.5,150.4)	(150.5,250.4)	(250.5,500.4)
NO_2 (ppm)	(0.0,0.059)	(0.060,0.075)	(0.076,0.095)	(0.096,0.115)	(0.116,0.374)	(0.375,0.604)
SO_2 (ppm)	(0.0,0.034)	(0.035,0.144)	(0.145,0.224)	(0.225,0.304)	(0.305,0.604)	(0.605,1.004)
CO (ppm)	(0.0,4.4)	(4.5,9.4)	(9.5,12.4)	(12.5,15.4)	(15.5,30.4)	(30.5,50.4)

Based on Table 5-1, the concentration intervals can be transformed into fuzzy sets, which are represented with classifying representative values (e_i) and benchmarks (s_i). Six fuzzy sets, i.e. six risk levels are defined to represent air quality within 'Good', 'Moderate', 'Low unhealthy', 'Unhealthy', 'Very unhealthy' and 'Hazardous'. For the first risk level, the upper limit concentration values are taken as the classifying representative values (e_1) since they are close to the annual mean values of national air quality standard for the pollutants (for CO, it's half of 8-hour mean) (USEPA, 2012); while for the rest, the average concentration values of each interval are taken as the classifying representative values (e_i). According to the AQI, the third risk level means "members of sensitive groups may experience health effects, while the general public is not likely to be affected" and the fourth risk level means "everyone may begin to experience health effects". Thus, the third risk level is considered as the safe level limit and its upper limit concentration values are taken as the benchmarks (s_i), as shown in Table 5-2.

Table 5-2 Fuzzy air quality evaluation criterion.

Pollution Factors	Classifying Representative Values (e_i)						Benchmarks (s_i)
	e_1	e_2	e_3	e_4	e_5	e_6	s_i
$PM_{2.5}$ (μg/m^3)	15.40	25.45	50.45	107.95	200.45	375.45	65.40
NO_2 (ppm)	0.059	0.068	0.086	0.106	0.245	0.490	0.095
SO_2 (ppm)	0.034	0.090	0.185	0.265	0.455	0.805	0.224
CO (ppm)	4.40	6.95	10.95	13.95	22.95	40.45	12.40

5.1.2 Construction of fuzzy membership functions

The membership function represents the degree of a specified concentration that belongs to the fuzzy evaluation criteria of air quality. Fuzzy set theory is used to determine the membership functions according to the characteristics of air quality evaluation criterion. The linear membership functions are shown as follows:

$$r_m(x)=\begin{cases}1 & x \le e(1) \quad or \quad x \ge e(6)\\ \left[e(m+1)-x\right]/\left[e(m+1)-e(m)\right] & e(m) \le x < e(m+1)\\ 0 & else\end{cases} \tag{5-1}$$

$$r_{m+1}(x)=1-r_m(x) \qquad e(m) \le x < e(m+1)$$

where m is the number of fuzzy set; $e(m)$ denotes the classifying representative value of each fuzzy set; $r_m(x)$ denotes the membership grade of each pollution factor belongs to each classifying representative value. Following the membership functions, the fuzzy function curves for risk levels are created, as shown in Figure 5-1.

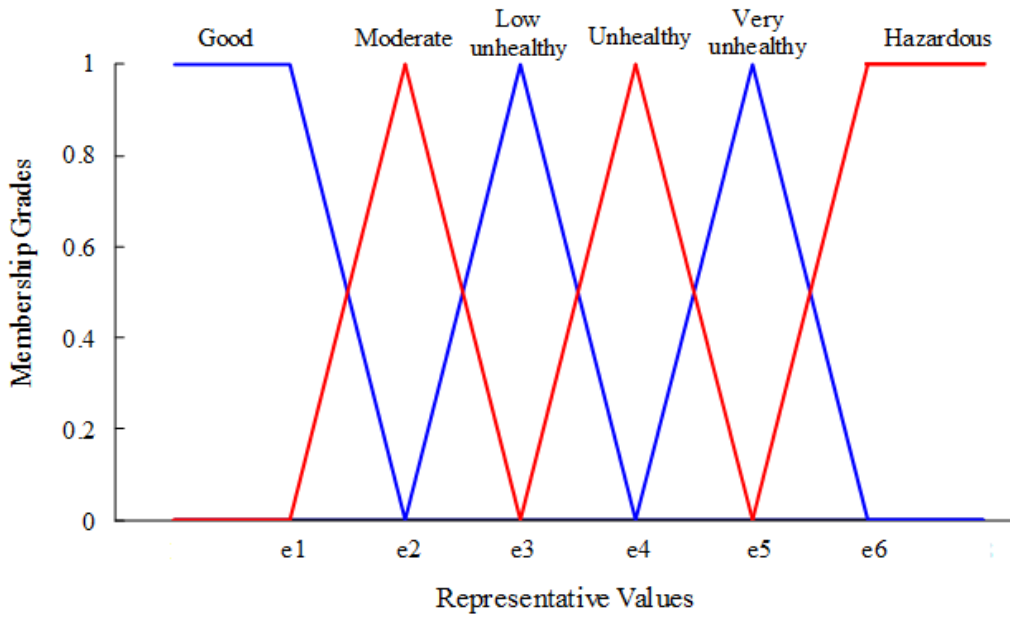

Figure 5-1 Curves of the membership functions for risk levels of air quality criterion.

5.1.3 Calculation of weighting coefficient

In this study, the relative importance, i.e. weighting coefficient w_i of each pollution factor is measured by the corresponding benchmark (s_i) which is the safe level limit. When the concentration of pollutant is lower than the benchmark, this pollutant factor is considered to have a smaller impact on air quality meaning that it causes a smaller risk. Conversely, when the concentration of pollutant is higher than the benchmark, it is considered that this pollution factor has a larger impact on air quality and causes a greater risk. Therefore, the weighting coefficient w_i can be calculated using the following formula:

$$w_i = \frac{C_i}{S_i} \tag{5-2}$$

where C_i is the predicted concentration of each pollutant; S_i is the benchmark of fuzzy air quality criterion of each pollution factor.

In this case, the weight coefficient w_i is more than 1 when the predicted concentration of pollutant is higher than the safety limit. Consequently, the definition of the aggregation function given by F: $[0, 1]^n \rightarrow [0,1]$ should be extended to R: $[0, r_j \cdot max(w_1, w_2, \ldots, w_n)]$, where r_j is the jth largest membership grade of $(r_1, r_2, \ldots, r_n)$.

5.1.4 Construction of fuzzy aggregation-OWA modeling

This has been discussed in section 3.4.3. The two models (i.e. the Max-min composition model and the Max-* composition model) are used in the fuzzy aggregation-OWA modeling system.

5.1.5 Assessment of integrated risk level

By loading the pollutant concentrations from the GMSMB modeling system, the integrated risk levels of air pollutants can be assessed in the fuzzy aggregation-OWA modeling system. The results from two models (eq. 3-44, 3-45) can cross-verify each other and the maximum integrated risk level is taken as the result of risk assessment.

An arbitrary grid in the study area is taken as an example to illustrate the details of computational process. The concentrations of four criteria pollutants, $PM_{2.5}$, NO_2, SO_2

and CO in this grid are 18.5 μg/m^3, 0.063 ppm, 0.045 ppm, and 3.3 ppm, respectively. The procedure of integrated risk assessment is as following:

(1) Calculation of the membership grades (r_{ij}) of pollutant concentrations. The membership grade (r_{ij}) is the degree of predicted concentration of each pollution factor in the grid that belongs to each classifying representative value of the fuzzy air quality criterion (see Table 5-2). The membership grade matrix R is obtained using eq. (5-1):

$$R = \left[r_{ij} \right] = \begin{bmatrix} 0.6900 & 0.3100 & 0 & 0 & 0 & 0 \\ 0.3750 & 0.6250 & 0 & 0 & 0 & 0 \\ 0.8000 & 0.2000 & 0 & 0 & 0 & 0 \\ 1 & 0 & 0 & 0 & 0 & 0 \end{bmatrix}$$

(2) Calculation of the weighting coefficient w_i of each pollution factor. The vector of weighting coefficient W is determined by eq. (5-2):

$$W = (0.2829, 0.6737, 0.2009, 0.2661)$$

(3) Calculation of the integrated risk level from four pollution factors. Two integrated risk assessment results are obtained using the two fuzzy aggregation-OWA modeling (eq. (3-44), (3-45)):

$$F_1 = (0.3750, 0.6250, 0, 0, 0, 0)$$

$$F_2 = (0.2661, 0.4211, 0, 0, 0, 0)$$

The results are illustrated in Figure 5-2, which show the relationships between the integrated risk levels and the fuzzy air quality criterion.

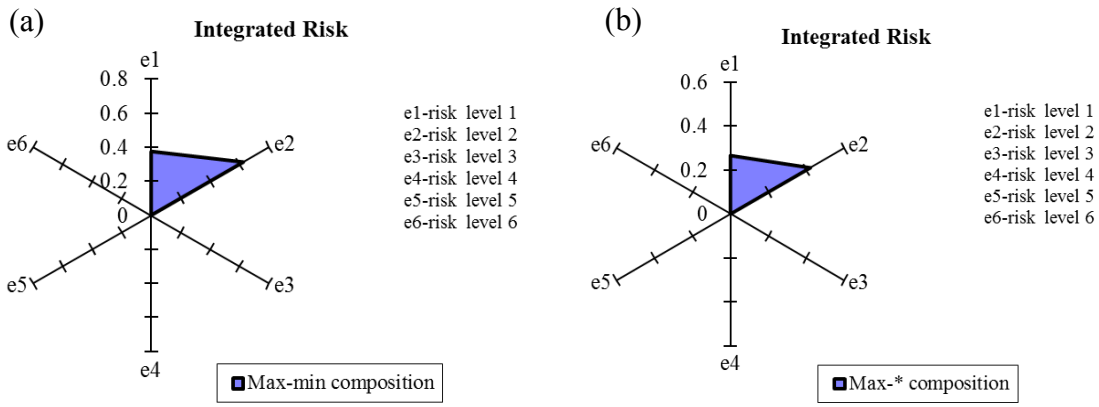

Figure 5-2 Integrated risk assessment results using Max-min composition and Max-* composition models: (a) the solution from the Max-min composition model; and (b) the solution from the Max-* composition model. The shaded parts are the areas with higher membership grade.

Figure 5-2 (a) is the solution from the Max-min composition model, which indicates that the integrated risk level is between level 1 (membership grade is 0.3750) and level 2 (membership grade is 0.6250), with a maximum membership grade corresponding to the fuzzy criteria level 2. Figure 5-2 (b) is the solution from the Max-* composition model, which also shows that the integrated risk level is between level 1 (membership grade is 0.2661) and level 2 (membership grade is 0.4211). Both of them show the maximum membership grade corresponding to the fuzzy risk level 2, which cross-verifies that the air quality in this grid belongs to the fuzzy risk level 2. This means the air quality is moderate, i.e. the air quality is acceptable; however, there may be a moderate health concern for people who are more sensitive to air pollution.

5.2 Result and Validation

Using the GMSMB and fuzzy aggregation-OWA modeling system, the air quality integrated risk assessment result is achieved on 10 km × 10 km grid cells for the state of California in 2008, which is visually presented in ArcGIS, as shown in Figure 5-3 (a).

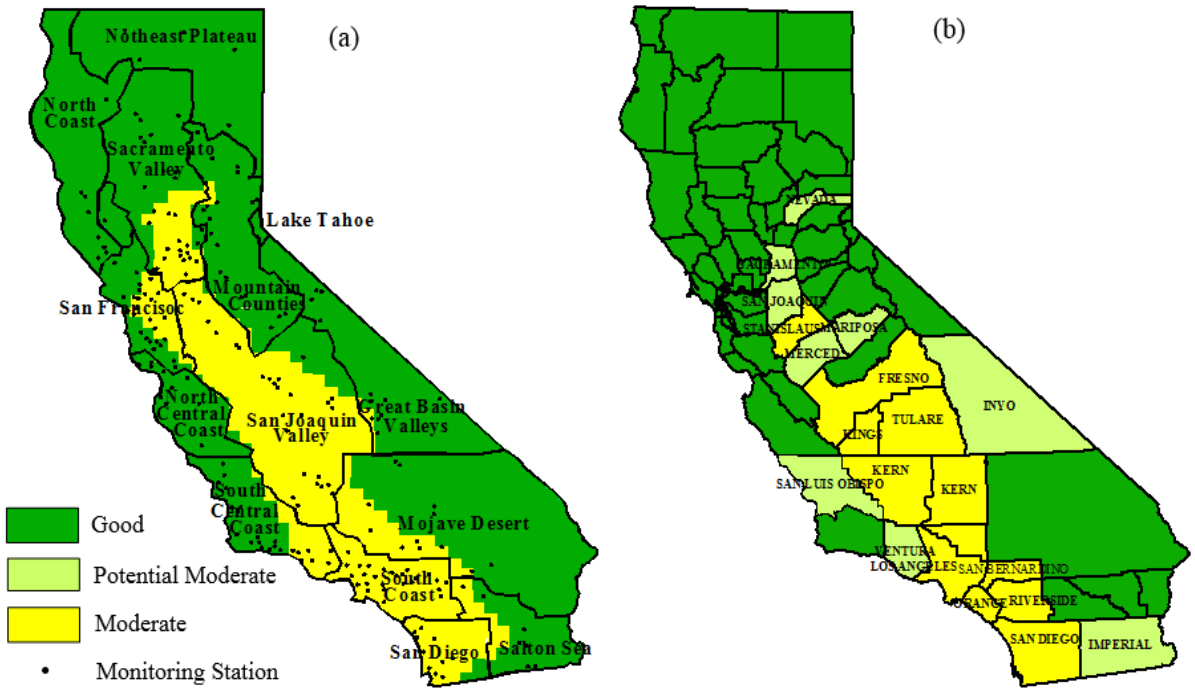

Figure 5-3 (a) Result of air quality integrated risk assessment for the state of California in 2008 from this study; (b) Integrated risk assessment according to the AQI values based on county (USEPA, 2010b).

In general, the air quality in most areas of the state of California belongs to the first level of fuzzy air quality criterion, namely, air quality is considered satisfactory, and air pollution poses little or no risk. Only a few areas (e.g. the South Coast, San Diego, San Joaquin Valley, Mojave Desert and the San Francisco Bay Areas) belong to level 2 indicating moderate air quality and some health concerns for more sensitive people. There is no area that belongs to the rest of risk levels.

The integrated risk assessment results are compared with the U.S. EPA AQI Report created by county in 2008 (US EPA, 2010b). In the AQI report, the days are counted as five categories: “good”, “moderate”, “unhealthy for sensitive group”, “unhealthy”, and “very unhealthy” based on the AQI values. The report shows that the AQI values are ranging from 12 to 92, which indicate the days of “good” and “moderate” dominate the air quality in the state of California. Table 5-3 lists the counties with AQI values higher than 45. The air quality with $0 < AQI < 45$ is thought as good, $45 < AQI < 50$ is thought as potential moderate, and $50 < AQI < 100$ is thought as moderate, as shown in Figure 5-3 (b).

Table 5-3 Air Quality Index statistics for the state of California in 2008 (US EPA, 2010b).

County	Days with AQI	AQI	Days due to pollutant			
			CO	NO_2	SO_2	$PM_{2.5}$
Fresno	366	71		8		167
Kern	366	92		9		129
Kings	366	67.5				130
Los Angeles	366	76		94	1	116
Orange	366	57		81		175
Riverside	366	80.5		34		91
San Bernardino	366	71		84		26
San Diego	366	64		72		97
Stanislaus	366	54		5		157
Tulare	366	69		31		43
Imperial	366	49	2	101		15
Inyo	366	45.5				1
Mariposa	366	46				
Merced	366	47		35		35
Nevada	366	45		2		53
Sacramento	366	47		81		31
San Joaquin	366	45		59		84
San Luis Obispo	366	47		3	1	9
Ventura	366	46		25		24

Figure 5-3 shows that the air quality integrated risk assessment from this study (Figure 5-3 (a)) is quite consistent with the AQI statistical results (Figure 5-3 (b)) in most counties. The differences only occur in a few counties, such as the San Francisco Bay Areas, Imperial, Inyo, Mariposa, and San Luis Obispo. This is not surprised because different air pollutants are used in this study and the AQI statistics. In this study, four

criteria pollutants, i.e. $PM_{2.5}$, NO_2, SO_2 and CO are used for the air quality integrated risk assessment. While in the AQI statistics, two more criteria pollutants, i.e. O_3 and PM_{10} are also used (US EPA, 2010b). The differences are possibly caused by these two pollutants. From the results of this study (Figure 5-3 (a)), it can be seen that the integrated risk assessment results are more concordant with the $PM_{2.5}$ concentration distribution than other pollutants (Figure 4-3 (a)), which implies the $PM_{2.5}$ is the main factor of integrated risk level. From Table 5-3, it can also be seen that the $PM_{2.5}$ is the dominant pollutant of AQI values among the four criteria pollutants ($PM_{2.5}$, NO_2, SO_2 and CO) except the counties with differences as mentioned above. This further suggests that the differences are caused by O_3 and PM_{10} that don't use in this study.

The integrated risk assessment results are also compared to the statistical analysis in the California Almanac of Emissions & Air Quality (Cox et al., 2009). From the statistical analysis, the main factors of air pollution in the state of California are $PM_{2.5}$, NO_x, and reactive organic gas (ROG). The emissions based on the air basins in 2008 are illustrated in Figure 5-4 (Cox et al., 2009).

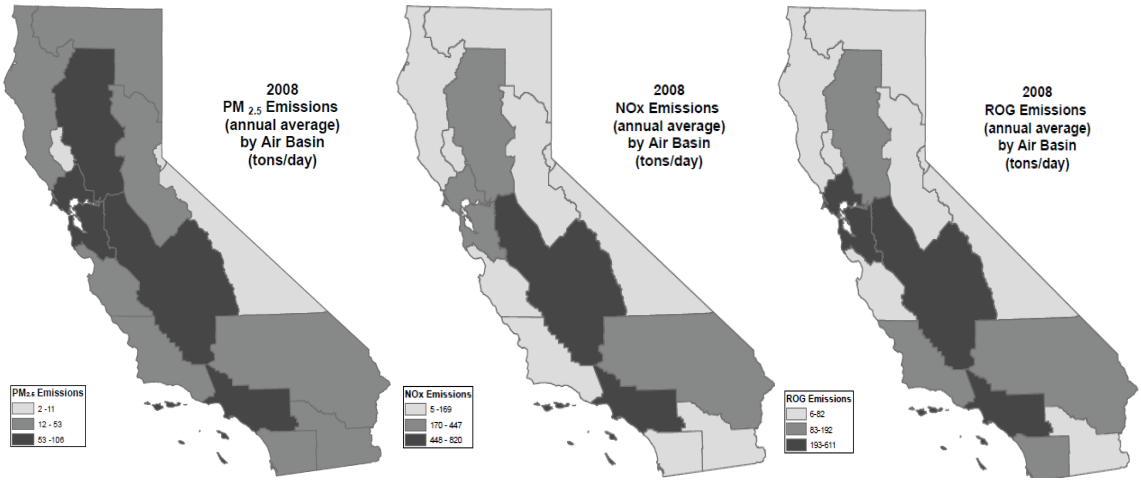

(a) (b) (c)

Figure 5-4 Main factors of air pollution in the state of California in 2008 (from the California Almanac of Emissions and Air Quality - 2009 Edition) (Cox et al., 2009).

Basically, the integrated risk assessment results are in accordance with the emissions, particularly, $PM_{2.5}$ emissions (Figure 5-4 (a)), namely, the areas with higher

$PM_{2.5}$ emissions have higher integrated risk levels. This illustrates that the $PM_{2.5}$ has more significant impact on the air pollution integrated risk level in the state of California, which is agreed with the California Almanac of Emissions & Air Quality (Cox et al., 2009). This is also in line with the results from the comparison with AQI statistics that the $PM_{2.5}$ is the most important pollution factor among the four criteria pollutants ($PM_{2.5}$, NO_2, SO_2 and CO).

All of these verify that the fuzzy aggregation-OWA modeling system is useful and feasible for air pollution integrated risk assessment. Furthermore, the fuzzy aggregation-OWA modeling system is based on the 10 km × 10 km grids, while the AQI statistics are based on the counties, and the statistical analysis in the California Almanac is based on the air basins, therefore the results from this study are more detailed and accurate than the AQI statistics and Almanac.

5.3 Summary

A case study is conducted using the developed fuzzy aggregation - OWA approach based on the spatial concentration distributions of four criteria pollutants (i.e. $PM_{2.5}$, NO_2, SO_2, and CO) in the state of California predicted by the GMSMB modeling in chapter 4. The integrated risk caused by these four pollutants is estimated. The results are visually displayed in GIS and compared with the AQI report and literatures. Good agreement illustrated that the developed approach is useful for the evaluation of integrated risk resulting from multiple air pollution factors and may also be applied to other areas.

Chapter 6 Satellite-based Estimates of Ground-level NO_2 from OMI

This case study still focuses on the state of California region (32º32´N to 42º00´N, 114º08´W to 124º26´W). The annual mean ground-level NO_2 concentrations are derived from the OMI tropospheric NO_2 column retrievals, which are cross-verified by comparison analysis with the in-situ surface measurements and the GMSMB modeling results.

6.1 Derivation of Ground-level NO_2 from OMI

The regional monthly mean tropospheric NO_2 vertical column densities (VCDs) from DOMINO (Dutch OMI NO_2) (version 2.0) for North America in 2008 are obtained from the European Space Agency (ESA)'s Tropospheric Emission Monitoring Internet Service (TEMIS) project website (http://www.temis.nl). March, April, and May are treated as the spring months; June, July, and August as the summer months; September, October and November as the fall months; and December, January, and February as the winter months. As given in Boersma et al. (2011), only scenes with cloud fractions < 20 % are selected, and scenes with snow or ice are not considered in this study. The seasonal mean tropospheric NO_2 vertical column densities (VCDs) are presented in Figure 6-1.

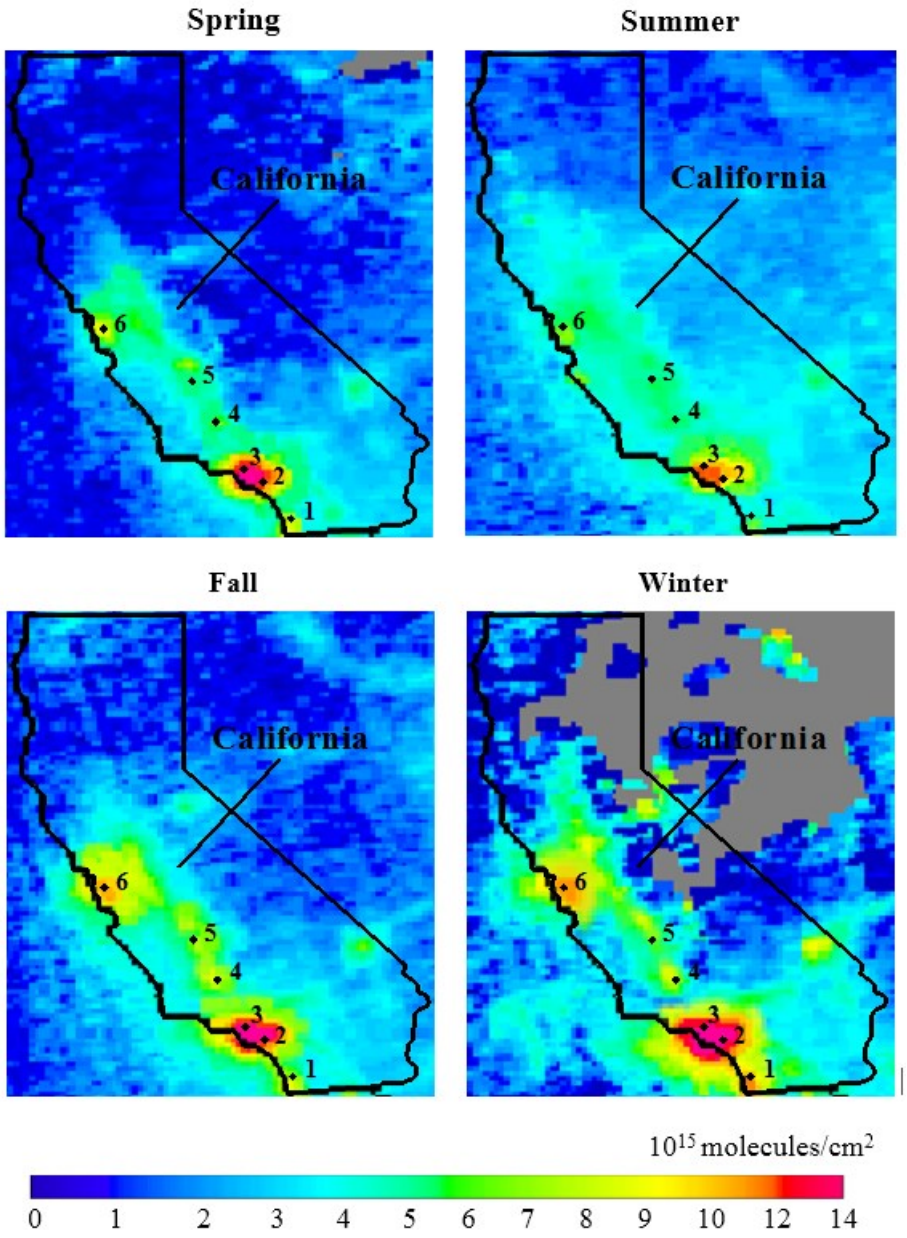

Figure 6-1 Seasonal average tropospheric NO_2 vertical column densities (VCDs) retrieved from OMI (in 10^{15} molecules/cm^2) for the state of California in 2008. The black dots with numbers are the representative locations of the monitoring stations for comparison.

The grey areas in Figure 6-1 indicate the locations with no valid satellite-derived data, probably due to the absence of sunlight (e.g., at high latitudes in winter, where there is persistent cloud cover) (Boersma et al., 2008a).

The GEOS-Chem simulation is performed to obtain the local scale factors, see section 3. The GEOS-5 meteorological field is used in the simulation at 0.5° × 0.667° horizontal resolution for North America. The data for NO_2 profiles at 47 vertical levels are established starting from the ground surface to a height of 0.01 hPa (approximately 80 km). Among the 47 vertical levels, 35 are in the troposphere, including 14 levels below 2 km. The boundary conditions are created at a coarse resolution, i.e., to run a 2° × 2.5° global simulation first, and then recompile the GEOS-Chem model for the 0.5° × 0.667° nested simulation. The U.S. EPA/NEI2005 emission inventory is used for this simulation (USEPA, 2011). The OMI-derived NO_2 mixing ratio at the lowest vertical layer (100 m) represents the ground-level NO_2 concentrations (Lamasal et al., 2008).

Figure 6-2 shows the seasonal average ground-level NO_2 concentrations derived from the OMI tropospheric NO_2 VCDs for the state of California in 2008.

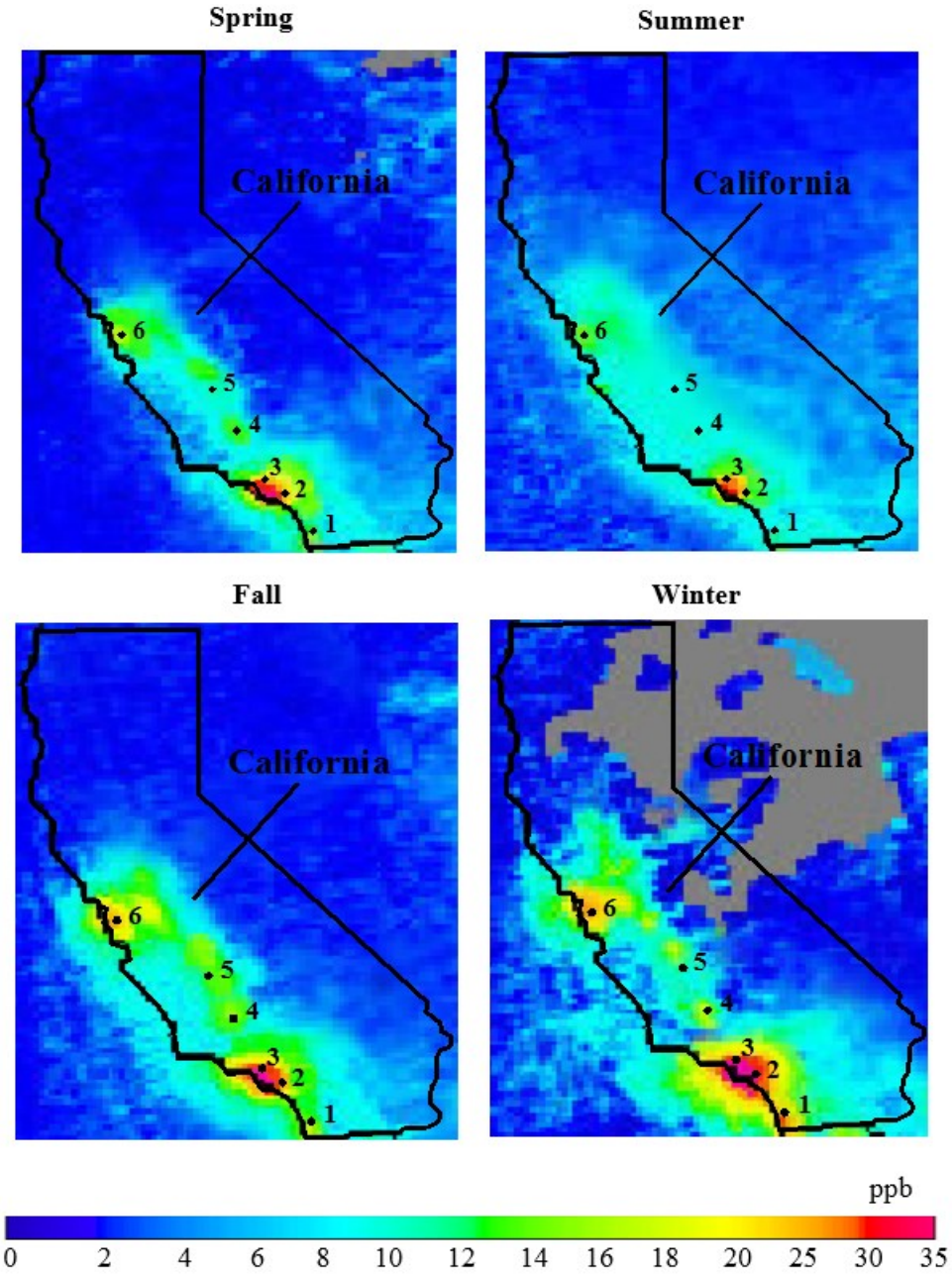

Figure 6-2 Seasonal average ground-level NO_2 concentrations derived from OMI for the state of California (ppb). The black dots with numbers are the locations of the monitoring stations.

The ground-level results in Figure 6-2 reveal relatively high NO_2 concentrations in urban areas such as Los Angeles, San Francisco, and San Diego being consistent with the NO_2 column retrievals (see Figure 6-1). This implies that the boundary NO_2 dominates the tropospheric NO_2 VCDs (Lamasal et al., 2008). The seasonal pattern with low concentrations in summer season is attributed to the higher mixing height,

photolysis rate, and the shorter NO_2 lifetime (Kramer et al., 2008). The mean OMI-derived ground-level NO_2 concentration in winter is higher than the corresponding values in spring, summer and fall by 31 %, 35 %, and 25 %, respectively.

6.2 The GMSMB Modeling Results

To compare with the OMI-derived surface NO_2 concentrations, the GMSMB modeling results for the ground-level NO_2 concentrations are recalculated at the OMI overpass time period (12:00 to 14:00 local time) to match the OMI-derived ground-level NO_2 concentrations. The horizontal resolution takes 10 km × 10 km grid cells and the mixing height is vertically divided into equal layers of 100 m. The NO_2 concentrations at the grid centers of the lowest vertical layer are generated for the state of California in 2008.

6.3 In-situ Surface Measurements

Two sources of in-situ surface measurement data are used to validate the OMI-derived ground-level NO_2 concentrations and the GMSMB modeling results. One source is acquired from the U.S. EPA Air Quality System (AQS) database (USEPA, 2010a), and the other source is from the Interagency Monitoring of Protected Visual Environments (IMPROVE) monitoring network (IMPROVE, 2010). There are 102 monitoring stations found from the AQS database for the state of California in 2008. The annual mean of monitoring values are ranging from 1- 29 ppb, which meet the California Ambient Air Quality Standard (CAAQS) annual arithmetic mean value (30 ppb) (CARB, 2009d) and the National Ambient Air Quality Standards (NAAQS) annual arithmetic mean value (53 ppb) (USEPA, 2012). All of them are available and can be used in the comparison. In addition, there are 25 monitoring stations found from the IMPROVE monitoring network for the state of California. Unfortunately, the monitoring data of the monitoring stations in this network are Intermittent. Only 4 monitoring stations have complete data in 2008 which can be used. Therefore, a total of 106 data sets from 106 monitoring stations are used in this study. A brief review of the collected data indicates that the majority of monitoring data are lower than the California Ambient Air Quality Standard and the National Ambient Air Quality Standards (CARB,

2007). The hourly average NO_2 monitoring data during 12:00 to 14:00 local time are extracted from these monitoring stations and are averaged for four seasons to obtain annual average values for comparison.

To reduce the interferences in ground-level NO_2 measurements caused by the sampler with a molybdenum converter and by calculating NO_2 from the NO and O_3 measurements (Dunlea et al., 2007), a correction factor (CF) is introduced (Lamasal et al., 2008):

$$CF = \frac{NO_2}{NO_2 + \Sigma AN + (0.95PAN) + (0.35HNO_3)} \quad (6\text{-}1)$$

where ΣAN is the sum of all alkyl nitrates (ppb), and PAN is the peroxyacyl nitrates (ppb). The NO_2 mixing ratio, all alkyl nitrates, PAN, and HNO_3 are obtained from the GEOS-Chem model simulation. The two-hour (12:00 to 14:00 local time) average correction factor is calculated with a range varying from 0.45 to 0.92 which are in line with the estimates of Lamsal et al. (2010) (modeled correct factor ranges 0.4 - 0.9) and applied to all in-situ surface measurements. Other nitrogen-containing species of NO_y, such as NO_3, N_2O_5, HONO and $ClNO_2$ are not considered here, since these species are photolabile and have very low atmospheric concentrations during the day (Parrish et al., 1990; Ryerson et al., 2000).

6.4 Comparison between Seasonal Mean OMI Tropospheric NO_2 VCDs and In-situ Surface Measurements

Recent studies have shown that OMI-retrieved tropospheric NO_2 VCDs correlate temporally and spatially with the near-surface NO_2 concentrations under cloud-free conditions (e.g., Boersma et al., 2009; Geddes et al., 2012). A correlation analysis is then performed for the seasonal average OMI-retrieved tropospheric NO_2 VCDs and the in-situ surface measurements for the state of California. For the spring and summer seasons, the high correlation coefficients (r = 0.89 and 0.90, respectively) are found, and it may indicate that most of the variability of ground-level NO_2 concentrations can be explained by the OMI-retrieved tropospheric NO_2 VCDs under cloud-free conditions (cloud fractions < 20 %) (Boersma et al., 2011). For the fall and winter seasons, the correlation

coefficients are found to be relatively lower (r = 0.74 and 0.68, respectively). These imply that there is a seasonal bias in the OMI-retrieved tropospheric NO_2 VCDs. There are several possible explanations for the seasonal bias: (i) using annual average instead of seasonal average the a-priori NO_2 profile in the OMI air mass factor calculation may yield lower tropospheric column retrievals during the wintertime (Eskes and Boersma, 2003); (ii) low temperatures and stagnant air masses in the later fall and wintertime result in an overestimation in the cloud fraction and a lower cloud height, which tends to increase the light path through the troposphere. In turn, they lead to overestimation of the tropospheric air mass factor and underestimation of the column retrievals than in reality (Boersma et al., 2004; Kramer et al., 2008); (iii) cloud-free condition (cloud fractions < 0.2) in retrieval of tropospheric NO_2 VCDs influences the results. Especially in the later fall and wintertime, more cloudy days (cloud fractions > 0.2) are omitted than in summer, resulting in a larger underestimate in retrieved NO_2 columns (Geddes et al., 2012); (iv) seasonal variation in surface albedo could also contribute to the seasonal bias (Lamsal et al., 2008).

6.5 OMI-Derived and Observed Seasonal Average Ground-level NO_2 Concentrations

The seasonal average ground-level NO_2 concentrations are validated by comparing them with the in-situ surface measurements (total of 106 values used for each season), as shown in Figure 6-3. The x-axis measurements are corrected using the correction factor (CF) in eq. (6-1) to make sure the values are only for NO_2 without other nitrogen-containing species, such as alkyl nitrates, PAN, and HNO_3. The regression analysis exhibits the strong correlations and good agreement in spring (r = 0.87, slope = 0.75 ± 0.04, intercept = 1.42 ± 0.60) and summer (r = 0.88, slope = 0.81 ± 0.04, intercept = 0.59 ± 0.57), as shown in Figure 6-3 (a) and (b). Despite that the correlations are still strong in fall and winter (r = 0.87 and 0.85, respectively), the slopes decline to 0.70 ± 0.04 with an intercept of 0.47 ± 0.30 in fall and 0.64 ± 0.03 with an intercept of 1.71 ± 0.70 in winter, as shown in Figure 6-3 (c) and (d). The hereinafter referred uncertainties incorporating slope and intercept are standard errors, which are determined following the approach described in Celarier et al. (2008). The error analysis shows that the biases

(defined by $\frac{\text{OMI-measurement}}{\text{measurement}} \times 100\%$) between the OMI-derived ground-level NO_2 concentrations and the in-situ surface measurements range: from 35.75 % to – 42.28 %, with a mean bias of - 13.03 % for spring; from 32.11 % to – 40.89 %, with a mean bias of -12.88 % for summer; from 20.42 % to – 47.87 %, with a mean bias of - 25.88 % for fall; and from 7.94 % to – 51.33 %, with a mean bias of - 26.99 % for winter. These results illustrate that the OMI derived ground-level NO_2 concentrations are underestimated compared to the measurements by 13 – 27 % on average with a more negative bias in winter. More details are discussed in the section 6.7.

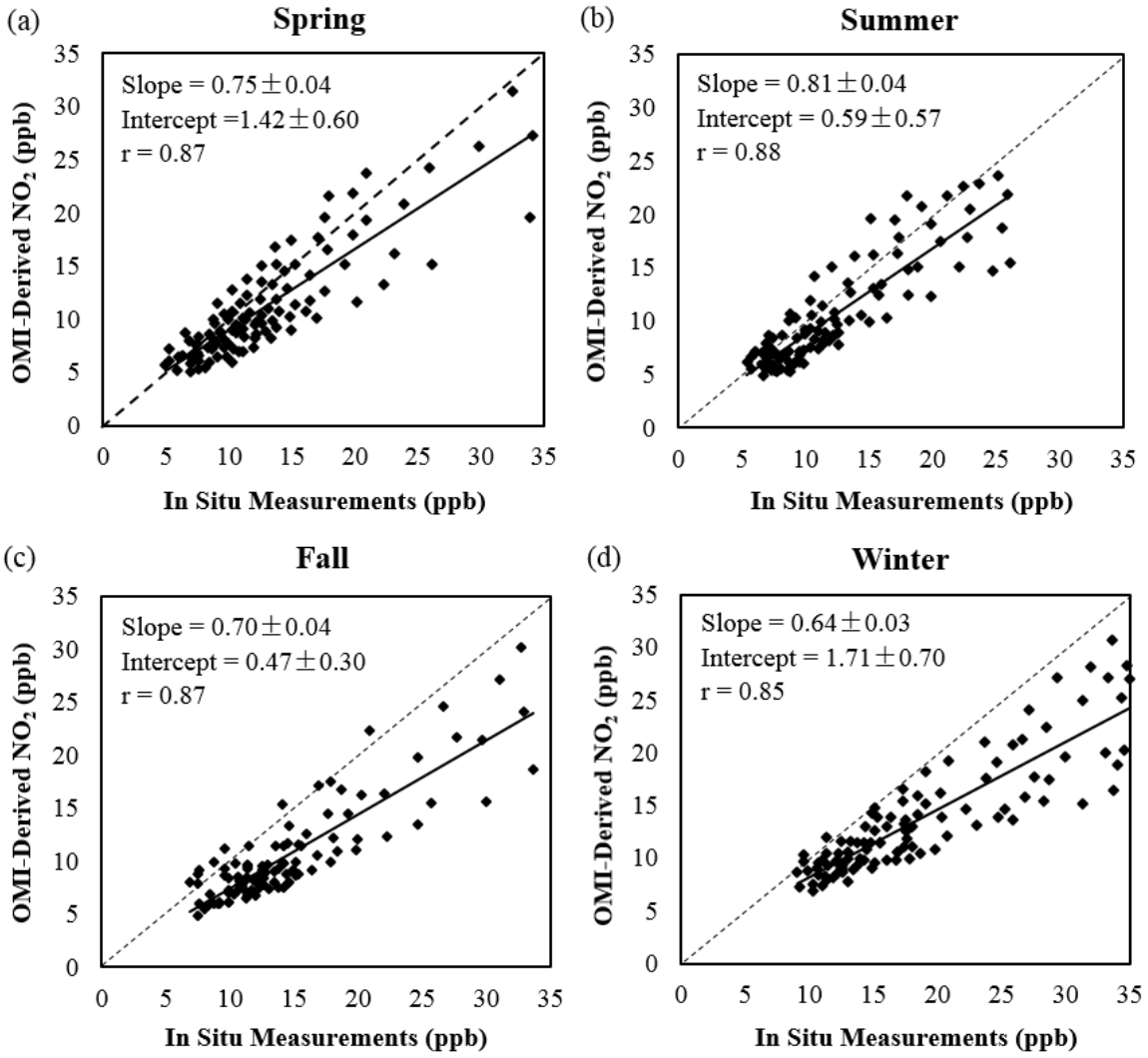

Figure 6-3 A comparison of the seasonal average OMI-derived ground-level NO_2 concentrations with the in-situ surface measurements for the year 2008. (a) Spring; (b)

Summer; (c) Fall; (d) Winter. The dashed line is the 1:1 line. The bold solid line is the regression line.

The correlation between the seasonal average OMI-retrieved tropospheric NO_2 VCDs and the seasonal average OMI-derived ground-level NO_2 concentrations are also analyzed to illustrate how influential the GEOS-Chem adjustment is. The strong correlations are found with correlation coefficient of 0.92 for spring, 0.95 for summer, 0.88 for fall and 0.84 for winter, which exhibit that the GEOS-Chem simulation is very efficient for deriving the ground–level NO_2 concentrations from OMI tropospheric NO_2 VCDs, and it is more effective for spring and summer seasons than fall and winter seasons.

6.6 GMSMB Modeling and OMI-Derived Ground-level Yearly NO_2 Concentrations

The yearly spatial concentration distributions of NO_2 in three dimensions at different layers are simulated using the GMSMB modeling approach for the state of California at the OMI overpass time (12:00 to 14:00 local time) in 2008. The modeling results of the first layer (i.e., the first 100 m from the ground) are shown in Figure 6-4 (a).

The modeling results show that the highest NO_2 concentrations occur in the South Coast, the San Joaquin Valley, the San Francisco Bay Area and San Diego, with a maximum of 27 ppb. In those areas, the relatively high concentrations are due to the local major point emission sources, the ambient temperatures, and the trapping effects of nearby mountains on the dispersion of air pollutants. The air quality in the North Coast, Northeast Plateau and Great Basin Valleys is better because of fewer air emission sources, a moderate climate, and sea breeze effects (Cox et al., 2009).

The annual average OMI-derived ground-level NO_2 concentrations are obtained from the OMI tropospheric NO_2 VCDs based on the GEOS-Chem simulation. The results are re-gridded and interpolated to have grid size of $0.1^o \times 0.1^o$ (approximately 10 km × 10 km at midlatitudes), as shown in Figure 6-4 (b), to compare with the GMSMB modeling results at the same grid size.

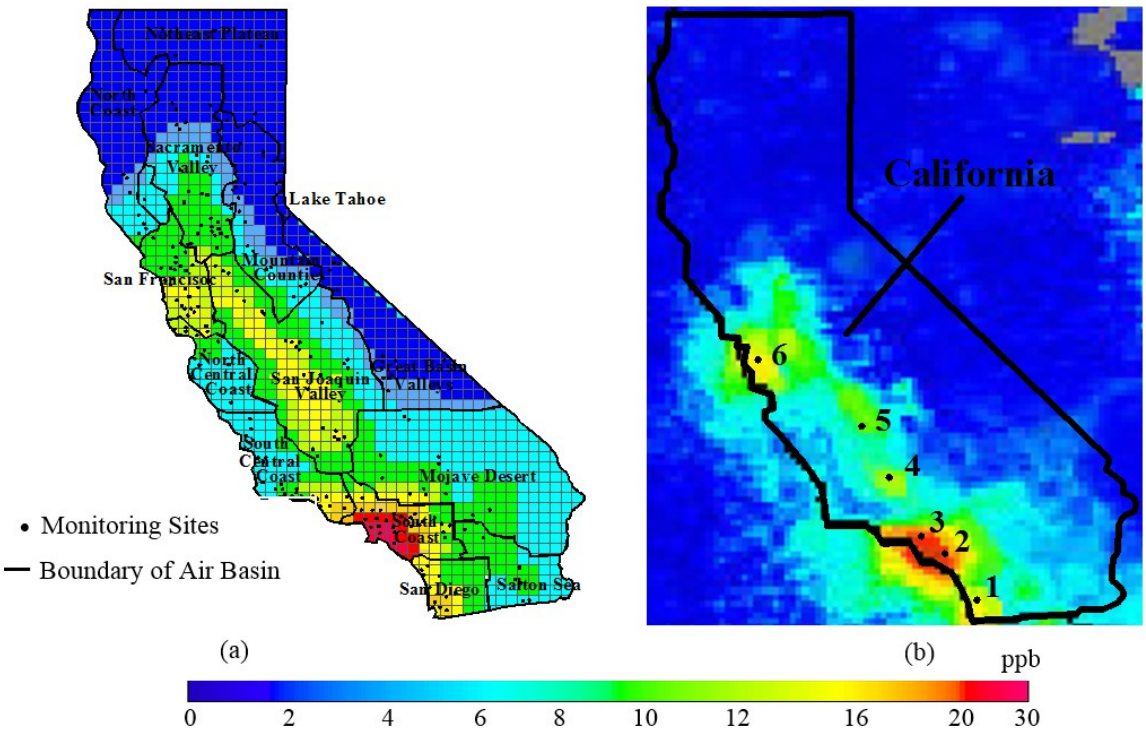

Figure 6-4 (a) GMSMB modeling results of annual average NO_2 concentration distribution at the OMI overpass time (12:00 to 14:00 local time) and (b) OMI-derived annual average ground-level NO_2 concentrations over the state of California in 2008. The grey spaces indicate locations where no value is available.

The OMI-derived yearly ground-level NO_2 results show higher NO_2 concentrations in the San Francisco Bay area, the South Coast, and San Diego, which are consistent with the GMSMB modeling results in Figure 6-4 (a). These results are also in accordance with the seasonal results. The OMI-derived ground-level NO_2 concentrations are compared with the GMSMB modeling results and the corrected in-situ surface measurements on an annual basis. Total 106 measurements from the AQS and IMPROVE are used in the comparison. The OMI-derived and GMSMB modeling results are averaged for 10 km × 10 km grids, and the in-situ surface measurements are point values at monitoring stations frequently located close to sources. Therefore, it is expected that the in-situ surface measurements will have higher values than the OMI-derived and GMSMB modeling results.

The error analysis illustrates that the biases between the OMI-derived ground-level NO_2 concentrations and the corrected in-situ surface measurements are varying from +

14.4 % to – 47.7 %, with a mean bias of – 25.0 % on an annual basis. The scatter plots and correlation analysis between them is given in Figure 6-5 (a), which shows a slope of 0.75 ± 0.05 with an intercept of 0.004 ± 0.75. The correlation coefficient is 0.84.

Similarly, the biases between the GMSMB modeling results and the corrected in-situ surface measurements are varying from + 22.2 % to – 39.3 %, with a mean bias of – 15.1 %. Figure 6-5 (b) shows a better slope of 0.82 ± 0.04, an intercept of 0.40 ± 0.65, and a stronger correlation of 0.88 compared to the OMI-derived ground-level NO_2 concentrations.

The biases between the OMI-derived ground-level NO_2 concentrations and the GMSMB modeling results are varying from + 22.4 % to – 46.0 %, and the mean bias is – 11.2 %. Figure 6-5 (c) shows two data sets in a good consistency with a slope of 0.87 ± 0.04 and an intercept of 0.20 ± 0.56 at the OMI overpass time (12:00-14:00 local time). The comparison analysis attests the accuracy of the OMI-derived ground-level NO_2 concentrations and the GMSMB modeling results.

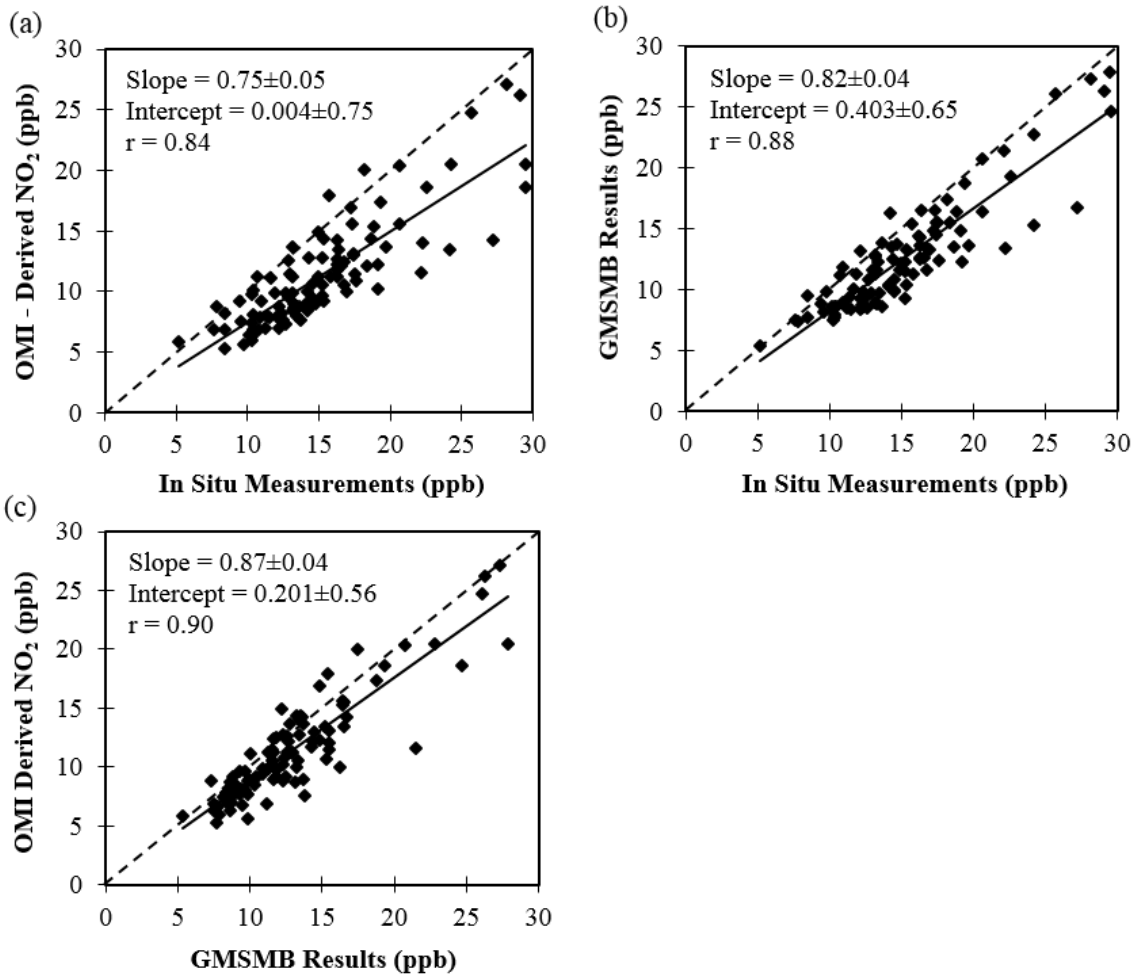

Figure 6-5 Scatter plots of (a) the OMI-derived ground-level NO_2 concentrations and the in-situ surface measurements; (b) the GMSMB modeling results and the in-situ surface measurements; (c) the OMI-derived ground-level NO_2 concentrations and the GMSMB modeling results. The dashed lines are the 1:1 line. The solid line is the regression line.

6.7 Discussion

6.7.1 Intercomparison analysis

As shown in Figure 6-3 and Figure 6-5, general agreement and strong correlations are attained among the OMI-derived, GMSMB model, and in-situ surface measurement results. The observed discrepancies are possibly caused by the spatial mismatch between the 10 km × 10 km grid cell values (i.e., the OMI-derived and GMSMB model) or the OMI tropospheric column retrievals (13 km × 24 km) and the in-situ surface point

measurements (i.e., at monitoring stations) (Brinksma et al., 2008; Lamsal et al., 2008; 2010; Lee et al., 2011), and also other uncertainties which are analyzed as following.

(A) The uncertainties in the seasonal mean OMI tropospheric NO_2 column retrievals

A strong correlation is found between the seasonal mean OMI-retrieved tropospheric NO_2 VCDs and the in-situ surface measurements with an average correlation coefficient of 0.80. This implies that the boundary layer NO_2 makes a larger contribution to the tropospheric columns in the state of California, which is in line with the conclusions from literatures (Boersma et al., 2004; 2007; Lamsal et al., 2008). It demonstrates that the retrieved tropospheric NO_2 VCDs can be used to derive the ground-level pollutant concentration distributions under cloud-free conditions (cloud fractions < 20 %). However, there are inherent uncertainties leading to the errors in OMI-retrieved NO_2 VCDs, which could include the following:

- The most critical source of error is the tropospheric air mass factor, which is dominated by the uncertainties associated with the cloud fraction, the aerosol characterization, the surface albedo, and the a priori NO_2 profile (Martin et al., 2002; Boersma et al., 2007). The uncertainties in the air mass factor may account for 20 - 45 % of errors in the tropospheric NO_2 column retrievals for polluted regions with small cloud fractions (Boersma et al., 2004).
- The retrieval of tropospheric NO_2 depends on a priori assumptions on the vertical NO_2 profiles in the troposphere. Systematic errors in the a priori profile shape can cause a 5 - 15 % error in the retrieved columns (Boersma et al., 2004). Additionally, using the annual average instead of the seasonal average NO_2 profile in the OMI air mass factor calculation may yield lower tropospheric column retrievals (Eskes, 2003).
- Low temperatures and stagnant air masses in the wintertime result in an overestimation in the cloud fraction and a lower cloud height, which lead to an increase in the tropospheric air mass factor and lower column retrievals (Kramer et al., 2008).
- The seasonal variation in mixing height and surface albedo could also contribute to the errors (Lamsal et al., 2008).

All of these factors may contribute to the underestimates and seasonal biases in tropospheric NO_2 column retrievals.

(B) The difference between the OMI-derived ground-level NO_2 concentrations and the in-situ measurements

On a seasonal mean basis, the error analysis shows that the OMI-derived ground-level NO_2 concentrations are underestimated compared to the in-situ measurements by 13 - 27 % (relative errors) with a more negative bias in winter. The underestimation, in addition to the point-to-cell comparison, may be attributed to the uncertainties associated with the OMI tropospheric NO_2 column retrievals (Boersma et al., 2004; 2007; 2008; Bucsela et al., 2008; Celarier et al., 2008), the GEOS-Chem NO_2 profile (Lamsal et al., 2008; 2010), and the in-situ surface measurements (Dunlea et al., 2007; Lamsal et al., 2008; 2010). The examinations into these biases by Celarier et al. (2008) and Lamsal et al. (2008), reveal that the key contributors were seasonal variations in (i) the mixing height, (ii) the NO_2 profile, (iii) the surface albedo, and (v) the spatial and temporal inhomogeneity of the boundary layer NO_2.

On an annual mean basis, Figure 6-3 (a) compares the OMI-derived ground-level NO_2 concentrations with the corrected in-situ surface measurements. The figure shows a slope of 0.75 ± 0.05 with an intercept of 0.004 ± 0.75. The linear regression, constrained to pass through the origin, gives a slope of 0.75 ± 0.01. This suggests that, on a yearly basis, the OMI-derived ground-level NO_2 concentrations are underestimated by 25 ± 1 %. In addition to the reasons mentioned in the seasonal average analysis, the possible explanations also include the following (Blond et al., 2007; Zhou et al. 2009):

- The air mass factor sensitivity is much more significant for polluted areas than for unpolluted areas at surface albedos < 0.2 (Boersma et al., 2004), which results in an underestimate in tropospheric NO_2 column retrievals in urban and suburban areas;
- The ground-level NO_2 gradients are sharp around cities (Blond et al., 2007), which may lead to an underestimate in the OMI-derived ground-level NO_2 concentrations compared to the surface measurements.

(C) The difference between the GMSMB modeling results and the in-situ measurements

Figure 6-5 (b) compares the GMSMB modeling results with the corrected in-situ surface measurements on an annual average basis. The higher slope of 0.82 ± 0.04, the intercept of 0.40 ± 0.65, and the higher correlation coefficient of 0.88 show that the GMSMB modeling results are more consistent with the in-situ surface measurements than the OMI-derived ground-level NO_2 concentrations. This is probably due to the better spatial resolution (10 km × 10 km) than the GEOS-Chem simulation (0.5° × 0.667°, approximately 50 km × 67 km) and better GMSMB modeling results using the updated 2008 National Emissions Inventory (NEI, version 2) (US EPA, 2012). The slope is changed to 0.84 ± 0.01 when the intercept is set to zero. This indicates that the modeling results are generally underestimated compared to the in-situ surface measurement data by 16 ± 1 %. This bias is possibly due to the comparison between the grid average cell-area values and the point measurements.

(D) The difference between the OMI-derived ground-level NO_2 concentrations and the GMSMB modeling results

Figure 6-5 (c) compares the OMI-derived ground-level NO_2 concentrations with the GMSMB modeling results on an annual average basis. The figure shows the slope of 0.87 ± 0.04 and the intercept of 0.20 ± 0.56. The slope becomes to 0.90 ± 0.00 with the intercept at zero, and this indicates that the OMI-derived NO_2 concentrations are slightly underestimated with respect to the GMSMB modeling results by 10 %. The strong correlation (r = 0.90) shows that the GMSMB modeling results and the OMI-derived ground-level NO_2 concentrations are positively correlated on a yearly basis. The differences between them can be attributed to the errors from the OMI data analysis as discussed previously. In addition, there are some uncertainties in the GMSMB modeling results caused by the unconsidered NO_2 reactions in the atmosphere and the limited accuracy of the emission inventory data.

6.7.2. Exposures assessment and air quality management

Figure 6-6 gives the population-weighted results of the annual average NO_2 exposure concentrations at the OMI overpass time (12:00 to 14:00 local time) for the state of California in 2008. The results are calculated for the categorized air basins in California based on the OMI-derived ground-level NO_2 concentrations (Figure 6-4(b))

and are weighted by the local population density distributions achieved from the U.S. Census Bureau (2011). The figure shows that the south coast area has the highest NO_2 exposure concentration (20.05 ppb). The San Francisco Bay Area, San Diego, and the San Joaquin Valley have medium level NO_2 exposure concentrations (13.85 ppb, 12.32 ppb, and 10.86 ppb, respectively). The remaining areas have lower NO_2 exposure concentrations (< 10 ppb). The assessment results are in agreement with findings in Wang and Chen (2013).

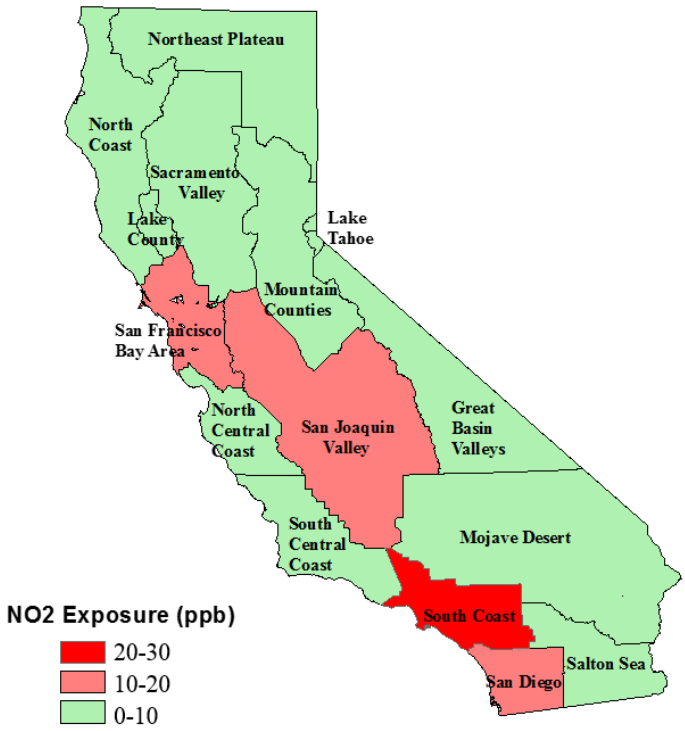

Figure 6-6 Annual average population-weighted NO_2 exposure concentrations at OMI overpass time (12:00 to 14:00 local time) map for the state of California in 2008.

Lastly, satellite remote sensing technology and new environmental sensors such as OMI provide a novel method to monitor NO_2 in the atmosphere. The on-going evolution of satellite remote sensing technology is expected to further improve the spatial and temporal coverage (i.e., monitoring on cloudy days in winter time as the no-data grey areas indicated in Figure 6-1 and Figure 6-2) as well as the accuracy of NO_2 monitoring to support air quality management (e.g., Kassianov and Ovtchinnikov, 2008).

6.8 Summary

This study explores the ground-level NO_2 concentration derived from the satellite OMI tropospheric NO_2 vertical column densities based on the global 3-D chemical transport model GEOS-Chem for the state of California. The results are cross-verified by a GMSMB modeling approach and the local in-situ surface measurements.

The OMI tropospheric NO_2 VCDs and the OMI-derived ground-level NO_2 concentrations correlate well with the surface measurements spatially and temporally for location coverage and seasonal variations, which demonstrates that most of the variability of ground-level NO_2 concentrations can be explained by the OMI-retrieved tropospheric NO_2 VCDs under cloud-free conditions (cloud fractions < 20 %). The correlation coefficients between the seasonal average OMI tropospheric NO_2 VCDs and the OMI-derived ground-level NO_2 concentrations are greater than 0.84 for the four seasons, which exhibit that the GEOS-Chem simulation is very efficient for deriving the ground–level NO_2 concentrations from OMI tropospheric NO_2 VCDs. The comparison between the seasonal average OMI-derived NO_2 concentrations and the corrected surface measurements illustrates that the OMI derived ground-level NO_2 concentrations are underestimated compared to the measurements by 13 – 27 % on average with a more negative bias in winter.

The intercomparison among the OMI-derived, the GMSMB modeling and the corrected surface measurement results shows that the OMI derived ground-level NO_2 concentrations are underestimated compared to the corrected measurements by 25 ± 1 %, to the GMSMB modeling results by 10 % on a yearly basis. While the GMSMB modeling results are generally underestimated compared to the corrected measurement data by 16 ± 1 %. Despite the proportionate bias in the OMI-derived and the GMSMB modeling results, the presented results demonstrate that the satellite derived data could make up for the limited monitoring stations on the ground, quantitatively monitor the regional transport and fate of NO_2, and validate the effective air quality models. This study also reveals that a multi-disciplinary consideration of the dynamic satellite data analysis, meteorology, pollutants' fate and transport, air quality modeling, and in-situ measurements provides the best results of the exposure assessment and effectively supports the regional air pollution control management.

The related uncertainties have been analyzed in this study including results variations among different methods and regional and seasonal biases in tropospheric NO_2 column retrievals. It points out that the OMI tropospheric NO_2 column retrievals for monitoring ground level NO_2 can be improved, suggesting further studies on the tropospheric air mass factor, the local NO_2 profile, and the high-resolution cloud fraction and surface albedo maps.

Chapter 7 Satellite-derived Concentration Distribution of Ground-level $PM_{2.5}$

---A Case Study for Montreal, Canada

This chapter presents a case study to evaluate the improved aerosol optical depth (AOD) retrieval algorithm (see Chapter 3) for the MODIS satellite instrument at 1-km resolution over the city of Montreal, Canada in the year of 2009. The satellite-retrieved AODs at 1-km resolution are used to derive the ground-level $PM_{2.5}$ concentrations using the aerosol vertical profiles obtained from the GEOS-Chem simulation.

7.1 Overview of the Study Area

Montreal is the largest city in the Quebec province of Canada, which is also the second-largest city in Canada and the fifteenth-largest city in North America. This study focuses on the most populous area – the island of Montreal (45°30′N, 73°35′W). The city of Montreal is situated on the island of Montreal on the Saint Lawrence River with a population of 1,649,519 as of the 2011 census (Statistics Canada, 2012). The land area is about 365.13 km^2 with a population density of 4,517.6 persons / km^2 (Statistics Canada, 2012).

There are 17 monitoring stations located throughout the island of Montreal, as shown in Figure 7-1, which are part of the Réseau de surveillance de la qualité de l'air (RSQA) (Boulet and Melancon, 2009) and are integrated into the National Air Pollution Surveillance Network (NAPS) (Environment Canada, 2010). Among these monitoring stations, only 11 monitoring stations have $PM_{2.5}$ measurements. Data collected in these monitoring networks in 2009 showed that there were 68 days with air quality rating of "poor", fine particles alone accounted for 67 of the poor air quality days (Boulet and Melancon, 2009).

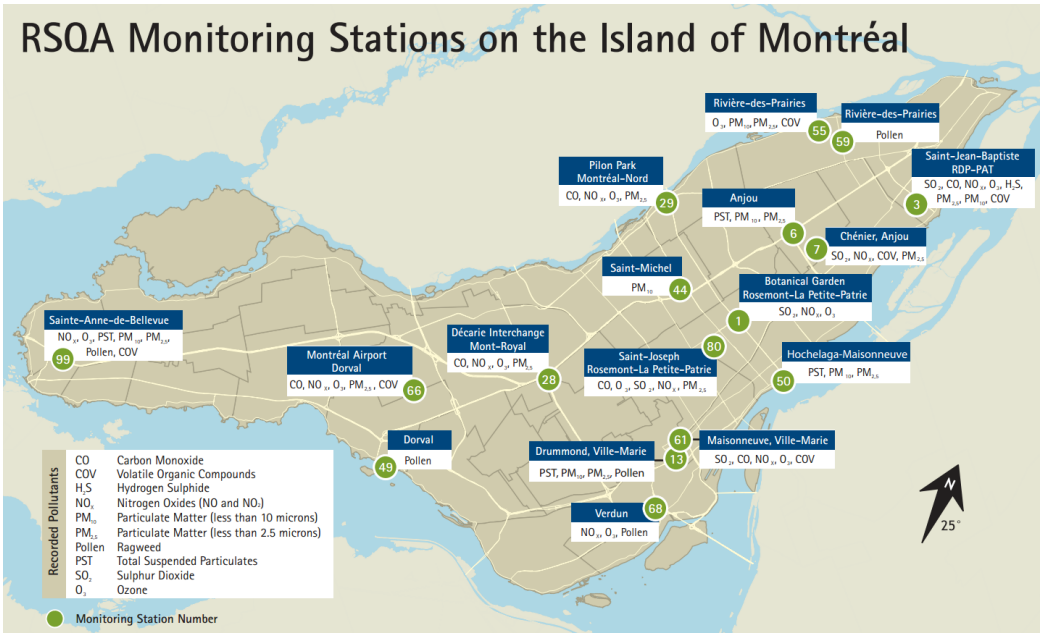

Figure 7-1 RSQA monitoring stations on the island of Montreal (Boulet and Melancon, 2009).

7.2 MODIS AOD Retrieval at 1-km Resolution

The new algorithm described in section 3.3 is used to retrieve AOD at 1 km × 1 km resolution over the city of Montreal, Canada in 2009. The 1 km resolution Terra/MODIS level 1B calibrated reflectances (MOD021km), MODIS geolocation data (MOD03, including a DEM and Sun-Sat geometry), MODIS level 2 1 km surface reflectance products (MOD09), MODIS cloud mask products (MOD35), and MODIS level 2 aerosol products (MOD04) of the year 2009 in collection 5, are downloaded from the NASA Goddard Space Flight Center Level 1 and Atmosphere Archive and Distribution System (LAADS) (NASA, 2012a).

The pixels are first selected by cloud and water masks as described in section 3.3. Then the Rayleigh path reflectance is calculated based on the spectral dependence of the Rayleigh optical depth and phase function (Wong et al., 2010). The surface reflectances at 0.47 and 0.66 μm ($\rho^{s}_{0.47}$, $\rho^{s}_{0.66}$) are first derived from the top-of-atmosphere (TOA) reflectance at 2.13 μm ($\rho^{*}_{2.13}$) in the MODIS L1B 1 km calibrated data using the empirical relationships, and then validated with MODIS surface reflectance products (MOD09) at 1 km. Finally, the aerosol reflectances ρ^{a}_{λ} at 0.47 and 0.66 μm are

decomposed from TOA reflectance, Rayleigh path reflectances and surface reflectances and fitted with the LUT created by the 6S Radiative Transfer Code. The aerosol optical properties modeled by the 6S code are iteratively updated until the error term of x^2 is minimum (Drury et al., 2008). The aerosol optical depths at 0.47 μm and 0.66 μm ($\tau_{0.47}$, $\tau_{0.66}$) are obtained from the LUT and are interpolated to 0.55 μm AOD ($\tau_{0.55}$).

7.3 Estimating Ground-level $PM_{2.5}$ from 1 km × 1 km AOD Retrievals

The satellite-retrieved AODs are used to derive the ground-level $PM_{2.5}$ concentrations using the local scaling factors obtained from the GEOS-Chem aerosol simulation. The local scaling factors η from 0.5° × 0.667° grid cells (the resolution of the GEOS-Chem simulation), are interpolated to 0.01° × 0.01° (approximately 1 km × 1 km) to derive the ground-level $PM_{2.5}$ concentrations from the retrieved AOD values at the satellite overpass time (10:30 local time).

7.4 Results and Validation

7.4.1. Validation of retrieved aerosol optical depth

The annual mean AODs at 1 km × 1 km resolution are retrieved from the 1-km resolution Terra/MODIS level 1B calibrated reflectance (MOD021km) for Montreal, as shown in Figure 7-2(a). Since there is no aerosol measurement in Montreal, the annual mean MODIS level 2 aerosol products (MOD04) at 10 km × 10 km, which are interpolated to 1 km × 1 km, as shown in Figure 7-2(b), are used to validate the AOD retrievals in this study. The main road network is overlayed on the annual mean AODs to illustrate the geographic information.

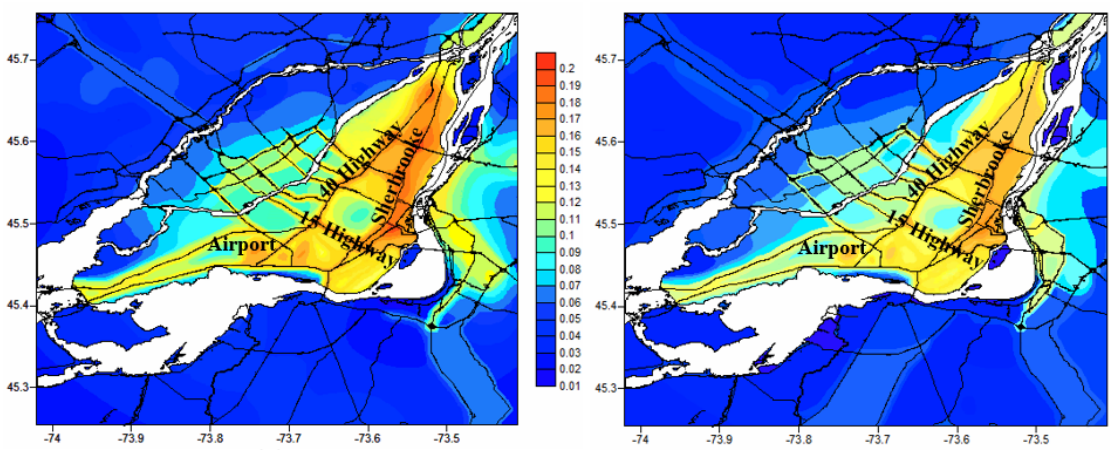

Figure 7-2 Annual mean aerosol optical depth at 0.55 μm for Montreal in 2009. (a) AODs retrieved at 1-km resolution in this study. (b) AODs from MODIS level 2 aerosol products (MOD04) interpolated to 1 km × 1 km. The white areas are water bodies.

Figure 7-2 shows there are generally agreement between the retrieved AODs from this study and the MODIS standard products level 2 of AODs in collection 5. Both of them illustrate that the higher AOD values mainly occur in the island of Montreal, especially in downtown (around rue Sherbrooke and Ville-Marie), the airport of Dorval, and some industrial resources, such as gas and oil facilities, mining pit and waste treatment plant. There are relatively lower AOD values in the areas around the island of Montreal. This is reasonable since the island of Montreal has the most dense population and commercial activities than the surrounding areas. The higher AOD values also occur along the main roads and highways, for example, the rue Sherbrooke, highway 15 and 40, which imply that the traffic emissions are also main reason for the higher AODs in Montreal. The error analysis for the sampling locations shows an average bias (relative error) of 10 %. All of these tend to confirm that the results in this study are at least equivalent to the standard MODIS product with a spatial resolution 100 times higher.

However, there are some differences between the AODs retrieved from this study and the MODIS collection 5 AODs. The AOD values in this study are ranging from 0.01 to 0.19, while in MODIS collection 5 are ranging from 0.01 to 0.17. The retrieved AODs from this study are slightly higher than the MODIS collection 5 AODs. This is possibly due to the different grid sizes used in the retrieval. In MODIS collection 5 aerosol products, the coarser resolution (10 km × 10 km) is used which not only results less

accurate in the products, but also visually and spatially inferior. The AOD values have to be interpolated to the same size (1 km × 1 km) as the AOD retrievals from this study. It is also ineffective for aerosol mapping in urban areas since their high reflectance values cannot meet the criteria in the operational algorithm. While the method developed in this study can retrieve AODs at a higher spatial resolution than previously and can operate over both bright and dark surfaces. This also demonstrates that there are significant improvements in the retrieved AODs from this study than the MODIS collection 5 level 2 aerosol products. However, there are also some limitations in our retrieval algorithm. One is the Lambertian approximation which results errors from incomplete removal of atmospheric scattering effects, and largely simplifies the radiative transfer model. The other one is the aerosol model set in the 6S code which is fixed to the urban case. It is possible to prescribe the model of aerosol as it is suggested by Kaufman et al. (1997), depending on the geographic location. However, the actual model may differ significantly from the actual aerosol (Vermote and Kotchenova, 2008). The choice of the aerosol model is critical to improve the AOD retrieval accuracy.

7.4.2 Validation of ground-level $PM_{2.5}$

The satellite-derived annual mean $PM_{2.5}$ concentrations at the satellite overpass time (10:30 local time) for Montreal in 2009 is shown in Figure 7-3(a). The satellite-derived $PM_{2.5}$ concentrations are compared with the in-situ surface measurements at the satellite overpass time from the National Air Pollution Surveillance (NAPS) Network (Environment Canada, 2010). There are 10 surface monitoring stations available for $PM_{2.5}$ measurement in Montreal, as shown in Figure 7-3(b).

Figure 7-3 (a) shows the satellite-derived ground-level $PM_{2.5}$ concentrations are ranging from 1 to 14 $\mu g/m^3$. The upper bound slightly exceeds the U.S EPA National Ambient Air Quality Standard (NAAQS) (annual mean 12 $\mu g/m^3$) (USEPA, 2012), and the World Health Organization (WHO) guideline (10 $\mu g/m^3$) (WHO, 2009). In Canada, the National Ambient Air Quality Objectives (NAAQO) only set a limit for total suspended particulates, but not $PM_{2.5}$ (Environment Canada, 2012). The higher $PM_{2.5}$ concentrations occur in downtown, the airport and industrial areas since there are more local emissions, such as the wood heating of restaurants, superimposed upon the regional background resulting in a deterioration of air quality in its immediate surroundings

(Boulet and Melancon, 2009). The higher $PM_{2.5}$ concentrations also occur along the main roads and highways, which imply that traffic emissions are the major sources of $PM_{2.5}$ in Montreal. This is consistent with the retrieved AODs from this study (Figure 7-2 (a)).

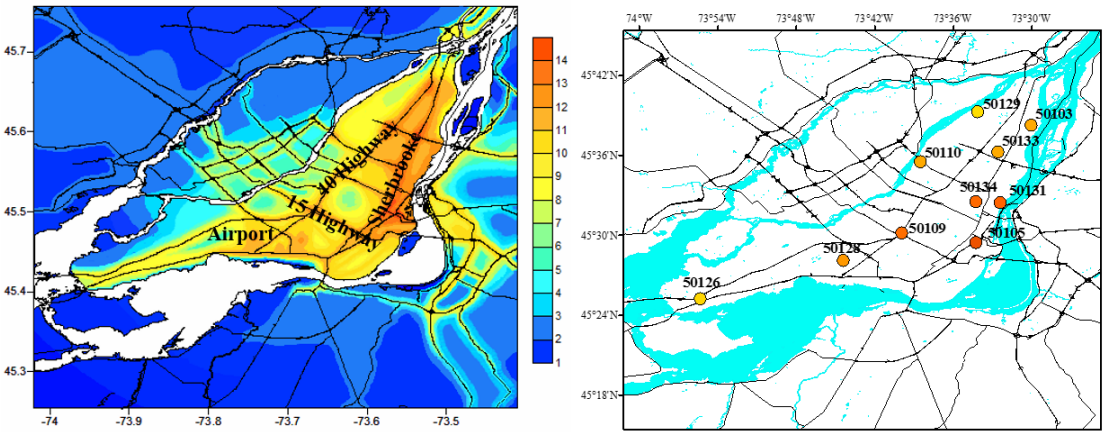

(a) (b)

Figure 7-3 Comparison between satellite-derived annual mean ground-level $PM_{2.5}$ and in-situ surface measurements. (a) satellite-derived annual mean ground-level $PM_{2.5}$ concentrations ($\mu g/m^3$) at 1 km × 1 km resolution from this study for Montreal in 2009; (b) in-situ surface measurement stations in the NAPS Network (Environment Canada, 2010). The numbers are the station codes and the colors illustrate the annual mean measurement values at the satellite overpass time (10:30 local time).

Figure 7-3 (b) shows the in-situ surface measurement stations in the NAPS Network (Environment Canada, 2010), with the colors to illustrate the annual mean measurement values at the satellite overpass time (10:30 local time). It can be seen that the satellite-derived annual mean ground-level $PM_{2.5}$ concentrations from this study are quiet consistent with the in-situ surface measurements at the monitoring stations.

To further evaluate the satellite-derived annual mean ground-level $PM_{2.5}$ concentrations and indirectly validate our retrieval algorithm, the ground-level $PM_{2.5}$ concentrations are also derived from the MODIS level 2 aerosol products which is at 10 km × 10 km resolution, using the same method as used in the 1 km × 1 km aerosol retrievals from this study. The local scale factors are obtained from the GEOS-Chem simulation. Both of the satellite-derived annual mean ground-level $PM_{2.5}$ concentrations

(from 1-km and 10-km resolution AOD) at the NAPS measurement stations are list in Table 7-1, and compared with the in-situ measurements.

Table 7-1 Comparison among the annual average $PM_{2.5}$ concentrations derived from the AODs at 1-km resolution, derived from the MODIS level 2 aerosol products at 10-km resolution, and the NAPS in-situ measurements (Environment Canada, 2010).

NAPS Station	1-km resolution ($\mu g/m^3$)	10-km resolution ($\mu g/m^3$)	NAPS measurements ($\mu g/m^3$)	Dev. 1 (%)	Dev. 2 (%)
50103	10.12	10.81	11.36	-11.09	-4.93
50105	12.83	11.82	13.31	-3.83	-11.34
50109	11.31	10.35	12.46	-9.31	-17.34
50110	9.83	9.41	11.31	-13.35	-16.89
50126	9.15	9.52	9.36	-2.78	1.50
50128	11.23	9.71	11.70	-4.27	-17.09
50129	9.72	8.94	10.03	-3.29	-11.27
50131	12.63	11.52	12.54	0.48	-8.29
50133	11.91	10.64	11.76	1.19	-9.86
50134	10.82	10.21	11.40	-5.26	-10.53
Mean				-5.15	-10.60

Note: Dev 1 is the deviation between the annual average $PM_{2.5}$ concentrations derived from the AODs retrieved in this study at 1-km resolution and the NAPS in-situ measurements;
Dev 2 is the deviation between the annual average $PM_{2.5}$ concentrations derived from the MODIS level 2 aerosol products at 10-km resolution and the NAPS in-situ measurements.

From Table 7-1, it can be seen that the biases (relative error) of ground-level $PM_{2.5}$ concentrations derived from the AODs retrieved in this study are ranging from 1.19 % to -13.35 %, with a mean bias of -5.15 %. The biases of ground-level $PM_{2.5}$ concentrations derived from the MODIS level 2 aerosol products at 10-km resolution are ranging from 1.5 % to -17.34 %, with a mean bias of -10.60 %. It is evident that the ground-level $PM_{2.5}$ concentrations derived from the AODs retrieved in this study are better than that derived from the MODIS level 2 aerosol products at 10-km resolution. This indirectly validates the AOD retrieval algorithm developed in this study.

7.4.3 Discussion

The regression analysis shows the same conclusion as the error analysis, as shown in Figure 7-4.

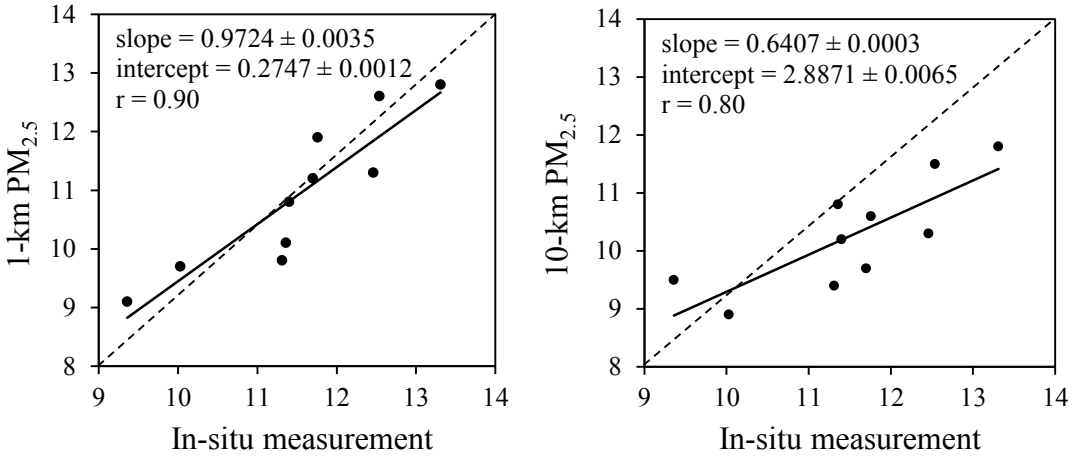

Figure 7-4 Scatter plot of satellite-derived annual mean ground-level $PM_{2.5}$ concentrations ($\mu g/m^3$) compared with the in-situ measurements from the NAPS Network (Environment Canada, 2009): (a) derived from the AODs retrieved at 1 km × 1 km resolution in this study; (b) derived from the MODIS level 2 aerosol products at 10 km × 10 km resolution. The dashed line is the 1:1 line and the solid line is the trend line.

Figure 7-4 (a) shows a good agreement ($r = 0.90$, slope = 0.9724 ± 0.0035, intercept = 0.2747 ± 0.0012) between the satellite-derived annual average $PM_{2.5}$ concentrations and the in-situ surface measurements at all monitoring stations. The hereinafter referred uncertainties incorporating slope and intercept are standard errors, which are determined following the approach described in Celarier et al. (2008). This validates the satellite-derived annual mean $PM_{2.5}$ concentrations and indirectly validates the AOD retrieval algorithm developed in this study. However, the satellite-derived annual average $PM_{2.5}$ concentrations are slightly underestimated compared to the in-situ measurements. This is probably due to the comparison between the point values (in-situ measurements) to grid values (satellite-derived), as discussed in Wang and Chen (2013). All monitoring stations are located at the downtown, intersections of main roads or highways where there are the highest $PM_{2.5}$ concentrations in Montreal. This is likely another reason. In addition, the $PM_{2.5}$ measurement methods in Canada lead to a significant error in the determination of annual average $PM_{2.5}$ concentrations (Brook et

al., 2007). Therefore, the underestimates is not a sign of errors in the satellite-derived $PM_{2.5}$ concentrations, while probably due to the shortcoming in the in-situ measurements. On the other hand, it is true that the AOD retrievals may be affected by the uncertainties on ancillary data, such as pressure, ozone amount, and water vapor amount.

Figure 7-4 (b) shows the comparison between the $PM_{2.5}$ concentrations derived from the MODIS level 2 aerosol products at 10 km × 10 km resolution and the in-situ measurements at all monitoring stations. The agreement decreases to a lower level (r = 0.80, slope = 0.6407 ± 0.0003, intercept = 2.8871 ± 0.0065). This illustrates that the 1 km × 1 km aerosol retrievals from this study have significant improvements than the MODIS standard aerosol products.

Besides the in-situ surface measurements, some results for $PM_{2.5}$ in Montreal are found from other studies. One is from the study of van Donkelaar et al. (2010). They mapped global ground-level $PM_{2.5}$ concentrations using total column AOD from the MODIS and MISR satellite instruments and coincident aerosol vertical profiles from the GEOS-Chem model. The mean $PM_{2.5}$ concentrations in Montreal between 2001 and 2006 are ranging from 1 to 13 $\mu g/m^3$, which is in line with our results (1 - 14 $\mu g/m^3$). The other one is from the study of Martin (2011). He used various statistical analysis methods to forecast the $PM_{2.5}$ concentrations in the island of Montreal from 2004 - 2007. According to his study, at the Maisonneuve station, the annual average $PM_{2.5}$ concentration is 7.9 $\mu g/m^3$, and at the Airport Station, the $PM_{2.5}$ concentration is 8.2 $\mu g/m^3$. These results are lower than both our results and the in-situ measurements from the NAPS Network (Environment Canada, 2010). This is possibly due to the different periods used in the studies and the biases in the statistical analysis methods.

7.5 Summary

This chapter presents a case study of aerosol optical depth (AOD) retrieval using the developed algorithm for the MODIS satellite instrument at 1-km resolution over the island of Montreal, Canada in the year of 2009. The AOD retrievals from this study are spatially consistent with the MODIS collection 5 level 2 aerosol products with a much better resolution (1 km × 1 km vs. 10 km × 10 km). The satellite-retrieved AODs at 1-km resolution are used to derive the ground-level $PM_{2.5}$ concentrations using the local

scaling factors obtained from the GEOS-Chem aerosol simulation. The satellite-derived ground-level $PM_{2.5}$ concentrations are ranging from 1 to 14 $\mu g/m^3$ which are in line with the results from other literatures. The estimates are in good agreement (r = 0.90, slope = 0.9724 ± 0.0035, intercept = 0.2747 ± 0.0012) with the in-situ surface measurements at all monitoring stations, which are much better than the $PM_{2.5}$ concentrations derived from the standard MODIS 10-km AOD products compared with the in-situ measurements level (r = 0.80, slope = 0.6407 ± 0.0003, intercept = 2.8871 ± 0.0065). All of these validate the $PM_{2.5}$ results derived from the AODs retrieved at 1-km resolution in this study. This also indirectly validates the developed AOD retrieval algorithm. It is suggested that the method in this study can retrieve AODs at a higher spatial resolution than previously and can operate on an urban scale for $PM_{2.5}$ assessment.

Chapter 8 Ground-level $PM_{2.5}$ Investigation and Health Risk Assessment in the Extended East Asia

An environmental performance index (EPI) developed by the Yale Center for Environmental Law and Policy and Columbia's Center for International Earth Information Science Network (CIESIN) has ranked 132 countries based on 25 performance indicators (including $PM_{2.5}$, SO_2 and CO_2 emission per unit GDP, air effects on human health, Mortality, etc.) (Yale University, 2012). These indicators provide a gauge of how environmental performance at a national scale. According to the 2012 EPI and pilot trend results, China, South Korea and Japan (belong to the East Asia) are ranked at 116, 43, and 23, respectively; India (belongs to the South Asia) is ranked at 125 among 132 countries (Yale University, 2012). These four countries represent the general environmental situations in developing and developed countries. It is highly significant to study the air quality in these areas. However, none has presented year-by-year trends with up-to-date activity rates and regression analysis with influential factors for the East Asia and India, even the highest $PM_{2.5}$ concentrations in the world have been identified in these areas (van Donkelaar et al., 2006; 2010). Therefore, this case study investigates the ground-level $PM_{2.5}$ concentrations for the extended East Asia by applying the local scaling factors obtained from the global atmospheric chemical transport model (GEOS-Chem) to MODIS and MISR columnar AODs.

8.1 Derivation of Ground-level $PM_{2.5}$ Concentration from Satellite-based AOD

This study focuses on the East Asia extended to India (18°N to 54°N, 70°E to 142°E) which includes China, India, Japan, and South Korea for the period of 2001 to 2011. The MODIS Terra Level-2 aerosol data (collection 5) covering the East Asia and India are downloaded from the Earth Observing System Data Gateway at the NASA Goddard Space Flight Center (NASA, 2012a). The MISR Level-2 data (Version 17) covering the same areas are obtained from the Atmospheric Sciences Data Center at the

NASA Langley Research Center (NASA, 2012b). The aerosol vertical profiles, which are used to calculate the local scaling factors of AOD in the lower atmosphere, are simulated by the GEOS-Chem model at 0.5º × 0.667º horizontal resolution and 47 vertical levels for the extended East Asia. The assimilated meteorology of GEOS-5 is used in the simulation to compute the surface factor AOD. Anthropogenic emissions are replaced by the NASA's 2006 Intercontinental Chemical Transport Experiment-Phase B (INTEX-B) emission inventory (Zhang et al., 2009).

The methods developed by Liu et al. (2007) and van Donkelaar et al. (2010) are combined to derive the ground-level $PM_{2.5}$ concentrations (see Chapter 3.3.2). The factor that relates satellite-derived surface factor AOD to ground-level $PM_{2.5}$ concentrations, η, determined from the ratio of simulated dry aerosol mass to simulated surface factor AOD at satellite overpass (van Donkelaar et al., 2006). In this study, η is estimated at 50 % relative humidity for the extended East Asia (which is in agreement with the European ground-based measurements). The values of η from 0.5º × 0.667º grid cells (the resolution of the GEOS-Chem simulation) are interpolated to 0.1° × 0.1° (approximately 10 km × 10 km, which is consistent with MODIS resolution) for applying to satellite-derived surface factor AOD.

8.2 Regression Analysis

Take Beijing as an example, the ground-level $PM_{2.5}$ concentrations are associated with many factors, such as economic growth, population, coal consumption, soot and dust discharge, gas emission, and meteorological conditions. The general linear regression model (GLM) in the SPSS (Statistical Package for the Social Science) (IBM, 2012) is used to build the regression equation between $PM_{2.5}$ concentrations and influential factors. The adjusted R^2 value serves as the primary measure of model performance and selection criterion. The physical interpretations of parameter estimates also serve as an important model selection criterion. At the comparable adjusted R^2 levels, the model with positive regression coefficients for economic growth, population, coal consumption, soot and dust discharge, gas emission, and negative regression coefficient for precipitation is selected as the final model because it is physically

meaningful. Based on the regression equation, the future trend of $PM_{2.5}$ for the next 4 years (2012 - 2015) is predicted for Beijing.

8.3 Results and Analysis

8.3.1 Validation with surface truth and literatures

The annual average ground-level $PM_{2.5}$ concentrations are derived from the satellite AOD for the extended East Asia during 2001-2011. The results are evaluated by the in-situ surface measurements or literatures in six major cities: Beijing, Hong Kong, New Delhi, Kolkata, Tokyo, and Seoul.

In Beijing, there is no official $PM_{2.5}$ monitoring values available during 2001 to 2011. Thereby, the published results from literatures (He et al., 2001; Duan et al., 2006; Zhao et al., 2009; Yang et al., 2011; U.S. Embassy, 2012) and PM_{10} monitoring values (Beijing Municipal Environmental Protection Bureau, 2001 - 2011) are used to evaluate the satellite-derived annual average ground-level $PM_{2.5}$ concentrations. In Hong Kong, the $PM_{2.5}$ and PM_{10} monitoring values are obtained from the Environmental Protection Department of the Government of the Hong Kong Special Administrative Region (Environmental Protection Department of Hong Kong, 2001 - 2011). In India, the Respirable Suspended Particulate Matter (RSPM), i.e. PM_{10} monitoring values are obtained from the Ministry of Environment & Forests Government of India (Ministry of Environment & Forests Government of India, 2009). It has been reported that the average ratio of $PM_{2.5}$ to PM_{10} is 0.61 to 0.91 in India by Kumar and Joseph (2006). The $PM_{2.5}$ monitoring values are achieved by a factor of 0.7 with PM_{10} monitoring values. For Tokyo, the monitoring values of PM_{10} are obtained from the Environment of Tokyo (Environment of Tokyo, 2011). A $PM_{2.5}/PM_{10}$ ratio of 0.5 - 0.8 is the typical range found in developed country urban areas (WHO, 2006b). Thus, the ratio of 0.7 is taken as the factor to convert the PM_{10} monitoring values to $PM_{2.5}$. For Seoul, the monitoring values of PM_{10} are obtained from the Ministry of Environment of Korea (Ministry of Environment of Korea, 2011), and are converted to $PM_{2.5}$ using the same factor as Tokyo. Figure 8-1 presents the comparisons of satellite-derived annual average ground-level $PM_{2.5}$ concentrations with the monitoring values or literatures for major cities in the East Asia and India.

WHO has set 10 μg/m^3 as the guideline value for annual average $PM_{2.5}$ concentration. Besides the guideline value, three interim targets (IT) are defined for $PM_{2.5}$. The first target level (IT-1) is set as 35 μg/m^3, the second level (IT-2) is set as 25 μg/m^3, and third target level (IT-3) is set as 15 μg/m^3 (WHO, 2006b). The first target level (IT-1) is also marked in Figure 8-1 because this level has been shown to be associated with significant mortality in the world (WHO, 2006b).

Figure 8-1 (a) shows the comparison between the satellite-derived annual average ground-level $PM_{2.5}$ concentrations and the published results or the monitoring values converted from PM_{10} monitoring values for Beijing (He et al., 2001; Duan et al., 2006; Zhao et al., 2009; Yang et al., 2011; U.S. Embassy, 2010). The differences vary from -1.4 μg/m^3 to -8.0 μg/m^3. The linear regression analysis illustrates that the satellite-derived annual average ground-level $PM_{2.5}$ concentrations are quite consistent with the published results (r = 0.96, slope = 0.87, intercept = 4.86). It also can be seen that the annual average ground-level $PM_{2.5}$ concentrations are three times higher than the WHO IT-1 level (35 μg/m^3) in Beijing.

Figure 8-1 (b) shows the comparison between the satellite-derived annual average ground-level $PM_{2.5}$ concentrations and the monitoring values in Hong Kong. The differences vary from -1.1 μg/m^3 to 3.6 μg/m^3. The linear regression between satellite-derived and monitored $PM_{2.5}$ concentrations shows good agreement (r = 0.86, slope = 0.93, intercept = 2.83).

Figure 8-1 (c) and (d) show the comparisons between the satellite-derived annual average ground-level $PM_{2.5}$ concentrations and the converted $PM_{2.5}$ from PM_{10} monitoring values in India. Only 2001-2008 PM_{10} monitoring values are found. The differences for New Delhi and Kolkata vary from -10.1 μg/m^3 to 2.6 μg/m^3 and -3.2 μg/m^3 to -6.4 μg/m^3. The linear regression yields r = 0.90, slope = 1.02, intercept = 3.12 for New Delhi, and r = 0.96, slope = 1.19, intercept = 2.01 for Kolkata.

Figure 8-1 (e) shows the comparison between the satellite-derived annual average ground-level $PM_{2.5}$ concentrations and the monitoring values in Tokyo. The differences vary from 0.6 μg/m^3 to 3.1 μg/m^3. The linear regression shows good agreement (r = 0.98, slope = 0.91, intercept = 0.32).

Figure 8-1 (f) shows the comparison between the satellite-derived annual average ground-level $PM_{2.5}$ concentrations and the monitoring values in Seoul. The differences vary from -4.7 μg/m^3 to 1.4 μg/m^3. The linear regression shows r = 0.97, slope = 1.14, intercept = 1.82.

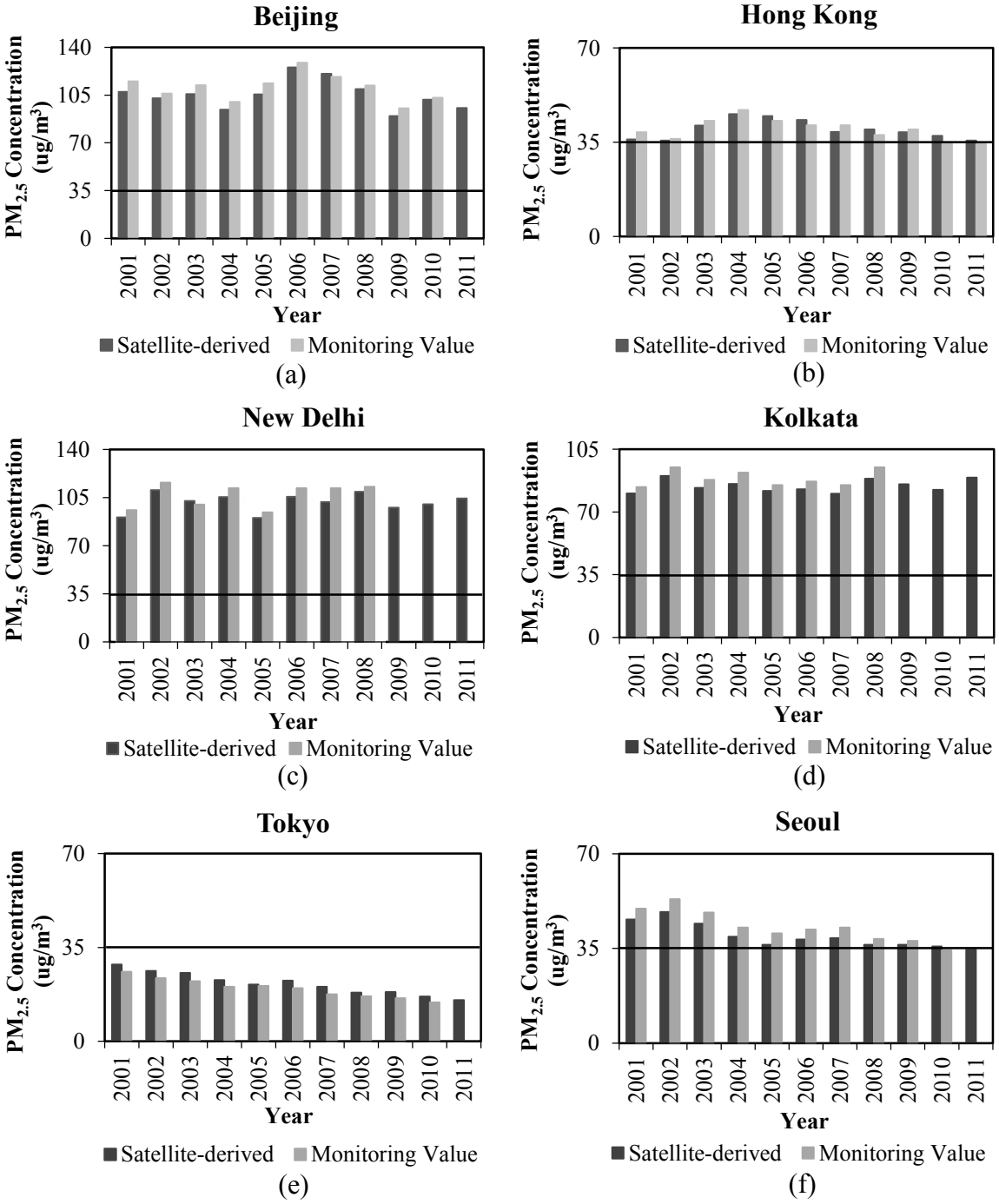

Figure 8-1 Comparisons between satellite-derived annual average ground-level $PM_{2.5}$ concentrations and monitoring values or literatures. The black solid line is the WHO IT-1 level (35 μg/m^3) (WHO, 2006b).

In general, the satellite-derived ground-level $PM_{2.5}$ concentrations tend to be slightly lower than the monitoring values in the cities with higher $PM_{2.5}$ concentrations, such as Beijing, New Delhi, Kolkata, Hong Kong and Seoul, while tend to be slightly higher than the monitoring values in the cities with lower $PM_{2.5}$ concentrations, such as Tokyo. This is in line with the conclusions from other literatures that satellite data underestimate the ground-level pollutant concentrations in highly polluted areas and overestimate the ground-level pollutant concentrations in less polluted areas (Suutari et al., 2001; Vautard et al., 2003). This is probably due to that the monitoring sites are primarily clustered in populated and more polluted areas while the satellite-derived values provide more complete coverage of hundred square kilometers.

8.3.2 Annual average ground-level $PM_{2.5}$ concentrations

The annual average ground-level $PM_{2.5}$ concentrations derived from the satellite data in eight representative cities: Beijing, Shanghai, Guangzhou, Hong Kong, New Delhi, Kolkata, Tokyo, and Seoul, are presented in Table 8-1.

Table 8-1 Satellite-derived annual average ground-level $PM_{2.5}$ concentrations for eight representative cities in the extended East Asia (unit: $\mu g/m^3$).

Year	Beijing	Shanghai	Guangzhou	Hong Kong	New Delhi	Kolkata	Tokyo	Seoul
2001	107.4	103.3	70.6	36.1	90.7	80.4	28.6	45.7
2002	102.7	98.2	73.4	35.6	110.5	90.2	26.2	48.5
2003	105.8	101.8	86.5	41.2	102.6	83.5	25.5	44.2
2004	94.3	90.1	92.8	45.5	105.4	85.6	22.8	39.3
2005	105.6	98.6	92.3	44.7	90.3	81.8	21.2	36.4
2006	125.2	113.7	93.6	43.3	105.7	82.7	22.6	38.3
2007	120.5	108.4	88.2	38.9	101.9	80.3	20.3	38.8
2008	109.4	105.5	90.7	39.8	109.3	88.6	18.2	36.4
2009	89.7	97.3	76.5	38.7	97.8	85.5	18.4	36.3
2010	101.6	94.5	74.1	37.4	100.2	82.4	16.7	35.7
2011	95.5	103.4	78.4	35.6	104.5	89.3	15.4	34.5
Average	105.3	101.4	83.4	39.7	101.7	84.6	21.5	39.5

From Table 8-1, it can be seen that, in most cities except Tokyo, the annual average $PM_{2.5}$ concentrations all exceed the WHO IT-1 level (35 μg/m^3). Figure 8-2 illustrates the areas with $PM_{2.5}$ concentrations exceeding the WHO three interim targets (35 μg/m^3, 25 μg/m^3, and 15 μg/m^3) (WHO, 2006b) in 2002, 2006, 2008, and 2010, respectively.

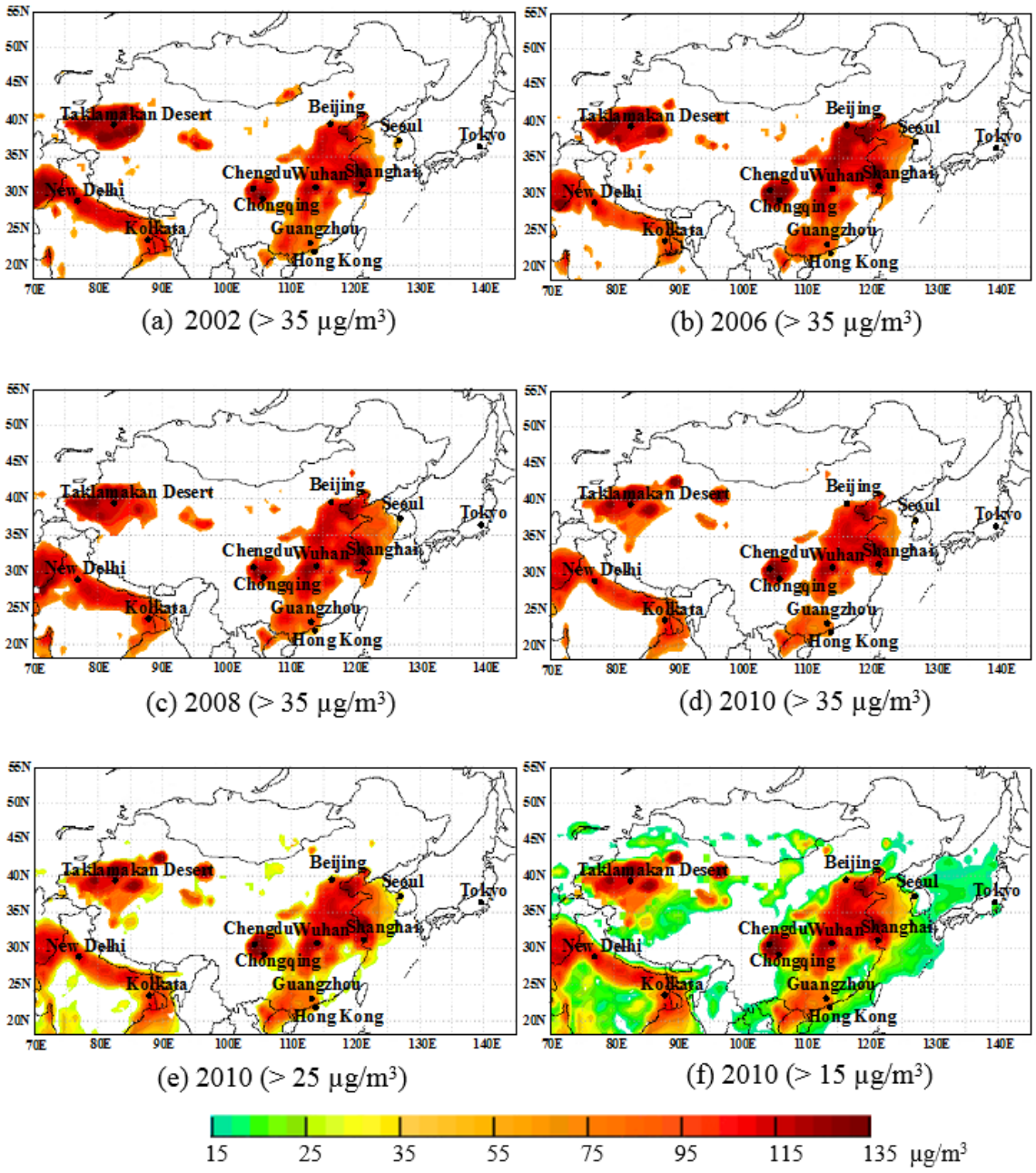

Figure 8-2 Areas with annual average ground-level $PM_{2.5}$ concentrations derived from the satellite data exceeding: (a) - (d) the WHO IT-1 level (35 μg/m^3) in 2002, 2006, 2008, and 2010, respectively; (e) the WHO IT-2 level (25 μg/m^3) in 2010; and (f) the WHO IT-3 level (15 μg/m^3) in 2010.

Figure 8-2 (a) - (d) show that the areas with $PM_{2.5}$ concentrations exceeding the WHO IT-1 level (35 $\mu g/m^3$) are most located in the developing countries China and India. In China, the higher $PM_{2.5}$ concentrations focus on the northern and southern large cities, such as Beijing, Shanghai, Chongqing, Wuhan, and Guangzhou, where there are large populations and fast economic growth. The highest $PM_{2.5}$ concentration (125.2 $\mu g/m^3$) is found in Beijing in 2006, which is higher than the WHOIT-1 level by 3.6 times. Hong Kong lightly exceeds the WHO IT-1 level due to suffering from cross-boundary pollutants which are emitted from the industries in Pearl River Delta Region (Yang et al., 2011). The western Taklamakan Desert, which is the largest desert in China, second largest desert in the world, also has higher $PM_{2.5}$ concentrations due to the industries in surrounding cities and dry and cold climate (Yang et al., 2011). In India, the higher $PM_{2.5}$ concentrations occur along the northern and eastern urban areas, such as New Delhi and Kolkata. The highest $PM_{2.5}$ concentration (110.5 $\mu g/m^3$) is found in New Delhi in 2002, which is 3.2 times higher than the WHO IT-1 level. There are relative lower $PM_{2.5}$ concentrations in the developed countries Japan and Korea. There is no area exceeds the WHO IT-1 level except Seoul in these countries.

Figure 8-2 (e) shows that the areas with $PM_{2.5}$ concentrations exceeding the WHOIT-2 level (25 $\mu g/m^3$) are also most located in the developing countries China and India and extended to Seoul. Figure 8-2 (f) shows that the areas with $PM_{2.5}$ concentrations exceeding the WHOIT-3 level (15 $\mu g/m^3$) are most located in China, India and extended to Seoul and Tokyo.

Figure 8-3 shows the change trends in 8 representative cities. In general, there are increasing trends in most cities during 2001-2006, and there are slightly decreasing trends since then. Especially in Beijing, Shanghai, Guangzhou, and Hong Kong, there are obvious decreasing trends on $PM_{2.5}$ concentrations in these cities. While there are slightly increasing trends in New Delhi and Kolkata.

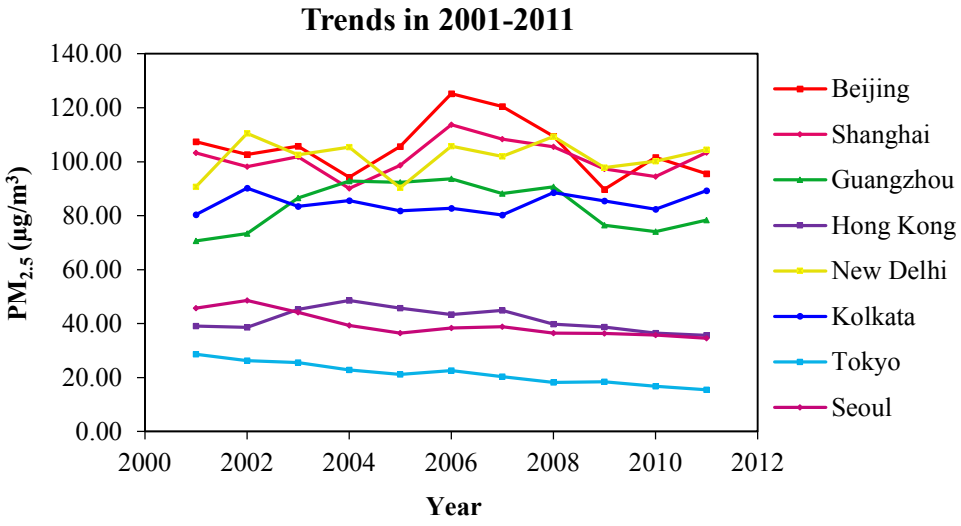

Figure 8-3 $PM_{2.5}$ change trends in eight representative cities: Beijing, Shanghai, Guangzhou, Hong Kong, New Delhi, Kolkata, Tokyo, and Seoul during 2001-2011.

8.3.3 11-year average ground-level $PM_{2.5}$ concentrations

Figure 8-4 shows the 11-year average ground-level $PM_{2.5}$ concentrations derived from satellite data during 2001 - 2011. The mean $PM_{2.5}$ concentrations vary spatially by more than an order of magnitude. A large-scale $PM_{2.5}$ enhancement is apparent over the northern and southern urban areas and the western desert regions in China, and the northern and eastern urban areas in India. The eastern and northern parts of the East Asia are generally characterized by low $PM_{2.5}$ concentrations, with a few exceptions.

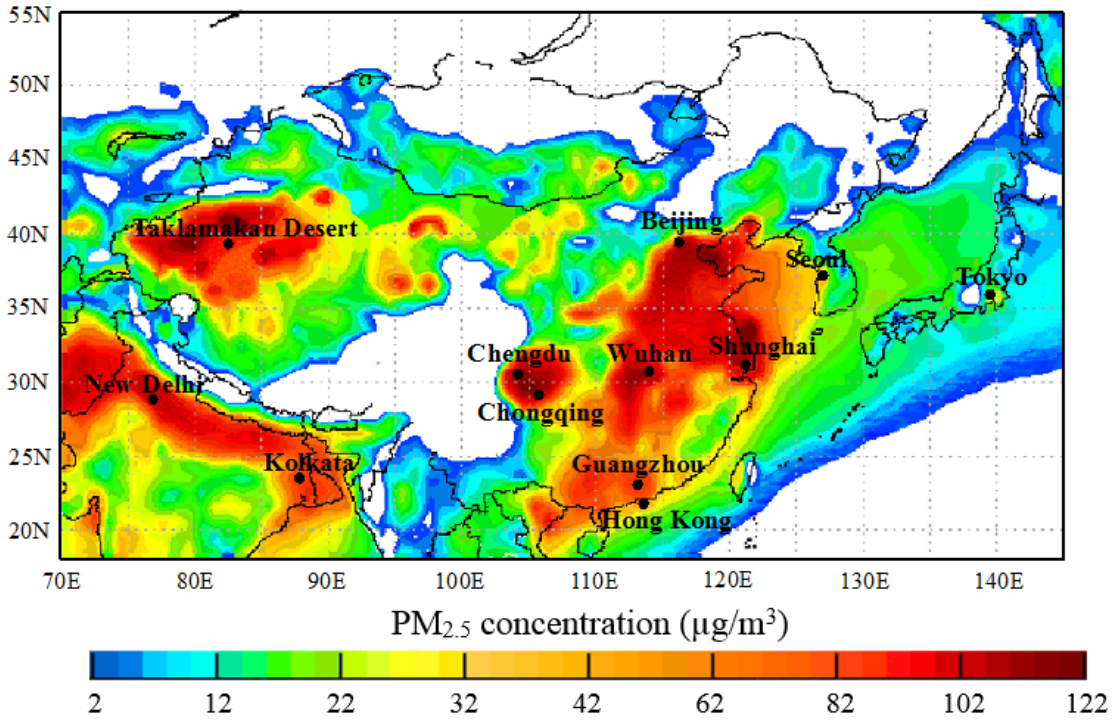

Figure 8-4 11-year average satellite-derived ground-level $PM_{2.5}$ concentrations during 2001-2011. White parts are the areas with values lower than 2 μg/m^3.

The 11-year average $PM_{2.5}$ concentrations are lower than 20 μg/m^3 for the large regions of the East Asia. In contrast, the values are 21.45 μg/m^3 (monitoring values is 19.74 μg/m^3) in Tokyo, 39.46 μg/m^3 (monitoring values is 42.98 μg/m^3) in Seoul (Table 8-1). The $PM_{2.5}$ concentrations of 60 - 100 μg/m^3 are found over the northern and southern China. The values higher than 100 μg/m^3 occur in the major industrial regions and the western desert areas. Especially, in Beijing, the 11-year average $PM_{2.5}$ concentration is 105.25 μg/m^3 (monitoring values is 110.47 μg/m^3). In India, the highest $PM_{2.5}$ concentrations occur in the areas from New Delhi east-ward to Kolkata, with values of 60 - 110 μg/m^3.

Figure 8-5 shows the changes of 11-year average ground-level $PM_{2.5}$ concentrations since 2001. Four representative cities, Guangzhou, Hong Kong, New Delhi, and Kolkata, have increased 18 %, 10 %, 12 %, and 5 %, respectively. Guangzhou and New Delhi have the largest increases during the period of 2001 - 2011. The other four cities, Beijing, Shanghai, Tokyo and Seoul, have decreased 2 %, 2 %, 25 %, and 13 %, respectively.

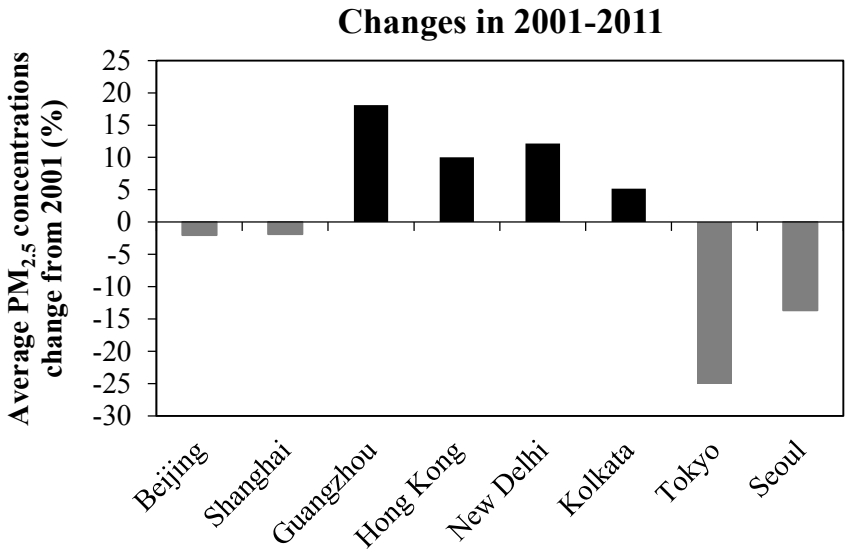

Figure 8-5 General changes of 11-year average ground-level $PM_{2.5}$ concentrations during 2001 - 2011 compared to 2001.

8.3.4 Comparison with literatures

The satellite-derived 11-year average ground-level $PM_{2.5}$ concentrations during 2001 - 2011 are compared with the results of van Donkelaar et al. (2010) over 2001 - 2006. In the study of van Donkelaar et al. (2010), $PM_{2.5}$ concentrations of 60 - 90 $\mu g/m^3$ are found over the eastern China, with values > 100 $\mu g/m^3$ for the major industrial regions. The Indo-Gangetic plain, from New Delhi east-ward contains the highest $PM_{2.5}$ concentrations in India, with values of 80 - 100 $\mu g/m^3$. In this study, the satellite-derived 11-year average ground-level $PM_{2.5}$ concentration (2001 - 2011) for Beijing is 105.25 $\mu g/m^3$, Shanghai is 101.35 $\mu g/m^3$, Guangzhou is 83.37 $\mu g/m^3$, New Delhi is 101.72 $\mu g/m^3$, and Kolkata is 84.57 $\mu g/m^3$, which are in good agreement with the study of van Donkelaar et al. (2010). In addition, the van Donkelaar et al. (2010)'s study just provided the global 6-year average $PM_{2.5}$ concentrations. The results in this study provide more spatial and temporal details and change trends on $PM_{2.5}$ concentrations in the East Asia and India.

The results illustrate that there are much higher $PM_{2.5}$ concentrations in the East Asia and India than other areas in the world. For example, van Donkelaar et al. (2010) derived $PM_{2.5}$ values are < 10 $\mu g/m^3$ for large regions of the earth. The geographic

average $PM_{2.5}$ concentrations over the eastern and western North America are 6.9 $\mu g/m^3$ and 6.2 $\mu g/m^3$, respectively. Liu et al. (2005) estimated the $PM_{2.5}$ concentrations ranged between 10 and 15 $\mu g/m^3$ in the majority of the eastern United States in 2001. From this study, the $PM_{2.5}$ concentrations in the major cities in the East Asia and India are almost 10 times higher than that in the North America based on the satellite-derived ground-level $PM_{2.5}$ results for the period 2001 - 2011. This situation can be worsened during the poor dispersion conditions, such as low wind speed and cool temperature during winter. For example, the heavy haze occurred in China in January 2013, and extremely high $PM_{2.5}$ concentrations were measured with the maximum 993 $\mu g/m^3$ in Beijing. This event was mainly caused by the coal combustion from power plants, boilers and residents and affected 17 provinces (cities), six hundred million people (http://news.xinhuanet.com/).

8.4 Health Impact Assessment

$PM_{2.5}$ is considered as the most hazardous air pollutant to human health because it is more prone to carry a variety of toxic heavy metals, PAHs (Polycyclic Aromatic Hydrocarbons) and other chemicals, as well as microorganisms such as bacteria and viruses in the air. It can carry these toxic pollutants to enter and deposit in human alveoli, causing respiratory inflammation and lung cancer. It can also enter the human blood circulation and affect the normal functions of human cardiovascular system, leading to significantly increased mortality due to cardiovascular, cerebrovascular diseases (Environmental organization Greenpeace, 2012).

Since 1985, lung cancer has been ranked the highest incidence and mortality rates among various theriomas. Many studies have reported the positive associations between $PM_{2.5}$ and lung cancer mortality. For example, Pope et al. (2002) found that each 10 $\mu g/m^3$ increase in long-term average $PM_{2.5}$ concentrations was associated with approximately a 4 % increased risk of death from all natural causes, a 6 % increased risk of death from cardiopulmonary disease, and an 8 % increased risk of death from lung cancer. Laden et al. (2006) reported a relative risk for lung cancer mortality of 1.27 (95 % CI 0.96, 1.69) per 10 $\mu g/m^3$ increase of $PM_{2.5}$ in the Harvard Six Cities. Turner et al. (2011) also reported that each 10 $\mu g/m^3$ increase in $PM_{2.5}$ concentrations was associated

with a 15 - 27 % increase in lung cancer mortality. While the latest research conducted by Lepeule et al. (2012) reported that each 10 μg/m^3 increase in $PM_{2.5}$ was associated with a 14 % increased risk of all cause death, a 26 % increase in cardiovascular death, and a 37 % increase in lung cancer death. However, few studies have examined the association between $PM_{2.5}$ exposure and lung cancer incidence. One study conducted in Europe reported no association between $PM_{2.5}$ and lung cancer incidence (Vineis et al., 2006). The other study conducted by the U.S. EPA found the positive trend between the $PM_{2.5}$ concentrations and the lung cancer incidence and mortality rates in North Carolina although variability was high (Vinikoor-Imler et al., 2011).

The high $PM_{2.5}$ concentrations have caused severe health impacts in the industrial areas and megacities in China. Zhao et al. (2013) analyzed the $PM_{2.5}$ concentrations and chemical compositions in the regions of Beijing, Tianjin, and Hebei (BTH), China. The annual average concentrations of $PM_{2.5}$ were 71.8 - 191.2 μg/m^3 with exceeding 100 μg/m^3 at Beijing, Tianjin, and Shijiazhuang. Nineteen elements (Al, As, Ba, Ca, Cd, Co, Cr, Cu, Fe, K, Mg, Mn, Ni, P, Pb, Sr, Ti, V, and Zn), eight water-soluble ions (Na^+, NH_4^+, K^+, Mg^{2+}, Ca^{2+}, Cl^-, NO_3^- , and SO_4^{2-}), carbon fractions (OC and EC) and PAHs were found in the $PM_{2.5}$ mass. The concentrations of heavy metals, such as Zn, Pb, Mn, Cu and Cr, were also at higher levels in $PM_{2.5}$ in the BTH area. The most abundant heavy metals were Pb and Zn, which had always been found together from minerals to industrial productions and processes. It can be concluded that the $PM_{2.5}$ in the BTH area is more hazardous to human health compared to the other areas, such as the western desert area where the $PM_{2.5}$ is mainly caused by natural dust fall.

The environmental organization Greenpeace projected that poor air quality caused premature deaths of nearly 8,600 people in the Chinese cities of Beijing, Shanghai, Guangzhou, and Xi'an in 2012 (Environmental organization Greenpeace, 2012). The Beijing Municipal Health Bureau has announced that there were 4729 lung cancer mortality in 2007, which were 56 % increase compared to 2000, but the amount of smokers wasn't increased (Beijing Municipal Health Bureau, 2012). The statistic data from the Beijing Cancer Hospital shows that the lung cancer incidence rates have been dramatically increased since 2001, as shown in Figure 8-6 (a) (blue part), and it has been ranked the first for man and second for woman among various theriomas incidence rates

in Beijing (Beijing Cancer Hospital, 2012). From this study, we found that the ground-level $PM_{2.5}$ concentrations were kept at a high level (three times higher than the WHO IT-1 level) during the same period in Beijing, also as shown in Figure 8-6 (a) (pink part). The monitoring values from literatures are also presented in this figure (green part).

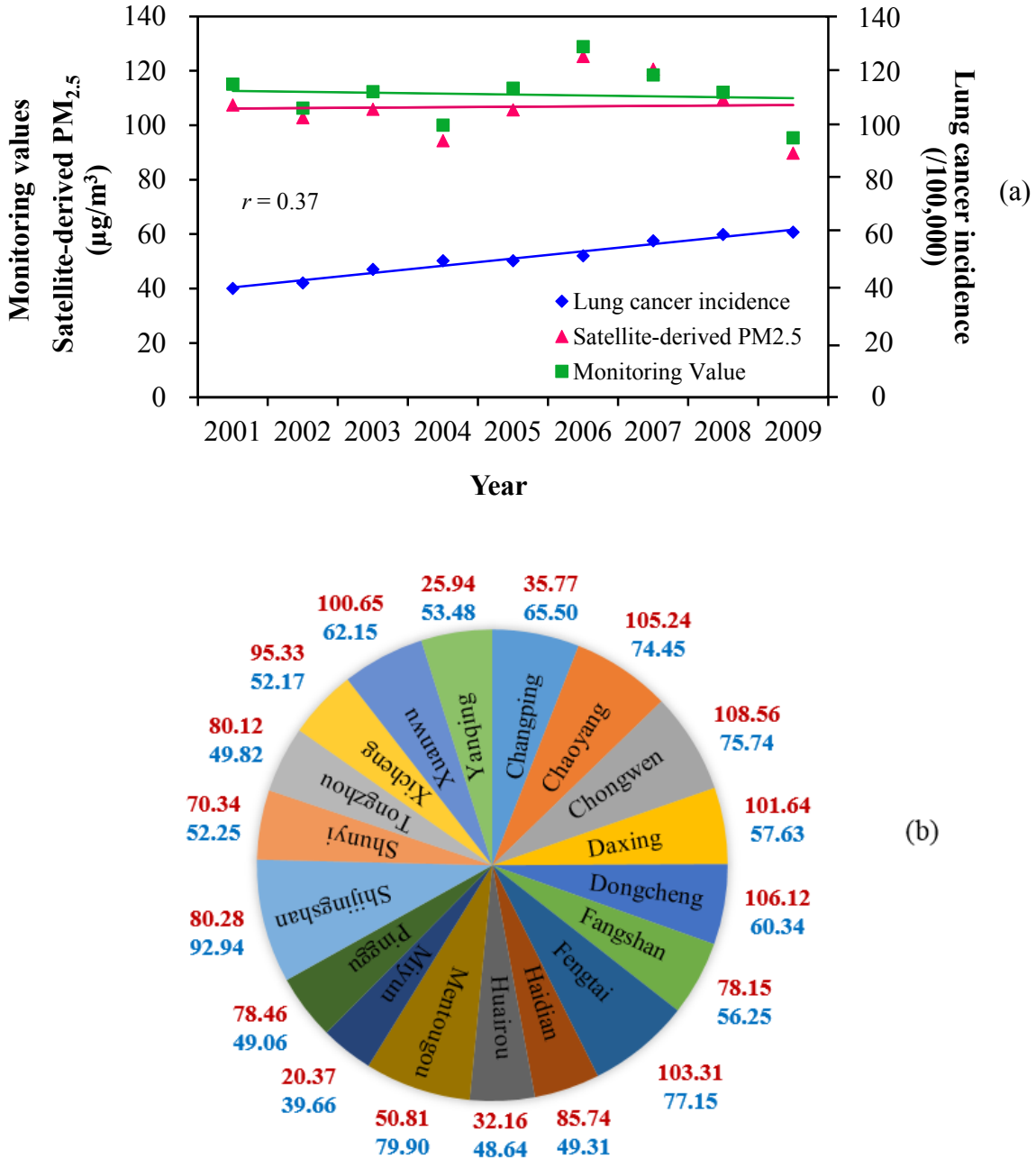

Figure 8-6 $PM_{2.5}$ concentrations and lung cancer incidence rates in Beijing. (a) satellite-derived annual average ground-level $PM_{2.5}$ concentrations, monitoring values from

literatures ($\mu g/m^3$) and lung cancer incidence rates (/100,000) from 2001-2009 in Beijing (Beijing Cancer Hospital, 2012); (b) Satellite-derived $PM_{2.5}$ concentrations and lung cancer incidence rates in 18 counties (or cities) of Beijing in 2009 (Beijing Cancer Hospital, 2012).

We use linear regression to examine the association between satellite-derived $PM_{2.5}$ concentrations and lung cancer incidence rates in Beijing from 2001-2009. The correlation coefficient is 0.37 (also shown in Figure 8-7 (a)) and the unadjusted slope for the linear trend between satellite-derived $PM_{2.5}$ concentrations and lung cancer incidence rates is 0.83 (95 % CI 0.21, 1.45, ρ-value 0.01) per 1 $\mu g/m^3$ $PM_{2.5}$. We also perform a linear regression analysis for 18 counties (or cities) in Beijing in 2009 (Beijing Cancer Hospital, 2012) to further examine the association between $PM_{2.5}$ concentrations and lung cancer incidence rates on spatial scale, as shown in Figure 8-8 (b). The correlation coefficient is 0.32 and the unadjusted slope for the linear trend between $PM_{2.5}$ concentrations and lung cancer incidence rates is 0.76 (95 % CI 0.19, 1.33, ρ-value 0.01) per 1 $\mu g/m^3$ $PM_{2.5}$.

The regression analysis shows that there are positive associations between the $PM_{2.5}$ concentrations and the lung cancer incidences on both temporal and spatial scales. The low correlation coefficients (r = 0.37 and 0.32, respectively) imply that there are multi-factors contribute to the lung cancer incidences and $PM_{2.5}$ is not the only agent responsible for the increased lung cancer incidence rates. Even so, the results still provide limited evidences to support the association between $PM_{2.5}$ and lung cancer incidences, which is consistent with previous studies (Vinikoor-Imler et al., 2011).

8.5 Regression Analysis - Beijing

8.5.1 Descriptive statistics

The results in this study indicate that there are very severe $PM_{2.5}$ pollution in the major cities in China and India (more than three times higher than the WHO IT-1 level and ten times higher than that in North America). It is essential to understand the speciation and sources of $PM_{2.5}$ for making cost-effective strategy to control and improve this situation. However, there are different speciation and sources of $PM_{2.5}$ in different

countries and cities due to the different conditions. Therefore, we take Beijing as an example, use the satellite-derived ground-level $PM_{2.5}$ concentrations to find out the main factors associated with $PM_{2.5}$ by regression analysis, and explore the mitigation measures in this city.

There are many reasons for the high $PM_{2.5}$ concentrations in Beijing. Numerous research findings have indicated that the fast economic growth and urbanization is one of the main reasons. The GDP growth rates which were associated with the industrial productions and economic activities were maintained greater than 8 % during the period 2001-2011 in Beijing, as shown in Figure 8-2. These GDP growth rates were much higher than the other countries in the world, especially, the developed countries, such as the United States (mean GDP growth rate 1.58 % during the same period), Canada (mean GDP growth rate 1.93 %), and Japan (mean GDP growth rate 0.65 %) (Knoema, 2012). Thus, the GDP growth rate is expected as one of the major factors associated with $PM_{2.5}$ in Beijing. The statistic shows that the amount of motor vehicles has been increased from three millions to five millions in four years (2008 - 2012). According to the statistical analysis of Beijing Environmental Protection Bureau, the most major source of $PM_{2.5}$ is traffic emission, which accounts for 22 % of $PM_{2.5}$ in Beijing due to the reduction of coal consumption and sharply increasing of cars in recent years (Beijing Environmental Protection Bureau, 2012). The second largest source of $PM_{2.5}$ in Beijing is coal combustion which accounts for 19 % of $PM_{2.5}$ in Beijing (Environmental organization Greenpeace, 2012). There are still 78 % energy come from coal electricity in China at present. Coal combustion contributes to 80 % of total sulfur dioxide emissions and 70 % of total nitrogen oxide emissions which are the major sources of secondary $PM_{2.5}$. Despite the Beijing Municipal Government has shut down or moved out the heavily polluting section eliminating the large pollution sources, the surrounding areas, such as Tianjin, Hebei, Inner Mongolia, and Shanxi are continued to emit a large amount of air pollutants, which are transferred to Beijing by wind. The regional transportation and dust fall account for 18 % of $PM_{2.5}$ in Beijing due to the topgraphic feature surrounded by mountains (Environmental organization Greenpeace, 2012).

Due to a lack of available data, the emissions from motor vehicles are represented by the population for the regression analysis. Since the emissions of sulfur dioxide and

nitrogen oxide and industrial soot and dust discharge mainly come from the coal consumptions in Beijing (Ohara et al., 2007; Hao et al., 2007), they are represented by the coal consumptions. Consequently, the GDP growth rate, population growth rate, coal consumption, dust fall and precipitation are selected as the major factors associated with $PM_{2.5}$ in this case study. The data from 2001 to 2011 for Beijing are list in Table 8-2. The PM_{10} monitoring values in the same period are also list in Table 8-2.

Table 8-2 Major factors associated with $PM_{2.5}$ in Beijing.

Year	GDP growth rate[a] (%)	Population growth rate[a] (%)	Coal[b] (million ton)	Dust fall[c] (ton/km^2• month)	Precipitation[c] (mm)	PM_{10}[c] (ug/m^3)
2001	11.7	0.60	26.75	15.20	338.90	165.00
2002	11.5	4.28	25.31	13.20	370.40	166.00
2003	11.0	2.33	26.77	12.00	444.50	141.00
2004	13.2	2.49	28.00	12.30	483.50	149.00
2005	11.8	3.03	30.69	12.50	467.00	142.00
2006	12.8	2.80	30.56	12.80	448.00	161.00
2007	12.3	3.29	29.85	14.70	483.90	148.00
2008	9.0	3.80	27.48	13.40	626.30	122.00
2009	10.1	3.54	26.65	11.60	480.60	121.00
2010	10.2	11.74	27.00	14.20	533.80	121.00
2011	8.1	1.99		11.30	721.10	114.00

a. Beijing Statistical Yearbook 2011 (Beijing Municipal Bureau of Statistics, 2001 - 2011).
b. Beijing coal production and consumption and demand outlook (Li et al., 2011).
c. Beijing Environmental Statement (2001 - 2011) (Beijing Municipal Environmental Protection Bureau, 2001 - 2011).

From Table 8-2, we can see that the GDP growth rates range from 8.1 % to 13.2 % with an average of 11.1 % in Beijing during 2001 - 2011. The population growth rates change from 0.6 to 11.74 with an average of 3.6 %. The coal consumptions reached to the peak in 2005 and 2006, which were corresponding to the highest annual average $PM_{2.5}$ concentration (125. 2 μg/m^3) in Beijing. The dust fall and precipitation were randomly changed by year with a relative small precipitation (448 mm) in 2006. All of these resulted in a higher PM_{10} monitoring value (161.0 μg/m^3) and a $PM_{2.5}$ peak in 2006. The relative lower $PM_{2.5}$ concentrations were found in 2004 (94.3 μg/m^3) and 2009 (89.7

$\mu g/m^3$). Especially in 2009, the lowest $PM_{2.5}$ concentration occurred when the coal consumption and dust fall were lower than other years. From the above analysis, it can be expected that there are significant correlations among the ground-level $PM_{2.5}$ concentrations and the GDP growth rates, coal consumptions, and dust fall in Beijing.

Figure 8-7 shows the comparison of variations among the GDP growth rates, coal consumptions, and ground-level $PM_{2.5}$ concentrations in Beijing from 2001 to 2011. Figure 8-7 (a) and (b) present the variations of GDP growth rates and coal consumptions, respectively. Figure 8-7 (c) shows the variations of satellite-derived annual average ground-level $PM_{2.5}$ concentrations and the monitoring values from literatures (He et al., 2001; Duan et al., 2006; Zhao et al., 2009; Yang et al., 2011; U.S. Embassy, 2012). The satellite-derived annual average ground-level $PM_{2.5}$ concentrations from two grids are also presented for the comparison. Grid 1 is located at the center of Beijing where is occupied by 62 % of the population and includes most of the commercial and industrial activities, but its area is only 8 % of the city (Wang et al., 2010b). This area includes the more urbanized districts and several large economic-technological and industrial development zones where the highest $PM_{2.5}$ concentrations mostly occur around here, as shown in Figure 8-8. On the contrary, the $PM_{2.5}$ concentrations decrease progressively with the distance away from the central part. In the mountain and rural areas with less residential or industrial activities, the $PM_{2.5}$ concentrations become much lower. Grid 2 is located at Shunyi (Figure 8-8) where there are several industrial and economic development zones associated with automobile, electron, plastic, leather industries (Beijing Municipal Commission of Economy and Information Technology, 2010a). The $PM_{2.5}$ concentration is lower than the center urban but higher than the mountain and rural areas.

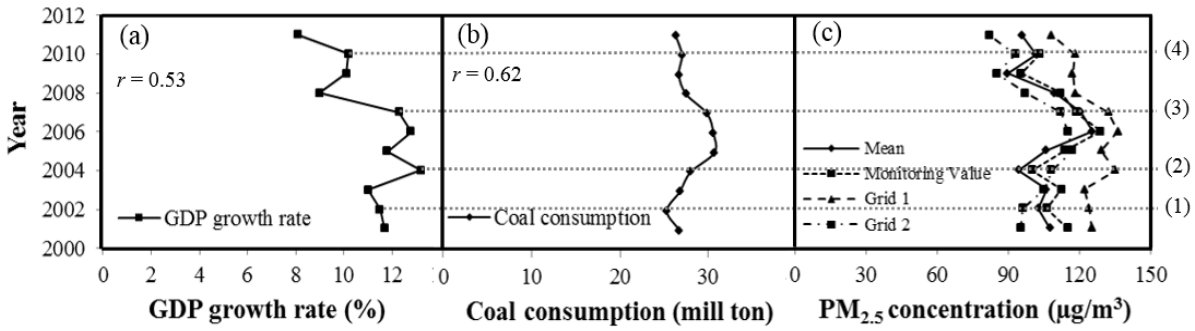

Note: (1) the annual average $PM_{2.5}$ concentrations decreased with the coal consumptions declined due to the implement of government policy – Beijing Environmental Control Target and Measures (1999 - 2002) (Beijing Municipal Environmental Protection Bureau, 2002); (2) the $PM_{2.5}$ concentrations in grid 1 and 2 increased due to the GDP growth rates and coal consumptions increased, whereas the mean value and monitoring value decreased due to the surrounding decreased; (3) the $PM_{2.5}$ concentrations decreased due to the measures of air quality control for the 2008 Olympics; (4) the $PM_{2.5}$ concentrations increased due to a number of new industrial projects carried out, especially in Shunyi (grid 2), five new projects including manufacture and power plant were implemented in 2010 (Beijing Municipal Commission of Economy and Information Technology, 2010b).

Figure 8-7 Comparison of variations among the GDP growth rates, coal consumptions and the ground-level $PM_{2.5}$ concentrations in Beijing from 2001 to 2011. (a) and (b) show the variations of GDP growth rates and coal consumptions, respectively. (c) shows the variations of satellite-derived mean ground-level $PM_{2.5}$ concentrations (solid line), the monitoring values from literatures (dot line), and the $PM_{2.5}$ concentrations in two grids (dash lines).

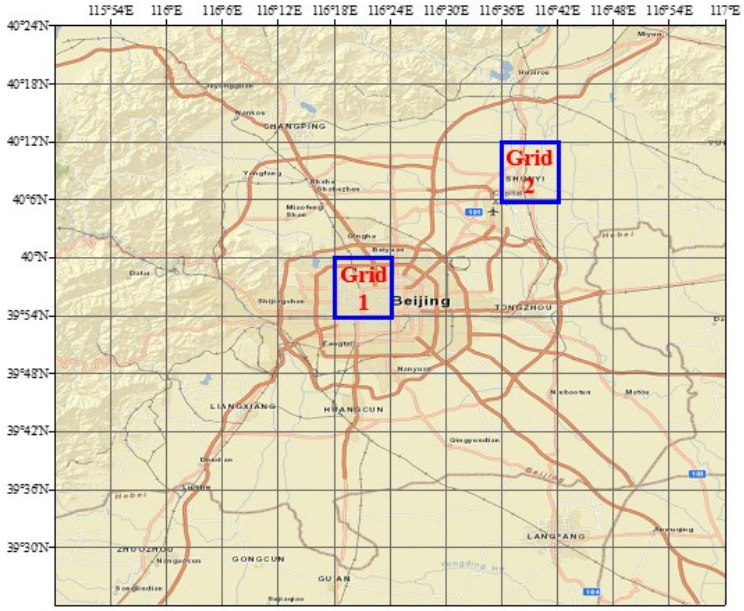

Figure 8-8 Beijing map with 10 km × 10 km grid cells. Grid 1 and grid 2 are the locations for the comparison in Figure 8-7.

From Figure 8-7, we can see that the variations of $PM_{2.5}$ concentrations in grid 1 are quite similar with the GDP growth rates, implies that the commercial activities are the main reasons for the high $PM_{2.5}$ concentrations in the center urban. The variations in grid 2 are more consistent with the coal consumptions, reveals that the coal consumptions are the major reason except commercial activities for the $PM_{2.5}$ concentrations in this area. The widespread installations of fuel-gas desulfurization (FGD) devices in coal-fired boilers decline the SO_2 emissions, but cannot help the organic carbon emissions which are also a major source of the $PM_{2.5}$ in Beijing (Yang et al., 2011). The variations of mean and monitoring values are generally similar with the variations of GDP growth rates. This illustrates that the commercial and industrial activities are the main reasons for the $PM_{2.5}$ concentrations in Beijing. However, there are some differences between the $PM_{2.5}$ concentrations and the GDP growth rates in recent years (after 2009). This is probably due to the rapid increase in population and the number of motor vehicles resulting in the sharp increase of NO_x emissions from vehicle exhausts which is another source of $PM_{2.5}$ (Yang et al., 2011).

From the satellite-derived annual average ground-level $PM_{2.5}$ concentrations in Table 8-1 and PM_{10} monitoring values in Table 8-2, the range of ratio between PM_{10} and $PM_{2.5}$ are calculated as 0.65 - 0.90 (average is 0.75), which is in line with the conclusions from publications (0.61 – 0.91 in Mumbai) by WHO (2006a) and Kumar and Joseph (2006). This shows that the $PM_{2.5}$ fraction comprises the majority of PM_{10} in Beijing.

8.5.2 Regression analysis

To further examine the association between the ground-level $PM_{2.5}$ concentration and the influential factors, a regression analysis is conducted using the SPSS (Statistical Package for the Social Science) (IBM, 2012) and data in Table 8-1. First, a correlation analysis is performed. The stronger correlations are found among the $PM_{2.5}$ concentrations and the GDP growth rates (Pearson correlation coefficient r = 0.58), population growth rates (r = 0.42), coal consumptions (r = 0.62), There are weaker correlations among the $PM_{2.5}$ concentrations and the dust fall (r = 0.14) and precipitation (r = - 0.18). As expected, most of the influential factors have positive impacts on the ground-level $PM_{2.5}$ concentrations except the precipitation has a negative impact.

Then the general linear regression model (GLM) with power law functional forms, accounting for the nonlinear relationships between $PM_{2.5}$ concentrations and influential factors, is used to build the regression equation. The satellite-derived annual average ground-level $PM_{2.5}$ concentration is set as the dependent variable. The predictor variables include the GDP growth rate, population growth rate, and coal consumption, which are set as primary predictors, the dust fall and precipitation are set as secondary predictors. The regression equation shows a well goodness fit ($R^2 = 0.82$).

The sensitivity analysis based on the regression equation indicates that the fast economic growth (average GDP growth rate is 11 % in 2001 - 2011) is a major factor for the high $PM_{2.5}$ concentrations in Beijing. The coal consumption has been the second source of $PM_{2.5}$. The fast population growth is also responsible for a large part of the $PM_{2.5}$. By contrast, the dust fall takes charge of relatively smaller scale of the $PM_{2.5}$. The precipitation has good effects on the $PM_{2.5}$. Unfortunately, there are smaller precipitations (average 490.73 mm in 2001 - 2011) in Beijing compared to Shanghai (average 1169.65 mm in 2001 - 2011).

It can be concluded that the deteriorating urban air quality in Beijing is closely related to the China's fast economic growth and the over-reliance on coal consumptions. Managing $PM_{2.5}$ pollution must begin with properly controlling GDP and population growth rates, controlling the emissions from traffic and coal combustions, replacing urban coal consumptions with clean alternative energy sources. The low-carbon energy policy (i.e. improved energy efficiency; using clean energy sources, such as natural gas, wind electricity, etc.) and green development should be a good way to reduce the $PM_{2.5}$ pollution in Beijing.

8.5.3 Future trend prediction

Fortunately, Beijing government has recognized the fast economic growth and enormous coal consumption have made the people live in Beijing pay great costs on the severe environment. They have made some decisions to slow the economic growth and decrease the coal consumption. It has been reported that the GDP growth rate is 7.2 % during the first half of the year 2012, which is the first time breaking 8 %. Assuming that the GDP growth rate decreases 0.5 % every year from 2011 to 2015, it would decline

to 6.1 % by 2015. Beijing government also issued a coal consumption amount control plan which proposed the coal consumption should be reduced to 20 million ton by 2015 (Beijing government, 2011). This means the coal consumption will be decreased 7 million ton from 2010 to 2015 in Beijing. In addition, according to the Beijing Environmental Protection and Construction Plan in 12th Five-Year Period, the SO_2 emission will be decreased 13.3 % by 2015 compared to 2010 (Beijing Municipal Environmental Protection Bureau, Beijing Municipal Development and Reform Commission, 2011).

In February 2012, Ministry of Environmental Protection renewed the ambient air quality standards, first set a limit of 35 $\mu g/m^3$ for annual average $PM_{2.5}$ in China. It will be implemented on January 1st, 2016. These control measures and large reduction represent a human-perturbation experiment of unprecedented scale, and provide a rare opportunity to study the future trend of $PM_{2.5}$ in Beijing.

Assuming all targets mentioned above will be reached, using the regression equation we created and considering other possibilities, the ground-level $PM_{2.5}$ concentration are predicted for 2012 - 2015. It would be 85.3 $\mu g/m^3$ in 2012, 74.7 $\mu g/m^3$ in 2013, 63.5 $\mu g/m^3$ in 2014, and 52.1 $\mu g/m^3$ in 2015. It is difficult to reach the limit (35 $\mu g/m^3$) in 2016 when the new ambient air quality standards are implemented.

8.6 Discussion

A number of interesting conclusions can be drawn from the satellite-derived annual average ground-level $PM_{2.5}$ concentration results, the regression analysis, the future trend prediction and health impact assessment.

8.6.1 Implications of the study results

The validation of the satellite-derived annual average ground-level $PM_{2.5}$ concentration results (Figure 8-1) demonstrate that the satellite remote sensing can provide a long-term dataset with complete spatial coverage for predicting ground-level $PM_{2.5}$. This capability is particularly useful in the areas without existing ground-level monitoring capabilities (Liu et al., 2005). The use of satellite-based air pollution

information may also help in reconfiguring and refining existing ground monitoring networks. It could serve as an important extension of ground measurement networks by providing an independent and supplemental data source to in-situ monitoring. However, the satellite remote sensing cannot be used to replace the compliance monitoring network since the coverage is not guaranteed due to the cloud cover and a narrow observation time window. By examining the trajectory over which air packets travel on days when the source strength is high for a given source category, it is possible to find potential locations of sources. Whereas source apportionment can effectively identify the source type of air pollutants (e.g., coal burning, biomass burning, or crustal sources), and back trajectory analysis can point to the direction where the pollutants come from. Since additional geospatial data are required, the source location identify is not included in this study.

Figure 8-1 (a) shows an undulation on $PM_{2.5}$ concentrations in Beijing. There is a slight decrease from 2001 to 2004, then a dramatic increase to the peak in 2006. After that, there is a decrease again from 2006 to 2009, and then a slight increase again. This can be explained by economic growth and industry emission in China. With the economic boom after 2000, emissions from industry increased dramatically. Black carbon (BC) and organic carbon (OC) emissions increased by 46 % and 33 % to 1.85 Tg and 4.03 Tg in 2010. SO_2 emissions first increased by 61 % to 34.0 Tg in 2006, and then decreased by 9.2 % to 30.8 Tg in 2010 due to the control measures, such as wide application of flue-gas desulfurization (FGD) equipment in power plants. The annual average SO_2 emission is 22.58 Tg during 2005 – 2011, which is 85 % contribution from industry emission (The World Bank, 2012). Since 2005, when a "Resource Efficient and Environment-Friendly (REEF) Society" concept was first integrated into China's development strategy in the Eleventh Five Year Plan for National Economic and Social Development (2006 - 2010), the Chinese government has achieved a 19.1 % reduction in countrywide energy-use intensity from 2005 levels (NDRC, 2011). This change is general consistent with the $PM_{2.5}$ concentration changes in Beijing.

Figure 8-1 (b) shows an increase from 2001 to 2004, then a monotonous decrease from 2004 to 2011 in Hong Kong. This is consistent with the change in Guangzhou

(Table 8-1), which implies the transport $PM_{2.5}$ from Guangzhou dominates the $PM_{2.5}$ concentrations in Hong Kong.

Figure 8-1 (c) and (d) shows irregular changes on $PM_{2.5}$ concentrations in New Delhi and Kolkata, which reveals the economic growth is not stable in India. Driven by the remarkable energy consumption growth and relatively lax emission controls, emissions increased by 70 %, 41 %, and 35 % to 8.81 Tg, 1.02 Tg, and 2.74 Tg in 2010 for SO_2, BC, and OC, respectively (The World Bank, 2012).

Figure 8-1 (e) shows the lower and stable $PM_{2.5}$ concentrations in Tokyo. Japan was the first Asian country to industrialize, and thus it was also the first to face air quality problems serious enough to encourage the formulation and implementation of policies to address the situation. In Japan, the annual average SO_2 emission is only 0.50 Tg during the same period. Strict control measures are the main reason of lower $PM_{2.5}$ concentration in Tokyo (The World Bank, 2012).

Figure 8-1 (f) shows an obvious decrease of $PM_{2.5}$ concentrations in Seoul. Newly industrialized country, the South Korea, is at a stage of development which is also beginning to reduce the ground-level $PM_{2.5}$ concentration since 2004. The Five-Year Plan for Green Growth with an investment component representing 2 % of the annual GDP is announced in 2009 (ESCAP and KOICA, 2012). This may explain the decrease trend of $PM_{2.5}$ concentration in Seoul.

8.6.2 Implications of health impact assessment

Despite the low R^2 values are found, an overall trend is observed, with years and counties (or cities) that have higher levels of $PM_{2.5}$ concentration also having higher lung cancer incidence rates. The associations between $PM_{2.5}$ concentration and lung cancer incidence rates provide limited evidence that $PM_{2.5}$ exposure potentially contributes to lung cancer incidence and are consistent with previous studies that have reported an association between $PM_{2.5}$ exposure and lung cancer mortality (Pope et al., 2002; Jerrett et al., 2005; Laden et al., 2006; Naess et al., 2007; Nawrot et al., 2007; Krewski et al., 2009).

The low R^2 values represent the multifaceted factors that contribute to lung cancer incidence. $PM_{2.5}$ is not likely to be the sole etiologic agent responsible for increased lung cancer incidence rates. The high variability demonstrates that tobacco smoking and other factors are also contributing to lung cancer incidence rates. However, the results presented above support an association between $PM_{2.5}$ and lung cancer incidence. This study is an important contribution to the limited literature available on the association between $PM_{2.5}$ concentration and lung cancer incidence.

8.6.3 Regression analysis and discussion

The regression analysis reveals a significant relationship between the ground-level $PM_{2.5}$ concentration and economic growth. This explains the high ground-level $PM_{2.5}$ concentrations in developing countries, such as China (11-year average GDP growth rate 10.37 %) and India (11-year average GDP growth rate 7.46 %), and lower $PM_{2.5}$ concentrations in developed countries, such as Japan (11-year average GDP growth rate 0.65 %) and South Korea (11-year average GDP growth rate 4.13 %) (The World Bank, 2012). The weighted average economic growth rates of emerging economies represented by China and India in 2001 - 2011 were about two times of the world average (The World Bank, 2012). Especially, China has become the second largest economy in the world in the past decade. The rising China and India have been facing more development issues. One of them is the severe air pollution. As demonstrated in this study, the ground-level $PM_{2.5}$ concentrations in major cities of China and India exceed the WHO IT-1 level by 2.4 - 3 times. In contrast, Japan has a lower $PM_{2.5}$ concentration due to the formulation and implementation, the ground-level $PM_{2.5}$ concentration in Tokyo is well within the guideline suggested by the WHO. Same as the South Korea, the concept on Low Carbon, Green Growth was first proposed in 2008 and the Framework Act was enacted in 2010. Based on this act, the Government set a 30 % carbon emissions reduction target by 2020.

In response to the economic growth and the rapid expansion in industrial production, the energy consumptions have been increased. The share of energy use in China and India to the total world energy consumption increased from about 10 % in 1990 to 21 % in 2008 (IEA, 2010). Especially coal consumption, in China, the annual average coal consumption is 2.46 billion short ton during 2001 - 2010, which accounts for 37 % of the annual average coal consumption in the world. The annual average soot and dust

discharge is 10.05 Tg during 2005 - 2011, which is accounted for 80 % by industry discharge (Ministry of Environmental Protection of PRC, 2012b). The second larger annual average coal consumption is 0.54 billion short ton in India. In contrast, the annual average coal consumptions are 0.19 billion short ton in Japan, and 0.10 billion short ton in South Korea during 2001 - 2010 (The World Bank, 2012). The annual average soot and dust discharge is 0.05 Tg in Japan (Ministry of the Environment of Japan, 2012), which is 200 times lower than China. These data probably explain the higher $PM_{2.5}$ concentration in China and India, whereas lower $PM_{2.5}$ concentration in Japan and Korea, as see in Figure 8-2 to Figure 8-4.

Clearly, there are some other factors, such as transported pollutant from surrounding areas and meteorological condition, are also associated with the ground-level $PM_{2.5}$ concentration. They are not discussed in this paper.

8.6.4 Future trend prediction

Figure 8-3 shows that there are obvious decreasing trend since 2007 in Beijing and Figure 8-5 shows that Beijing has a decrease of 2 % since 2001. China's Twelfth Five Year Plan for National Economic and Social Development (2011 - 2015) built on the Eleven Five Year Plan' success by prioritizing new achievements in environmental protection and clean energy technology development. It also establishes landmark energy efficiency goals, striving to decrease China's energy-use intensity by 16 percent and carbon-emission per GDP by 17 percent from 2005 levels by 2015 (NDRC, 2012). All of these imply a definite decrease on $PM_{2.5}$ concentration in China in the future. This is agreement with the future trend prediction.

8.7 Summary

This chapter provided a case study of investigation of the ground-level $PM_{2.5}$ concentrations from the aerosol optical depths (AODs) retrieved by the MODIS and MISR satellite instrument in the extended East Asia. The GEOS-Chem model is used to relate AOD to ground-level $PM_{2.5}$ concentrations. The annual and 11-year (2001 - 2011) average ground-level $PM_{2.5}$ concentrations are evaluated for the extended East Asia. Good agreement is achieved when the satellite-derived annual average $PM_{2.5}$

concentrations are compared with the monitoring values or literatures in six major cities: Beijing, Hong Kong, New Delhi, Kolkata, Tokyo, and Seoul.

A number of interesting conclusions are found from the satellite-derived ground-level $PM_{2.5}$ concentration results, the health impact assessment, the regression analysis, and the future trend prediction.

i). The areas with $PM_{2.5}$ concentration exceeding the WHO IT-1 level (35 $\mu g/m^3$) are mostly located in the developing countries, such as China and India. The values higher than 100 $\mu g/m^3$ occur in the major industrial regions and the western desert area in China. In India, the highest $PM_{2.5}$ concentrations occur in the areas from New Delhi east-ward to Kolkata, with values of 60 - 110 $\mu g/m^3$. There are relatively lower $PM_{2.5}$ concentration in the developed countries, Japan and Korea.

ii). A correlation analysis is performed between the satellite-derived annual average $PM_{2.5}$ concentrations and lung cancer incidence rates in Beijing from 2001-2009. The positive association is found, which implies that the high $PM_{2.5}$ concentration is a reason for the high cancer incidence rates.

iii). The regression analysis reveals that there are significant correlations among the ground-level $PM_{2.5}$ concentration and the GDP growth rate, population growth rate and coal consumption in Beijing. By contrast, dust fall takes charge of relatively smaller scale of $PM_{2.5}$. The precipitation has a good effect on $PM_{2.5}$. Based on the regression equation, a sensitivity analysis is carried out and some mitigating measurements are proposed for Beijing.

iv). The future trend (2012 - 2015) prediction based on the regression equation and the considerations of various control measurements and possibilities concludes that it is difficult to reach the limit (35 $\mu g/m^3$) in 2016 when the new ambient air quality standards are implemented in Beijing.

Chapter 9 Conclusions and Recommendations

9.1 Conclusions

This thesis was dedicated to explore the new spatial information technology for air pollution risk assessment. GIS, satellite remote sensing (RS) and air quality modeling are the main research objectives, and fuzzy aggregation is extended to assess the air pollution risk. A series of research works are implemented, which are summarized as follows:

(a) A spatial GIS-based multi-source and multi-box (GMSMB) air quality modeling approach has been developed through a novel integration of an improved spatial multi-box model with a multi-source and multi-grid Gaussian model. It extends the traditional box model to consider point and mobile sources for regional air quality prediction with local characteristics. The main chemical interactions and physical removal mechanisms of pollutants in the atmosphere are taken into account in GMSMB. Particularly, GMSMB is developed within the GIS environment through a fully-coupled mode which allows the spatial analysis on both regional and local scales, and enhances the spatial representation as all GIS functions and spatial database can be directly accessed. The developed modeling approach, through an integrated and object-oriented simulation environment, allows more detailed investigations of the spatial variations of emission sources, meteorological conditions, complex terrain, as well as their impacts on the ambient air quality. A case study for the state of California is performed to evaluate the developed modeling approach. The concentration distributions of four criteria pollutants (CO, NO_2, SO_2 and $PM_{2.5}$) in the study area are predicted using GMSMB and traditional box model. The results from both GMSMB and traditional box model are compared with the monitoring data. The results show that the modeling results from GMSMB are more consistent with the monitoring values and other local observations compared to that from the traditional box model. It confirms that the traditional box model has limitation on assessing point and mobile emission sources. Further error analysis shows the GMSMB modeling results meet the field scale model performance guideline. This case

study illustrates the developed modeling approach GMSMB is an exploration that technically combines the point source dispersion model with the multi-box based spatial modeling system in GIS framework. The case study demonstrates that GMSMB has a sound performance for predicting airborne pollutant concentration distributions though quantifying the complex interactions between sources and receptors with spatial geo-referenced data. The modeling results from GMSMB can deliver an effective air pollution assessment to support decision making on air pollution control and management planning.

(b) Based on the validation of the GMSMB modeling results, a fuzzy aggregation-ordered weighted averaging (OWA) risk assessment approach is developed and applied to the case study for the state of California. This approach is used to quantify the integrated risk associated with multiple pollution factors based on the spatially gridded four criteria pollutant concentrations predicted by GMSMB. The comparisons with the AQI statistic report and other statistical analysis have illustrated the developed fuzzy aggregation-OWA method has advantages on quantifying the uncertainties of integrative impact associated with multiple pollution factors. The fuzzy aggregation-OWA approach has provided an effective, systematic and more realistic way for combining and comparing fuzzy quantities to achieve reliable integrated risk assessment results.

(c) To further evaluate the GMSMB modeling approach, a satellite remote sensing data analysis method is explored. The ground-level NO_2 concentrations are derived from the satellite OMI tropospheric NO_2 vertical column densities (VCDs) based on the global 3-D chemical transport model GEOS-Chem for the state of California. The results are cross-verified by an intercomparison with the GMSMB modeling results and the local in-situ surface measurements. The OMI tropospheric NO_2 vertical column densities and the OMI-derived ground-level NO_2 concentrations correlate well with the in-situ surface measurements spatially and temporally for location coverage and seasonal variations. It indicates that the satellite derived data could make up for the limited monitoring stations on the ground and quantitatively monitor the regional transport and fate of NO_2. The OMI-derived ground-level NO_2 concentrations are also in line with the GMSMB modeling results, suggesting that it is possible to apply satellite derived data in effective air quality model validations.

(d) To further explore satellite remote sensing technology for air quality assessment, an improved aerosol optical depth (AOD) retrieval algorithm is developed for the MODIS satellite instrument at 1-km resolution over the city of Montreal, Canada in 2009. The satellite-derived annual mean ground-level $PM_{2.5}$ concentrations are ranging from 1 to 14 $\mu g/m^3$ in Montreal which are in line with the results from literatures. The estimates are in good agreement ($r = 0.90$, slope = 0.9724 ± 0.0035, intercept = 0.2747 ± 0.0012) with the in-situ surface measurements at all monitoring stations, which are much better than the $PM_{2.5}$ concentrations derived from the standard MODIS 10-km AOD products compared with the in-situ surface measurements ($r = 0.80$, slope = 0.6407 ± 0.0003, intercept = 2.8871 ± 0.0065). All of these validate the $PM_{2.5}$ results derived from the AODs retrieved in this study at 1-km resolution. This also indirectly validates the developed AOD retrieval algorithm.

(e) Since the highest $PM_{2.5}$ concentrations in the world have been identified in the East Asia and India, a case study of investigating the ground-level $PM_{2.5}$ concentrations is also performed for the extended East Asia by applying the local scaling factors obtained from the GEOS-Chem model to the MODIS and MISR combined columnar AODs. The annual and 11-year mean ground-level $PM_{2.5}$ concentrations are evaluated for the period of 2001-2011. Good agreement is achieved when the satellite-derived annual mean $PM_{2.5}$ concentrations are compared with the monitoring values or literatures in six major cities: Beijing, Hong Kong, New Delhi, Kolkata, Tokyo, and Seoul. A number of interesting conclusions are found from the health impact assessment, regression analysis, and the future trend prediction, which are useful for understanding the air pollution situations and their health impact in these areas. The mitigating measurements and future trend prediction based on the regression analysis have some guiding significances for the air quality management in these areas.

In conclusion, the research works presented in this thesis have demonstrated that it is possible to apply the new spatial information technology in effective air quality assessment and management. A number of results indicate that a multi-disciplinary consideration of the GIS, dynamic satellite data analysis, air quality modeling, and in-

situ measurements provides the best solutions for air pollution exposure assessment and effectively supports the regional air pollution control management.

9.2 Contributions

This thesis explored the applications of new spatial information technology for air pollution assessment. Several specific contributions in this thesis are summarized as follows:

i). Developed a spatial GIS-based multi-source and multi-box (GMSMB) air quality modeling approach through a novel integration of an improved spatial multi-box model with a multi-source and multi-grid Gaussian model. It extends the traditional box model to consider point and mobile sources for regional air quality prediction with local characteristics. Particularly, GMSMB is developed within the GIS environment through a fully-coupled mode which is an important contribution to the limited literature available on the integrating air quality modeling with GIS.

ii). Developed a fuzzy aggregation-OWA approach for air pollution risk assessment. A degree of fuzziness is incorporated into the assessment criterion by using fuzzy sets and thereby avoiding absolute criterion. The integrated impact and relative importance of various pollution factors are aggregated with the considerations of uncertainties in evaluation criterion and multiple pollutant impacts. The fuzzy aggregation-OWA approach has provided an effective, systematic and more realistic way for combining and comparing fuzzy quantities to achieve reliable integrated risk assessment results to support decision making on air quality control and management planning.

iii). Explored the OMI tropospheric NO_2 column retrievals for monitoring ground level NO_2, with related uncertainties analysis including results variations among different methods and regional and seasonal biases in tropospheric NO_2 column retrievals. The intercomparison study reveals that a multi-disciplinary consideration of dynamic satellite data analysis, meteorology, pollutants' fate and transport, air quality modeling, and in-situ measurements provides more insights and better solutions for air pollution exposure assessment.

iv). Developed an improved aerosol optical depth (AOD) retrieval algorithm for the MODIS satellite instrument at 1-km resolution. The results are much better than the standard MODIS 10-km AOD products on spatial resolution and accuracy, which reveals that the method developed in this thesis can retrieve satellite-observed AODs at a higher spatial resolution than previously and can operate on an urban scale for $PM_{2.5}$ assessment. This extends the applications of MODIS AOD data from global or regional scales to local even urban scale.

v). Investigated the ground-level $PM_{2.5}$ concentrations using satellite-retrieved AODs for the extended East Asia. The corresponding health impact is analyzed which is an important contribution to the limited literature available on the association between $PM_{2.5}$ concentration and lung cancer incidence. A first research of year-by-year trends with up-to-date activity rates and regression analysis with influential factors is performed for the East Asia and India, which could be a guide for regional air pollution control management.

9.3 Recommendations for Future Work

The further studies will focus on the exploration of new technologies of satellite data analysis for regional and local air quality assessment. The related uncertainties in retrievals of satellite observations will be further investigated to improve the accuracy in tropospheric NO_2 column density and aerosol optical depth (AOD). This will specifically focus on the tropospheric air mass factor (AMF), the local NO_2 profile, and the aerosol optical depth (AOD) retrieval algorithm. The high-resolution cloud fraction and surface albedo maps, the snow-detection algorithm to differentiate cloudy from cloud-free pixels will be helpful (Deneke et al., 2008). More case studies are needed to improve and extend the developed approach in this study.

In addition, the developed GMSMB modeling system, the ground-level NO_2 assessment from satellite tropospheric NO_2 column density, the $PM_{2.5}$ assessment from the satellite aerosol optical depth (AOD) and the fuzzy aggregation risk assessment approach can be integrated into a unified air quality assessment system with a user-friendly graphics interface.

References

Abdou, W.A Diner, D.J., Martonchik, J.V., et al. 2005. Comparison of coincident Multiangle Imaging Spectroradiometer and Moderate Resolution Imaging Spectroradiometer aerosol optical depths over land and ocean scenes containing Aerosol Robotic Network sites. Journal of Geophysical Research 110(D10).

Ackerman, S.A., Strabala, K.L., Menzel, W.P., Frey, R.A., Moeller, C.C., Gumley, L.E. 1998. Discriminating clear sky from clouds with MODIS. Journal of Geophysical Research 103(D24), 32141–32157.

Alexander, B., Savarino, J., Lee, C.C.W., Park, R.J., Jacob, D.J., Thiemens, M.H., Li, Q.B., Yantosca, R.M. 2005. Sulfate formation in sea-salt aerosols: Constraints from oxygen isotopes. Journal of Geophysical Research 110(D10), D10307.

Al-Saadi, J., Szykman, J., Pierce, R.B., Kittaka, C., Neil, D., Chu, D.A., et al. 2005. Improving National Air Quality Forecasts with Satellite Aerosol Observations. Bulletin of the American Meteorological Society 86, 1249–1261.

Appel, K.W., Gilliland, A.B., Sarwar, G., Gilliam, R.C. 2007. Evaluation of the community multi-scale air quality (CMAQ) model version 4.5: Sensitivities impacting model performance, Part I-ozone. Atmospheric Environment 41, 9603-9615.

Arystanbekova, N.K. 2004. Application of Gaussian Plume Models for Air Pollution Simulation at Instantaneous Emissions. Mathematics and Computers in Simulation 67, 451-458.

Asrar, G., Dozier, J. 1994. EOS: Science Strategy for the Earth Observing System. American Institute of Physics, Woodbury, NY. pp. 119.

Ayres, J., Maynard, R., Richards, R. 2006. Air Pollution and Health, Imperial College Press, London, pp. 20-24.

Aumont, B., Chervier, F., Laval, S. 2003. Contribution of HONO Sources to The NO_x /HOx/O_3 Chemistry in The Polluted Boundary Layer. Atmospheric Environment 37, 487-498.

Austin, J., Brimblecombe, P., Sturges, W. 2002. Air Pollution Science for the 21th Century. Elsevier Science Ltd. New York.

Baertsch-Ritter, N., Prevot, A.S.H., Dommen, J., Andreani-Aksoyoglu, S., Keller, J. 2003. Model Study with UAMV in The Milan Area During PIPAPO: Simulations with Changed Emissions Compared to Ground and Airborne Measurements. Atmospheric Environment 37, 4133-4147.

Barone, G., Ambra, P.D., Serafino, D., Giunta, G., Murli, A., Riccio, A. 2000.

Application of A Parallel Photochemical Air Quality Model to the Campania Region (Southern Italy). Environmental Modelling and Software 15, 503-511.

Batty, M., Xie, Y. 1994. Modeling Inside GIS: Part 1. Model Structures, Exploratory Spatial Data Analysis and Aggregation. International Journal of Geographical Information Systems 8, 291-307.

Beelen, R., Marita Voogt, M., Duyzer, J., Zandveld, P., Hoek, G. 2010. Comparison of the performances of land use regression modelling and dispersion modelling in estimating small-scale variations in long-term air pollution concentrations in a Dutch urban area. Atmospheric Environment 44, 4614-4621.

Beijing Government, 2011. Beijing Clean Air Action Plan (2011-2015 Air Pollution Control Measures).

Beijing Municipal Environmental Protection Bureau, 2001-2011. Beijing Environmental Statement, 2001-2011.

Beijing Municipal Health Bureau, 2012. Available at: http://english.bjhb.gov.cn/ (accessed in December, 2012).

Beijing Cancer Hospital, 2012. Available at: http://www.bjcancer.org/English/Service.html (accessed in December, 2012).

Beijing Municipal Environmental Protection Bureau, Beijing Municipal Development and Reform Commission, 2011. Beijing Environmental Protection and Construction Plan in 12th Five-Year Period.

Beijing Municipal Bureau of Statistics, 2001-2011. Beijing Statistical Yearbook, 2001-2011.

Beliakov, G., Pradera, A., Calvo, T. 2007. Aggregation Functions: A Guide for Practitioners. Springer-Verlag, Berlin, Heidelberg.

Bey, I., Jacob, D.J., Yantosca, R.M., Logan, J.A., Field, B.D., Fiore, A.M., Li, Q., Liu, H.Y., Mickley, L.J., Schultz, M.G. 2001. Global modeling of tropospheric chemistry with assimilated meteorology: Model description and evaluation. Journal of Geophysical Research 106, 23073-23095.

Bezy, J.L., Delwart, S., Rast, M. 2000. MERIS – a new generation of ocean colour sensor onboard ENVISAT. ESA Bulletin 103, 48-56.

Bhattacharya, J., Chaulya, S.K., Oruganti, S.S. 2000. Probabilistic health risk assessment of industrial workers exposed to the air pollution. Practice Periodical of Hazardous, Toxic, Waste Management 4(4), 148–155.

Blond, N., Boersma, K.F., Eskes, H.J., van der A, R.J., Van Roozendael, M., De Smedt, I., Bergametti, G., Vautard, R. 2007. Intercomparison of SCIAMACHY nitrogen

dioxide observations, in-situ measurements and air quality modeling results over Western Europe. Journal of Geophysical Research 112(103111), 1-20.

Boersma, K.F., Eskes, H.J., Dirksen, R.J., van der A, R.J., Veefkind, J.P., Stammes, P., Huijnen, V., Kleipool, Q.L., Sneep, M., Claas, J., Leitao, J., Richter, A., Zhou, Y., Brunner, D. 2011. An improved tropospheric NO_2 column retrieval algorithm for the ozone monitoring instrument. Atmospheric Measurement Techniques 4, 1905-1928.

Boersma, K.F., Jacob, D.J., Trainic, M., Rudich, Y., DeSmedt, I., Dirksen, R., et al. 2009. Validation of urban NO_2 concentrations and their diurnal and seasonal variations observed from the SCIAMACHY and OMI sensors using in-situ surface measurements in Israeli cities. Atmospheric Chemistry and Physics 9, 3867-3879.

Boersma, K.F., Jacob, D.J., Eskes, H.J., Pinder, R.W., Wang, J., van der A, R.J. 2008a. Intercomparison of SCIAMACHY and OMI tropospheric NO_2 columns: Observing the diurnal evolution of chemistry and emissions from space. Journal of Geophysical Research 113, 16-26.

Boersma, K.F., Jocob, D.J., Bucsela, E.J., Perring, A.E., Dirksen, R., van der A, R.J., Yantosca, R., Park, R.J., Wenig, M.O., Bertram, T.H., Cohen, R. 2008b. Validation of OMI tropospheric NO_2 observations during INTEX-B and application to constrain NO_x emissions over the eastern United States and Mexico. Atmospheric Environment 42, 4480-4497.

Boersma, K.F., Eskes, H.J., Veefkind, J.P., Brinksma, E.J., van der A, R.J., Sneep, M., van der Oord, G.H.J., Levelt, P.F., Stammes, P., Gleason, J.F., Bucsela, E.J. 2007. Near-real time retrieval of tropospheric NO_2 from OMI. Atmospheric Chemistry and Physics 7, 2103-2118.

Boersma, K.F., Eskes, H.J., Brinksma, E.J. 2004. Error analysis for tropospheric NO_2 retrieval from space. Journal of Geophysical Research 109, 1-20.

Boersma, K.F., Bucsela, E.J., Brinksma, E.J., Gleason, J.F. 2002. NO_2, in OMI Algorithm Theoretical Basis Document, OMI Trace Gas Algorithms, ATB-OMI-04, Version 2.0, vol. 4, edited by K. Chance, NASA Distributed Active Archive Centers, Greenbelt, Md.

Bond, T.C., Bhardwaj, E., Dong, R., Jogani, R., Jung, S., Roden, C., Streets, D.G., Trautmann, N.M. 2007. Historical emissions of black and organic carbon aerosol from energy-related combustion, 1850–2000. Global Biogeochem Cy., 21, GB2018, doi:10.1029/2006GB002840.

Boulet, D., Melancon, S. 2009. Environmental Assessment Report. Air Quality in Montréal. 2009 Annual Report. Ville de Montréal, Service des infrastructures, du transport et de l'environnement, Direction de'environnement et du développement durable, Division de la planification et du suivi environnemental, RSQA, pp. 8-12.

Bovensmann, H., Burrows, J.P., Buchwitz, M., Frerick, J., Noel, S., Rozanov, V.V., Chance, K.V., Goede, A.P.H. 1999. SCIAMACHY: Mission objectives and

measurement modes, Journal of Atmospheric Science 56, 127-150, doi:10.1175/1520-0469.

Brandmeyer, J.E. 2000. Coupling Environmental Models and Geospatial Data Processing; University of North Carolina at Chapel Hill publisher, Chapel Hill, pp. 230-235.

Brandmeyer, J.E., Karimi, H.A. 2000. Coupling methodologies for environmental models. Environmental Modelling and Software 15(5), 479-488.

Brewer, A.W., McElroy, C.T., Kerr, J.B. 1973. Nitrogen dioxide concentrations in the atmosphere. Nature 246, 129-133.

Briggs, G.A. 1984. Plume rise and buoyancy effects, in: Randerson, D (Ed.), Atmospheric Science and Power Production, US Department of Energy, Washington, pp. 327-366.

Brimicombe, A. 2010. GIS, environmental modeling and engineering, 2nd ed. Taylor and Francis Group, LLC. Boca Raton. U.S.

Brinksma, E.J., Pinardi, G., Volten, H., Braak, R., Richter, A., Schonhardt, A. 2008. The 2005 and 2006 DANDELIONS NO_2 and aerosol intercomparison campaigns. Journal of Geophysical Research 113, D16S46.

British Columbia Ministry of Environment. 2008. Guidelines for Air Quality Dispersion Modeling in British Columbia; Environmental Quality Branch, Air Protection Section: Victoria, British Columbia, Canada, pp.1-44.

Brook, J.R., Brunett, R.T., Dann, T.F., Cakmak, S., Goldberg, M.S., Fan, X., Wheeler, A.J. 2007. Further interpretation of the acute effect of nitrogen dioxide observed in Canadian time series studies. Journal of Exposure Science & Environmental Epidemiology 17, S36-S44.

Bucholtz, A. 1995. Rayleigh-scattering calculations for the terrestrial atmosphere. Applied Optics 34(15), 2765-2773.

Bucsela, E.J., Perring, A.E., Cohen, R.C., Boersma, K.F., Celarier, E.A., Gleason, J.F., Wenig, M.O., Bertram, T.H., Wooldridge, P.J., Dirksen, R., Veefkind, J.P. 2008. Comparison of tropospheric NO_2 from in-situ aircraft measurements with near-real-time and standard product data from OMI. Journal of Geophysical Research 113, 16-31.

Bucsela, E.J., Celarier, E.A., Wenig, M.O., Gleason, J.F., Veefkind, J.P., Boersma, K.F., Brinksma, E.J. 2006. Algorithm for NO_2 vertical column retrieval from the ozone monitoring instrument. IEEE Transactions on Geoscience Remote Sensing 44, 1245-1258.

Burrows, J.P., Holzle, E., Goede, A.P.H., Visser, H., Fricke, W. 1995. SCIAMACHY-scanning imaging absorption spectrometer for atmospheric chartography. Acta Astronautica 35, 445-451.

Burrows, J.P., Weber, M., Buchwitz, M., Rozanov, V., Ladstatter-Weissenmayer, A., Richter, A., DeBeek, R., Hoogen, R., Bramstedt, K., Eichmann, K., Eisinger, M., Perner, D. 1999. The Global Ozone Monitoring Experiment (GOME): mission concept and first scientific results. Journal of the Atmospheric Sciences 56, 151-175.

Burnett, R.T., Steib, D., Brook, J.R., Cakmak, S., Dales, R., Raizenne, M., Vincent, R., Dann, T. 2004. The short-term effects of nitrogen dioxide on mortality in Canadian cities. Archives of Environment Health 59, 228-237.

California Air Resources Board (CARB), 2009a. California Air Basin Map. Available at: http://www.census.gov/prod/cen2000/phc3-us-pt1.pdf (accessed in February 2010).

California Air Resources Board (CARB), 2009b. Air Emission Inventory Database. Available at: http://www.arb.ca.gov/app/emsinv/facinfo/facinfo.php (accessed April 2009).

California Air Resources Board (CARB), 2009c. AQMIS 2 - Air Quality and Meteorological Information System. Available at: http://www.arb.ca.gov/aqmis2 /aqmis2.php (accessed April 2009).

California Air Resources Board (CARB), 2009d. California Ambient Air Quality Standards (CAAQS). Available at: http://www.arb.ca.gov/research/aaqs/caaqs/caaqs.htm (accessed in February 2010).

Callies, J., Corpaccioli, E., Eisinger, M., Hahne, A., Lefebvre, A. 2000. GOME-2 - metop's second-generation sensor for operational ozone monitoring. European Space Agency Camara, A. Environmental Systems: A Multidimensional Approach. New York: Oxford Univ. Press. 2002.

Canepa, E., D'Alberti, F., D'Amati, F., Triacchini, G. 2007. The GIS-based SafeAirView software for the concentration assessment of radioactive pollutants after an accidental release. Science of the Total Environment 373, 32–42.

Canter, L.W. 1996. Environmental Impact Assessment, 2nd Edition. McGraw-Hill Book Company, New York,

Cangialosi, F., Intini, G., Liberti, L., Notarnicola, M., Stellacci, P. 2008. Health risk assessment of air emissions from a municipal solid waste incineration plant – A case study. Waste Management 28, 885–895.

Carnevale, C., Finzi, G., Pisoni, E., Volta, M., Guariso, G., Gianfreda, R., et al. 2012. An integrated assessment tool to define effective air quality policies at regional scale. Environmental Modelling and Software 38, 306–315.

Celarier, E.A., Brinksma, E.J., Gleason, J.F., Veefkind, J.P., Cede, A., Herman, J.R., et al. 2008. Validation of Ozone Monitoring Instrument nitrogen dioxide columns. Journal of Geophysical Research 113(D15S15), 1-23.

CCRS (Canada Centre for Remote Sensing), 2010. Normalized Difference Vegetation Index (NDVI). Available at: http://geogratis.cgdi.gc.ca/geogratis/ (accessed in August, 2012).

Chate, D.M., Murugavel, P., Ali, K., Tiwari, S., Beig, G. 2011. Below-cloud rain scavenging of atmospheric aerosols for aerosol deposition models. Atmospheric Research 99, 528-536.

Chance, K., Palmer, P.I., Spurr, R.J.D., Martin, R.V., Kurosu, T.P., Jacob, D.J. 2000. Satellite observations of formaldehyde over North America from GOME. Journal of Geophysical Research 27, 3461-3464.

Chen, Z., Huang, G.H., Chakma, A. 1998. Integrated environmental risk assessment for petroleum-contaminated sites—a North American case study. Water Science and Technology 38(4–5), 131–138.

Chen, Z., Huang, G.H., Chakma, A. 2003. Hybrid fuzzy-stochastic modeling approach for assessing environmental risks at contaminated groundwater systems. Journal of Environmental Engineering 129(1), 79–88.

Chu, D.A., Kaufman, Y., et al. 2003. Global monitoring of air pollution over land from the earth observing system-terra moderate resolution imaging spectroradiometer (MODIS). Journal of Geophysical Research 108(D21), 4661.

Cimorelli, A.J., Steven, G.P., Akula, V., Jeffrey, C.W., Robert, J.P., Robert, B.W., Russell, F.L., Warren, D.P., Roger, W.B., James, O.P. 2004. AERMOD: Description of Model Formulation (EPA-454/R-03-004). Technological report, US Environmental Protection Agency, Office of Air Quality Planning and Standards, Emissions Monitoring and Analysis Division, Triangle Park, NC.

Clarke, K.C., Parks, B.O., Crane, M.P. 2002. Geographic Information Systems and Environmental Modeling. Upper Saddle River, NJ, Prentice Hall.

Cornelis, C., Deschrijver, G., Nachtegael, M., Schockaert, S., Shi, Y. 2010. 35 Years of Fuzzy Set Theory. Springer-Verlag Berlin Heidelberg. pp. 4-14.

Cox, P., Delao, A., Komorniczak, A., Weller, R. 2009. The California Almanac of Emissions & Air Quality-2009 Ed. Chapter 1, 1-15; Chapter 2, 2-23. Air Resources Board of California EPA, Sacramento, California.

Crutzen, P.J. 1970. The influence of nitrogen oxides on the atmospheric ozone content. Quarterly Journal of the Royal Meteorological Society 96, 320-325.

Dai, J., Rocke, D.M. 2000. A Spatial Information Technology Based approach to spatial allocation of area source solvent emissions. Environmental Modelling and Software

15, 293-302.

Defra. 2007. The Air Quality Strategy for England, Scotland. Wales and Northern Ireland (Volume 1). HMSO. Available at: www.defra.gov.uk (accessed in April, 2009).

Dentener, F., Peter, W., Krol, M., van Weele, M., Bergamaschi, P., Lelieveld, J. 2003. Interannual variability and trend of OH and the lifetime of CH4: 1979–1993 global chemical transport model calculations. Journal of Geophysical Research 108, 4442.

Deneke, H.M., Feijt, A.J., Roebeling, R.A. 2008. Estimating surface solar irradiance from METEOSAT SEVIRI-derived cloud properties. Remote Sensing of Environment 112, 3131-3141.

Di Nicolantonio, W., Cacciari, A., Tomasi, C. 2009. Particulate matter at surface: Northern Italy monitoring based on satellite remote sensing, meteorological fields, and in-situ sampling. IEEE Journal of Selected Topics in Applied Earth Observations and Remote Sensing 2, 284-292.

Diner, D.J., Braswell, B.H., Davies, R., Gobron, N., Hu, J., Jin, Y., et al. 2005. The value of multiangle measurements for retrieving structurally and radiatively consistent properties of clouds, aerosols, and surfaces. Remote Sensing of Environment 97, 495–518.

Diner, D.J., Beckert, J.C., Reilly, T.H., Bruegge, C.J., Conel, J.E., Kahn, R.A., et al. 1998. Multi-angle Imaging Spectroradiometer (MISR) instrument description and experiment overview. IEEE Transactions on Geoscience and Remote Sensing 36, 1072-1087.

Drury, E., Jacob, D.J., Spurr, R.J.D., Wang, J., Shinozuka, Y., Anderson, B.E., Clarke, A.D., Dibb, J., McNaughton, C., Weber, R. 2010. Synthesis of satellite (MODIS), aircraft (ICARTT), and surface (IMPROVE, EPA-AQS, AERONET) aerosol observations over eastern North America to improve MODIS aerosol retrievals and constrain surface aerosol concentrations and sources. Journal of Geophysical Research-Atmospheres 115.

Drury, E., Jacob, D.J., Wang, J., Spurr, R.J.D., Chance, K. 2008. Improved algorithm for MODIS satellite retrievals of aerosol optical depths over western North America. Journal of Geophysical Research 113, D16204.

Duan, F.K., He, K., Ma, Y.L., Yang, F.M., Yu, X.C., Cadle, S.H., Chan, T., Mulawa, P.A. 2006. Concentration and chemical characteristics of PM2.5 in Beijing, China: 2001–2002. The Science of the Total Environment 355, 264–275.

Dunlea, E.J., Herndon, S.C., Nelson, D.D., Volkamer, R.M., San Martini, F., Sheehy, P.M., et al. 2007. Evaluation of nitrogen dioxide chemiluminescence monitors in a polluted urban environment. Atmospheric Chemistry and Physics 7, 2691-2704.

Economopoulou, A.A., Economopoulos, A.P. 2002. Air pollution in Athens basins and health risk assessment. Environmental Monitoring and Assessment 80, 277–299.

Edwards, D.P. 2006. Air quality remote sensing from space. Eos, Transactions American Geophysical Union 87(33), 327-338.

Elbir, T., Mangir, N., Kara, M., Simsir, S., Eren, T., Ozdemir, S. 2010. Development of a GIS-based decision support system for urban air quality management in the city of Istanbul. Atmospheric Environment 44, 441-454.

Engel-Cox, J., Hoff, R.M., Haymet, A.D.J. 2004. Recommendations on the use of satellite remote-sensing data for urban air quality. Journal of the Air and Waste Management Association 54, 1360-1371.

Engel-Cox, J., Hoff, R.M., Rogers, R., Dimmick, F., Rush, A.C., Szykman, J.J., et al. 2006. Integrating lidar and satellite optical depth with ambient monitoring for 3-dimensional particulate characterization. Atmospheric Environment 40, 8056.

Environment Canada. 2012. Air Quality and Health. Available at: http://www.ec.gc.ca/cas-aqhi/ (Accessed in March, 2012).

Environment Canada. 2009. National Pollutant Release Inventory, Tracking Pollution in Canada. Available at: http://www.ec.gc.ca/inrp-npri/ (Accessed in April, 2011).

Environment Canada. 2010. National Air Pollution Surveillance Program (NAPS). Available at: http://www.ec.gc.ca/rnspa-naps/ (Accessed in July, 2012).

Environmental Protection Department of Hong Kong, 2001-2011. Air Quality in Hong Kong 2001-2011. A report on the results from the Air Quality Monitoring Network (AQMN). Air Science Group, Environmental Protection Department, the Government of the Hong Kong Special Administrative Region. 2010. Available at: http://www.epd-asg.gov.hk/english/report/aqr.html (Accessed in July, 2012).

Environmental Protection Department of Hong Kong, 2009. Agreement No CE 57/2006 (EP) Review of Air Quality Objectives and Development of a Long Term Air Quality Strategy for Hong Kong - Feasibility Study. Final report.

Environment of Tokyo, 2011. The Environment of Tokyo 2011. Available at: http://www.kankyo.metro.tokyo.jp/en/documents/ (accessed in July, 2012).

Environmental organization Greenpeace, 2012. Dangerous breathing. $PM_{2.5}$: Measuring the human health and economic impacts on China's largest cities. Available at: http://www.greenpeace.org/eastasia/ (accessed in July, 2012).

Eskes, H.J., Boersma, K.F. 2003. Averaging kernels for DOAS total-column satellite retrievals. Atmospheric Chemistry and Physics 3, 1285-1291.

ERSI. An Overview of the Geodatabase. 2009. Available at: http://webhelp.esri.com/arcgisdesktop/9.3/ (accessed in April, 2009).

Eskes, H.J. 2003. Combined retrieval, modeling and assimilation approach to GOME NO_2, in GOA final report, European Commission 5th framework program. 1998-2002, EESD-ENV-99-2, 116-122, Eur. Comm., De Bilt, Netherlands.

ESCAP and KOICA, 2012. Low Carbon Green Growth Roadmap for Asia and the Pacific, Turning resource constraints and the climate crisis into economic growth opportunities. ST/ESCAP/2631, United Nations publication, Bangkok, ISBN: 978-974-680-329-8.

Fairlie, T.D., Jacob, D.J., Park, R.J. 2007. The impact of transpacific transport of mineral dust in the United States. Atmospheric Environment 125, 1-1266.

Fisher, B. 2003. Fuzzy environmental decision-making: applications to air pollution. Atmospheric Environment 37, 1865-1877.

Fotheringham, S.A., Wegener, M. 2000. Spatial Models and GIS: New Potential and New Models. CRC Press, Philadelphia, PA, pp. 11-13.

Friedemann, A. 2007. Lessons for California and the U.S. from movie "How Cuba survived Peak Oil". Culture Change. Available at: http://www.culturechange.org/cms/ (accessed April 20, 2009).

Gao, B., Kaufman, Y.J., Tanre, D., Li, R. 2002. Distinguishing tropospheric aerosols from thin cirrus clouds for improved aerosol retrievals using the ratio of 1.38 μm and 1.24 μm channels. Geophysical Research Letters 29(18), 361-364. DOI: 10.1029/2002GL015475.

Geddes, J.A., Murphy, J.G., O'Brien, J.M., Celarier, E.A. 2012. Biases in long-term NO_2 averages inferred from satellite observations due to cloud selection criteria. Remote Sensing of Environment 124, 210–216.

Gerboles, M., Lagler, F., Rembges, D., Brun, C. 2003. Assessment of uncertainty of NO_2 measurements by the chemiluminescence method and discussion of the quality objective of the NO_2 European Directive. Journal of Environmental Monitoring 5(4), 529-540.

Ghude, S.D., Van der A, R.J., Beig, G., Fadnavis, S., Polade, S.D. 2009. Satellite derived trends in NO_2 over the major global hotspot regions during the past decade and their inter-comparison. Environmental Pollution 157, 1873-1878.

Gillani, N.V., Godowitch, J.M. 2005. A plume-in-grid (PinG) technique of major point source emissions. EPA/600/R-99/030, Chapter 9.

Goodchild, M.F., Parks, B.O., Steyaert, L.T. 1993. Environmental Modeling with GIS. Oxford University Press, New York, pp. 96-138.

Goodchild, M.F., Steyaert, L.T., Parks, B.O., Johnston, C.A., Maidment, D.R., Crane, M.P., Glendinning, S. 1996. GIS and Environmental Modeling: Progress and Research Issues. John Wiley & Sons, New York, pp. 383-385.

Goodchild, M.F. 2003. Geographic Information Science and Systems for Environmental Management. Annual Review of Environment and Resources 28, 493-519.

Gulliver, J., Briggs, D. 2011. STEMS-Air: A simple GIS-based air pollution dispersion model for city-wide exposure assessment. Science of the Total Environment 409, 2419-2429.

Gupta, P., Christopher, S.A., Wang, J., Gehrig, R., Lee, Y., Kumar, N. 2006. Satellite remote sensing of particulate matter and air quality assessment over global cities. Atmospheric Environment 40, 5880-5892.

Gupta, P., Christopher, S.A. 2008. Seven year particulate matter air quality assessment from surface and satellite measurements. Atmospheric Chemistry and Physics 8, 3311–3324.

Hains, J.C., Boersma, K.F., Kroon, M., Dirksen, R.J., Cohen, R.C., Perring, A.E., Bucsela, E., et al. 2010. Testing and improving OMI DOMINO tropospheric NO_2 using observations from the DANDELIONS and INTEX-B validation campaigns. Journal of Geophysical Research 115(D05301), 1-20.

Han, Z.W. 2007. A Regional Air Quality Model: Evaluation and Simulation of O_3 and Relevant Gaseous Species in East Asia During Spring 2001. Environmental Modelling and Software 22, 1328-1336.

Hanna, S.R., Paine, R.J. 1989. Hybrid plume dispersion model (HPDM) development and evaluation. Journal of Applied Meteorology 28, 206-24.

Halla, J.D., Wagner, T., Beirle, S., Brook, J.R., Hayden, K.L., O'Brien, J.M., Ng, A., Majonis, D., Wenig, M.O., McLaren, R. 2011. Determination of tropospheric vertical columns of NO_2 and aerosol optical properties in a rural setting using MAX-DOAS. Atmospheric Chemistry and Physics 11, 12475-12498.

Hao, J., Wang, L., Shen, M., Li, L., Hu, J. 2007. Air quality impacts of power plant emissions in Beijing. Environmental Pollution 147, 401-408.

Harrop, D.O. 2002. Air Quality Assessment and Management: A Practical Guide, 1st ed. Taylor & Francis e-Library, New York.

Hatefi Afshar, I., Delavar, M.R. 2007. A GIS-based Air Pollution Modeling in Tehran. Environmental Informatics achieves 5, 557-566.

Hauglustaine, D.A., Granier, C., Brasseur, G.P., Megie, G. 1994. The importance of atmospheric chemistry in the calculation of radiative forcing on the climate system. Journal of Geophysical Research 99, 1173-86.

He, K., Yang, F., Ma, Y., Zhang, Q., Yao, X.H., Chan, C.K., Cadle, S.H., Chan, T., Mulawa, P.A. 2001. The characteristics of $PM_{2.5}$ in Beijing, China. Atmospheric Environment 35, 4959–4970.

Herman, J.R., Celarier, E.A. 1997. Earth surface reflectivity climatology at 340–380 nm from TOMS data. Journal of Geophysical Research 102, D23, 28 003–28 011.

Holmes, N.S., Morawska, L. 2006. A review of dispersion modelling and its application to the dispersion of particles: An overview of different dispersion models available. Atmospheric Environment 40, 5902-5928.

Horowitz, L.W. et al. 2003. A global simulation of tropospheric ozone and related tracers: Description and evaluation of MOZART, version 2. Journal of Geophysical Research 108(D24), 4784.

Huang, B., Jiang, B. 2002. AVTOP: A Full Integration of TOPMODEL into GIS. Environmental Modelling and Software 17, 261–268.

Huijnen, V., Eskes, H.J., Poupkou, A., et al. 2010. Comparison of OMI NO_2 tropospheric columns with an ensemble of global and European regional air quality models. Atmospheric Chemistry and Physics 10, 3273-3296.

IBM. 2012. SPSS software, Predictive analytics software and solutions. Available at: http://www-01.ibm.com/software/analytics/spss/ (Accessed in July, 2012).

International Energy Agency (IEA). 2010. Energy Statistics of Non-OECD Countries, Paris, France.

Interagency Monitoring of Protected Visual Environments (IMPROVE), 2010. IMPROVE Data Resources. Available at: http://vista.cira.colostate.edu/improve/Data/data.htm (accessed in February 2010).

Iliadis, L.S. 2005. A decision support system applying an integrated fuzzy model for long-term forest fire risk estimation. Environmental Modelling and Software 20, 613–621.

Isakov, V., Irwin, J.S., Ching, J. 2007. Using CMAQ for exposure modeling and characterizing the subgrid variability for exposure estimates. Journal of Applied Meteorology and Climatology 46, 1354-71.

Isakov, V., Venkatram, A. 2006. Resolving neighborhood scale in air toxics modeling: A case study in Wilmington, CA. Journal of the Air and Waste Management Association 56, 559–568.

Ishii, S., Bell, J.N.B., Marshall, F.M. 2007. Phytotoxic risk assessment of ambient air pollution on agricultural crops in Selangor State, Malaysia. Environmental Pollution 150, 267–279.

Ivanov, A.Y., Zatyagalova, V.V. 2008. A GIS approach to mapping oil spills in a marine environment. International Journal of Remote Sensing 29, 6297–6313.

Jacob, D. 1999. Introduction to Atmospheric Chemistry, 1st ed. Princeton University Press. ISBN 0-691-00185-5. pp. 75–85.

Jacob, D. 2000. Heterogeneous chemistry and tropospheric ozone. Atmospheric Environment 34, 2131-2159.

Jerrett, M., Burnett, R.T., Ma, R., Pope, C.A., Krewski, D., Newbold, K.B., et al. 2005. Spatial analysis of air pollution and mortality in Los Angeles. Epidemiology 16, 727-736.

Jorquera, H. 2002a. Air Quality at Santiago, Chile: A Box Modeling Approach I. Carbon Monoxide, Nitrogen Oxides and Sulfur Dioxide. Atmospheric Environment 36, 315–330.

Jorquera, H. 2002b. Air Quality at Santiago, Chile: A Box Modeling Approach II. $PM_{2.5}$, Coarse and PM_{10} Particulate Matter Fractions. Atmospheric Environment 36, 331-344.

Kahn, R.A., Li, W.H., Moroney, C., Diner, D.J., Martonchik, J.V., Fishbein, E. 2007a. Aerosol source plume physical characteristics from space-based multiangle imaging. Journal of Geophysical Research 112, D11205.

Kahn, R.A., Garay, M.J., Nelson, D.L., Yau, K.K., Bull, M.A., Gaitley, B.J., et al. 2007b. Satellite-derived aerosol optical depth over dark water from MISR and MODIS: Comparisons with AERONET and implications for climatological studies. Journal of Geophysical Research 112, doi:10.1029/2006JD008175.

Karimi, H.A., Houston, B.H. 1996. Evaluating strategies for integrating environmental models with GIS: Current trends and future needs. Computers, Environment and Urban Systems 20, 413-25.

Karnosky, D.F., Percy, K.E., Chappelka, A.H., Simpsonb, C., Pikkarainen, J. 2003. Air Pollution, Global Change and Forests in the New Millennium. Elsevier Ltd., Oxford, UK.

Kassianov, E.I., Ovtchinnikov, M. 2008. On reflectance ratios and aerosol optical depth retrieval in the presence of cumulus clouds. Geophysical Research Letters 35(6), DOI:10.1029/2008GL033231.

Kaufman, Y.J., Gobron, N., Pinty, B., Widlowski, J., Verstraete, M. 2002. Relationship between surface reflectance in the visible and mid-IR used in MODIS aerosol algorithm – theory. Geophysical Research Letters 29(23), 2116.

Kaufman, Y.J., Tanré, D. 1998. Algorithm for Remote Sensing of Tropospheric Aerosol From MODIS, NASA MOD04 product ATBD report.

Kaufman, Y.J., Tanré, D., Remer, L.A., Vermote, E.F., Chu, A., Holben, B.N. 1997. Operational remote sensing of tropospheric aerosol over land from EOS Moderate Resolution Imaging Spectroradiometer. Journal of Geophysical Research 102(14), 17051–17067.

Kaya, I., Kahraman, C. 2009. Fuzzy robust process capability indices for risk assessment of air pollution. Stochastic Environmental Research and Risk Assessment 23, 529–541.

Kelm, M., Yoshida, K. 1996. Metabolic Fate of Nitric Oxide and Related N-oxides. Methods in Nitric Oxide Research. Feelisch, M., Stamler. J.S. John Wiley and Sons, Chichester, pp. 47-58.

Kim, S.W., Heckel, A., McKeen, S.A., Frost, G.J., Hsie, E.Y., Trainer, M.K., et al. 2006. Satellite-observed U.S. power plant NO_x emission reductions and their impact on air quality. Geophysical Research Letters 33, doi:10.1029/2006GL027749.

King, M.D., Kaufman, Y.J., Tanré, D., Nakajima, T. 1999. Remote sensing of tropospheric aerosols from space: Past, present, and future. Bulletin of the American Meteorological Society 80(11), 2229–2259.

Klir, G.J., Yuan, B. 1995. Fuzzy Sets and Fuzzy Logic: Theory and Applications. Published by Prentice Hall, Upper Saddle River, NJ.

Koelemeijer, R.B.A., Homan, C.D., Matthijsen, J. 2006. Comparison of spatial and temporal variations of aerosol optical thickness and particulate matter over Europe. Atmospheric Environment 40(27), 5304-5315.

Koelemeijer, R.B.A., de Haan, J.F., Stammes, P., 2003. A database of spectral surface reflectivity in the range 335–772 nm derived from 5.5 years of GOME observations Journal of Geophysical Research 108, 28003-28011.

Knoema, 2012. Economic Outlook. 2012. Available at: http://knoema.com/OECDEO92/economic-outlook (accessed in June, 2012).

Kontos, A., Fassois, S., Deli, M. 1999. Short-term effects of air pollution on childhood respiratory illness in Piraeus, Greece, 1987–1992: nonparametric stochastic dynamic analysis. Environmental Research 81(4), 275–297.

Kramer, L.J., Leigh, R.J., Remedios, J.J., Monks, P.S. 2008. Comparison of OMI and ground-based in-situ and MAX-DOAS measurements of tropospheric nitrogen dioxide in an urban area. Journal of Geophysical Research 113, 16-39.

Krewski, D., Jerrett, M., Burnett, R.T., Ma, R., Hughes, E., Shi, Y., Turner, M.C., Pope, C.A., et al. 2009. Extended follow-up and spatial analysis of the American Cancer Society study linking particulate air pollution and mortality. Research report (Health Effects Institute) 140, 5-114; discussion 115-136.

Krzyzanowski, M., Kuna-Dibbert, B., Schneider, J. 2005. Health Eeffects of Ttransport-Related Air Pollution. NLM Classification: WA 754, World Health Organization (WHO), Denmark.

Kuhlwein, J., Wickert, B., Trukenmuller, A., Theloke, J., Friedrich, R. 2002. Emission modelling in high spatial and temporal resolution and calculation of pollutant

concentrations for comparisons with measured concentrations. Atmospheric Environment 36, 7-18.

Kumar, N., Chu, A., Foster, A. 2007. An empirical relationship between $PM_{2.5}$ and aerosol optical depth in Delhi metropolitan. Atmospheric Environment 41(21), 4492-4503.

Kumar, R., Joseph, A.E. 2006. Air pollution concentrations of $PM_{2.5}$, PM_{10} and NO_2 at ambient and Kerbsite and their correlation in metro city – Mumbai. Environmental Monitoring and Assessment 119, 191–199.

Laden, F., Schwartz, J., Speizer, F.E., Dockery, D.W. 2006. Reduction in fine particulate air pollution and mortality: Extended follow-up of the Harvard Six Cities study. American Journal of Respiratory and Critical Care Medicine 173, 667-672.

Lakhan, V.C. 2003. Advances in Coastal Modeling, Elsevier, San Diego, California, pp. 561-562.

Lamsal, L.N., Martin, R.V., van Donkelaar, A., Steinbacher, M., Celarier, E.A., Bucsela, E., Dunlea, E.J., Pinto, J.P. 2008. Ground-level nitrogen dioxide concentrations inferred from the satellite-borne ozone monitoring instrument. Journal of Geophysical Research 113(D16308).

Lamsal, L.N., Martin, R.V., van Donkelaar, A., Celarier, E.A., Bucsela, E.J., Boersma, K.F., et al. 2010. Indirect validation of tropospheric nitrogen dioxide retrieved from the OMI satellite instrument: Insight into the seasonal variation of nitrogen oxides at northern midlatitudes. Journal of Geophysical Research 115, D05302.

Lashmar, M., Cope, M. 1995. Development of a photochemical airshed model for Sydney, New South Wales, Australia. Mathematical and Computer Modelling 21, 85-97.

Lauer, A., Dameris, M., Richter, A., Burrows, J.P. 2002. Tropospheric NO_2 column: a comparison between model and retrieved data from GOME measurements. Atmospheric Chemistry and Physics 2, 67-87.

Lee, C.J., Brook, J.R., Evans, G.J., Martin, R.V., Mihele, C. 2011. Novel application of satellite and in-situ measurements to map surface-level NO_2 in the Great Lakes region. Atmospheric Chemistry and Physics 11, 11761–11775.

Lee, C.J., Martin, R.V., van Donkelaar, A., O'Byrne, G., Krotkov, N., Richter, A., Huey, G., Holloways, J.S. 2009. Retrieval of vertical columns of sulfur dioxide from SCIAMACHY and OMI: Air mass factor algorithm development and validation. Journal of Geophysical Research 114, D22303.

Lee, K.H., Kim, Y.J., von Hoyningen-Huene, W., Burrow, J.P. 2007. Spatio-temporal variability of atmospheric aerosol from MODIS data over Northeast Asia in 2004. Atmospheric Environment 41(19), 3959–3973.

Leitao, J., Richter, A., Vrekoussis, M., Kokhanovsky, A., Zhang, Q.J., Beekmann, M., Burrows, J.P. 2010. On the improvement of NO_2 satellite retrievals-aerosol impact on the airmass factors. Atmospheric Measurement Techniques 3, 475-493.

Leonard, M.L. 2010. Air Dispersion Modeling Guidelines for Air Quality Permitting. City of Albuquerque Environmental Health Department, Air Quality Division Permitting and Technical Analysis Section, Albuquerque, New Mexico, USA.

Lepeule, J., Laden, F., Dockery, D., Schwartz, J. 2012. Chronic exposure to fine particles and mortality: an extended follow-up of the Harvard Six Cities Study from 1974 to 2009. Environmental Health Perspectives 120(7), 965.

Levelt, P.F., van denOord, G.H.J., Dobber, M.R., Malkki, A., Visser, H., de Vries, J., Stammes, P., Lundell, J.O.V., Saari, H. 2006. The ozone monitoring instrument. IEEE Transactions on Geoscience Remote Sensing 44, 1093-1101.

Leue, C., Wenig, M., Wagner, T., Klimm, O., Platt, U., Jahne, B. 2001. Quantitative analysis of NO_2 emissions from GOME satellite image sequences. Journal of Geophysical Research 6, 5493-5505.

Levy, R.C., Remer, L.A., Mattoo, S., Vermote, E.F., Kaufman, Y.J. 2007a. Second-generation operational algorithm: retrieval of aerosol properties over land from inversion of moderate resolution imaging spectroradiometer spectral reflectance. Journal of Geophysical Research 112, D13211, DOI: 10.1029/2006JD007811.

Levy, R., Remer, L., Dubovik, O. 2007b. Global aerosol optical properties and application to Moderate Resolution Imaging Spectroradiometer aerosol retrieval over land. Journal of Geophysical Research 112, D13210, doi:10.1029/2006JD007815.

Li, C.C., Kai-Hon Lau, A., Mao, J.T., Chu, D.A. 2005a. Retrieval, validation, and application of the 1-km aerosol optical depth from MODIS measurements over Hong Kong. IEEE Transactions on Geoscience and Remote Sensing 43, 11.

Li, R., Remer, L., Kaufman, Y., Mattoo, S., Gao, B., Vermote, E. 2005b. Snow and ice mask for the MODIS aerosol products. IEEE Transactions on Geoscience and Remote Sensing 2(3), 306–310.

Li, H.L., Huang, G.H., Zou, Y. 2008. An integrated fuzzy-stochastic modeling approach for assessing health-impact risk from air pollution. Stochastic Environmental Research and Risk Assessment 22, 789–803.

Li, X.Z., Rao, R., Song, Y.H., Tan, Z.F. 2011. Beijing coal production and consumption and demand outlook. Energy of China 12.

Lin, C.H., Wu, Y.L., Chang, K.H., Lai, C.H. 2004. Method for locating influential pollution sources and estimating their contributions. Environmental Modeling and Assessment 9, 129-136.

Liu, P.G. 2009. Simulation of the Daily Average PM_{10} Concentrations at Ta-Liao with Box-Jenkins Time Series Models and Multivariate Analysis. Atmospheric Environment 43, 2104-2113.

Liu, K.F.R., Yu, C.W. 2009. Integrating case-based and fuzzy reasoning to qualitatively predict risk in an environmental impact assessment review. Environmental Modeling and Software 24, 1241–1251.

Liu, Y., Koutrakis, P., Kahn, R. 2007a. Estimating fine particulate matter component concentrations and size distribution using satellite-retrieved fractional aerosol optical depth: Part 1 – method development. Journal of the Air and Waste Management Association 57(11), 1351–1359.

Liu, Y., Koutrakis, P., Kahn, R., Turquety, S., Yantosca, R.M. 2007b. Estimating Fine Particulate Matter Component Concentrations and Size Distributions Using Satellite-Retrieved Fractional Aerosol Optical Depth: Part 2: a Case Study. Journal of the Air and Waste Management Association 57, 1360-1369.

Liu, Y., Sarnat, J.A., Kilaru, A., Jacob, D.J., Koutrakis, P. 2005. Estimating ground-level PM2.5 in the eastern United States using satellite remote sensing. Environmental Science and Technology 39(9), 3269–3278.

Liu, Y., Park, R.J., Jacob, D.J., Li, Q.B., Kilaru, V., Sarnat, J.A. 2004. Mapping annual average ground-level $PM_{2.5}$ concentrations using multiangle imaging spectroradiometer aerosol optical thickness over the contiguous United States. Journal of Geophysical Research 109, 22206.

Liu, X., Chance, K., Sioris, C.E., Kurosu, T.P., Spurr, R.J.D., Martin, R.V., et al. 2006. First directly retrieved global distribution of tropospheric column ozone from GOME: Comparison with the GEOS-CHEM model. Journal of Geophysical Research 111, D02308.

Longley, P.A., Batty, M. 1996. Spatial analyst: Modeling in a GIS Environment; John Wiley & Sons, New York, pp. 381-385.

Macdonald, K.M., Cheng, L., Olson, M.P. 1996. A Comparison of Box and Plume Model Calculations for Ssulphur Deposition and Flux in Alberta, Canada. Atmospheric Environment 30, 2969-2980.

Maguire, D., Batty, M., Goodchild, M.F. 2005. GIS, Spatial analyst, and Modeling. Redlands, CA, ESRI Press. pp. 480-502.

Malm, W.C. 2000. Spatial and Seasonal Patterns and Temporal Variability of Haze and its Constituents in the United States, Report III. Cooperative Institute for Research in the Atmosphere, Colorado State University.

Martin, E.P. 2011. Comparative Performance of Different Statistical Models for Predicting Ground-Level Ozone (O_3) and Fine Particulate Matter ($PM_{2.5}$)

Concentrations in Montréal, Canada. Master Thesis, Concordia University, Montréal, Québec, Canada.

Martin, R.V. 2008. Satellite remote sensing of surface air quality. Atmospheric Environment 42(34), 7823-7843.

Martin, R.V., Sioris, C.E., Chance, K., Ryerson, T.B., Bertram, T.H., Wooldridge, P.J., Cohen, R.C., Neuman, J.A., Swanson, A., Flocke, F.M. 2006. Evaluation of space-based constraints on global nitrogen oxide emissions with regional aircraft measurements over and downwind of eastern North America. Journal of Geophysical Research 111, D15308.

Martin, S.T., Hung, H.M., Park, R.J., Jacob, D.J., Spurr, R.J., Chance, D.K.V., Chin, M. 2004. Effects of the physical state of tropospheric ammonium-sulfate-nitrate particles on global aerosol direct radiative forcing. Atmospheric Chemistry and Physics 4, 183– 214.

Martin, R.V., Jacob, D.J., Chance, K., Kurosu, T.P., Palmer, P.I., Evans, M.J. 2003. Global inventory of nitrogen oxide emissions constrained by space-based observations of NO_2 columns. Journal of Geophysical Research 108, 4537-4548.

Martin, R.V., Chance, K., Jacob, D.J., Kurosu, T.P., Spurr, R.J.D., Bucsela, E., Gleason, J.F., Palmer, P.I., Bey, I., Fiori, A.M., Li, Q., Yantosca, R.M., Koelemeijer, R.B.A. 2002. An improved retrieval of tropospheric nitrogen dioxide from GOME. Journal of Geophysical Research 107(D20), 4437. doi:10.1029/2001JD001027.

Martonchik, J.V., Kahn, R.A., Diner, D.J. 2009. Retrieval of aerosol properties over land using MISR observations. In: Satellite Aerosol Remote Sensing Over Land (Kokhanovsky AA, de Leeuw G, eds). Springer, Berlin. pp. 267–291.

Matejicek, L., Engst, P., Janour, Z. 2006. A GIS-based approach to spatio-temporal analysis of environmental pollution in urban areas: A case study of Prague's environment extended by LIDAR data. Ecological Modelling 199, 261-277.

Menesguen, A., Cugier, P., Loyer, S., Brunier, A.V., Hoch, T., Guillaud, J.F., Gohin, F. 2007. Two- or Three-Layered Box-Models Versus Fine 3D Models for Coastal Ecological Modelling? A Comparative Study in the English Channel (Western Europe). Journal of Marine Systems 64, 47-65.

Meszaros, T., Haszpra, L., Gelencser, A. 2004. The Assessment of The Seasonal Contribution of The Anthropogenic Sources to The Carbon Monoxide Budget in Europe. Atmospheric Environment 38, 4147-4154.

Miao, J.F., Chen, D., Wyser, K. 2006. Modelling subgrid scale dry deposition velocity of O_3 over the Swedish west coast with MM5-PX model. Atmospheric Environment 40, 415-429.

Michael, S., Verkuilen, J. 2006. Fuzzy Set Theory: Applications in the Social Sciences. Sage Publications, Inc. Thousand Oaks, California.

Middleton, D.R. 1998. A New Box Model to Forecast Urban Air Quality: BOXURB. Environmental Monitoring and Assessment 52, 315-335.

Ministry of Environment & Forests Government of India, 2009. State of Environment Report India-2009. Available at: http://www.moef.gov.in, http://envfor.nic.in (accessed in June, 2012).

Ministry of Environment of Korea, 2011. 2011 Environment Statistical Yearbook. Available at: http://eng.me.go.kr/main.do (accessed in June, 2012).

Ministry of the Environment of Japan, 2012. Environmental Statistics 2012. Available at: http://www.env.go.jp/en/statistics/ (accessed in June, 2012).

Ministry of Environmental Protection of PRC, 2012a. Ambient Air Quality Standards. GB 3095-2012.

Ministry of Environmental Protection of PRC, 2012b. State of the Environment in China (2001-2011). Available at: http://jcs.mep.gov.cn/hjzl/zkgb/ (accessed in June, 2012).

Mishchenko, M.I., Dlugach, J.M., Yanovitskij, E.G., Zakharova, N.T. 1999. Bidirectional reflectance of flat optically thick particulate layers: an efficient radiative transfer solution and applications to snow and soil surfaces. Journal of Quantitative Spectroscopy and Radiative Transfer 63, 409-432.

Muller, F., Schlunzen, K. H., Schatzmann, M. 2000. Test of Two Numerical Solvers for Chemical Reaction Mechanisms in A 3D-Air Quality Model. Environmental Modelling and Software 15, 639-646.

Murphy, D., Fahey, D., Proffitt, M., Liu, S., Eubank, C., Kawa, S., Kelly, K. 1993. Reactive odd nitrogen and its correlation with ozone in the lower stratosphere and upper troposphere. Journal of Geophysical Research 98, 8751-8774.

Naess, O., Nafstad, P., Aamodt, G., Claussen, B., Rosland, P. 2007. Relation between concentration of air pollution and cause-specific mortality: Four-year exposures to nitrogen dioxide and particulate matter pollutants in 470 neighborhoods in Oslo, Norway. American Journal of Epidemiology 165, 435-443.

Natural Resources Canada (NRCan, 2010). The National Topographic System of Canada. Available at: http://www.nrcan.gc.ca/earth-sciences/ (accessed in June, 2011).

NSIDC (National Snow and Ice Data Center). 2010. Near-Real-Time SSM/I-SSMIS EASE-Grid Daily Global Ice Concentration and Snow Extent. Available at: http://nsidc.org/data/docs/daac/nise1_nise.gd.html (accessed in August, 2012).

National Development and Reform Commission (NDRC) People's Republic of China, 2011. China’s Eleven Five Year Plan for National Economic and Social Development (2005-2010).

National Development and Reform Commission (NDRC) People's Republic of China, 2012. China's Twelfth Five Year Plan for National Economic and Social Development (2011-2015).

NASA. 2012a. Goddard Space Flight Center Atmosphere Archive Level 1 and Atmosphere Archive and Distribution System (LAADS). Available at: http://ladsweb.nascom.nasa.gov/ (accessed in August, 2012).

NASA. 2012b. Processing, archiving, and distributing Earth science data at NASA Langley Research Center. Available at: http://edg.larc.nasa.gov/ (accessed in August, 2012).

NOAA (National Oceanic and Atmospheric Administration). 2010. Upper-Air Data. Available at: http://www.ncdc.noaa.gov/oa/upperair.html (accessed in April, 2009).

Noxon, J.F. 1975. Nitrogen dioxide in the stratosphere and troposphere measured by ground-based absorption spectroscopy. Science 189, 547-549.

NRCS (National Water & Climate Center). 2009. Wind rose data. Available at: http://www.wcc.nrcs.usda.gov/ (accessed in April, 2009).

Oanh, N.T.K., Zhang, B. 2004. Photochemical Smog Modeling for Assessment of Potential Impacts of Different Management Strategies on Air Quality of The Bangkok Metropolitan Region, Thailand. Journal of the Air and Waste Management Association 54, 1321-1338.

Oettl, D., Almbauer, R.A., Sturm, P.J., Pretterhofer, G. 2003. Dispersion modelling of air pollution caused by road traffic using a Markov Chain–Monte Carlo model. Stochastic Environmental Research and Risk Assessment 17(1), 58–76.

Ohara, T., Akimoto, H., Kurokawa, J., Horii, N., Yamaji, K., Yan, X., and Hayasaka, T. 2007. An Asian emission inventory of anthropogenic emission sources for the period 1980–2020. Atmospheric Chemistry and Physics 7, 4419–4444.

Ott, W.R. 1978. Environmental Indices: Theory and Practice. Ann Arbor Science Publishers, Michigan.

Owen, B., Edmunds, H.A., Carruthers, D.J., Singles, R.J. 2000. Prediction of total oxides of nitrogen and nitrogen dioxide concentrations in a large urban area using a new generation urban scale dispersion model with integral chemistry model. Atmospheric Environment 34, 397-406.

Palmer, P.I., Jacob, D.J., Chance, K., Martin, R.V., Spurr, R.J.D., Kurosu, T.P., Bey, I., Yantosca, R., Fiore, A., Li, Q. 2001. Air mass factor formulation for spectroscopic measurements from satellites: Application to formaldehyde retrievals from the Global Ozone Monitoring Experiment. Journal of Geophysical Research 106, 14539–14550.

Park, R.J., Jacob, D.J., Kumar, N., Yantosca, R.M. 2006. Regional visibility statistics in

the United States: Natural and transboundary pollution influences, and implications for the Regional Haze Rule. Atmospheric Environment 40, 5405-5423.

Park, R.J., Jacob, D.J., Field, B.D., Yantosca, R.M., Chin, M. 2004. Natural and transboundary pollution influences on sulfate-nitrate-ammonium aerosols in the United States: Implications for policy. Journal of Geophysical Research 109, D15204.

Park, R.J., Jacob, D.J., Chin, M., Martin, R.V. 2003. Sources of carbonaceous aerosols over the United States and implications for natural visibility. Journal of Geophysical Research 108, 4355.

Parrish, D.D., Liu, S.C., Hsie, E.Y., Trainer, M., Murphy, P.C., Buhr, M.P., et al. 1990. Systematic variations in the concentration of NO_x (NO plus NO_2) at Niwot Ridge, Colorado. Journal of Geophysical Research 95, 1817–1836.

Pedrycz, W., Gomide, F. 2007. Fuzzy Systems Engineering Toward Human-Centric Computing. John Wiley & Sons, Inc., Hoboken, New Jersey.

Peled, R. 2011. Air pollution exposure: Who is at high risk? Atmospheric Environment 45, 1781-1785.

Perry, S.G., Cimorelli, A.J., Paine, R.J., Brode, R.W., Weil, J.C., Venkatram, A., Wilson, R.B., Lee, R.F., Peters, W.D. 2005. AERMOD: A dispersion model for industrial source applications. Part II: Model performance against 17 field study databases. Journal of Applied Meteorology (1989-2005, after 2005, Journal of Applied Meteorology and Climatology) 44, 694-708.

Platnick, S, King, M.D., Ackerman, S.A., Menzel, W.P., Baum, B.A., Riedi, J.C., Frey, R.A. 2003. The MODIS cloud products: Algorithms and examples from Terra. IEEE Transaction Geosciences Remote Sensing 41, 459-473.

Platt, U. 1994. Differential optical absorption spectroscopy (DOAS), in Air Monitoring by Spectroscopic Techniques, Siegrist, M. W. (ed.), Chemical Analysis Series, Wiley, New York, 127, 27-84.

Platt, K.H. 2007. Chinese Air Pollution Deadliest in World. Available at: http://news.nationalgeographic.com/news/ (accessed in April, 2009).

Pleim, J., Venkatram, A., Yamartino, R.J. 1984. The Dry Deposition Model. ADOM/TADAP Model Development Program, Vol. 4. Ontario Ministry of the Environment, Rexdale, Qntario, Canada.

Pope, C.A., Dockery, D.W. 2006. Health Effects of Fine Particulate Air Pollution: Lines that Connect; Journal of the Air and Waste Management Association 56, 709-742.

Pope, C.A., Burnett, R.T., Thun, M.J., Calle, E.E., Krewski, D., Ito, K., Thurston, G.D. 2002. Lung cancer, cardiopulmonary mortality, and long-term exposure to fine particulate air pollution. American Medical Association 287, 1132-1141.

Remer, L.A., Kaufman, Y.J., et al. 2005. The MODIS aerosol algorithm, products, and validation. Journal of the Atmospheric Sciences 62(4), 947-973.

Remer, L.A., Tanre, D., Kaufman, Y.J., Levy, R., Mattoo, S. 2006. Algorithm for remote sensing of Tropospheric aerosol from MODIS: Collection 005, Product ID MOD04/MYD04 Ref. No. ATBD-MOD-96. Available at: http://modis-atmos.gsfc.nasa.gov/_docs/MOD04:-MYD04_ATBD_C005_revl.pdf (accessed in May, 2011).

Reshetin, V.P. 2008. Fuzzy assessment of human-health risks due to air pollution. International Journal of Risk Assessment and Management 9, 160–177.

Richter, A., Burrows, J.P. 2002. Tropospheric NO_2 for GOME measurements. Advances in Space Research 10, 1673-1683.

Richter, A., Eyring, V., Burrows, J.P., Bovensmann, H., Lauer, A., Sierk, B., Crutzen, P.J. 2004. Satellite measurements of NO_2 from international shipping emissions. Geophysical Research Letters 31, doi:10.1029/2004GL020822.

Richter, A., Burrows, J.P., N¨uß, H., Granier, C., Niemeier, U. 2005. Increase in tropospheric nitrogen dioxide over China observed from space. Nature, 437, 129-132.

Rix, M., Valks, P., Hao, N., Erbertseder, T., van Geffen, J. 2008. Monitoring of volcanic SO_2 emissions using GOME-2 satellite instrument. 1-4244-2547-1/08, IEEE.

Ryerson, T.B., Williams, E.J., Fehsenfeld, F.C. 2000. An efficient photolysis system for fast-response NO_2 measurements. Journal of Geophysical Research 105, 26447–26461.

Sadiqa, R., Husain, T. 2005. A fuzzy-based methodology for an aggregative environmental risk assessment: a case study of drilling waste. Environmental Modelling and Software 20, 33–46.

Sadiq, R., Tesfamariam, S. 2009. Environmental decision-making under uncertainty using intuitionistic fuzzy analytic hierarchy process (IF-AHP). Stochastic Environmental Research and Risk Assessment 23, 75–91.

Samoli, E., Aga, E., Touloumi, G., Nislotis, K., Forsberg, B., Lefranc, A., et al. 2006. Short-term effects of nitrogen dioxide on mortality: an analysis within the APHEA project. European Respiratory Journal 27(6),1129–1137.

Sasikala, K.R., Petrou, M. 2001. Generalized fuzzy aggregation in estimating the risk of desertification of a burned forest. Fuzzy Sets and Systems 118, 121–137.

Schaap, M., Apituley, A., Timmermans, R.M.A., Koelemeijer, R.B.A., de Leeuw, G. 2009. Exploring the relation between aerosol optical depth and $PM_{2.5}$ at Cabauw, the Netherlands. Atmospheric Chemistry and Physics 9, 909–925.

Schaub, D., Boersma, K.F., Kaiser, J.W., Weiss1, A.K., Folini1, D., Eskes, H.J., Buchmann, B. 2006. Comparison of GOME tropospheric NO_2 columns with NO_2 profiles deduced from ground-based in-situ measurements. Atmospheric Chemistry and Physics 6, 3211-3229.

Scire, J.S., Strimaitis, D.G., Yamartino, R.J. 2000. A User's Guide for the CALPUFF Dispersion Model (Version 5). Earth Tech Inc., Concard, Massachusetts.

Sehmel, G.A., Hodgson, W.H. 1978. A Model for Predicting Dry Deposition of Partic Environmental Surfaces. Battelle Pacific Northwest Laboratories, Richland, Washington.

Seinfeld, J.H., Pandis, S.N. 2006. Atmospheric Chemistry and Physics: From Air Pollution to Climate Change, 2nd ed. John Wiley and Sons Inc., Hoboken, New Jersey, pp. 900-1127.

Sheel, V., Lal, S., Richter, A., Burrows, J.P. 2010. Comparison of satellite observed tropospheric NO_2 over India with model simulations. Atmospheric Environment 44, 3314-3321.

Shindell, D.T., Faluvegi, G., Koch, D.M., Schmidt, G.A., Unger, N., Bauer, S.E. 2009. Improved Attribution of Climate Forcing to Emissions. Science 326 (5953), 716-718.

Shon, Z.H., Kim, K.H., Kim, M.Y., Lee, M. 2005. Modeling Study of Reactive Gaseous Mercury in The Urban Air. Atmospheric Environment 39, 749-761.

Shrouds, J.M. 2010. Air Quality Community of Practice Establishing Air Quality Background Concentration Levels for Projects State-of-the-Practice. American Association of State Highway and Transportation Officials (AASHTO), Center for Environmental Excellence, Washington, DC.

Skidmore, A.K., Prins, H. 2002. Environmental Modelling with GIS and Remote Sensing. New York, Taylor & Francis.

Smith, P.N. 1995. Environmental evaluation: fuzzy impact aggregation. Journal of Environmental and System 24(2), 191–204.

Solomon, S., Portmann, R., Sandres, W., Daniel, J.S., Madsen, W., Bartram, B., Dutton, E.G. 1999. On the role of nitrogen dioxide in the absorption of solar radiation. Journal of Geophysical Research 104(D10), 12047-12058.

Stammes, P., Sneep, M., de Haan, J.F., Veefkind, J.P., Wang, P., Levelt, P.F. 2008. Effective cloud fractions from the Ozone Monitoring Instrument: Theoretical framework and validation. Journal of Geophysical Research 113, D16S38.

Statistics Canada. 2012. 2011 Census. Statistics Canada Catalogue no. 92-142-XWE. Data updated October 24, 2012. Available at: http://geodepot.statcan.gc.ca/ (accessed in October, 2012).

Stein, A.F., Isakov, V., Godowitch, J., Draxler, R.R. 2007. A hybrid modeling approach to resolve pollutant concentrations in an urban area. Atmospheric Environment 41, 9410-9426.

Steyn, D.G., Rao, S.T. 2009. Air Pollution Modeling and Its Application XX. Published by Springer, Dordrecht, Netherlands.

Suutari, R., Amann, M., Cofala, J., Klimont, Z., Schöpp, W., Posch, M. 2001. From Economic Activities to Ecosystem Protection in Europe – An Uncertainty Analysis of Two Scenarios of the RAINS Integrated Assessment Model. CIAM/CCE Report, International Institute for Applied Systems Analysis, Laxenburg, Austria. Available at: http://www.iiasa.ac.at/rains (accessed in April, 2011).

Tsuang, B., Chen, C., Lin, C., Cheng, M., Tsai, Y., Chio, C., Pan, R., Kuo, P. 2003. Quantification on the source/receptor relationship of primary pollutants and secondary aerosols by a Gaussian plume trajectory model: Part II. case study. Atmospheric Environment 37, 3993-4006.

Turner, M.C., Krewski, D., Pope, C.A., Chen, Y., Gapstur, S.M., Thun, M.J. 2011. Long-term ambient fine particulate matter air pollution and lung cancer in a large cohort of never-smokers. American Journal of Respiratory and Critical Care Medicine 184(12), 1374–1381.

Uno, I., He, Y., Ohara, T., Yamaji, K., Kurokawa, J.I., Katayama, M., Wang, Z., Noguchi, K., Hayashida, S., Richter, A., Burrows, J.P. 2007. Systematic analysis of interannual and seasonal variations of model-simulated tropospheric NO_2 in Asia and comparison with GOME-satellite data. Atmospheric Chemistry and Physics 7, 1671-1681.

U. S. Census Bureau. 2011. 2010 Census Data. Available at: http://www.census.gov/2010census/data/ (accessed in May 2011).

U.S. Embassy. 2012. U.S Embassy Beijing Air Quality Monitor. Available at: http://beijing.usembassy-china.org.cn/070109air.html (accessed in May 2012).

USEPA (U.S. Environmental Protection Agency). 2012. National Ambient Air Quality Standards (NAAQS). Available at: http://www.epa.gov/air/criteria.html (accessed in April 2012).

USEPA (U.S. Environmental Protection Agency). 2011. The National Emissions Inventory. Available at: http://www.epa.gov/ttn/chief/net/2008inventory.html (accessed in March, 2012).

USEPA (U.S. Environmental Protection Agency). 2010a. Air Quality System (AQS) Database. Available at: http://www.epa.gov/air/data/aqsdb.html (accessed in April 2010).

USEPA (U.S. Environmental Protection Agency). 2010b. Air Quality Index Report. Available at: http://www.epa.gov/airquality/airdata/ad_rep_aqi.html (accessed in March, 2012).

USEPA (U.S. Environmental Protection Agency). 2009a. Air Quality Index (AQI) - A Guide to Air Quality and Your Health. Office of Air Quality Planning and Standards, Outreach and Information Division Research Triangle Park, NC. EPA-456/F-09-002.

USEPA (U.S. Environmental Protection Agency). 2009b. AQI Calculator: AQI to Concentration. Available at: http://www.airnow.gov/index.cfm (accessed in December, 2009).

USEPA (U.S. Environmental Protection Agency). 2007. EPA's 2007 Report on the Environment: Science Report. Office of Research and Development U.S. Environmental Protection Agency, Washington, DC. EPA/600/R-07 /045.

USEPA (U.S. Environmental Protection Agency). 2005. Revision to the Guideline on Air Quality Models: Adoption of a Preferred General Purpose (Flat and Complex Terrain) Dispersion Model and Other Revisions, Final Rule. Federal Register Vol. 70, No. 216 Rules and Regulations.

USEPA (U.S. Environmental Protection Agency). 1997. Guidance on Cumulative Risk Assessment. Science Policy Council, Washington, D. C. 20460.

USEPA (U.S. Environmental Protection Agency). 1992. Protocol for Determining the Best Performing Model (EPA-454/R-92-025). U.S. Environmental Protection Agency, Research Triangle Park, NC.

USEPA (U.S. Environmental Protection Agency). 1991. Guideline for Regulatory Applications of the Urban Airshed Model (EPA-450/4-91-013199). Office of Air Quality Planning and Standards, Research Triangle Park, NC.

USGS (U.S. Geological Survey) 2010. USGS seamless data warehouse. Available at: http://seamless.usgs.gov/ (accessed in May, 2010).

Vallero, D.A. 2008. Fundamentals of Air Pollution, Fourth Edition. Elsevier Inc. Oxford, UK.

van der A, R.J., Eskes, H.J., Van Roozendael, M., De Smedt, I., Blond, N., Boersma, F., et al. 2010. Algorithm Document Tropospheric NO_2. Tropospheric Emission Monitoring Internet Service (TEMIS). TEM/AD1/001, pp. 5-9.

van Donkelaar, A., Martin, R.V., Levy, R.C., da Silva, A.M., Krzyzanowski, M., Chubarova, N.E., Semutnikova, E., Cohen, A.J. 2011. Satellite-based estimates of ground-level fine particulate matter during extreme events: A case study of the Moscow fires in 2010. Atmospheric Environment 45, 6225-6232.

van Donkelaar, A., Martin, R.V., Brauer, M., Kahn, R.A., Levy, R.C., Verduzco, C. 2010. Global estimates of ambient fine particulate matter concentrations from satellite-based aerosol optical depth: development and application. Environmental Health Perspectives 118.

van Donkelaar, A., Martin, R.V., Leaitch, W.R., Macdonald, A.M., Walker, T.W., Streets, D.G., Zhang, Q., Dunlea, E.J., Jimenez, J.L., Dibb, J.E., Huey, L.G., Weber, R., Andreae, M.O. 2008. Analysis of aircraft and satellite measurements from the Intercontinental Chemical Transport Experiment (INTEX-B) to quantify long-range transport of East Asian sulfur to Canada. Atmospheric Chemistry and Physics 8, 2999-3014.

van Donkelaar, A., Martin, R.V., Park, R.J. 2006. Estimating ground-level $PM_{2.5}$ using aerosol optical depth determined from satellite remote sensing. Journal of Geophysical Research 111, 21201.

van Noije, T.P.C., Eskes, H.J., Dentener, F.J., Stevenson, D.S., Ellingsen, K., Schultz, M.G., et al. 2006. Multi-model ensemble simulations of 10 tropospheric NO_2 compared with GOME retrievals for the year 2000. Atmospheric Chemistry and Physics 6, 2943-2979.

Vautard, R., Martin, D., Beekmann, M., Drobinski, P., Friedrich, R., Jaubertie, A., et al. 2003. Paris Emission Inventory Diagnostics from ESQUIF Airborne Measurements and A Chemistry Transport Model. Journal of Geophysical Research 108(D17), 8564.

Veiga, M.M. 1995. An adaptive fuzzy model for risk assessment of mercury pollution in the Amazon. IEEE int. conf. syst. Man Lybernetics. Vancouver, B.C., Canada.

Velders, G.J.M., Granier, C., Portmann, R.W., Pfeilsticker, K., Wenig, M., Wagner, T., Platt, U., Richter, A., Burrows, J.P. 2001. Global tropospheric NO_2 column distributions: comparing three-dimensional model calculations with GOME measurements. Journal of Geophysical Research 106, 12643-12660.

Venkatram, A. 1980. Estimating the monin-obukhov length in the stable boundary layer for dispersion calculations. Boundary-Layer Meteorology 19, 481-485.

Venkatram, A., Brode, R., Cimorelli, A., Lee, R., Paine, R., Perry, S., Peters, W., Weil, J., Wilson, R. 2001. A complex terrain dispersion model for regulatory applications. Atmospheric Environment 35, 4211-4221.

Vermote, E.F., Kotchenova, S.Y., Ray, J.P. 2011. MODIS Surface Reflectance User's Guide. Available at: http://modis-sr.ltdri.org (accessed in March, 2011).

Vermote, E.F., Tanré, D., Deuze, J.L., et al. 1997. Second simulation of the satellite signal in the solar spectrum, 6S: An overview. IEEE Transactions Geoscience and Remote Sensing 35(3), 675-686.

Vienneau, D., de Hoogh, K., Briggs, D. 2009. A Spatial Information Technology Based method for modelling air pollution exposures across Europe. Science of the Total

Environment 408, 255-266.

Vineis, P., Hoek, G., Krzyzanowski, M., Vigna-Taglianti, F., Veglia, F., Airoldi, L., et al. 2006. Air pollution and risk of lung cancer in a prospective study in Europe. International Journal of Cancer 119, 169-174.

Vinikoor-Imler, L.C., Davis, J.A., Luben, T.J. 2011. An ecologic analysis of county-level $PM_{2.5}$ concentrations and lung cancer incidence and mortality. International journal of environmental research and public health 8(6), 1865-1871.

Vivanco, M. G.; Palomino, I.; Vautard, R.; Bessagnet, B.; Martin, F.; Menut, L.; Jimenez, S. 2009. Multi-Year Assessment of Photochemical Air Quality Simulation Over Spain. Environmental Modelling and Software 24, 63-73.

Viggiano, A.A., Ehlerding, A., Hellberg, F., Thomas, R.D., Zhaunerchyk, V., Geppert, W.D., et al. 2005. Rate constants and branching ratios for the dissociative recombination of CO_2. Journal of Chemical Physics 122, 226101.

Vlachokostas, C.H., Nastis, S.A., Achillas, C.H., Kalogeropoulos, K., Karmiris, I., Moussiopoulos, N., Chourdakis, E., Banias, G., Limperi, N. 2010. Economic damages of ozone air pollution to crops using combined air quality and GIS modelling. Atmospheric Environment 44, 3352-3361.

von Hoyningen-Huene, W., Kokhanovsky, A.A., Wuttke, M.W., et al. 2007. Validation of SCIAMACHY top-of-atmosphere reflectance for aerosol remote sensing using MERIS L1 data. Atmospheric Chemistry and Physics 7(1), 96-106.

von Hoyningen-Huene, W., Freitag, M., Burrows, J.B. 2003. Retrieval of aerosol optical thickness over land surfaces from top-of-atmosphere radiance. Journal of Geophysical Research 108(D9), 4260, doi:10.1029/2001JD002018.

Voldner, E.C., Barrie, L.A., Sirois, A. 1986. A literature review of dry deposition of oxides of sulphur and nitrogen with emphasis on long-range transport modelling in North America. Atmospheric Environment 20, 2101-2123.

Wang, B.Z., Chen, Z. 2013. A GIS-based multi-source and multi-box modeling approach (GMSMB) for air pollution assessment - A North American case study. Journal of Environmental Science and Health, Part A 48, 14-25.

Wang, J., Christopher, S.A. 2003. Intercomparison between satellite-derived aerosol optical thickness and PM2.5 mass: implications for air quality studies. Geophysical Research Letters 30(21), 2095. doi:10.1029/2003GL018174.

Wang, J., Xu, X.G., Spurr, R., Wang, Y.X., Drury, E. 2010a. Improved algorithm for MODIS satellite retrievals of aerosol optical thickness over land in dusty atmosphere: implications for air quality monitoring in China. Remote Sensing of Environment 114, 2575-2583.

Wang, X.N., Mallet, V., Berroir, J.P., Herlin, I. 2011. Assimilation of OMI NO_2 retrievals

into a regional chemistry-transport model for improving air quality forecasts over Europe. Atmospheric Environment 45, 485-492.

Wang, Z., Chen, L., Tao, J., Zhang, Y., Su, L. 2010b. Satellite-based estimation of regional particulate matter (PM) in Beijing using vertical-and-RH correcting method. Remote Sensing of Environment 114, 50–63.

Wark, K., Warner, C.F., Davis, W.T. 1997. Air Pollution: Its Origin and Control, 3rd Ed.. Addison-Wesley Publisher, New York, pp. 546-558.

Weaver, C., da Silva, A., Chin, M., Ginoux, P., Dubovik, O., Flittner, D., Zia, A., Remer, L., Holben, B., Gregg, W. 2007. Direct insertion of MODIS radiances in a global aerosol transport model. Journal of Atmospheric Science 64, 808 – 826.

Weijers, E.P., Khlystov, A.Y., Kos, G.P.A., Erisman, J.W. 2004. Variability of particulate matter concentrations along roads and motorways determined by a moving measurement unit. Atmospheric Environment 38, 2993-3002.

Weil, J. C., Venkatram, A., Wyngaard, J. C. 1988. Plume Rise. Lectures in Air Pollution Modeling, American Meteorological Society, 119-162.

Wesely, M.L., Doskey, P.V., Shannon, J.D. 2001. Deposition parameterizations for the Industrial Source Complex (ISC3) Model. Report to U.S. EPA, Argonne National Laboratory, Argonne, Illinois 60439.

Wesely, M.L., Hicks, B.B. 1977. Some factors that affect the deposition rates of sulfur dioxide and similar gases on vegetation. Journal of the Air Pollution Control Association 27, 1110-1116.

WHO (World Health Organization). 2009. Global health risks: mortality and burden of disease attributable to selected major risks. WHO Press, Geneva, Switzerland. pp. 11-52.

WHO (World Health Organization). 2006a. Health risk of particulate matter from long-range transboundary air pollution. Joint WHO/Convention Task Force on the health aspects of air pollution. Denmark: World Health Organization Europe, Publication E88189.

WHO (World Health Organization). 2006b. WHO Air quality guidelines for particulate matter, ozone, nitrogen dioxide and sulfur dioxide, Global update 2005, Summary of risk assessment. WHO Press, World Health Organization, Geneva, Switzerland.

WHO (World Health Organization). 2008. Air quality and health. Available at: http://www.who.int/mediacentre/ (accessed in April, 2010).

WMO (World Meteorological Organization). 2010. Scientific Assessment of Ozone Depletion: 2010, Executive Summary.

Winkler, S.L., Chock, D.P. 1996. Air Quality Predictions of the Urban Airshed Model

Containing Improved Advection and Chemistry Alogrithms. Environmental Science and Technology 30, 1163-1175.

Winker, D.M., Pelon, J.R., McCormick, M.P. 2003. The CALIPSO mission: Spaceborne lidar for observation of aerosols and clouds, in: Proceedings of the Lidar Remote Sensing for Industry and Environment Monitoring III Conference, Hangzhou, China. 4893, 1–11.

Wong, M.S., Lee, K.H., Nichol, J.E., Li, Z.Q. 2010. Retrieval of aerosol optical thickness using MODIS 500 × 500 m^2, a study in Hong Kong and the Pearl River Delta Region. IEEE Transactions on Geoscience and Remote Sensing 48, 8.

World Bank, 2012. Explore. Create. Share - Development Data. Available at: http://databank.worldbank.org/data/Home.aspx (accessed in February, 2010).

Yager, R.R. 1988. On ordered weighted averaging aggregation operators in multicriteria decision making. IEEE Transactions on Systems, Man, and Cybernetics, Part B: Cybernetics 18(1), 183–190.

Yantosca, B., Long, M., Payer, M., Cooper, M. 2011. GEOS-Chem v9-01-02 Online User's Guide. Available at: http://acmg.seas.harvard.edu/geos/doc/man/ (accessed in February, 2010).

Yale University. 2012. Environmental Performance Index. Available at: http://epi.yale.edu/ (accessed in February 2012).

Yang, F., Huang, L., Duan, F., Zhang, W., He, K., Ma, Y., Brook, J.R., et al. 2008. Carbonaceous species in $PM_{2.5}$ at a pair of rural-urban sites in Beijing. Atmospheric Chemistry and Physics Discussion 11, 8719–8746.

Yang, F., Tan, J., Zhao, Q., Du, Z., He, K., Ma, Y., Duan, F., Chen, G., Zhao, Q. 2011. Characteristics of $PM_{2.5}$ speciation in representative megacities and across China. Atmospheric Chemistry and Physics Discussion 11, 1025–1051.

Ying, Q., Lu, J., Allen, P., Livingstone, P., Kaduwela, P., Kleeman, M. 2008. Modeling Air Quality During the California Regional $PM_{10}/PM_{2.5}$ Air Quality Study (CRPAQS) Using the UCD/CIT Source-Oriented Air Quality Model – Part I. Base Case Model Results. Atmospheric Environment 42, 8954-8966.

Zadeh, L.A. 1965. Fuzzy sets. Information and Control 8, 338–353.

Zadeh, L.A. 1971. Similarity relations and fuzzy orderings. Information Sciences 3, 177–200.

Zadeh, L.A. 1972. A fuzzy set theoretic interpretation of linguistic hedges. Journal of Cybernetics and Information Science 2(3), 4–34.

Zadeh, L.A. 1975. Fuzzy logic and approximate reasoning. Synthese 30(1), 407–428.

Zadeh, L.A. 1999. Fuzzy sets as a basis for a theory of possibility. Fuzzy Sets and Systems 100(1), 9–34.

Zhang, Q., Streets, D.G., Carmichael, G.R., He, K.B., Huo, H., Kannari, A., et al. 2009. Asian emissions in 2006 for the NASA INTEX-B mission. Atmospheric Chemistry and Physics 9, 5131-5153. Available at: http://mic.greenresource.cn/intex-b2006 (accessed in May, 2012).

Zhao, P.S., Dong, F., He, D., Zhao, X.J., Zhang, W.Z., Yao, Q., Liu, H.Y. 2013. Characteristics of concentrations and chemical compositions for $PM_{2.5}$ in the region of Beijing, Tianjin, and Hebei, China. Atmospheric Chemistry and Physics Discussion 13, 863-901.

Zhao, X.J., Zhang, X., Xu, X., Xu, J., Meng, W., Pu, W. 2009. Seasonal and diurnal variations of ambient $PM_{2.5}$ concentration in urban and rural environments in Beijing. Atmospheric Environment 43(18), 2893-2900.

Zhou, Y., Brunner, D., Boersma, K.F., Dirksen, R., Wang, P. 2009. An improved tropospheric NO_2 retrieval for satellite observations in the vicinity of mountainous terrain. Atmospheric Measurement Techniques Discussions 2, 781–824.

Zimmermann, H.J. 1992. Fuzzy Set Theory and Its Applications, second revised ed. Kluwer Academic Publishers, Norwell, Massachusttes, USA.

APPENDIX A Comparisons of annual mean NO_2 ground-level concentrations among OMI-derived, monitoring values and GMSMB modeling results in 2008 (only the areas with elevated concentrations are listed).

	Geographical coordinates		OMI Retrievals	OMI Derived	Monitoring Values	GMSMB Results	D1*	D2⁺	D3‡
	Longitude	Latitude	(molecs./cm^2)	ppb	ppb	ppb	%	%	%
San Diego	-116.97	33.46	5.04E+15	27.13	28.15	27.33	-3.6	-0.7	-2.9
	116.32	33.10	7.15E+15	20.50	29.46	27.85	-30.4	-26.4	-5.5
	116.74	33.32	7.34E+15	26.23	29.13	26.31	-10.0	-0.3	-9.7
	117.05	33.57	5.05E+15	24.72	25.73	26.11	-3.9	-5.3	1.5
	117.05	33.26	3.56E+15	13.69	19.65	13.66	-30.3	0.2	-30.5
	117.00	34.05	2.37E+15	15.53	17.32	16.48	-10.3	-5.8	-4.8
	117.67	33.79	2.85E+15	18.56	22.58	19.32	-17.8	-3.9	-14.4
South	-118.03	34.3	2.66E+15	20.38	20.64	20.78	-1.3	-1.9	0.7
Coast	-117.42	34	3.45E+15	14.27	27.25	16.68	-47.6	-14.4	-38.8
	118.61	34.12	2.49E+15	11.58	22.15	21.46	-47.7	-46.0	-3.1
	119.07	34.10	2.81E+15	17.31	19.36	18.73	-10.6	-7.6	-3.3
	116.04	34.27	2.54E+15	13.45	16.41	16.54	-18.0	-18.7	0.8
	118.21	34.08	2.19E+15	17.96	15.70	15.37	14.4	16.9	-2.1
	118.35	34.37	3.27E+15	20.03	18.20	17.41	10.1	15.0	-4.3

	118.19	34.45	7.45E+15	18.60	29.53	24.68	-37.0	-24.6	-16.4
	119.12	34.54	1.32E+15	9.19	10.94	11.84	-16.0	-22.4	8.2
Mojave	-116.91	34.19	2.27E+15	14.23	16.28	13.57	-12.6	4.9	-16.6
Desert	-119.15	37.22	2.06E+15	8.97	13.26	11.66	-32.4	-23.1	-12.1
	-116.39	34.07	1.86E+15	9.89	13.15	11.24	-24.8	-12.0	-14.5
	117.28	34.69	2.53E+15	12.73	14.30	13.46	-11.0	-5.4	-5.9
	117.15	34.80	1.84E+15	11.23	14.90	11.63	-24.6	-3.4	-21.9
	117.45	34.82	2.20E+15	14.88	14.93	12.16	-0.3	22.4	-18.6
	116.28	35.21	1.86E+15	14.32	15.36	13.26	-6.8	8.0	-13.7
	115.59	35.05	2.75E+15	16.92	17.23	14.82	-1.8	14.2	-14.0
South	-120.01	34.73	2.38E+15	11.23	13.16	12.87	-14.7	-12.7	-2.2
Center	119.94	35.18	2.38E+15	10.58	16.78	13.35	-36.9	-20.7	-20.4
Coast	120.44	34.84	2.46E+15	13.06	17.42	15.52	-25.0	-15.9	-10.9
	120.58	35.34	2.08E+15	10.00	14.23	16.27	-29.7	-38.5	14.3
	120.79	35.66	1.98E+15	7.62	13.67	13.81	-44.3	-44.8	1.0
San	118.91	35.74	2.97E+15	11.42	17.52	15.47	-34.8	-26.2	-11.7
Joaquin	119.27	35.36	1.21E+15	5.60	9.75	9.86	-42.6	-43.2	1.1
Valley	-119.77	36.78	2.59E+15	9.96	16.90	13.25	-41.1	-24.8	-21.6
	-118.83	36.49	1.56E+15	8.00	13.45	9.67	-40.5	-17.3	-28.1
	117.90	35.12	2.03E+15	7.82	11.51	8.35	-32.0	-6.3	-27.5

San	-122.91	38	2.91E+15	11.19	15.80	11.24	-29.2	-0.4	-28.9
Francisco	-122.62	38.25	2.27E+15	8.73	12.15	13.13	-28.1	-33.5	8.1
Bay	-122.29	38.36	1.18E+15	9.20	9.43	8.78	-2.4	4.8	-6.9
	-122.91	38.12	1.74E+15	6.69	10.35	7.75	-35.3	-13.6	-25.1

* The column D1 gives the differences between the OMI-derived ground-level NO_2 concentrations and the GMSMB modeling results. The mean difference is -16.6 %.

+ The column D2 gives the differences between the OMI-derived ground-level NO_2 concentrations and the in-situ surface measurements. The mean difference is -25.3 %.

‡ The column D3 gives the differences between the GMSMB modeling results and the in-situ surface measurements. The mean difference is -11.5 %.

APPENDIX B GEOS-Chem model

GEOS-Chem model is a tropospheric chemistry model which simulates the chemical composition of the atmosphere using a set of coupled non-linear partial differential equations of the type (Bey et al., 2001):

$$\frac{\partial C_i}{\partial t} + \boldsymbol{u}\cdot\nabla C_i = P_i - L_i, \quad i = 1, \ldots, N \tag{1}$$

where Ci (x, t) represents the spatio-temporal evolution of the concentration of species I, u(x,t) is the wind velocity, Pi = Pi ({Cj}, x, t) is the ensemble of atmospheric sources, and Li = Li ({Cj}, x, t) is the ensemble of atmospheric sinks. The species coupling shows up locally in Pi and Li, through the group of chemical species {Cj} that produce or react with species i. Pi and Li are also functions of the local radiative and meteorological environment. The number of species N is typically over 100.

In the simulation including detailed oxidant chemistry, the solution of the stiff system of ordinary differential equations (ODE):

$$\frac{\mathrm{d}C_i}{\mathrm{d}t} = P_i(\{C_j\}) - L_i(\{C_j\}), \quad i = 1, \ldots, N, \tag{2}$$

Re-write the chemistry operator as

$$\frac{\mathrm{d}C_i}{\mathrm{d}t} = P_i - k_i C_i, \quad i = 1, \ldots, N \tag{3}$$

since generally (though not always) the loss terms Li have first-order dependence on the species concentration Ci. Here ki is anHere ki is an effective loss rate constant.

At every grid box and time step t_n, calculate their concentrations $\{C_i^{n+1} = C_i\,(t_{n+1})\}$ at the next time step, $t_{n+1} = t_n + \Delta t$, in a coupled fashion using an efficient implicit ODE solver for stiff systems, to obtain the formula for the analytical solution:

$$C_i^{n+1} = \frac{P_i^*}{k_i^*} + \left(C_i^n - \frac{P_i^*}{k_i^*}\right) e^{-k_i^* \Delta t} \tag{4}$$

C_i is in the unit of molecules/cm^2, P_i is in the unit of molecules/cm^2•s, k_i is in the unit of /s.

The input for the GEOS-Chem model includes meteorological data which is from the Goddard Earth Observing System (GEOS) and emission data and tropospheric column retrievals. Table 1 lists the GEOS variables used as input to the model.

Table 1. GEOS Fields Used as Input to the GEOS-CHEM Model

Variable	Resolution [a]	Application
Wind vector	Inst 6 h	advection
Surface pressure	Inst 6 h	advection
Wet convective mass flux, detrainment[b]	Avg 6 h	convection
Mixed layer depth	Avg 3 h	boundary layer mixing
Temperature	Inst 6 h	chemistry
Specific humidity	Inst 6 h	chemistry
Cloud optical depth[b]	Avg 6 h	photolysis
Surface albedo	Inst 6 h	photolysis, dry deposition (snow cover)
Land-Water indices	Inst 6 h	dry deposition, lightning
Sensible heat flux	Avg 3 h	dry deposition
Solar radiation flux at surface	Avg 3 h	dry deposition
Surface air temperature	Avg 3 h	dry deposition, biogenic emissions
Surface wind (10 m altitude)	Avg 3 h	dry deposition, NO_x soil emissions
Friction velocity	Avg 3 h	dry deposition
Roughness height	Avg 3 h	dry deposition
Water condensation rate[c]	Avg 6 h	wet deposition
Total precipitation at the ground	Avg 3 h	wet deposition
Convective precipitation at the ground	Avg 3 h	wet deposition
Column cloud fraction[d]	Avg 3 h	biogenic emissions

Advection is computed every 15 min (2° × 2.5° horizontal resolution) or 30 min (4° × 5° horizontal resolution) with a flux-form semi-Lagrangian method.

Reference

Bey, I., Jacob, D.J., Yantosca, R.M., Logan, J.A., Field, B.D., Fiore, A.M., Li, Q., Liu, H.Y., Mickley, L.J., Schultz, M.G. 2001. Global modeling of tropospheric chemistry with assimilated meteorology: Model description and evaluation. Journal of Geophysical Research 106, 23073-23095.